UNIVERSITÀ
DEGLI STUDI
DI BRESCIA

DOTTORATO DI RICERCA IN
INGEGNERIA CIVILE, AMBIENTALE, DELLA COOPERAZIONE
INTERNAZIONALE E DI MATEMATICA

Settore Scientifico Disciplinare: ICAR/09-Tecnica delle Costruzioni

Recupero di Edifici Storici e Contemporanei

XXXVI CICLO

SEISMIC PERFORMANCE AND MODELLING OF REINFORCED CONCRETE FRAMES INFILLED WITH HORIZONTAL SLIDING JOINT DEFORMABLE INFILLS

DOTTORANDO:
Simone Pelucco

RELATORE:
Prof. Marco Preti

CO-RELATORE:
Dott.ssa Francesca Fantoni

SYNOPSIS

In recent years, the scientific community has been addressing the mitigation of post-earthquake damage. Numerous seismic events have demonstrated vulnerabilities related to the interaction of reinforced concrete frames with traditional masonry infills, resulting in in-plane and out-of-plane damage and mechanisms. Many solutions have been developed and experimentally tested to maintain their use while reducing their issues. However, their applicability requires further investigation to establish guidelines for the design of the infill and the structure, taking into account the local interaction with masonry panels. This paper aims to contribute to answering this need with reference to the horizontal sliding joint ductile infill solution proposed at the University of Brescia.

First of all, the effectiveness of this solution is further tested numerically by means of a refined FEM analysis in the case of different construction details and materials adopted. For example, the presence of a sliding joint at the base, the absence of the gap between the infill and the upper beam, and a continuous plaster layer over the entire wall. Particular importance is given to the use of a deformable material with elastic behaviour rather than a ductile material with plastic behaviour located at the contact between the infill and the columns. The stiffness of this material proved to be of fundamental importance for the overloading of the columns and the damage to the infill, while the filling of the gap between the infill and the upper beam mainly increases the lateral strength of the infilled frame. The analytical formulations describing the response of the infill and the overload on the columns, already available in the case of plastic contact material, are extended to the case of elastic material. They allow the calibration of an equivalent strut macromodel of the infill to be used in the global modelling of the frame.

Subsequently, the global behaviour of the structure in the presence of ductile infills and the ability of different analysis methods, linear and non-linear, to predict seismic demands are studied. In the non-linear analyses, the infills are modelled using concentric struts with non-linear behaviour. In the linear field, the use of elastic struts with equivalent secant stiffness is proposed. The case study is a planar reinforced concrete frame designed according to three ductility levels, each analysed in the bare and infilled configurations with three different infill thicknesses, with regular distribution, and without openings. The non-linear static analyses showed that the collapse mechanism and the overall ductile behaviour exhibited in the bare configuration are not significantly modified by the introduction of the infills; there is no activation of soft-storey mechanisms. The maximum top displacement and the maximum inter-storey drift estimated with the non-linear dynamic analyses are reduced by introducing the infills and increasing their thickness. Consequently, neglecting the contribution of the infills in the frame design leads to conservative

estimates of seismic deformation demands (top displacement and interstorey drift). The N2 method proved to be capable of estimating the results of non-linear dynamic analyses in infilled structures similarly to the bare configuration. For the case studies examined, the representation of the infills in the linear dynamic analyses using elastic struts proved to be effective in predicting deformation demands. The shear capacity design proved to be unable, in general, to cover the shear overload due to the infills; it must be considered explicitly in the design.
Non-linear static analyses are used to evaluate the repercussions of the presence of ductile infills on the capacity behaviour factor. Which, evaluated considering the overstrength in terms of base shear due to the presence of the infills, is not reduced compared to the bare configuration.

SOMMARIO

Negli ultimi anni, la comunità scientifica si sta occupando della mitigazione dei danni post-sisma. Numerosi eventi sismici hanno dimostrato le vulnerabilità legate all'interazione dei telai in calcestruzzo armato con i tamponamenti in muratura tradizionali, da cui conseguono danneggiamenti e meccanismi nel piano e fuori piano. Molte soluzioni sono state sviluppate e testate sperimentalmente per mantenerne l'utilizzo ma ridurne le problematiche. La loro applicabilità richiede, però, ulteriori indagini per definire delle linee guida per la progettazione del tamponamento e della struttura, considerando l'interazione locale con i pannelli in muratura. Questo lavoro si propone di contribuire a dare risposta a questa necessità, con riferimento alla soluzione di tamponamento duttile a giunti di scorrimento orizzontali proposta all'Università di Brescia.

Innanzitutto, l'efficacia di questa soluzione viene ulteriormente testata numericamente mediante una raffinata analisi FEM nel caso in cui si adottino dettagli costruttivi e materiali differenti; ad esempio, la presenza di un giunto di scorrimento alla base, del riempimento tra il tamponamento e la trave superiore e di un intonaco continuo su tutta la parete. Particolare importanza è data all''utilizzo di un materiale deformabile a comportamento elastico anziché duttile a comportamento plastico posizionato al contatto tra il tamponamento e le colonne. La rigidezza di questo materiale si è rivelata di fondamentale importanza per la sovrasollecitazione delle colonne ed il danno al tamponamento, mentre il riempimento del gap fra il tamponamento e la trave superiore incrementa principalmente la resistenza laterale del telaio tamponato. Le formulazioni analitiche, che descrivono la risposta del tamponamento e le sovrasollecitazioni sulle colonne, già disponibili nel caso di materiale di contatto plastico, vengono estese al caso di materiale elastico. Esse consentono la calibrazione di un macromodello a puntone equivalente del tamponamento da utilizzare nella modellazione globale del telaio.

Successivamente vengono studiati il comportamento globale della struttura in presenza di tamponamenti duttili e la capacità di diversi metodi analisi, lineari e non lineari, di prevedere le domande sismiche. Nelle analisi non lineari i tamponamenti sono modellati mediante puntoni concentrici a comportamento non lineare. In ambito lineare si propone l'utilizzo di puntoni elastici aventi rigidezza secante equivalente. Il caso studio è un telaio piano in calcestruzzo armato progettato secondo tre livelli di duttilità, ciascuno di essi è analizzato nelle configurazioni nuda e tamponata con tre diversi spessori di pannello, con distribuzione regolare ed in assenza di aperture. Le analisi statiche non lineari hanno mostrato che il meccanismo di collasso ed il comportamento duttile complessivo esibiti nella configurazione nuda non vengono significativamente modificati dall'introduzione dei tamponamenti, non vi è l'attivazione di meccanismi di piano debole. Lo spostamento massimo in

sommità ed il massimo drift di interpiano stimati con le analisi dinamiche non lineari si riducono introducendo i tamponamenti ed aumentandone lo spessore. Conseguentemente, trascurare il contributo dei tamponamenti nella progettazione del telaio porta a stime cautelative delle domande deformative sismiche (spostamento in sommità e drift d'interpiano). Il metodo N2 si è rivelato essere in grado di stimare i risultati delle analisi dinamiche non lineari nelle strutture tamponate similmente a quanto avviene nella configurazione nuda. Per i casi studio analizzati, la rappresentazione dei tamponamenti nelle analisi dinamiche lineari mediante puntoni elastici si è rivelata efficace nel prevedere le domande deformative. La progettazione a taglio in capacità si è rivelata non essere in grado, in generale, di coprire la sovrasollecitazione a taglio dovuta ai tamponamenti, essa va considerata esplicitamente nella progettazione.
Le analisi statiche non lineari sono state utilizzate per valutare le ripercussioni della presenza di tamponature duttili sul fattore di comportamento capacità. Quest'ultimo, valutato tenendo conto della sovraresistenza in termini di taglio alla base dovuta alla presenza dei tamponamenti, non subisce riduzioni rispetto a quanto si ottiene nella configurazione nuda.

CONTENTS

SEISMIC PERFORMANCE AND MODELLING OF REINFORCED CONCRETE FRAMES INFILLED WITH HORIZONTAL SLIDING JOINT DEFORMABLE INFILLS

1 INTRODUCTION

1.1 Motivation and scope of the research

In the last decades, the research community has been searching for construction solutions capable of mitigating post-earthquake damage. Reinforced concrete (RC) frames traditionally infilled by non-structural rigid masonry panels have demonstrated their seismic vulnerability in several earthquake events [1], [2], [3], [4], due to the interaction between the infill and the frame. Starting from the idea of Langenbach (2007) [5] and the work of Mohammadi and Akrami (2010) [6], a family of deformable infills was developed. The peculiarity of such proposals is to both reduce the high shear action demand on the columns and the significant in-plane damage of the traditional interacting masonry infills, keeping the advantage of the use of masonry panels for acoustic and thermal performances. Traditional masonry infills are characterised by high strength and stiffness but low deformation capacity. The result is the triggering of undesired collapse mechanisms, such as, for example, the soft storey or column shear collapse (Figure 1.1). The infill collapse is caused by the in-plane damage of the infill, which rapidly reduces the out-of-plane strength and stability of the infill, with possible consequent overturning. Seismic events showed [1] that the out-of-plane collapse of the infills may also occur in the upper storeys, where higher accelerations arise (Figure 1.2).

Figure 1.1: Example of collapse of infills at low storeys [1] a) and soft-storey mechanisms [4] b) after the 2009 L'Aquila earthquake.

Figure 1.2: Example of out-of-plane collapse of infills at upper levels after the 2009 L'Aquila earthquake [1].

Deformable infill construction techniques available in the literature [6], [7], [8], [9], [10], [11], [12], [13], [14], [15], [16], [17], [18], [19], [20], [21], [22], [23] have been tested on single-story, single-bay frames, with promising results. An example of infill with horizonal sliding joints is reported in Figure 1.3.

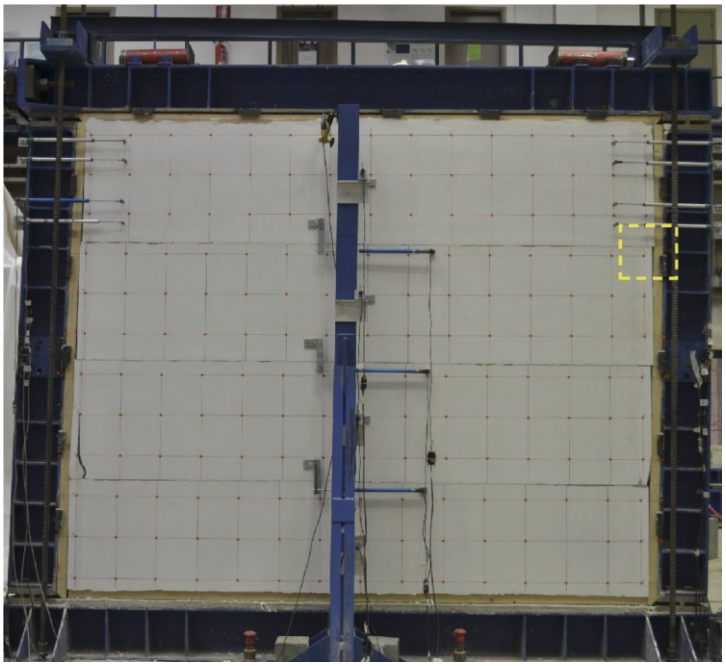

Figure 1.3: Deformed configuration at 2.5% drift level of the infill solution with horizontal sliding joints described in Preti et al. (2015) [15]

In order to define design guidelines, specific studies on the influence of construction details and related design parameters are required. The knowledge of the effect of such parameters on the local and global response of infilled frames is still lacking, as it is a design strategy and a well-established method of analysis. The thesis presents a numerical parametric study and an analytical formulation to quantify the infill in-plane response of a specific deformable infill solution with sliding joints, first proposed by Preti et al. (2012) [16]. The analytical description of the infill response allows the calibration of a simplified strut macromodel of the infill, which is used in the global analysis of infilled frames. Planar, regularly infilled RC frames are examined. The effects on the global behaviour of the presence of such infills are evaluated by non-linear dynamic and static analyses. The N2-method, commonly used to predict seismic demands by means of nonlinear static analyses, is tested for its applicability in the presence of ductile infills. Nonlinear dynamic analyses allow for evaluating the negligibility of infills in the design phase of regularly infilled frames. A modelling approach for ductile infills in linear dynamic analyses is proposed and tested to capture the deformation demands estimated by nonlinear analyses. Finally, the increase in shear action on the columns due to the thrust of the infills and the repercussions on the behaviour factor are examined.

1.2 Brief state of the art of deformable infills

The reduction in infill-frame interaction and infill damage has been under investigation in the last few years.
In the literature, two main approaches are followed. On one side, the infill is strengthened to provide it with the strength required by the seismic excitation. In this way, the infill becomes a load-bearing element coupled to the frame system, and it must be designed for this purpose. A discussion can be found in Furtado et al. (2020) [24]. On the other side, the reduction of the infill-frame interaction is assessed by decoupling the infills from the frame or by their weakening aimed at accommodating the frame sway deformation. Many solutions have been proposed in the literature, and the main goals are the following:

- Reduction of the in-plane stiffness of the infill to reduce the infill-frame interaction.
- Reduction of the infill damage.
- Provide ductility to the infill behaviour.
- Provide energy dissipation to the structure.

By following these objectives, some issues must be considered. The reduction in the in-plane (IP) stiffness may affect the out-of-plane (OOP) response. Specific construction details are required to constrain the infill in the OOP direction. While a reduction of stiffness in the IP direction could also correspond to a reduction of stiffness in the OOP direction, its period of vibration could be lengthened into the acceleration amplification range. The achieving of ductile behaviour can be followed by using the inelastic properties of the materials, but the corresponding damage in the in-plane may affect the OOP strength. The use of the dissipation energy contribution of the infills in the structural design collides with their non-structural nature.
The proposed solutions can be subdivided into the following main categories:

- Decoupled or isolated infills.
- Ductile panel infills.
- Hybrid solutions.

Regarding the decoupled and hybrid solutions, a brief discussion is presented in the following sections, while an emphasis is placed on the ductile panel infills, which is the objective of this study.

1.2.1 *Isolated or decoupled infill*

The infill is fully [9], [12], [13], [19], [25] or partially [11] isolated from the frame by interposing a gap. The OOP constraint is made by filling the gap with a soft material or by using mechanical links.
An example of a fully isolated infill is described in Marinković and Butenweg (2019) [13]. As represented in Figure 1.4, infill is isolated on all four sides. At the base, elastomeric strips allow upward movements but prevent OOP ones. At the columns and top beam sides, infill is connected to the frame by means of specific U-shaped elastomeric elements, characterised by low stiffness in the IP direction and high stiffness in the OOP one. A sliding surface is provided with respect to the columns and the top beam. Infill is constructed as usual in common practice, and it is glued to the elastomeric elements. The system was tested by applying both IP and OOP loads. The comparison of the global response to that of a bare frame and a traditionally infilled frame is represented in Figure 1.5. The infill activation was delayed, the damage to the infill was reduced and occurred at a drift level equal to 1.8%, and interstorey drift of more than 3% was investigated. Furthermore, the use of elastomeric materials allows for higher damping with respect to traditional masonry infill without experiencing damage. Despite all this, for large drift levels, the infill activates and adds a lateral strength contribution.

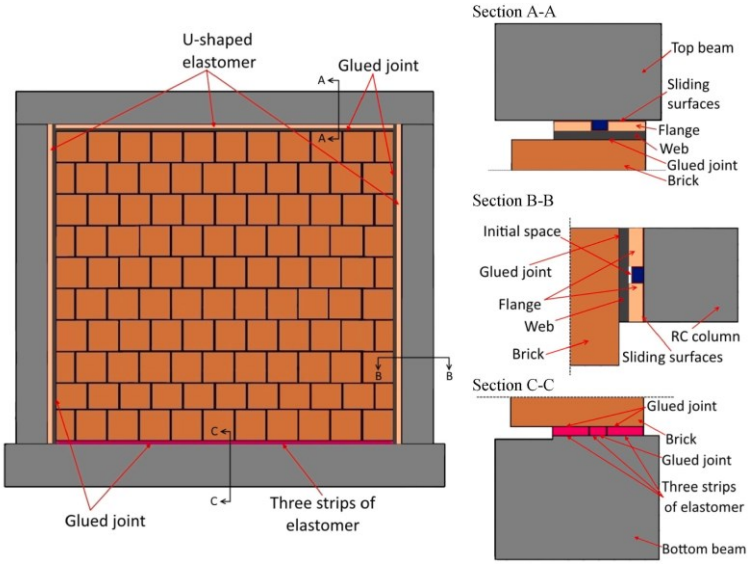

Figure 1.4: Representation of the INODIS decoupling system proposed in Marinković and Butenweg (2019) [13].

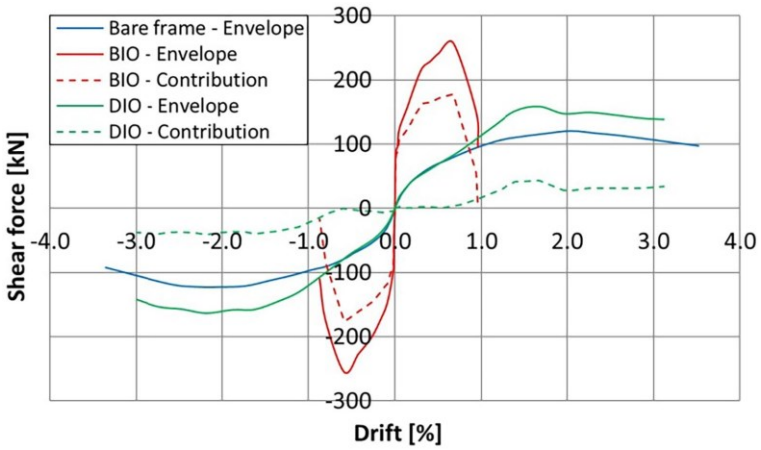

Figure 1.5: Comparison of lateral force versus drift curve for the bare frame, the traditional infilled solution (BIO), and the INODIS system (DIO), depicted from Marinković and Butenweg (2019) [13].

The same authors tested another solution [12] based on the detachment of the infill with respect to the frame by means of elastomeric strips on columns and the top beam and the use of lateral shear connectors to avoid the OOP displacement. Good performances were reached in the IP direction, but the connectors failed in the OOP. Another solution was proposed by Lyu et al. (2022) [11], which is graphically represented in Figure 1.6. A gap filled by polystyrene was ensured between the infill and columns, while the connection to the top beam ensured strength and stiffness for medium-low displacement levels. Infill is strengthened by a layer of highly ductile concrete. In the absence of the top gap, the infill is directly involved in the load-bearing mechanism through the direct shear transfer from the beam to the infill. High lateral strength is reached, and, as shown in Figure 1.7, a following strength loss occurs.

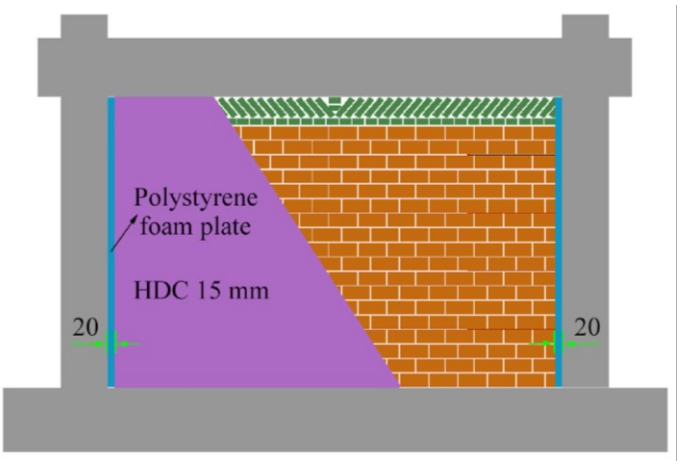

Figure 1.6: Isolated solution proposed by Lyu et al. (2022) [11], a gap is ensured between the infill and the columns, and the infill is strengthened and rigidly connected to the top beam.

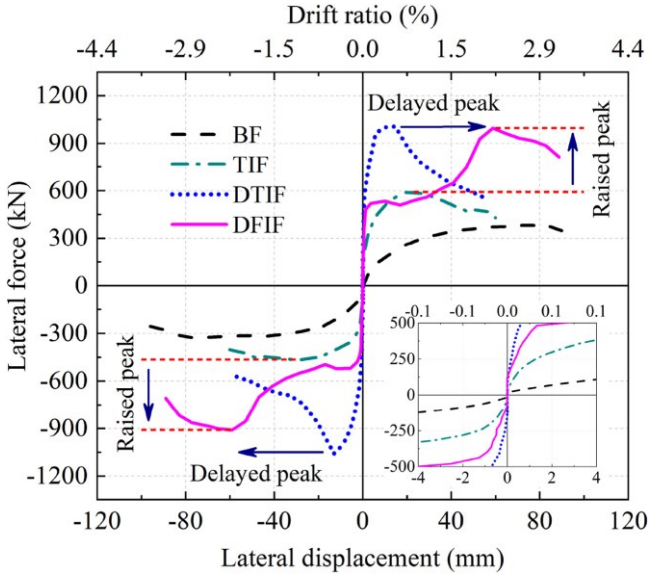

Figure 1.7: Comparison of lateral force versus drift curve for the bare frame (BF), the traditional infilled solution (TIF), the strengthened infill (DTIF), and the isolated system (DFIF), depicted from Lyu et al. (2022) [11].

1.2.2 *Ductile panel Infills*

Infill panels are made ductile by allowing the localised or spread relative displacement of masonry blocks. Infill panels can be subdivided by horizontal [6], [14], [15], [16], vertical [17], [18], or both of them [7] sliding joints that could be made by specific elements with low friction properties or deformable layers. In such a way, instead of one macro strut, multiple struts originate in the infill, allowing for a reduction of the local strain demand on the contact material. Soft material or low-strength plastic material interposed between the infill and the columns prevents the infill from the damage. Specific construction details, such as shear keys, are provided to ensure the OOP arching mechanism and avoid the OOP collapse. Other solutions involve the replacement of the mortar layer by means of dry joints [8], [10], [26] or deformable plastic joints [20], [21].
Here, the two proposals that will be considered in this study are further described.
Preti et al. (2015) [15] proposes the solution graphically represented in Figure 1.8: horizontal sliding joints are introduced in the infill to create preferential sliding planes between each masonry subpanel. Specifically, three sliding joints subdivide the infill into four elements; furthermore, a sliding joint is provided at the base of the infill. In such a way, reduced strength and stiffness with respect to traditional masonry infills and ductile behaviour in the IP response are reached. The hierarchy of strength principles is applied to provide a sliding mechanism and avoid the shear one that characterises traditional masonry infills. Specific wooden contact elements are placed at the infill-column interfaces. They provide the in-plane detachment of the infill, but, at the same time, a shear key constrains the infill in the OOP direction. Bending mechanisms generate into each subpanel in the horizontal direction, finding supports in correspondence with the shear keys, and a fibre-reinforced plaster ensures the required strength. Another function of the wooden board at the contact between the infill and the columns is that its low plastic strength prevents the masonry from local damage at the subpanel corners when the lateral deformation mechanism is activated. By ensuring a gap between the infill and the top beam, the confining effect exerted on the infill by the beam in the sway mechanism and the corresponding increase in the friction mechanism are avoided.

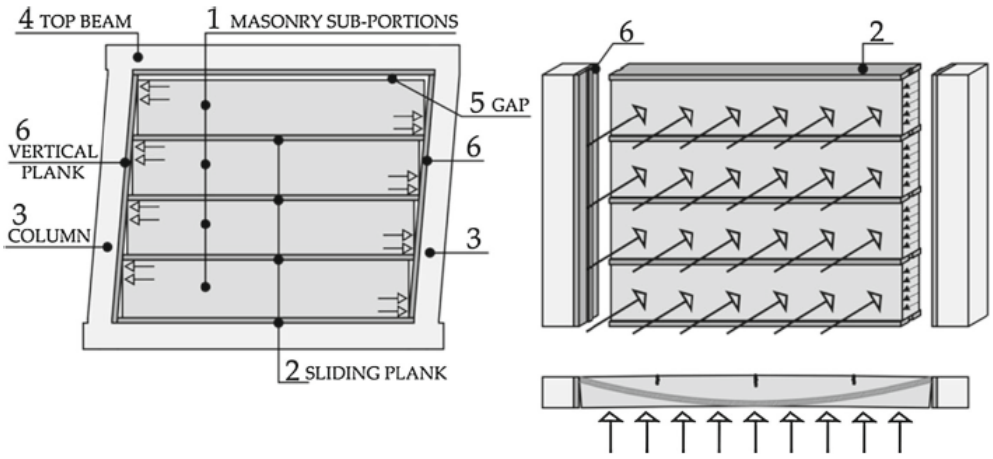

Figure 1.8: Concept of the in-plane sliding mechanism and of the resisting OOP mechanism of the ductile infill described in Preti et al. (2015) [15]

This solution was tested in a hinged steel portal frame; consequently, the influence of infill-frame interaction on the response is limited. Negligible damage was recognised until drift levels of 2.5% in plane drift, as shown in Figure 1.10. After this drift level, the specimen was successfully subjected to an out-of-plane test, and successively, a 3% in-plane drift level was reached without collapse. Wooden lateral boards were effective in limiting the damage to the corners of the masonry subpanels. As shown in Figure 1.9, a stable hysteretic response and no strength degradation are exhibited. By comparing the results to those of traditional infill, both stiffness and strength are strongly reduced, and as a consequence, the infill-frame interaction is also reduced.

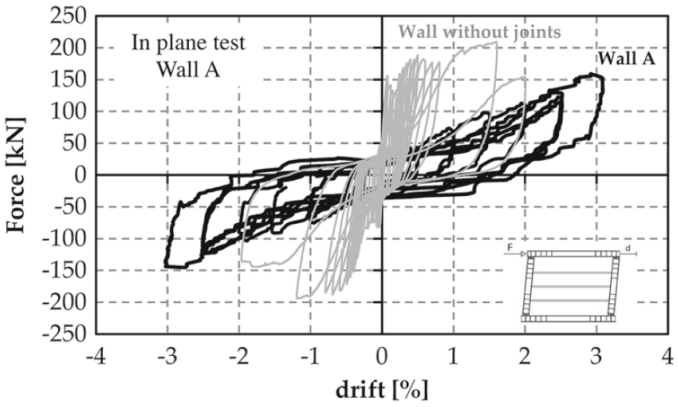

Figure 1.9: Comparison of the global response of the infill with sliding joints and the traditional one, depicted from Preti et al. (2015) [15].

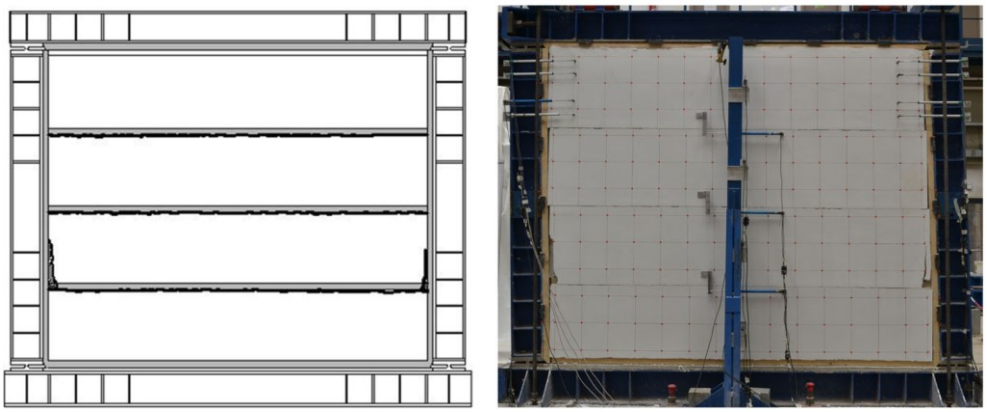

Figure 1.10: Crack pattern and photography of the tested infill after the third in-plane cycle at 2.5% drift, depicted from Preti et al. (2015) [15]

Successively, Morandi et al. (2018) [14], following the same approach, proposed the use of different construction details, represented in Figure 1.11. Horizontal sliding joints are realised by corrugated plastic elements, and the infill is directly constructed on the base beam. In this case, the infill-frame interaction is reduced by the use of a specifically designed mortar with an extremely low elastic modulus that fills the gap between the infill and the columns. The same mortar fills the top gap between the infill and the beam. The OOP stability is ensured by the use of "omega" steel profiles fixed to the columns and specific C-shaped clay elements placed at the infill edges. The flexural strength of the masonry subpanels in the OOP direction is guaranteed by a layer of fibre-reinforced plaster. Its thickness is reduced on the sliding joints. This solution was tested in an infilled RC portal frame configuration; consequently, the response also accounts for frame contribution. As shown in Figure 1.13, the results confirmed those of Preti et al. (2015) [15]: the global response is ductile and stable until large drift levels. The damage pattern of the infills is immediately characterised by cracks along the sliding joints, associated with the initial peak in the global response. While at high drift levels, it is limited to the plaster surrounding the sliding joints, the infill-column interfaces, and the subpanel corners. Figure 1.10 shows the damage pattern at 3.0% drift level, where the spalling of the concrete cover at the bottom of the columns is visible. At the end of the test (3.0% drift level), the infill was subjected to a dynamic out-of-plane test [27], and it did not manifest any significant damage up to a very large level of acceleration.

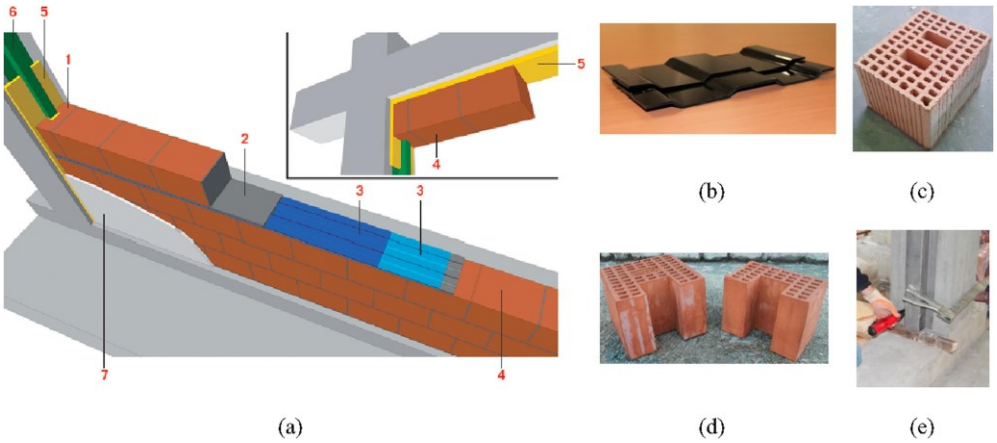

Figure 1.11: (a) Details of the innovative masonry infill with sliding joints: 1.(d) C-shape units; 2. mortar bed-joints; 3. (b) sliding joints; 4. (c) clay units; 5. interface joints; 6. (e) shear keys; 7. Plaster. Depicted from Morandi et al. (2018) [14].

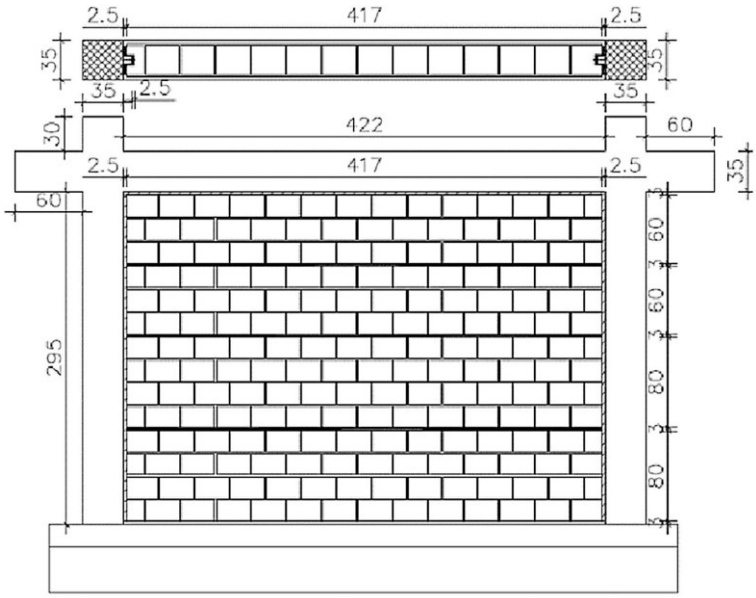

Figure 1.12: Representation of the infilled RC portal frame tested, depicted from Morandi et al. (2018)[14].

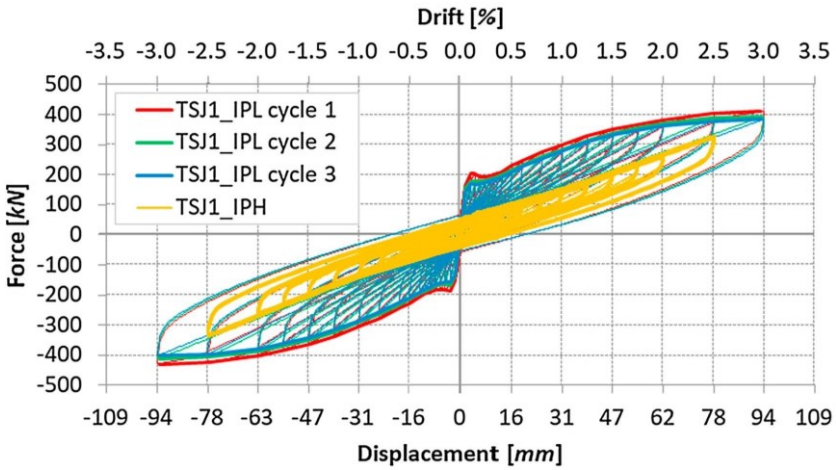

Figure 1.13: Force-displacement curve of the infilled frame for low velocity test (IPL) and the following high velocity test (IPH), depicted from Morandi et al. (2018)[14].

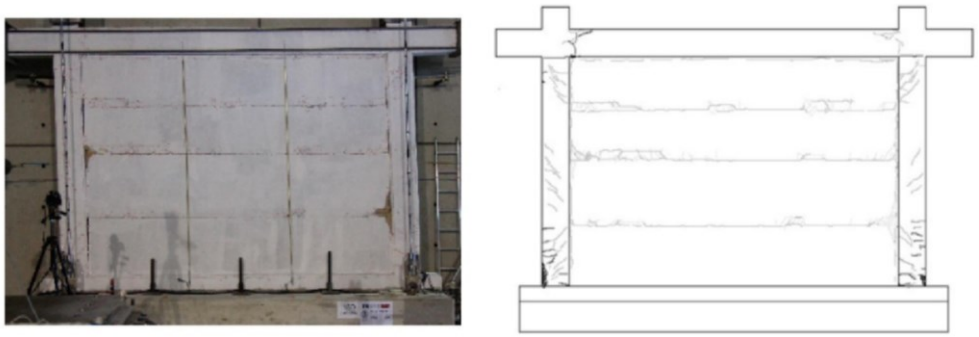

Figure 1.14: Crack pattern and photography of the tested infill at 3.0% drift, depicted from Morandi et al. (2018) [14].

1.2.3 *Hybrid solutions*

The previously described solutions can be combined to limit the gap required by decoupling solutions. An example is described by Zhang et al. (2023) [23] (Figure 1.15), where the infill consists of three horizontal prefabricated panels subdivided by sliding joints. The lower and upper panels are connected to the adjacent beams by steel connectors, and they move simultaneously. The inner panel slides between the outer panels, and it is connected for OOP actions by mid-height steel connectors. Soft material fills the gap and decouples the infill and frame lateral responses. No in-plane excessive damage appears until a drift level equal to 4%. Figure 1.16 shows a stable and ductile behaviour similar to that of the bare frame. Other possible solutions consist of the subdivision of the infill into vertical subpanels by means of soft material [22]. Soft material fills the gap between the vertical panels and the columns, while the connection to the top beam allows for the in-plane rocking mechanism. Bolis et al. (2020) [28] proposed a weakening solution for existing infills where the infill is isolated from the upper part of the columns and the top beam. A specific connection is provided at the top beam that, at the same time, constrains vertical and OOP displacements but allows in-plane sliding.

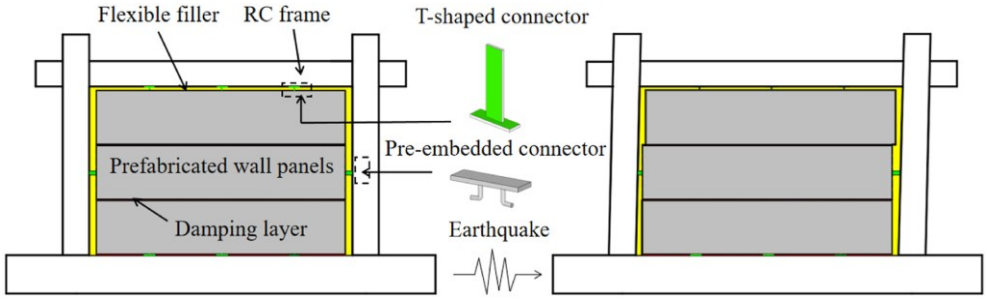

Figure 1.15: Hybrid solution with prefabricated damping wall panels with sliding joints proposed by Zhang et al. (2023) [23].

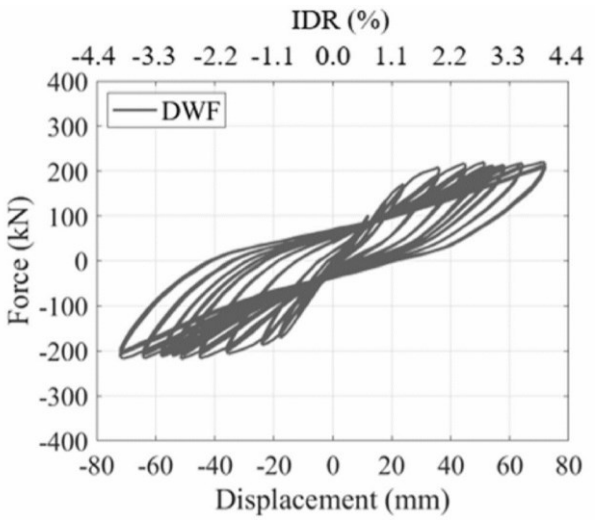

Figure 1.16: Force-displacement curve of the infilled frame, depicted from Zhang et al. (2023) [23].

1.2.4 *Numerical modelling of ductile infills*

According to Lourenco (1996) [29], the finite element analysis of masonry structures can be done at four different complexity levels:

- Detailed micro-modelling: units and mortar in the joints are represented by continuum elements, whereas the unit-mortar interface is represented by discontinuous elements.
- Simplified micro-modelling: units are represented by continuum elements, whereas the behaviour of the mortar joints and unit-mortar interface is lumped into discontinuous elements.
- Macro-modelling: units, mortar, and unit-mortar interfaces are smeared out in the continuum.
- Mono-dimensional macro element: infill global behaviour is modelled by one or more specifically calibrated struts.

As the modelling strategies become more detailed, the mechanical characteristics and the calibrations required become more complex. Detailed modelling approaches are required for research purposes since extended experimental tests are prevented by the times and costs required. Regarding deformable infills, many authors [30], [31] used detailed modelling approaches to numerically study the influence of the main design parameters of the proposed solutions. Referring to the specific solution of deformable infill with horizontal sliding joints, a discussion is presented in Section §2.1.1.
These approaches are not suitable for representing the global role of ductile infills when inserted into models of full-frame structures. Dhir et al. (2022) [32] proposed a macro-modelling approach (Figure 1.17) where the infill with sliding or rubber joints is represented by articulated quadrilaterals that interact between them and with the surrounding frame by mono or bidirectional links. The infill-frame interaction is directly accounted for, and the internal actions in the frame elements are also directly available. An easier approach was proposed by Preti et al. (2019) [33] to represent the deformable infills designed according to the construction details proposed at the University of Brescia [15]: a couple of nonlinear diagonal struts are calibrated by means of analytical models to represent the overall infill contribution. This approach will be used in this work, in Section §2.1.2 and Section §3.1.2 a brief discussion of the analytical model that represents the infill in-plane global behaviour and its application in the simplified modelling approach are presented, respectively. This simplified approach is applicable to entire frame structures for the investigation of the overall performance of structures infilled by such systems. The performance of sliding joint-infilled structures was investigated by Di Trapani et al. (2020) [34] by means of incremental dynamic analysis. The ductile behaviour at the level of a single

infill is reflected in the full structure. Sliding joint infilled frame achieved collapse in very similar spectral acceleration with respect to bare frame, and the maximum interstorey drift recorded is of the same magnitude. The first shear cracking is anticipated due to the interaction with the infills, but it is largely postponed with respect to those obtained by the traditional infilled structure. The operational and damage limitation limit states occur at similar intensity measures for traditional and sliding joint-infilled structures. But for ductile solutions, the interstorey drift limit is strongly larger than that defined for traditional infilled structures. Expected annual loss results in about half of the traditionally infilled frame. As a consequence, sliding joint infills result in an effective solution to improve reliability and reduce losses during the service of RC frame structures.

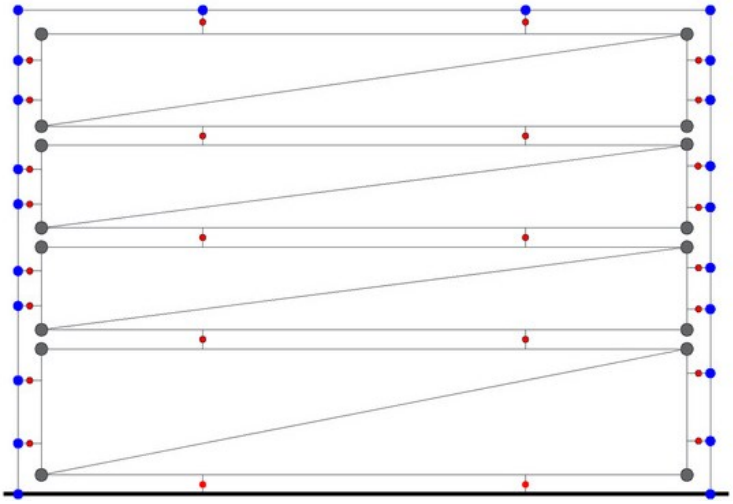

Figure 1.17: Discretisation scheme proposed by Dhir et al. (2022) [32] to represent the infill-frame interaction of infills with sliding joints.

1.3 Thesis outline

Starting from the work previously done and described in the literature about the deformable infill solution with horizontal sliding joints proposed by Preti et al. (2012, 2015) [15], [16], to pursue the objectives described in Section §1.1, the thesis is structured as follows.

Chapter 2 describes the extension of the numerical parametric analysis already done to study different construction details for deformable infills with horizontal sliding joints. Furthermore, it extends the analytical model previously proposed to describe the behaviour of the infill to the use of elastic, deformable material as contact material at the lateral joints. Firstly, a brief review of a detailed numerical modelling approach to simulate deformable infills with sliding joints and the analytical model originally proposed to represent the infill behaviour is described in Section §2.1. Successively, a new baseline model is defined by considering a deformable, elastic material at the lateral contact joints. Different design choices are numerically investigated, and the calibration with an experimental test available in the literature is presented in Section §2.2. Then, in Section §2.3, the baseline model is adopted to investigate the influence of the main design parameters by means of a numerical parametric analysis, and the main results and design suggestions are discussed. Finally, in Section §2.4, the existing analytical model is modified to account for an elastic material at the contact between the infill and the columns. The proposal accounts for the stiffness of the elastic material, the parameter that is revealed to be of main importance in the parametric analysis. The analytical model is suitable for representing infill in simplified strut macromodels.

Chapter 3 investigates the contribution of ductile infills to the global structural frame response, considering planar frames designed according to different ductility levels and infilled with ductile infills with different panel thicknesses. A brief literature review on the modelling of RC frame structures at the global level and the simplified modelling of ductile infills is presented in Section §3.1. The numerical framework constructed to manage the analyses is briefly discussed in Section §3.2. The modelling choices adopted for the representation of the RC frame in static and dynamic fields, beyond the simplified representation of the infills, and a modelling proposal to account for deformable infills in linear elastic analyses are presented in Section §3.3. The case studies considered are presented in Section §3.4, while the results of the numerical analyses are discussed in Section §3.5.

Finally, Chapter 4 summarises the main results of the work and suggests some topics that could be explored further.

2 NUMERICAL MODELLING AND ANALYTICAL PREDICTION OF A DUCTILE INFILL WITH HORIZONTAL SLIDING JOINTS

The chapter discusses the possibility of predicting the in-plane seismic response of ductile infill with sliding joints by means of design-oriented equations and simplified modelling. The parametric analysis on the role of design parameters in such infills conducted by Bolis et al. (2017) [30] and briefly reported in §2.1.1 is here extended to account for the role of some construction detailing alternatives. In particular, the study focuses on the option of using an elastic, deformable contact material in the lateral vertical joints instead of a yielding material with a cap plastic strength, as proposed by Preti et al. (2015) [15]. This option affects the contact forces between the panel and the frame column. Such forces are not limited by the cap in the compressive contact stress in this case; thus, they can exceed the local strength of the masonry panel, inducing undesired and premature local crushing. The study also discusses the effect of filling the top joint between the infill and the beam with similar elastic deformable material. In this case, a vertical confining action on the infill arises during the sway mechanism, which may jeopardize the subpanel sliding along the horizontal joint with consequent shear overstress of the masonry panels. A parametric study on the role of the contact material stiffness is discussed.
Other details and related design parameters are considered, namely:

- Presence of a mortar joint at the base of the masonry panel on the supporting beam instead of a sliding joint, which introduces a concentration of the contact force at the first masonry subpanel corner in contact with the windward column, with a concurrent reduction of the infill thrust on the leeward one.
- Presence of continuous plaster on both sides of the panel with a continuous layer above the sliding joints, which adds an initial strength contribution to the infill before the triggering of the sliding mechanism.

The study of these construction details is meant to extend the results obtained by Bolis et al. to other infill wall layouts adopted in some applications available in the literature [14], [22], [23]. In particular, the infill tested by Morandi et al. (2018) [14] will be used to validate the effectiveness of the proposed modelling choices.

2.1 Literature review

2.1.1 Detailed numerical modelling of ductile infills

The bidimensional modelling scheme adopted in Stavridis and Shing [35] to simulate the in-plane behaviour of traditional infilled RC frames was extended in Bolis et al. (2017) [30] to account for the sliding joints. The model, developed in the FEAP environment [36], uses a combination of smeared-crack and interface elements to represent both the smeared and discrete cracks that occur in the RC frame and in the infill.

The non-linear behaviour of the smeared crack elements is governed by the constitutive law defined in Lotfi and Shing (1991) [37]; the constitutive law adopted for the interface elements is based on the later proposal of Lotfi and Shing (1994) [38]. Their representation is reported, respectively, in Figure 2.1 and Figure 2.2.

The yield criterion of the interface elements is represented by a three-parameter hyperbolic surface expressed as described in Eqs. (2.1-1) and (2.1-2).

$$F(\sigma, q) = \tau^2 - \mu^2 \cdot (\sigma - s)^2 + 2r \cdot (\sigma - s) \tag{2.1-1}$$

$$r = (c^2 - \mu^2 s^2)/2s \tag{2.1-2}$$

Where μ is the slope of the asymptotes of the hyperbola, s is the tensile strength, r is the radius of the hyperbola at the vertex, and c is the cohesion. The evolution of the three internal variables is described in Eqs. (2.1-3), (2.1-4), and (2.1-5).

$$s = s_0 \cdot \left(1 - \frac{k_1}{G_f^I} - \frac{k_2}{G_f^{II}}\right) \geq 0 \tag{2.1-3}$$

$$r = r_r + (r_0 - r_r) \cdot e^{-\beta k_3} \tag{2.1-4}$$

$$\mu = \mu_r + (\mu_0 - \mu_r) \cdot e^{-\alpha k_3} \tag{2.1-5}$$

Where k_1, k_2, and k_3 are the work-softening variables, G_f^I and G_f^{II} are the mode-I and mode-II fracture energy, α and β are two material parameters that control the rate of

softening, and the subscripts 0 and r indicate the parameters of the initial and final yield surface, respectively.

The base and top RC beams of the frame are modelled by means of four-node smeared-crack elements. Columns are modelled using three-node smeared-crack elements connected by interface elements. Truss elements represent the longitudinal and transverse reinforcements. The masonry is modelled by four-node smeared crack elements connected by interface elements that represent the horizontal and vertical mortar joints and the capability of a vertical middle brick rupture. The modelling scheme is synthetically represented in Figure 2.3.

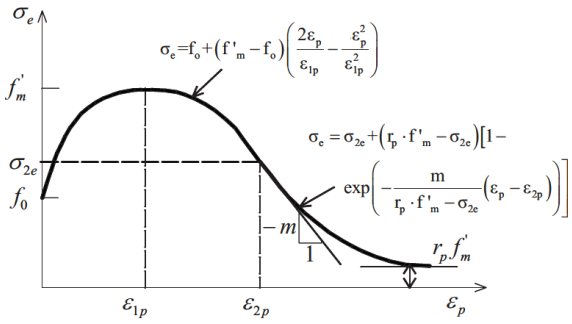

Compressive behaviour of the plasticity model

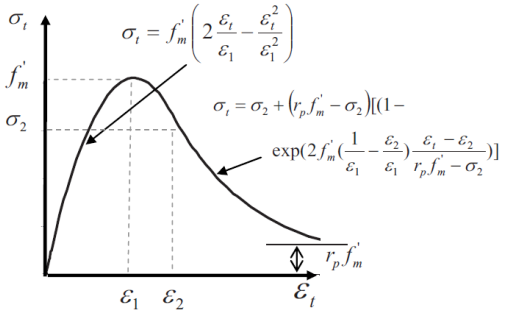

Compressive behaviour of the orthotropic model

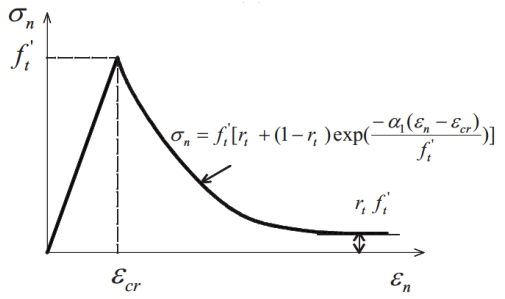

Tensile behaviour of the orthotropic model

Figure 2.1: Constitutive model for the smeared-crack element, depicted from Stavridis and Shing (2010) [35]

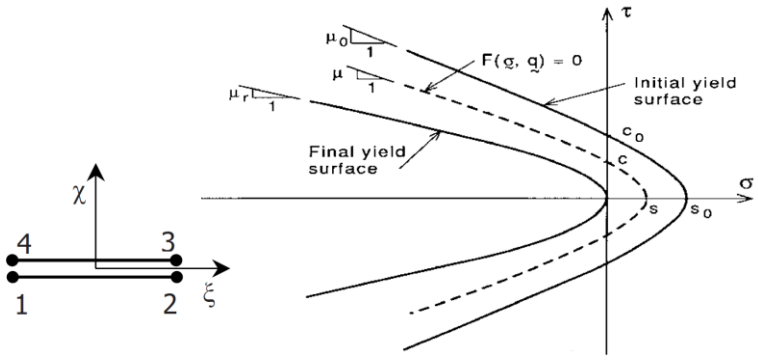

Figure 2.2: Geometry and yield criterion of the interface element, depicted from Stavridis and Shing (2010) [35]

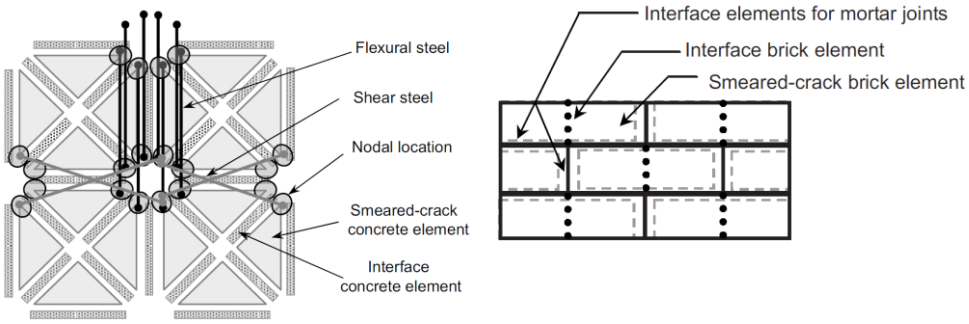

a) *b)*

Figure 2.3: Discretization scheme of the RC columns a) and of the masonry infill b), depicted from Stavridis and Shing (2010) [35]

The extension of the model to the representation of masonry infills partitioned by sliding joints [15] required some modifications, proposed in Bolis et al. (2017) [30].

- The nodes of the top RC beam and of the infill are not connected to represent the top gap.
- Four-node smeared crack elements are located between the RC columns and the infill to represent the lateral wooden boards working as lateral joints. These elements are connected to the infill by interface elements to represent the vertical sliding and the compression only contact.
- Horizontal interface elements, properly calibrated, represent the horizontal sliding joints.

Further details about the modelling scheme and the material calibration can be found in Bolis et al. (2017) [30] and Stavridis and Shing (2010) [35].

The proposal was validated first by simulating the experimental tests of the RC bare frame and of the traditional infilled one described in Calvi and Bolognini (2001) [39]. The results are reported in Figure 2.4. Afterwards, the simulation of the experimental tests conducted on a steel frame infilled by a solid infill and an infill with sliding joints [15] allowed to validate the modelling approach of the ductile masonry infill. The results are reported in Figure 2.5.

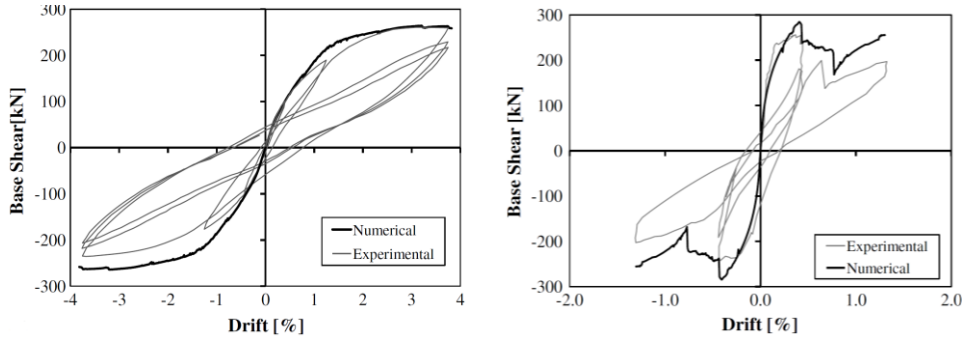

a) *b)*

Figure 2.4: Comparison of the numerical and experimental results of the bare a) and infilled b) frames, depicted from Bolis et al. (2017) [30].

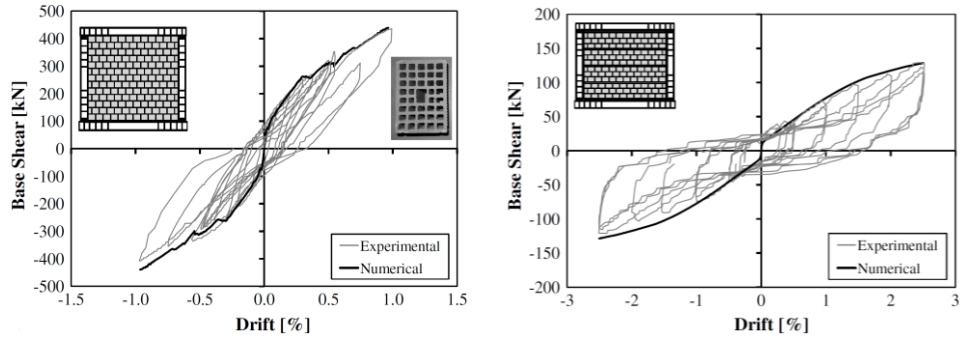

a) *b)*

Figure 2.5: Comparison of the numerical and experimental results of the solid infill a) and of the infill with sliding joints b), depicted from Bolis et al. (2017) [30].

Since the RC bare frame and the infill with sliding joints were well represented, the RC frame of Calvi and Bolognini (2001) [39] filled with the ductile infill described in Preti et al. (2015) [15] was tested as case study. The solid infill configuration (same mechanical properties but without sliding joints, vertical boards, and top gap) is also modelled for comparison. The numerical results reported in Figure 2.6 show that the

solid infill configuration is characterised by high initial stiffness, high peak strength, and a high level of damage that results in a significant lateral strength loss. The infill with sliding joints exhibits a behaviour characterised by an initial stiffness higher than that of the bare frame but lower than that of the solid infilled frame. As the friction along the horizontal joints is overcome, the slide of the subpanel starts, and the lateral stiffness reduces. Then, a ductile behaviour characterised by the rigid translation of the masonry subpanels follows, until a large drift level. The low compressive strength of the vertical wooden boards prevents the crushing of the infill. The stress distribution in the infill (Figure 2.7) is altered by the presence of the sliding joints. A load-transfer mechanism develops in each sub-portion, starting from the top of the windward side to the bottom of the leeward side.

The comparison of the shear action profiles on the columns for the three configurations (bare, solid infilled, and infilled with sliding joints) is reported in Figure 2.8. The drift level, equal to 0.8%, at the peak column shear action for the solid infill is considered. They are obtained by reading the shear action at the extremes of the columns and considering, in the horizontal equilibrium, the contact forces acting along the column height. The shear action is amplified in both the infilled configurations with respect to the bare frame; the maximum values occur at the top of the windward column and at the base of the leeward column. Figure 2.9 shows the trend of the maximum column shear action for the two infilled configurations; until the peak strength is reached, the column shear action in the solid infilled configuration is higher than in the configuration with sliding joints. Then, the column shear in the ductile infill exceeds that of the traditional infill, but at large drift levels.

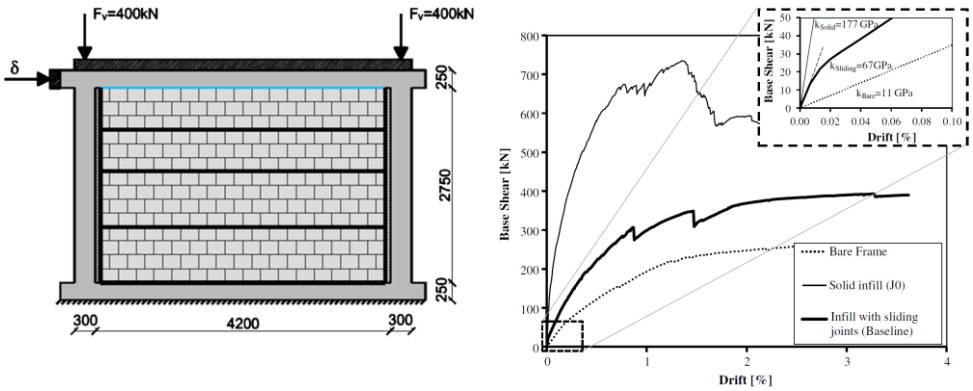

a) *b)*

Figure 2.6: Numerical model of the ductile-infilled RC frame a) and comparison of the numerical lateral strength vs. lateral drift of the bare RC frame, of the solid-infilled frame, and of the ductile-infilled frame b), depicted from Bolis et al. (2017) [30].

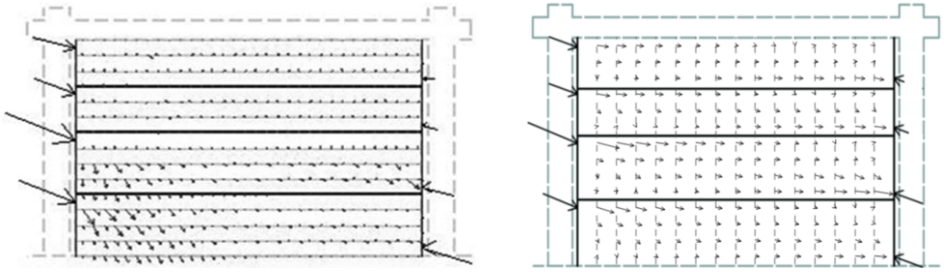

a) *b)*

Figure 2.7: Representation of the stress distribution at the horizontal a) and vertical b) interface elements at 0.8% drift, depicted from Bolis et al. (2017) [30].

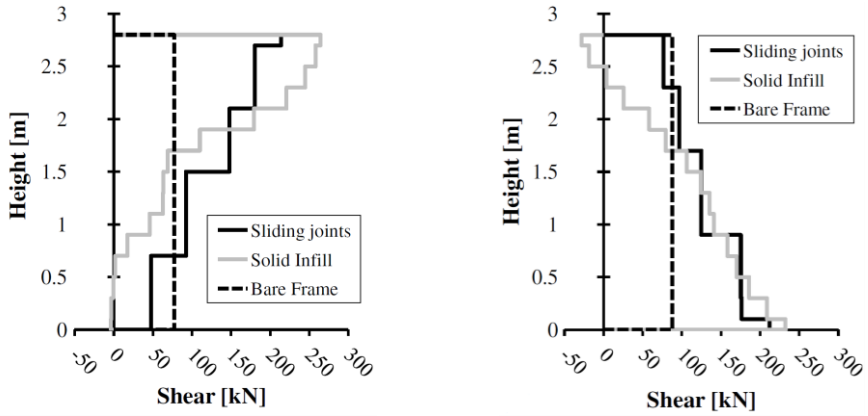

a) *b)*

Figure 2.8: Profiles of the shear action on the windward a) and leeward b) column for the three configurations at the 0.8% drift, reported in Preti et al. (2019) [33].

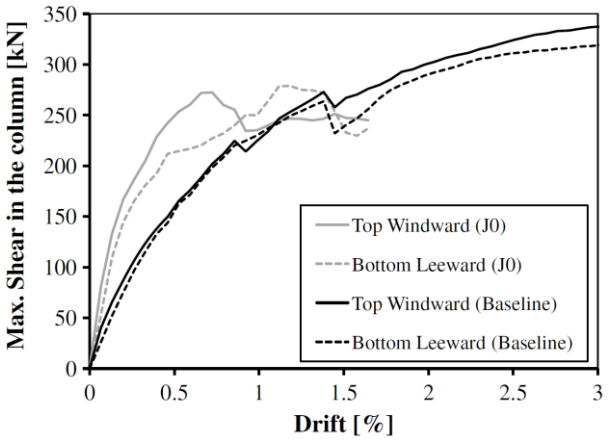

Figure 2.9: Comparison of the maximum shear action in the columns for the infilled configurations, reported in Preti et al. (2019) [33].

The parametric analysis showed the influence of the main design parameters:

- The reduced in-plane strength and stiffness are mainly given by the top gap and the horizontal sliding joints. The lateral wooden boards protect the masonry from crushing at the contact area. The presence of the gap allows for a more ductile response even in the absence of horizontal sliding joints.
- The introduction of a single sliding joint allows for a significant reduction of lateral strength and stiffness, but a minimum of three joints is required to have a damage-free structure in acceptable drift ranges. This is an important issue for the out-of-plane response.
- The lateral strength is not influenced by the infill length since no cohesion along the sliding joints is considered; this is contrary to what occurs for regular infills [40] where the lateral strength is initially provided by the cohesion.
- The friction coefficient of the sliding joints has a little influence on the lateral strength and stiffness of the infilled frame. This can be justified by the top gap, which avoids the vertical compression of the infill and the confining stresses resulting from the masonry dilatation during the horizontal deformation.
- The stiffness and strength of the infilled frame increase with the compressive strength of the masonry, but this is not linear. If the masonry is stiffer and stronger with respect to the lateral wooden boards, the wood crushes, and the masonry is undamaged. The opposite occurs when the masonry is weaker than the wooden boards. If the masonry is very deformable, it does not crush.

- The lateral strength increases as the stiffness of the lateral wooden boards increases, and vice versa. This phenomenon is justified since a deformable lateral contact material absorbs the deformations imposed on the infill and delays the crushing of the masonry.

The suggested design recommendations underline that the gap allows for ductile behaviour, the introduction of horizontal joints increases the deformability of the structure, a minimum of three joints is required to limit the masonry damage, and vertical lateral weak elements located between the infill and the columns reduce the local crushing of the masonry.
The parametric analyses conducted allowed for the estimation of the contact depth between each subpanel of the infill and the columns as a function of the imposed interstorey drift, δ. Since the plasticization of the lateral wooden boards is expected, a stress-block distribution of the contact stresses is considered at the corners of the subpanels, and the mean contact depth is derived from the contact forces by considering the compressive strength of the wood in the normal direction to the fibres (by the inversion of the stress block resultant formulation). The equations (2.1-6) and (2.1-7) are proposed to represent the mean contact depth trend, normalised to the mean subpanel height h, at the windward and leeward columns, respectively. The proposed equations fit the 85th percentile curve of the contact length functions derived from all the case studies analysed in the parametric analysis.

$$L_{c,Wind}/h = 0.35 \cdot \sqrt[3]{\delta\ (\%)} \qquad (2.1\text{-}6)$$

$$L_{c,Lee}/h = 0.30 \cdot \sqrt[3]{\delta\ (\%)} \qquad (2.1\text{-}7)$$

2.1.2 *Analytical representation of the infilled frame lateral response*

The response of the infill with sliding joints experimentally studied in Preti et al. (2015) [15] and numerically simulated and detailed in Bolis et al. (2017) [30] was analytically described in Preti et al. (2016, 2019) [33], [41]. The analytical formulation is calibrated based on the experimental tests conducted on the infilled steel portal frame with low-strength plastic hinges located at the column ends and on the results of the parametric numerical analyses.
The problem is simplified by separately evaluating the infill contribution on a perfectly hinged portal frame characterised by rigidly pinned columns. Referring to Figure 2.10, the interstorey lateral strength ΔF_s is given by the sum of the shear actions acting at the top of the windward, ΔF_s^{Win}, and leeward, ΔF_s^{Lee}, columns (Eq. (2.1-8)).

$$\Delta F_s = \Delta F_s^{Win} + \Delta F_s^{Lee} \tag{2.1-8}$$

The two shear actions are evaluated by the equilibrium to rotation at about the base of the pinned column members (Eqs. (2.1-9) and (2.1-10)), considering the horizontal and vertical forces acting on the infill-column interfaces during the frame sway mechanism (Figure 2.10). Assuming the yielding of the contact material at the lateral vertical joint interface, a simplified stress-block distribution of the contact stresses is assumed.

$$\Delta F_s^{Win} \cdot H = \sum_{n=1}^{N} \left[R_{h,n}^{Win} \cdot \left(Z_n - \beta/2 \cdot \overline{X}_n^{Win} \right) + \frac{1}{2} R_{v,n}^{Win} \cdot b_c \right] \tag{2.1-9}$$

$$\Delta F_s^{Lee} \cdot H = -\sum_{n=1}^{N} \left[R_{h,n}^{Lee} \cdot \left(Z_n - h_n + \beta/2 \cdot \overline{X}_n^{Lee} \right) - \frac{1}{2} R_{v,n}^{Lee} \cdot b_c \right] \tag{2.1-10}$$

Where H is the net column height, $R_{h,n}^{Win}$, $R_{v,n}^{Win}$, $R_{h,n}^{Lee}$, and $R_{v,n}^{Lee}$ are the resultants of the horizonal and vertical contact forces exerted by each subpanel to the windward and leeward columns, Z_n is the height of the n-th subpanel from the column base, h_n is the height of the n-th subpanel, b_c is the in-plane column height, β is the stress-block coefficient for the contact forces, and $\overline{X}_n^{Win}$ and $\overline{X}_n^{Lee}$ are the neutral axis depth of the windward and leeward columns.

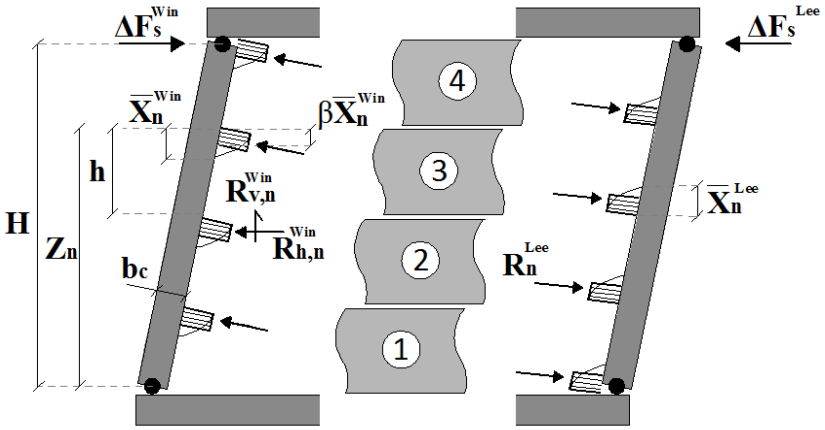

Figure 2.10: Static scheme considered in the analytical representation and indication of the contact forces, reported in Preti et al. (2019) [33].

The assessment of the contact forces considers two contributions corresponding to two simultaneous mechanisms: i) a strut mechanism in the absence of friction along the sliding joints, and ii) a friction mechanism without contacts on the leeward column.

The former arises from the diagonal compression of each subpanel that leads to the idealization of inclined struts into each subpanel element (Figure 2.11). In the absence of friction along the sliding joints, the horizontal equilibrium on the subpanel leads to the same horizontal component of the contact forces at the two opposite sides ($R_{h,n}^{Win,Strut} = R_{h,n}^{Lee,Strut} = R_{h,n}^{Strut}$), quantified by Eq. (2.1-11).

$$R_{h,n}^{Strut} = t \cdot \beta \cdot \overline{X}_n^{Lee} \cdot \sigma_c \qquad (2.1\text{-}11)$$

Where t is the column-infill effective contact thickness and σ_c is the yielding stress in compression of the contact material.

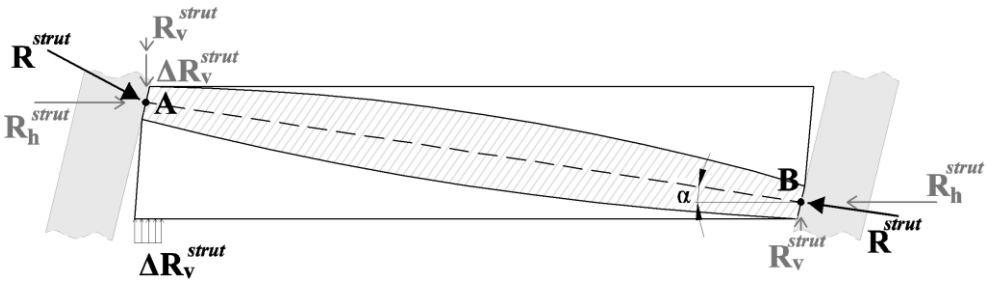

Figure 2.11: Strut mechanism contribution representation on the subpanel, represented in Preti et al. (2019) [33].

The inclination of the contact force at the windward side is higher than the strut inclination, α, (similar to the inclination of the subpanel diagonal) and equal to the friction coefficient, μ_c, of the lateral vertical joint to infill interface. In fact, the rotation of the windward column exerts an up-down force on the subpanel, and the unbalanced vertical component, ΔR_v^{Strut} (Eq. (2.1-12)), is equilibrated by the compression of the underlying sliding joint near the column. On the leeward side, the action exerted by the column is downward directed. Considering the rotational equilibrium around point "A" on the windward side (Figure 2.11), the unbalanced vertical force can be equilibrated only by the weight of the subpanel; no vertical action can be equilibrated by the upper subpanel. Consequently, the inclination of the contact force is slightly higher than the strut inclination. The quantification of the vertical components of the contact forces is reported in Eqs. (2.1-13) and (2.1-14). The lateral strength contribution due to the strut mechanism is derived by substituting in Eqs. (2.1-8), (2.1-9), and (2.1-10) the contact forces evaluated by Eqs. (2.1-11), (2.1-13), and (2.1-14). Contact forces and neutral axis depth are assumed to be equal along the height. The final equations are reported in (2.1-15), (2.1-16), and (2.1-17).

$$\Delta R_v^{Strut} = R_{h,n}^{strut} \cdot (\mu_c - tan\,\alpha) \tag{2.1-12}$$

$$R_{v,n}^{strut,Win} = R_{h,n}^{strut} \cdot \mu_c \tag{2.1-13}$$

$$R_{v,n}^{strut,Lee} = R_{h,n}^{strut} \cdot tan\,\alpha \tag{2.1-14}$$

$$\Delta F_s^{strut,wind} = V_{top}^{strut,wind} = R_{h,n}^{strut} \cdot \left[\frac{N+1}{2} - \frac{1}{2h}\left(\beta \cdot \overline{X}^{Lee} - \mu_c \cdot b_c\right)\right] \tag{2.1-15}$$

$$\Delta F_s^{strut,lee} = V_{top}^{strut,lee} = -R_{h,n}^{strut} \cdot \left[\frac{N-1}{2} + \frac{1}{2h}\left(\beta \cdot \overline{X}^{Lee} - tan\,\alpha \cdot b_c\right)\right] \quad (2.1\text{-}16)$$

$$\Delta F_s^{strut} = \sigma_c \cdot \beta \cdot \overline{X}^{Lee} \cdot t \cdot \left[\left(1 - \beta \cdot \frac{\overline{X}^{Lee}}{h}\right) + \frac{b_c}{2h}(\mu_c + tan\,\alpha)\right] \quad (2.1\text{-}17)$$

The friction contribution is studied considering a concentrated mid-height contact between each subpanel and the columns to avoid any strut. The schematic representation is reported in Figure 2.12. The friction strength along the sliding joints is generated by the subpanel weight, W_n, and by the unbalanced vertical reaction ΔR_v^{Strut}, previously described in Eq. (2.1-12). As the lateral deformation increases, the windward column rotates, and the relative sliding between the subpanel and the column leads to a vertical friction action along the contact. Consequently, the vertical action on the sliding joints increases, and a loop of increased vertical action starts. This phenomenon leads to the evaluation of an amplification factor that must be applied to the horizontal contact forces equal to $\left(\frac{1}{1-\mu_j \cdot \mu_c}\right)$. The resultant horizontal contact force can be expressed like in Eq. (2.1-18). Assuming that the forces are applied at the mid-height of each sub-panel, the lateral strength is expressed by introducing the horizontal reaction expressed in Eq. (2.1-18) in the rotational equilibrium on the windward column of Eq. (2.1-9). The result is expressed in Eq. (2.1-19). No friction contribution is given on the leeward column.

$$R_{h,n}^{frict} = \left[W_n + R_{h,n}^{strut} \cdot (\mu_c - tan\,\alpha)\right] \cdot \left(\frac{1}{1-\mu_j.\mu_c}\right) \cdot \mu_j \quad (2.1\text{-}18)$$

$$\Delta F_s^{frict} = V_{top}^{frict,wind} = \frac{1}{2} \cdot \left[W + N \cdot R_{h,n}^{strut} \cdot (\mu_c - tan\,\alpha)\right] \cdot \left(\frac{1}{1-\mu_j.\mu_c}\right) \cdot \mu_j \quad (2.1\text{-}19)$$

Where W is total weight of the infill, N is the number of the sub-panels, μ_j is the friction coefficient of the sliding joints, and μ_c is the friction coefficient between the masonry subpanel and the lateral contact material.

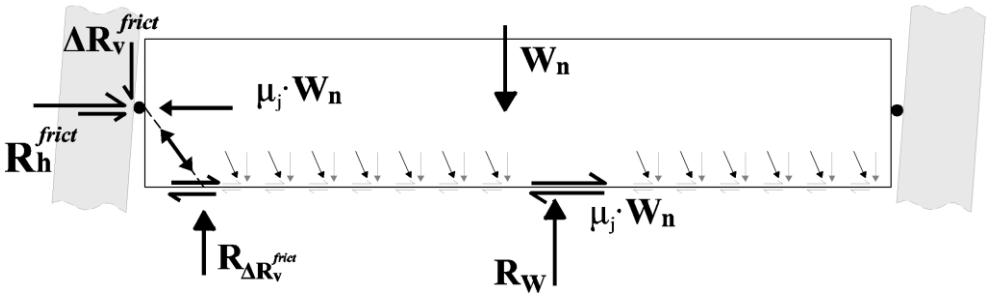

Figure 2.12: Strut mechanism contribution representation on the subpanel, represented in Preti et al. (2019) [33].

The total lateral strength is given by the sum of the two contributions.

$$\Delta F_s = \Delta F_s^{strut} + \Delta F_s^{frict} \tag{2.1-20}$$

The required neutral axis depth is derived from the numerical parametric study described in Bolis et al. (2017) [30], previously recalled. A first equation was proposed and then modified as in Eqs. (2.1-21) and (2.1-22): a linear backbone until 1% drift (δ), followed by a cubic relationship, and the dependency from the number of sliding joints is proposed.

$$\overline{X} = h \cdot [0.3 - 0.019 \cdot (N-4)] \cdot \delta(\%), \qquad \delta \leq 1\% \tag{2.1-21}$$

$$\overline{X} = h \cdot \left[0.3 \cdot \sqrt[3]{\delta(\%)} - 0.019 \cdot (N-4)\right], \qquad \delta > 1\% \tag{2.1-22}$$

The approach was verified by its application to simulate the experimental test on the infilled hinged steel frame described in Preti et al. (2015) [15], and the numerical simulation of the infilled RC frame described in Bolis et al. (2017) [30]. The latter was obtained by adding the lateral strength analytically estimated to the strength of the bare frame numerically evaluated. The results are reported in Figure 2.13. A better agreement was obtained by using the numerically estimated contact length instead of the approximated one.

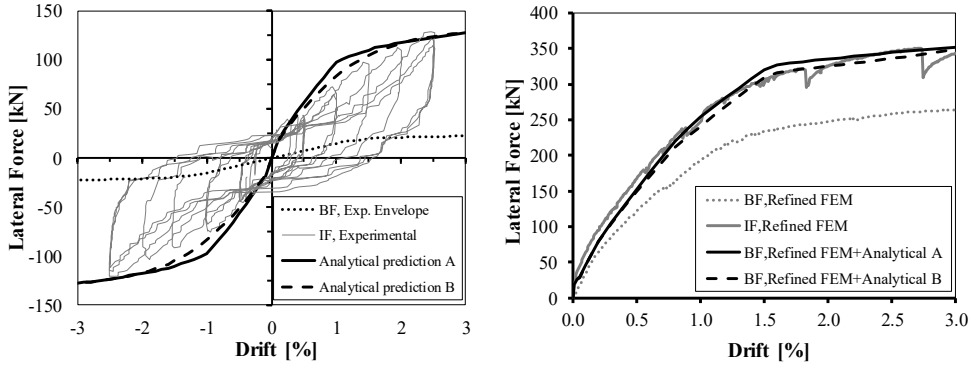

a) *b)*

Figure 2.13: Comparison of the analytical prediction of an infilled hinged steel frame [15] a), and of an infilled RC frame [30] b).

In the case of a real infilled RC frame, the total shear action on the columns is evaluated in an approximated manner by assuming a superposition of the effects (Eq. (2.1-23)); the shear action previously defined for the infill, V_{infill}, is summed to the shear evaluated on the bare frame, V_{bare}.

$$V = V_{infill} + V_{bare} \tag{2.1-23}$$

The shear action at the top of the windward column, Eq. (2.1-24), is given by both the strut mechanism, Eq. (2.1-15), and the friction mechanism, Eq. (2.1-19), while the shear action at the top of the leeward column, Eq. (2.1-25), is given only by the strut mechanism, Eq. (2.1-16). The shear actions at the base of the columns are evaluated by horizontal equilibrium; the horizontal contact forces acting on the columns are subtracted from the shear action at the top of the respective column, as expressed in Eq. (2.1-26) for the leeward column.

$$V_{top}^{Windward} = \left(\Delta F_s^{strut,wind} + \Delta F_s^{frict}\right) + V_{bare} \tag{2.1-24}$$

$$V_{top}^{Leeward} = \Delta F_s^{strut,lee} + V_{bare} \tag{2.1-25}$$

$$V_{base}^{Leeward} = V_{top}^{Leeward} - \sum R_{h,n}^{strut} \qquad (2.1\text{-}26)$$

Figure 2.14 compares the total (infill plus frame) shear profiles acting along the columns of a RC portal frame obtained by the analytical representation and the numerical one. A good match is highlighted. The peak shear action is reached at the top of the windward column and at the base of the leeward one.

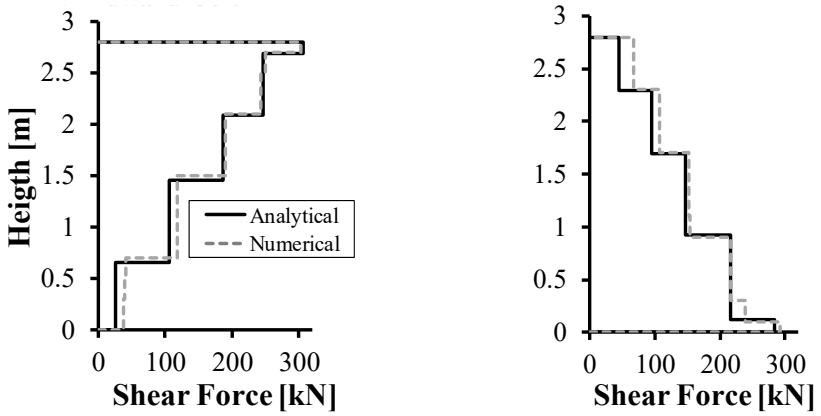

Figure 2.14: Comparison of the analytical and numerical prediction of the shear profiles along the columns at 2.0% drift of an infilled RC frame [30].

2.2 *Reference structure and model calibration*

2.2.1 *Numerical model description*

The modelling scheme and the material calibration procedure to represent infilled frames in this work are adapted from Bolis et al. (2017) [30] and Stavridis and Shing (2010) [35] . The following modifications are introduced to account for the modified design parameters previously defined:

- Smeared-crack elements that represent the lateral vertical joints are described by an elastic material.
- A layer of smeared-crack elements is added at the infill top, directly connected to the beam, separated by the infill with a layer of interface elements. The interface elements allow the beam to detach and slide with respect to the infill.
- The properties of the interface elements at the base of the infill are changed from those of the sliding joints to those of the cold mortar joint.
- The mechanical properties of the interface elements representing the sliding joints are modified to account for the contribution of the plaster, represented by a degrading cohesive strength.

The scheme of the model is represented in Figure 2.15.
These numerical choices are validated by comparison with the experimental responses of the bare frame and the infilled frame described in Morandi et al. (2018) [14] specimens. Available test data are the mechanical characterization of concrete, masonry, and steel and the shear behaviour of the sliding joints in the unplastered configuration. The lateral force versus top beam displacement hysteretic response of the infill frame and the local deformation of the lateral joints were monitored in the test. In particular, a series of eight potentiometric gauges, two per subpanel, monitored the horizontal relative displacement between each column and the adjoining masonry sub-panels, bridging over the lateral joints. Since the masonry panel and the concrete column are way stiffer than the lateral joint deformable material, the average strain of the lateral joint is quantified by dividing the measured displacement by the thickness of the lateral joint. The approximated deformation profile of the lateral vertical joints along the infill height is then derived by assuming a linear profile of strains along the subpanel height.
The calibration of the RC bare frame and of the masonry infill modelling is made following the approach described in Bolis et al. (2017) [30] and Stavridis and Shing (2010) [35]. The comparison of the numerical and experimental global base shear versus interstorey drift curves of the bare frame is reported in Figure 2.16. In the

following sections, further details will be given about the modelling choices and the calibrations of the lateral and top joints, as well as the sliding joints.

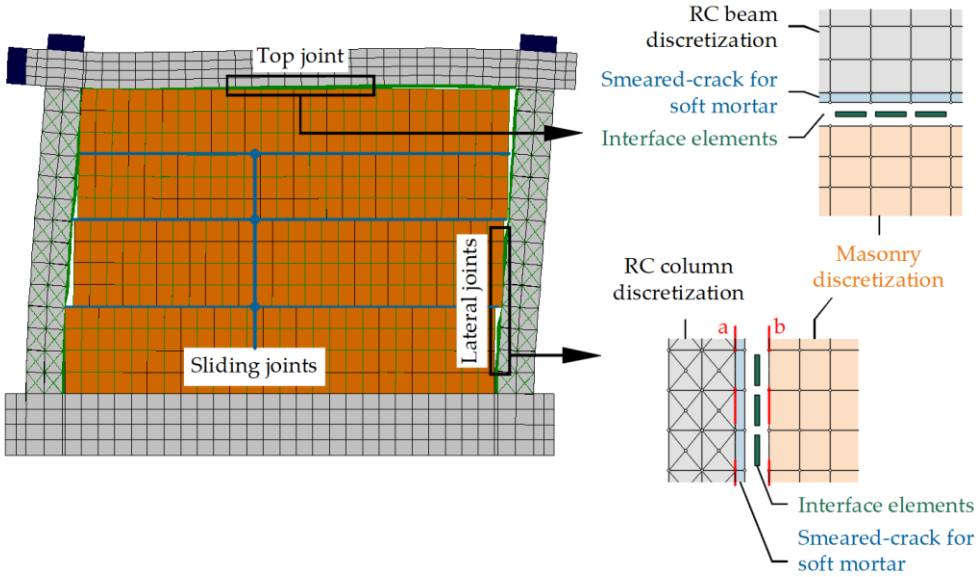

Figure 2.15: Representation of the numerical model (left figure). Detail of the modelling of the infill-to-beam (upper right figure) and the infill-to-columns (lower right figure) joints by using smeared-crack elements directly connected to the elements of the top beam and the columns, and connection to the infill by means of interface elements.

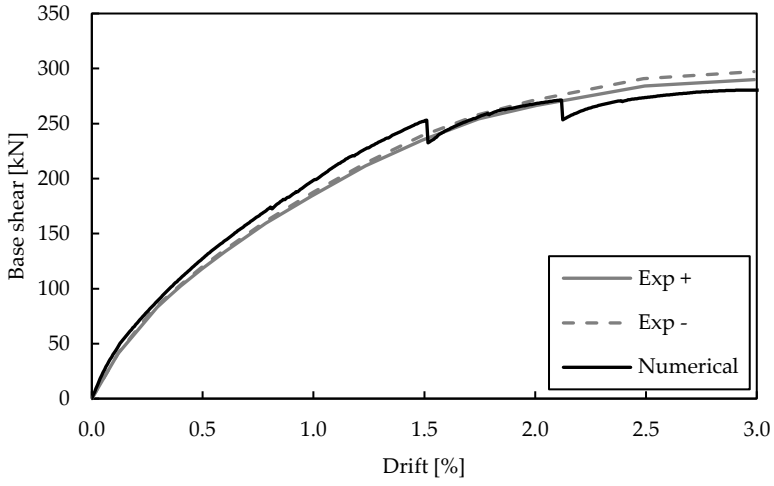

Figure 2.16: Comparison of the experimental and numerical base versus drift of the bare frame described in Morandi et al. (2018) [14].

2.2.2 *Calibration of the lateral and top contact joints*

The soft mortar material located between the infill and the RC frame is represented by smeared crack elements characterised by a linear elastic response. The constitutive laws assumed for the smeared-crack elements and the yield surfaces assumed for interface elements, calibrated by comparison with the experimental tests, are represented in Figure 2.17 and Figure 2.18. The nonlinear behaviour is linearized into an equivalent elastic material with secant stiffness at a target strain level, evaluated as follows:

- The approximated experimental strain profiles of the contact material along the lateral joints at a drift level equal to 2.0% are considered; the peak values of compressive strains range up to about 15-20% (Figure 2.29). Consequently, an equivalent secant stiffness in the range of up to 15% strain was calibrated for the smeared-crack elements, which model the lateral joints. The material compression test that reproduces the complete systems of the lateral joints (Figure 2.17) was chosen among the mechanical characterization tests available from the experimental campaign. The assumed value of the equivalent secant elastic modulus is equal to 8 MPa.
- For the top joint, a significant range of strains up to 10% was observed, based on the average vertical displacement of the compressed area at a drift level equal to 2.0%. In this case, the results of the other two tests (on the mortar prism and column pad) conducted on the soft mortar are considered (Figure 2.17), and a value of equivalent elastic modulus equal to 5 MPa is assumed.

Specific shear tests on the characterization of the soft mortar-infill and soft mortar-concrete interfaces are not available. No cohesion and a friction coefficient equal to 0.8 (coherent to that of masonry mortar-to-concrete interfaces) are considered for both the initial and final surfaces.

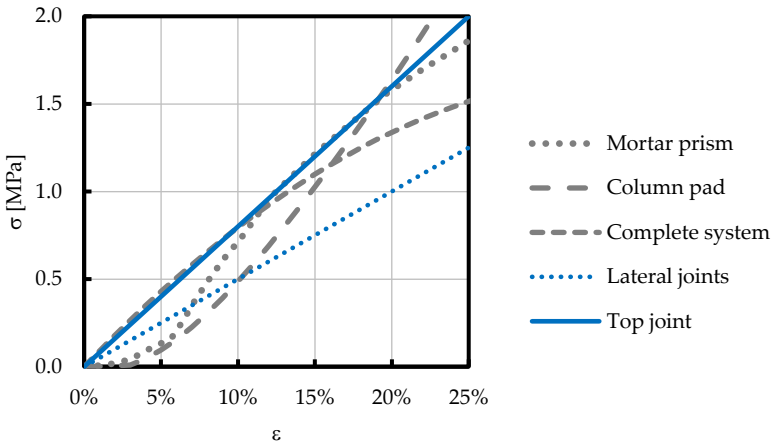

Figure 2.17: Comparison of the mechanical characterization tests of the soft mortar and the assumed elastic behaviour in the numerical model for three different test typologies.

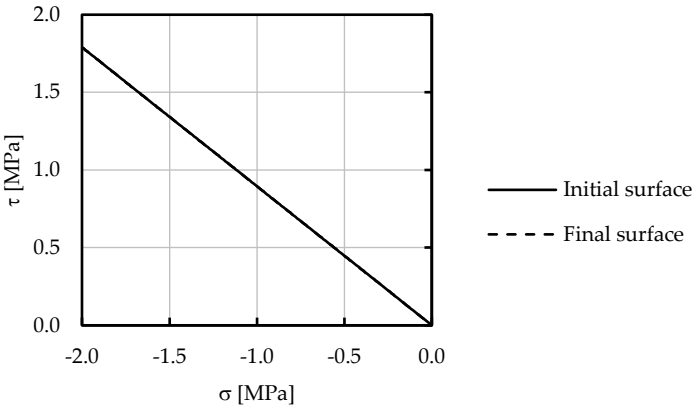

Figure 2.18: Initial and final yield surfaces assumed for the interfaces of the lateral and top joints.

2.2.3 *Calibration of the interfaces representing the sliding joints*

Since the shear behaviour of the sliding joints was experimentally investigated in the unplastered configuration, the contribution of the plaster is not easily quantifiable.
The adopted interface shear model allows the definition of an initial and final failure criterion. The final yield surface is calibrated to represent the shear behaviour of the unplastered sliding joints, a situation that occurs after plaster cracking and joint sliding. No final cohesion is considered, assuming a fast degradation of the cracked plaster strength, and the final friction coefficient, μ_r (equal to 0.361), is derived from low-velocity experimental tests conducted on un-plastered triplets with sliding joints [14], [42]. It is noteworthy that no specific tests to calibrate the softening behaviour and the dilatancy of the materials are available for such joints; consequently, simplifying hypotheses are taken. In particular, the Mohr-Coulomb criterion is considered for both the initial and final surfaces of such interface elements in shear. As no dilatancy is expected, the related parameter η is taken sufficiently high to avoid the increase in normal stress during the tangential loading and the consequent friction hardening. The other parameters required, as recalled in §2.1.1, are the initial friction coefficient, μ_0, and the initial tensile strength s_0.
The cohesive strength of the initial yield surface is used to account for the contribution of the plaster to the initial shear resistance of the sliding joints. An equivalent cohesion force, C_{eq}, is calculated as in Eq. (2.2-1) by evaluating the increase in the cohesion force in the experimental tests between plastered and un-plastered masonry triplets. Where $c_{unplastered,mas}$ (equal to 0.178 MPa [42]) and $c_{plastered,mas}$ (equal to 0.369 MPa [42]) are the cohesion coefficients evaluated on the un-plastered and plastered triplets, respectively; t_{infill} (equal to 290 mm [42]) and t_{mas} (equal to 250 mm [42]) are the thickness of the plastered and un-plastered masonry in the experimental test; and $t_{pl,mas}$ (equal to 20+20 mm [42]) and $t_{pl,joint}$ (equal to 5+5 mm [42]) are the thickness of the plaster of the plastered masonry and of the reduced plaster at the joints. The cohesion coefficient, c, is deduced as in Eq. (2.2-2) by considering the thickness of the wall in the numerical model t_{num} (equal to 250 mm). The initial friction coefficient, μ_0, is assumed to be equal to the one obtained by the triplet test on plastered masonry (equal to 0.862). The initial tensile strength, s_0, is consequently derived as the intercept of the Mohr-Coulomb criterium. It is checked that it does not exceed the plaster tensile strength, f_{fl}, (equal to 6.65 MPa [14]) corrected as in Eq. (2.2-3).

$$C_{eq} = \frac{c_{plastered,mas} \cdot t_{infill} - c_{unplastered,mas} \cdot t_{mas}}{t_{pl,mas}} \cdot t_{pl,joint} = 0.191MPa \quad (2.2\text{-}1)$$

$$c = \frac{C_{eq}}{t_{num}} = 0.0625MPa \quad (2.2\text{-}2)$$

$$s_0 = \frac{c}{\mu_0} = 0.0725MPa < f_{fl} \cdot \frac{t_{pl,joint}}{t_{num}} \quad (2.2\text{-}3)$$

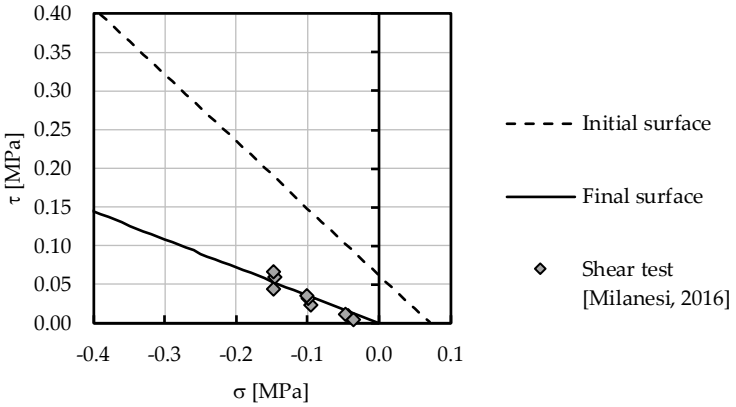

Figure 2.19: Initial and final yield surfaces characterise the interface elements of the sliding joints.

2.2.4 *Baseline model (no plaster and top gap)*

The calibration procedure starts with a baseline model where the hypotheses at the base of the analytical model proposed in Preti et al. (2019) [33] are introduced:

- Gap between the infill and the top beam (top gap).
- Sliding joint at the base of the infill.
- No plaster covering the sliding joints, thus no initial cohesion (the initial yield surface overlapped with the final one).

Thus, the sole variation with respect to the previous model is the modification to the lateral joints to account for an elastic, over-resistant material instead of a yielding one.
Figure 2.20 represents the comparison of the global storey shear versus interstorey drift curve of the infilled frame and the bare one. As expected, the infill adds a contribution to the lateral strength. The infill contribution to the overall response is derived by subtracting the lateral strength of the bare frame from the infilled one.
The shear internal action along the columns is evaluated by the horizontal equilibrium of the columns, as represented in Figure 2.21. The column shear profile shows a peak value measured at the top end, V_{top}, progressively reduced by the contact forces F_{cont} transmitted along the height by each masonry prism layer in infill-frame interaction. For low drift levels, the contact forces are mainly concentrated at the top of the infill on the windward side and at its base on the leeward side. The shear profiles progressively grow in magnitude as the drift increases. The comparison of the profiles with those of the bare frame at a drift level equal to 2.0% shows that they are amplified at the upper part of the windward column and at the lower part of the leeward one. The peak value is reached at the base of the leeward column, and it is about 80 kN higher than the design shear value derived from the equilibrium on the column in the bare frame configuration when plastic hinge moments are applied at its ends (shear on the Bare Frame derived by Capacity Design, BF CD). This amplification underlines the importance of taking into account the shear overload due to the infill-frame interaction in the design of the frame columns.

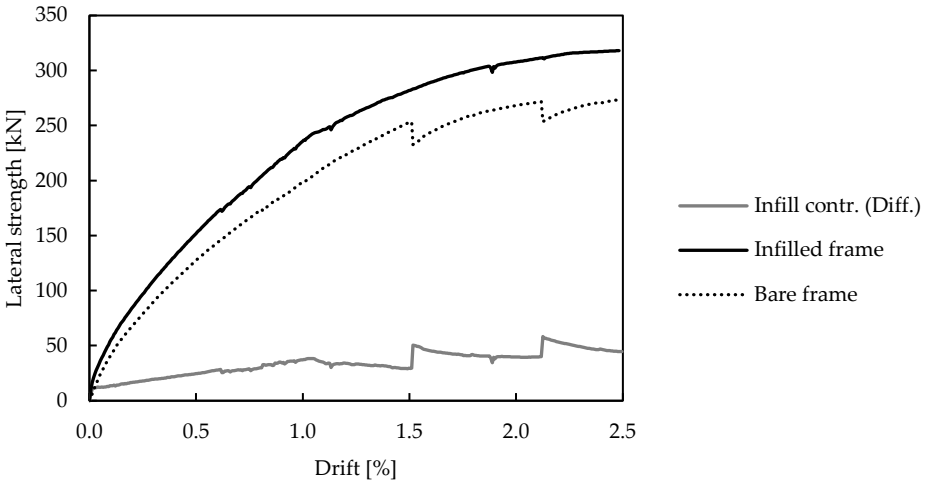

Figure 2.20: Comparison of the base shear vs. drift response of the infilled frame and the bare one. Representation of the infill contribution given by its difference.

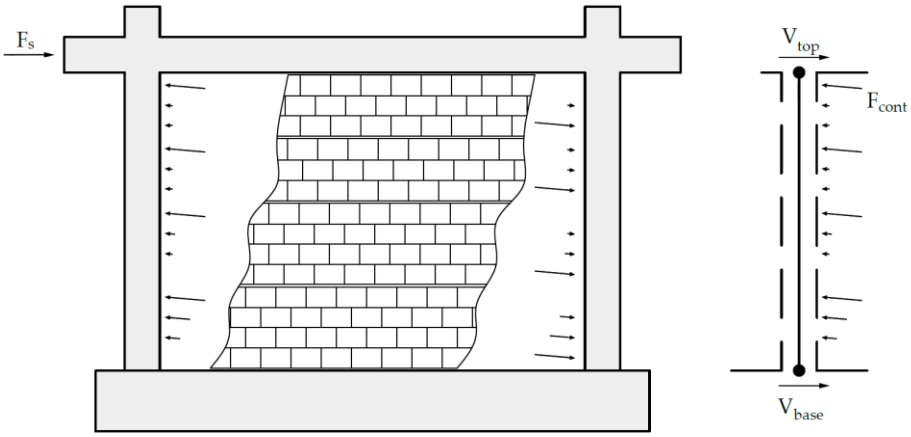

Figure 2.21: Indication of the contact forces acting on the RC frame in the infill-frame interaction mechanism (left figure) and static scheme (right figure) used in the evaluation of the shear profile.

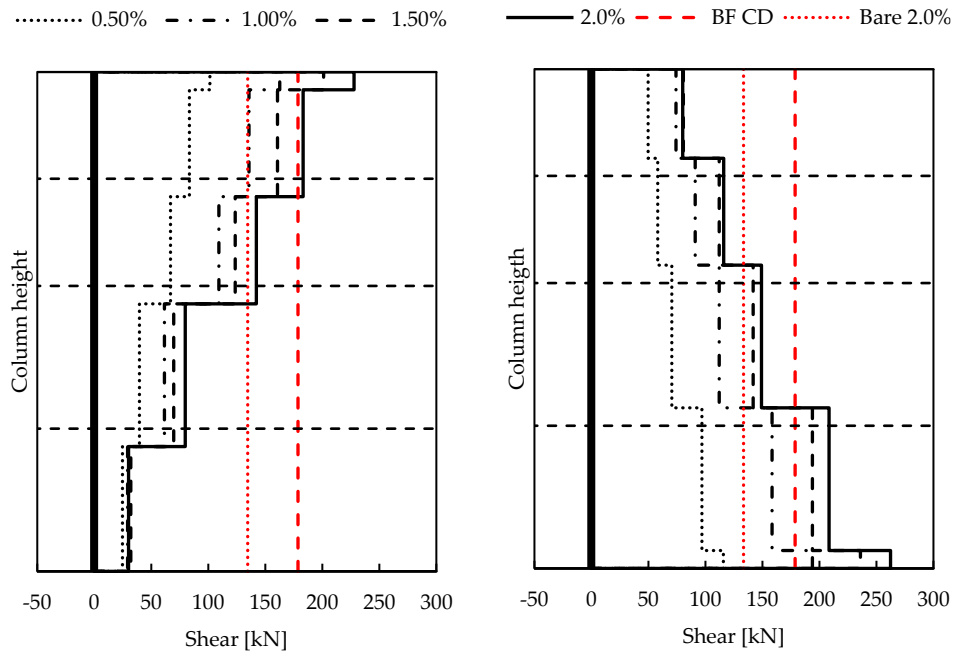

a) *b)*

Figure 2.22: Shear profiles along the windward a) and leeward b) columns for different drift levels of the infilled configuration and at the 2.0% drift level of the bare one. The "BF CD" is the shear profile derived from the capacity design on the bare frame.

2.2.5 *Modelling of the test infilled frame*

The construction details variation above described are progressively introduced in the modelling, one at a time, as described in §2.2.1. The examined models are summarised in Table 2.1. The effects on global behaviour are examined in Figure 2.23 through the comparison of the numerical and experimental base shear vs. drift curves.
The removal of the base sliding joint does not modify the global behaviour (Figure 2.23a), but it modifies the distribution of the contact forces that the infill exerts on the columns (Figure 2.24) and, consequently, the respective shear action profile along the columns (Figure 2.25). In fact, as shown in Figure 2.24, with the sliding joint at the base, the contact forces are almost uniform along the column, while without it, the first sub-panel remains stuck at the base, with the consequent significant increase of the corresponding local thrust on the windward column. The comparison of the profiles between the two configurations shows that the maximum shear action at the base of the leeward column reduces after removing the base sliding joint, while the shear profile is inverted at the base of the windward column. The shear values at the top of the columns do not change, proving that the global lateral strength is not altered.
By filling the top gap, the global lateral strength increases and matches the experimental response for drift values larger than 1.0% (Figure 2.23b). The initial lack of strength and stiffness is partially covered by accounting for the plaster contribution to the sliding joints by modifying the interface mechanical properties as described in §2.2.3 (Figure 2.23c). Little drops occur at the sliding joint activation. As shown in Figure 2.26, the shear profile along the windward column is not modified, while the one on the leeward column is a little amplified.

Model name	Base joint	Top gap	Plaster
BL (Baseline)	Yes	Yes	No
noBJ	**No**	Yes	No
noGap	Yes	**No**	No
Plast.	Yes	Yes	**Yes**
Numerical	**No**	**No**	**Yes**

Table 2.1: Summary of the models used for the calibration of the experimental test.

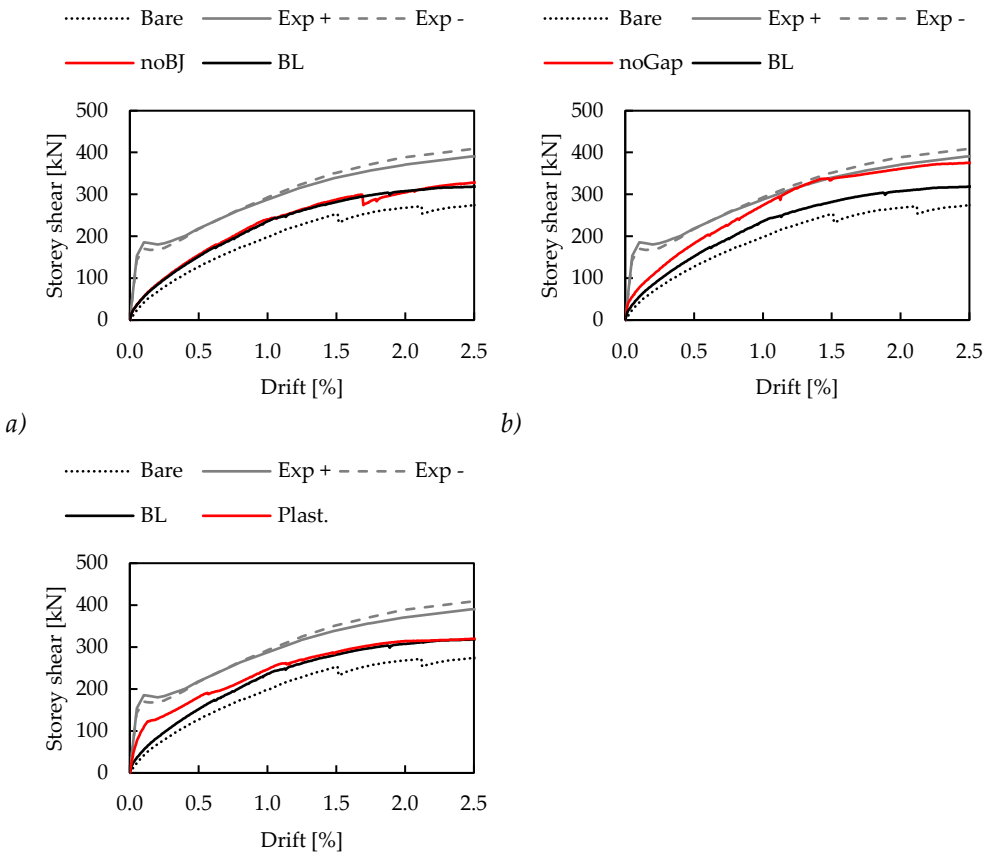

Figure 2.23: Study on the influence of each parameter on the global behaviour: absence of the sliding joint at the base ("noBJ") a), fill of the top gap ("noGap") b), and plaster on the sliding joints ("Plast.") c).

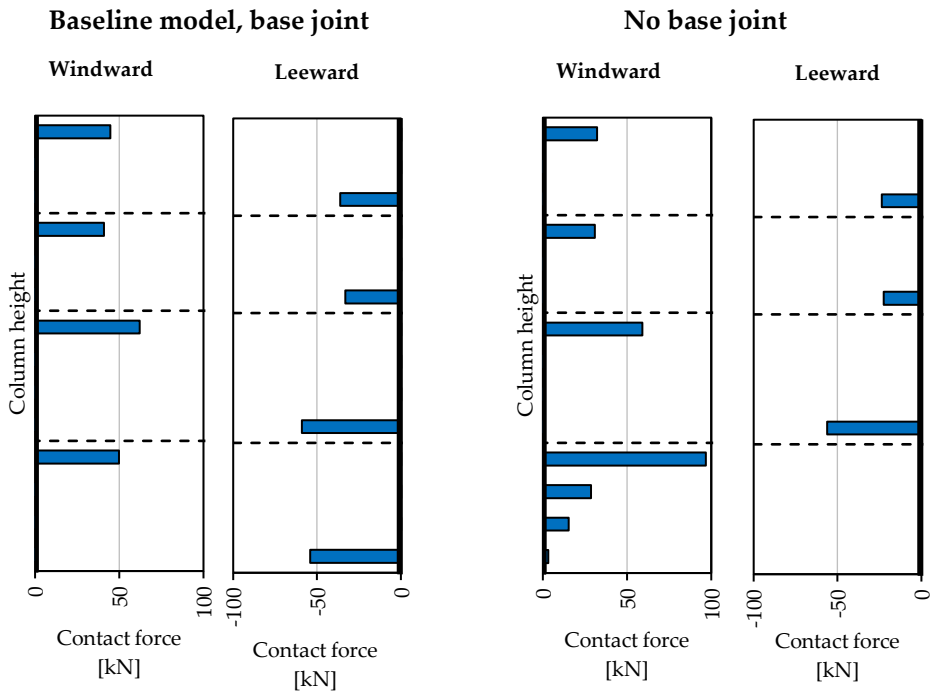

Figure 2.24: Comparison of the contact forces along the windward and leeward columns in the baseline model and in the absence of the sliding joint at the base at a drift level equal to 2.0%.

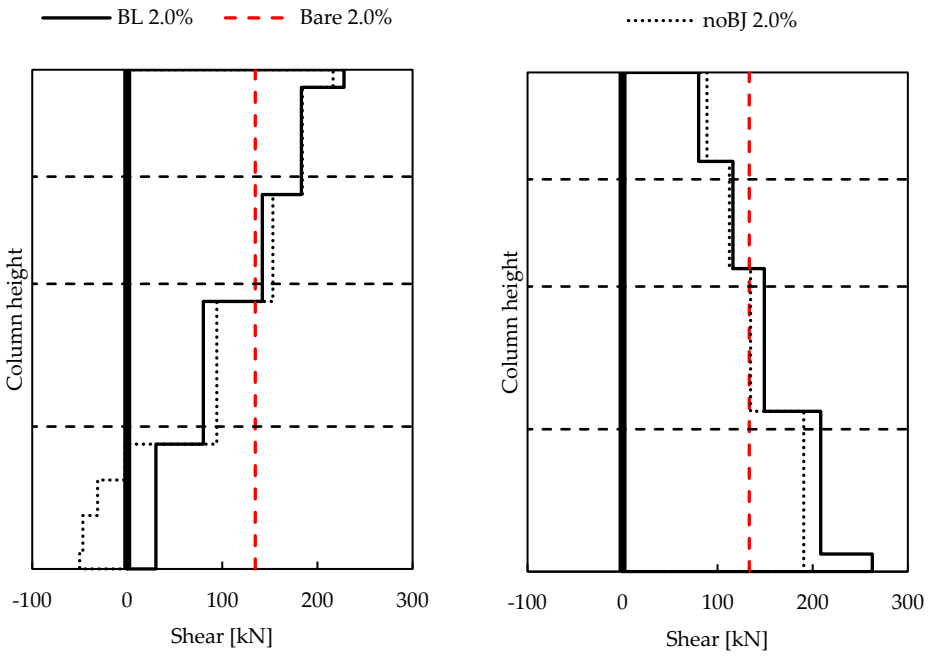

a) *b)*

Figure 2.25: Comparison of the shear profiles along the windward a) and leeward b) columns in the baseline model ("BL") and in the absence of the sliding joint at the base ("noBJ") at a drift level equal to 2.0%. The "BF CD" is the shear profile derived from the capacity design.

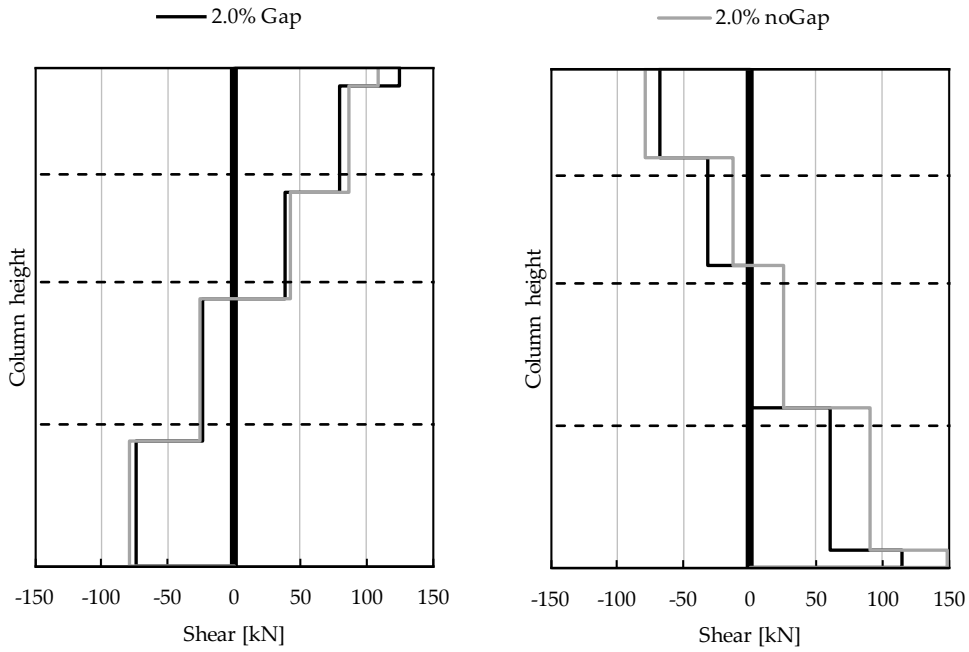

a) *b)*

Figure 2.26: Comparison of the shear profiles along the windward a) and leeward b) columns in the baseline model ("Gap") and in the absence of the top gap ("noGap") at a drift level equal to 2.0%, contribution of the infill only.

Finally, all the contributions of the discussed modifications are considered together. In Figure 2.27, the numerical response is compared to the experimental one. The envelope in the positive and negative directions of infill displacement in the cyclic experimental result is considered for comparison. The parameters used in the numerical model to define the smeared-crack elements and the interface elements are reported in Table 2-2 and Table 2-3.
The modelling choices allow for a good representation of the initial stiffness. The initial peak strength is better represented in the negative direction, while the lateral strength is better represented in the positive direction.

Material	E [MPa]	G [MPa]	ν [-]	t [mm]	f_c [MPa]	f_t [MPa]
Concrete	25000	10417	0.20	350	37	1.0
Masonry	2600	1150	0.13	250	2.9	0.6
Soft Mortar top	5	1.81	0.38	250	10.0	2.0
Soft Mortar lateral	8	2.9	0.38	250	10.0	2.0

Table 2-2: Material parameters of the smeared-crack elements (E=Elastic modulus, G=shear modulus, ν=Poisson modulus, t=material thickness, f_c= material compressive strength, f_t= material tensile strength).

Material	s_0 [MPa]	μ_0 [-]	μ_r [-]	r_0 [MPa]	r_r [MPa]	t [mm]
Bed joints	0.45	0.88	0.75	0.005	0.005	250
Brick head joints	0.70	1.00	0.80	0.28	0.21	250
Mortar vertical joints	0.90	0.862	0.75	0.005	0.005	250
Concrete joints	1.00	0.90	0.70	0.25	0.20	350
Lateral joints	0.00	0.80	0.80	0.00	0.00	250
Top joint	0.00	0.80	0.80	0.00	0.00	250
Sliding joints	0.0725	0.862	0.361	0.00	0.00	250

Table 2-3: Material parameters of the interface elements (s_0=initial tensile strength, μ_0=initial friction coefficient, μ_r= final friction coefficient, r_0=initial radius of the hyperbola at the vertex, and r_r=final radius of the hyperbola at the vertex.

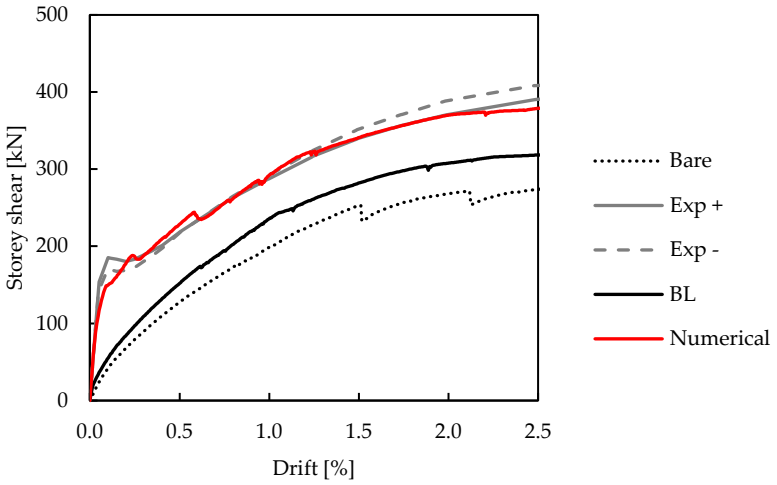

Figure 2.27: Comparison of the experimental and numerical results.

Focusing on local deformations, the deformation profile of the lateral joints derived from the numerical results is compared with the experimental one (evaluated as described in Section §2.2.1). In the numerical assessment, the profile is quantified as the relative displacement of the nodes belonging to the column elements and to the infill elements around the lateral joints (individuated by the red lines "a" and "b" indicated in Figure 2.15), divided by the lateral joint thickness.
Figure 2.28 shows the deformed structure at 2.0% drift. The results in terms of the deformation profile at the infill-to-column interface are reported in Figure 2.29. The extension of the compressed area (contact length) and the compressive strain level are reasonably well captured. A redistribution is noticed at the second sliding joint.

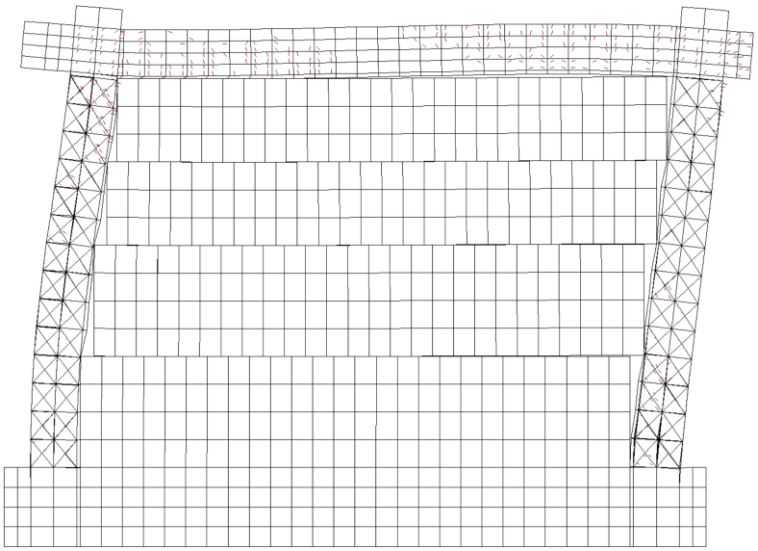

Figure 2.28. Deformed shape of the numerical model at 2.00% drift. Indication of the cracking on the RC elements; no damage occurs in the masonry.

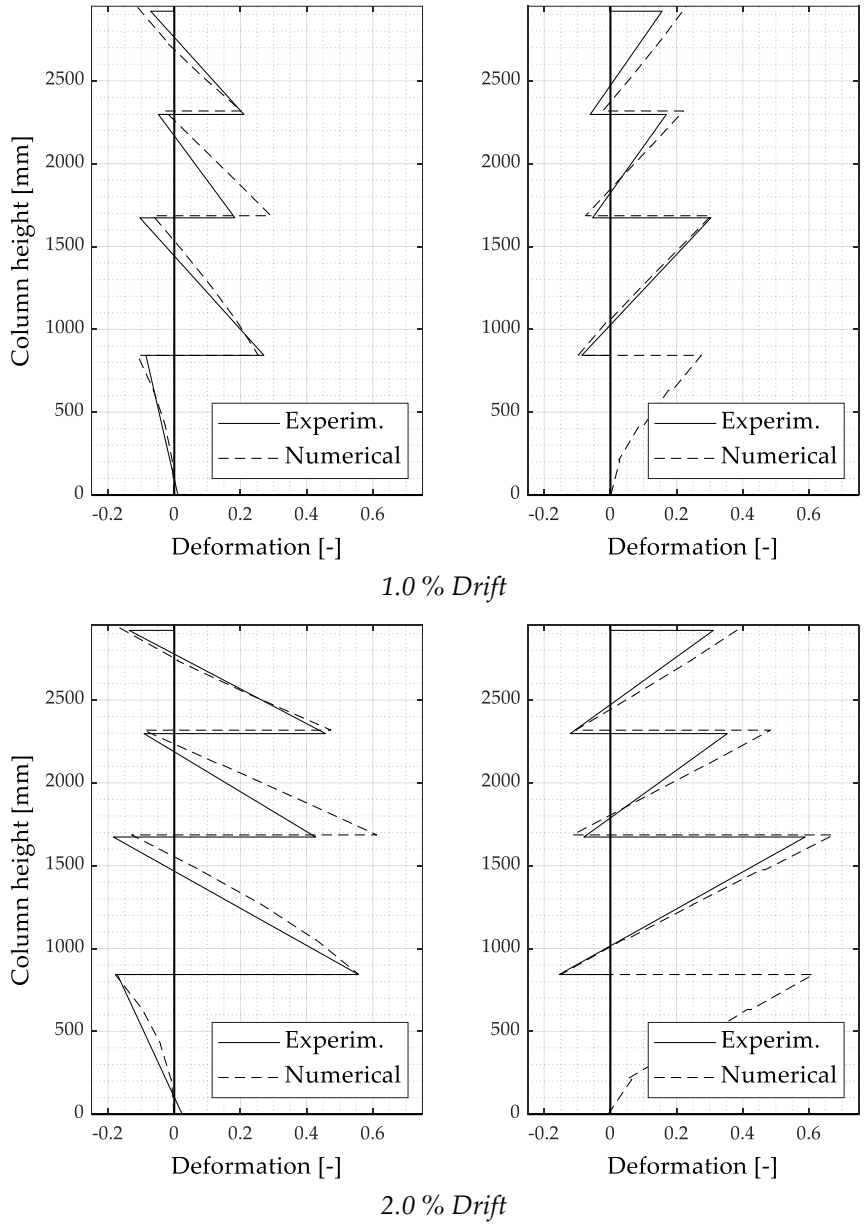

Figure 2.29: Comparison of the experimental and numerical deformation profiles of the windward a) and leeward b) lateral joints at 1.00% and 2.00% drift (negative deformations are for compressive actions).

2.3 *Parametric analysis*

2.3.1 *Parametric study description*

The parametric analysis is developed starting from the baseline model used for the calibration process (§2.2.4). It will investigate the following main design parameters:

- Stiffness of the lateral vertical joints (elastic stiffness of the contact material).
- Filling of the top gap with different elastic stiffness of the top joint.
- Number of sliding joints and their location.
- Length of the infill (aspect ratio).
- Mechanical and geometrical properties of the masonry.

Focus is given to the lateral joint and the top joint stiffness role; five increasing levels of elastic stiffness are investigated for each of them. The range investigated is calibrated to be significant in the design application. The study of the number of sliding joints starts from the case of no horizontal sliding joint, but maintaining the deformable contact material, to the one with sliding joints located at all the horizontal mortar joints. Different locations of the sliding joints are examined when a number of one, two, or three sliding joints are concerned. The aspect ratio is studied in a range of 3.2-6.1 m infill length. The masonry types considered in this study are the same as those adopted for the parametric analysis described in Bolis et al. (2017) [30].
Furthermore, in the absence of the top gap, the responses to different stiffnesses of the lateral joints and different aspect ratios are examined. The baseline stiffness of the top joint in this case is set equal to 5 MPa, the same as in the simulation of the experimental test.
The details of the parametric analyses are explained in Table 2-4 and Table 2-5. The comparison will be examined in terms of:

- Lateral strength versus interstorey drift response.
- Contribution of the infill to the lateral strength.
- Drift at the onset of masonry crushing.
- Maximum shear action on the columns.

Param.	**Code**	**Geometry**		**Material**						
		L *m*	**n_j**	**Masonry prism**					**Top j**	**Lat. j**
				Mat.	**E** *MPa*	**f_c** *MPa*	**f_t** *MPa*	**t** *mm*	**E** *MPa*	
Baseline	104	4.2	3	Hollow clay	2600	2.9	0.6	250	5.0	8.0
Lateral joint stiffness	El7.5	4.2	3	Hollow clay	2600	2.9	0.6	250	5.0	**7.5**
	El15									**15.0**
	El30									**30.0**
	El45									**45.0**
	El60									**60.0**
Number of sliding joints and their configuration	104c1	4.2	**0**	Hollow clay	2600	2.9	0.6	250	5.0	8.0
	104c2		**1**							
	104c3		**1**							
	104c4		**2**							
	104c5		**2**							
	104c6		**2**							
	104c7		**3**							
	104c8		**3**							
	104c9		**4**							
	104c10		**5**							
	104c11		**6**							
	104c12		**13**							
Aspect ratio	L320	**3.2**	3	Hollow clay	2600	2.9	0.6	250	5.0	8.0
	L520	**5.2**								
	L620	**6.1**								
Masonry properties	AAC200	4.2	3	**AAC200**	**1600**	**1.8**	**0.5**	**200**	5.0	8.0
	AAC300			**AAC300**				**300**		
	CU1			**Solid CU1**	**27579**	**23.44**	**4.82**	**190.5**		
	Mehrabi			**Mehrabi 9**	**15168**	**14.2**	**1.72**	**92.5**		

Table 2-4: Values adopted in the parametric study in the presence of the top gap ("Param." = parameter considered in the parametric analysis, "Code" = model code, "L" = infill length, "n_j" = number of sliding joints, "Mat." = masonry prism material, "E" = elastic modulus, "f_c" = prism compressive strength, "f_t" = prism tensile strength, "t" = infill thickness, "Top j" = top joint, "Lat. J" = Lateral joint).

Param.	**Code**	**Geometry**		**Material**						
		L *m*	**n_j**	**Masonry prism**					**Top j**	**Lat. j**
				Mat.	**E** *MPa*	**f_c** *MPa*	**f_t** *MPa*	**T** *mm*	**E** *MPa*	
Lateral joint stiffness	El7.5f	4.2	3	Hollow clay	2600	2.9	0.6	250	5.0	**7.5**
	El15f									**15.0**
	El30f									**30.0**
	El45f									**45.0**
	El60f									**60.0**
Top joint stiffness	Es7.5f	4.2	3	Hollow clay	2600	2.9	0.6	250	**7.5**	8.0
	Es15f								**15.0**	
	Es30f								**30.0**	
	Es45f								**45.0**	
	Es60f								**60.0**	
Aspect ratio	L320s	**3.2**	3	Hollow clay	2600	2.9	0.6	250	5.0	8.0
	L520s	**5.2**								
	L620s	**6.1**								

Table 2-5: Values adopted in the parametric study in the absence of the top gap (suffix "f" means top gap filled, "Param." = parameter considered in the parametric analysis, "Code" = model code, "L" = infill length, "n_j" = number of sliding joints, "Mat." = masonry prism material, "E" = elastic modulus, "f_c" = prism compressive strength, "f_t" = prism tensile strength, "t" = infill thickness, "Top j" = top joint, "Lat. J" = Lateral joint).

2.3.2 *Sensitivity of the global response to design parameters*

Figure 6.1a shows the trend variation of the capacity curve as a function of lateral joint stiffness. The lateral strength increases as the stiffness of the lateral joints increases. Figure 2.30b shows the trend of the infill contribution to the lateral strength ("infill lateral strength" in the following) at different drift levels, calculated by subtracting the strength of the bare frame from the total infilled frame lateral strength ("total lateral strength" in the following). Sudden drops in the infill lateral strength occur for the stiffer lateral joints, which are associated with the progressive local crushing at the compressed corners of subpanels.

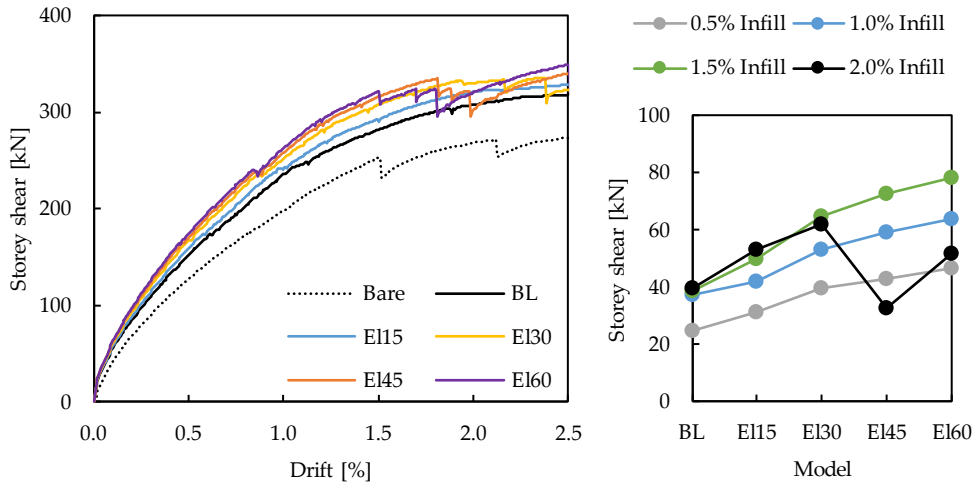

a) *b)*

Figure 2.30: Comparison of the global response a) and of the infill contribution to the lateral strength at fixed interstorey drift levels (0.5%, 1.0%, 1.5%, and 2.0%) b) for different stiffnesses of the lateral joints (BL=Baseline model, E=8MPa, El15=15MPa, El30=30MPa, El45=45MPa, and El60=60MPa)

Figure 2.31 shows the progressive reduction in the total initial stiffness and lateral strength by increasing the number of sliding joints introduced. The most pronounced reduction occurs with the introduction of the first two sliding joints. Different configurations of the same number of sliding joints modify the total lateral strength since the crushing of the masonry occurs at different drift levels.

The lateral strength is not appreciably influenced by the aspect ratio (Figure 2.32a): the response becomes slightly more deformable as the infill length increases, reaching slightly higher lateral strength.

The masonry properties influence the response depending on the balance of elastic modulus, thickness, and compressive strength (Figure 2.32b). If thickness and elastic modulus lead to a similar in-plane stiffness of the masonry (as for AAC200, AAC300, and CU1), the global response is similar. Finally, a significant deformable response occurs with materials characterised by very low stiffness, such as the "adobe" earthen masonry type.

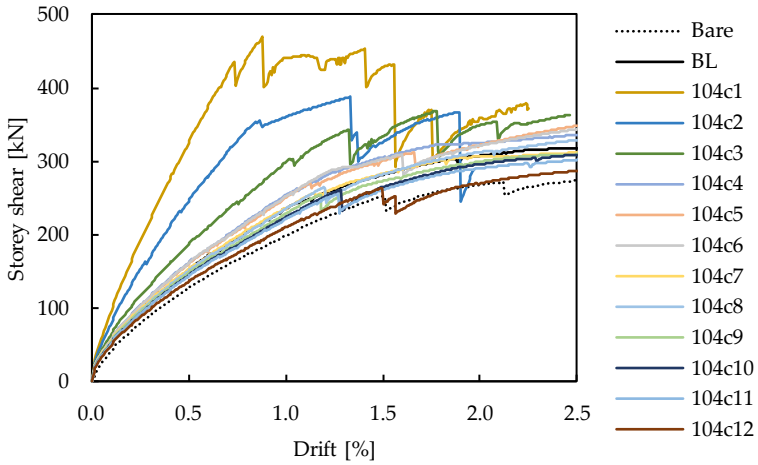

Figure 2.31: Comparison of the global response for different numbers and locations of the sliding joints (104=Baseline model, 104c1=0, 104c2=1, 104c3=1, 104c4=2, 104c5=2, 104c6=2, 104c7=3, 104c8=3, 104c9=4, 104c10=5, 104c11=6, and 104c12=13)

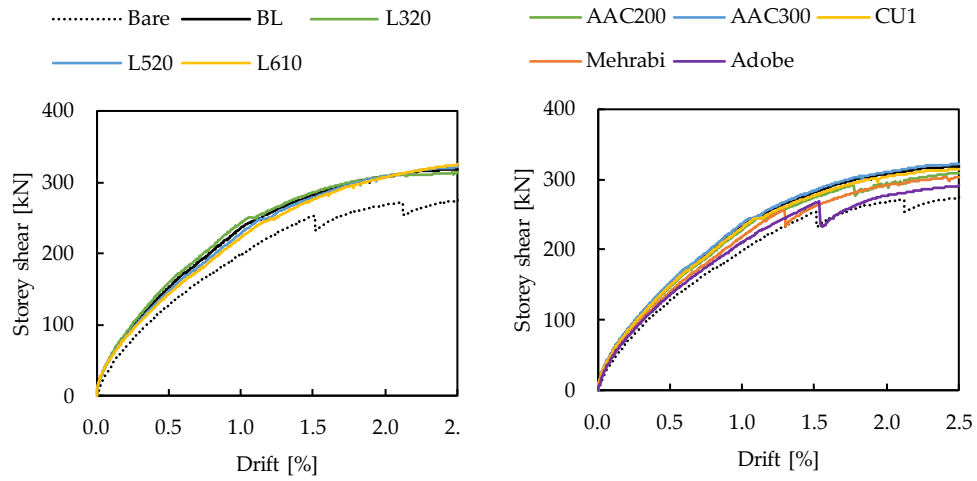

Figure 2.32: Comparison of the global response for different lengths of the infill a) and masonry properties b) (BL=Baseline model, L=420cm and hollow clay masonry).

A trend of lateral initial stiffness increase is shown in Figure 2.33 when the top gap is filled, more pronounced by increasing the lateral joint stiffness. At large drifts, response variability is limited. Also, in this case, the subpanel corner crushing occurs at the curve drops.

The stiffness of the top joint has a significant influence on global behaviour (Figure 2.34). The overall strength increases by increasing the stiffness of the sole top joint. The contribution to the lateral strength given by top beam contact (infill-to-beam shear transfer), as highlighted in Figure 2.34b, increases progressively with the drift level and the stiffness of the top joint. High stiffness of the top joint leads to the condition whereby the shear transfer through the top joint exceeds the estimated overall contribution of the infill. This phenomenon requires further specific investigation.

In the presence of the top contact joint, by increasing the infill length, the global behaviour remains unchanged until a drift of about 1.5% (Figure 2.35a); beyond that, the lateral strength increases with the frame span. The top contact shear transfer is strictly correlated to the infill length (Figure 2.35b), even if the total lateral response of the infilled frame is not significantly modified.

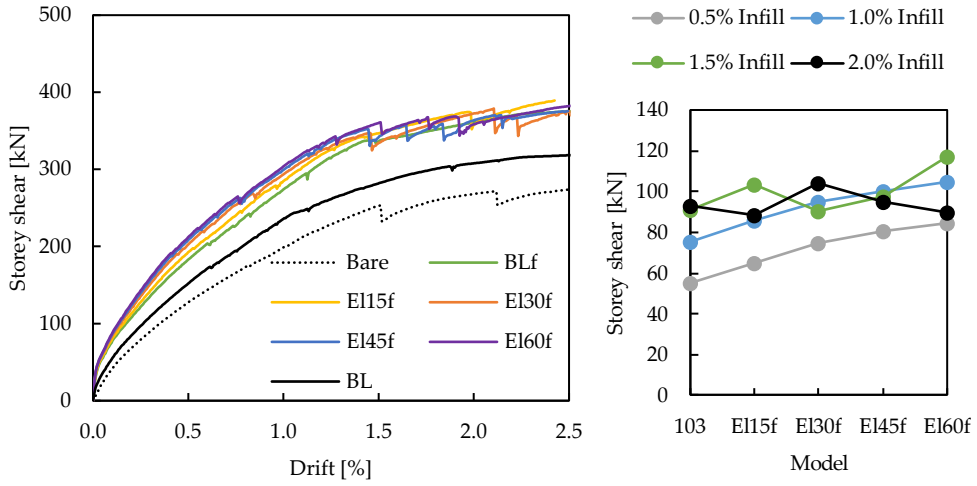

a) *b)*

Figure 2.33: Comparison of the global response a) and of the infill contribution to the lateral strength at fixed interstorey drift levels (0.5%, 1.0%, 1.5%, and 2.0%) b) for different stiffnesses of the lateral joints (BL=Baseline model with top gap, BLf=Baseline model without top gap, El15f=15MPa, El30f=30MPa, El45f=45MPa, and El60f=60MPa).

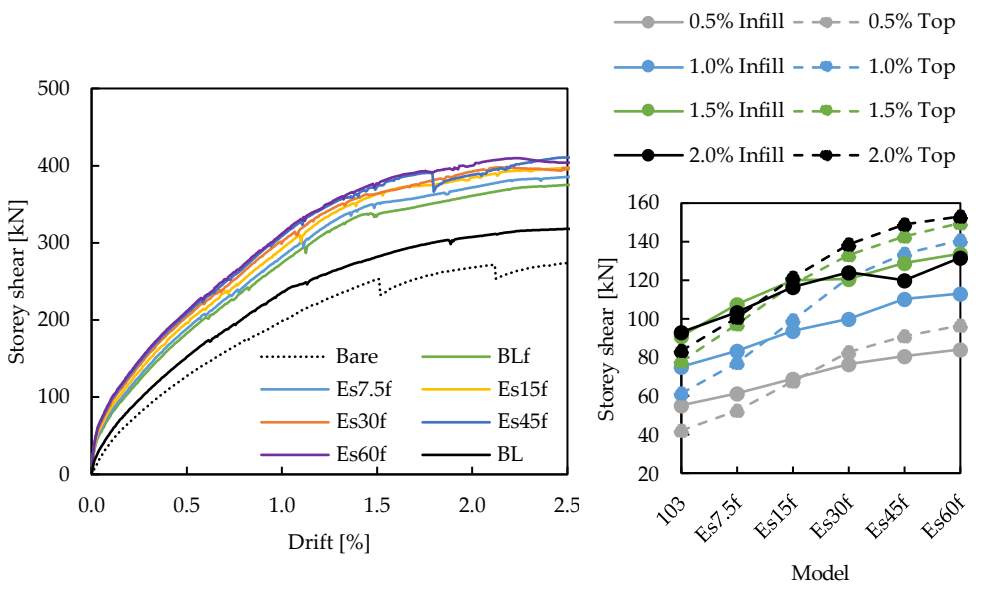

a) *b)*

Figure 2.34: Comparison of the global response a) and of the infill and the top beam contributions to the lateral strength at fixed interstorey drift levels (0.5%, 1.0%, 1.5%, and 2.0%) (b) for different stiffnesses of the top joint (BL=Baseline model with top gap, BLf=Baseline model with the top gap filled, Es7.5f=7.5MPa, Es15f=15MPa, Es30f=30MPa, Es45f=45MPa, and Es60f=60MPa).

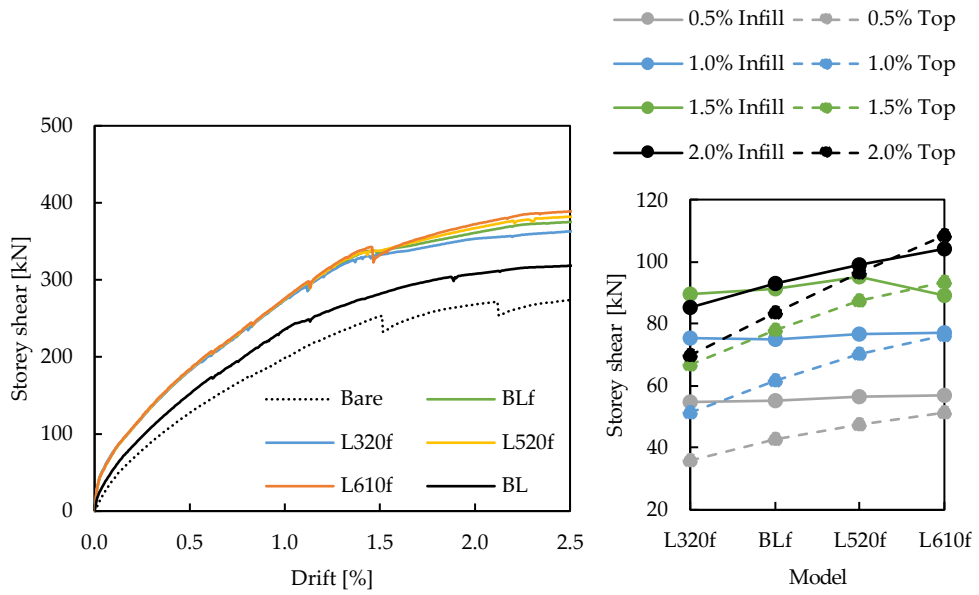

a) *b)*

Figure 2.35: Comparison of the global response (a) and of the infill contribution to the lateral strength together with the top joint shear transfer at fixed interstorey drift levels (0.5%, 1.0%, 1.5%, and 2.0%) (b) for different infill lengths (BL=Baseline model with top gap, L=420cm, BLf=Baseline model with the top joint).

2.3.3 *Sensitivity of the local response to design parameters*

2.3.3.1 Shear actions on the columns

The trend of the shear actions at the top of the windward column (W) and at the base of the leeward column (L) varying the design parameters is examined as a function of the drift level. Figure 2.36a compares the results of the baseline model with those of the models without the base sliding joint (noBJ), without the top gap (noGap), or both (101). The maximum shear action at the top of the windward column is about constant, while the one at the base of the leeward column increases in the models with the sliding joint at the base (BL and noGap) whereby the maximum shear action occurs at the base of the leeward column. For the two models without a sliding joint at the base (noBJ and 101) the trend is inverted, and the action in the windward column is higher than the leeward one.
The column shear actions for different bay aspect ratios are practically the same for both the configurations with and without the top gap. Also, the variation in the elastic stiffness of the top joint does not affect the shear action in the columns (Figure 2.37).
The increase in the stiffness of the lateral joints, instead, leads to a progressive shear action increase (Figure 2.36b-c), with the load that exceeds the shear action quantified by the hierarchy of strength rule applied to the bare frame (red dashed line).
The increase in the number of sliding joints reflects a reduction in the shear action in the columns (Figure 2.36d).
The maximum internal action mainly occurs at the base of the leeward column.

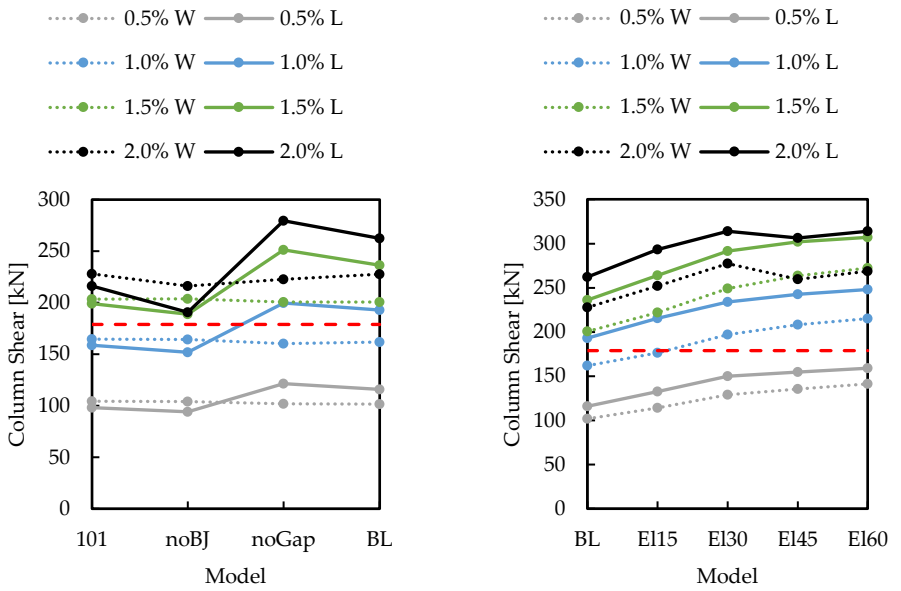

a) Main design choices

b) Stiffness of the lateral joint, top gap

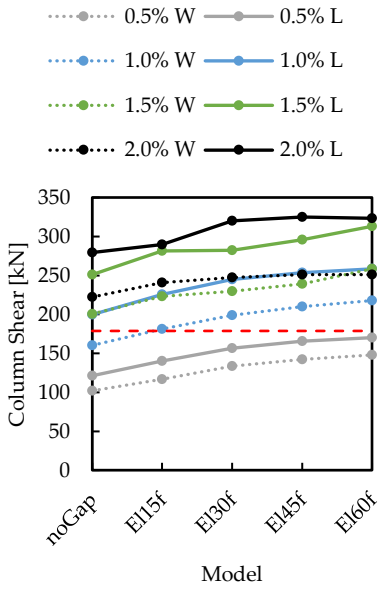

c) Stiffness of the lateral joints, no gap

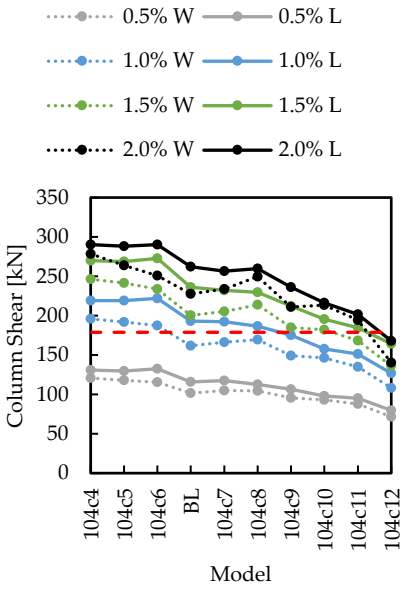

d) Number of sliding joints

Figure 2.36: Study of the influence of each parameter on the shear action on the top of the windward column ("W") and on the base of the leeward one ("L") at different interstorey drift levels (0.5%, 1.0%, 1.5%, and 2.0%). The dashed line represents the shear action

estimated at the activation of the plastic hinges at the column ends, according to the capacity design approach, in the bare frame configuration.

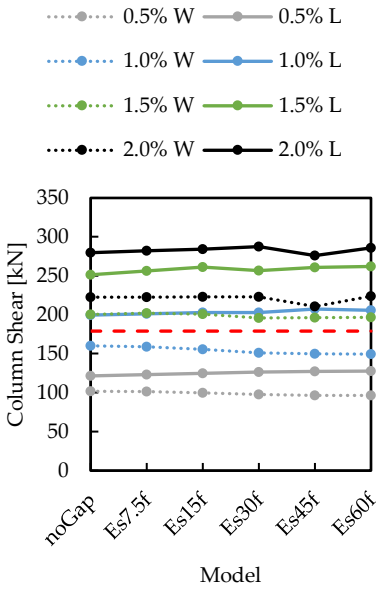

Figure 2.37: Study of the influence of the elastic stiffness of the top joints on the shear action on the top of the windward column ("W") and on the base of the leeward one ("L") at different interstorey drift levels (0.5%, 1.0%, 1.5%, and 2.0%). The dashed line represents the shear action estimated at the activation of the plastic hinges at the column ends, according to the capacity design approach, in the bare frame configuration.

2.3.3.2 *Local crushing of the masonry subpanels*

The damage level of the infill is evaluated by considering the local crushing at the corners of the subpanels in the range of drift up to 2.5%. This condition is numerically identified when the first Gauss Point of the smeared crack reaches its peak compressive strength. Figure 2.38 represents an example of the identification of the first local crushing for the case with a top gap and a stiffness of the lateral joints equal to 45 MPa; here, crushing is visible in the upper corner at the windward side of the second subpanel, in the upper left Gauss Point.

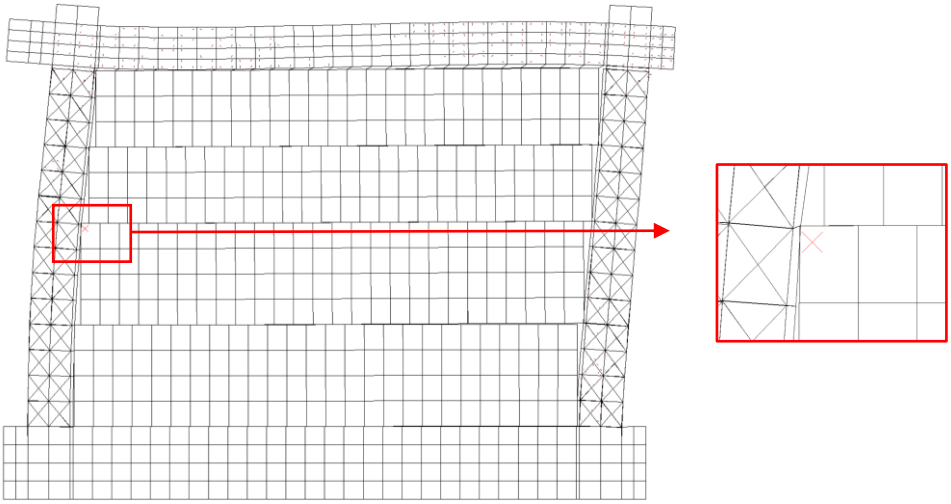

Figure 2.38: Identification of the first crushing at the windward side of the second subpanel in the parametric case characterised by a stiffness of the lateral joints equal to 45 MPa and a gap between the infill and the top beam (top gap).

No crushing was reached in the baseline models with and without the top gap, in the parametric analyses on the stiffness of the top joint, or in infills of different lengths with and without the top gap. The main parameter that influences the activation of the local crushing is the stiffness of the lateral joints (Figure 2.40a-b). Crushing occurs starting with a stiffness of the lateral joint equal to 30 MPa, and it is progressively anticipated by increasing the stiffness. A slightly anticipation is exhibited when the top gap is filled.

The local crushing develops at higher drift levels as the number of sliding joints increases (Figure 2.40c). In this case, the range of drift levels examined is extended to 3% since all the configurations with two sliding joints exhibited crushing at about 2.5% drift. A minimum of three sliding joints is required to postpone the crushing.

Among the analyses on the properties of masonry, only AAC200 reached the local crushing at a drift level lower than 2.5%, while AAC300 reached it at a drift level of about 3.0%. Since the material properties are the same (the only difference is the thickness), this phenomenon is investigated through parametric analyses on the infill thickness (by considering 150-200-250 and 300 mm of AAC infill thickness), whose results are reported in Figure 2.39. The first crushing occurs at the top corner of the windward side of the second subpanel, and it is progressively postponed as the thickness increases. This can be justified by observing the deformation profiles of the columns, visible in Figure 2.41. As the thickness increases, the local thrust exerted by the infill on the columns increases, and accordingly the outward deformation of the two columns. This implies a reduced local strain in the lateral joints and masonry corners, in particular for the second subpanel, where crushing mainly occurs.

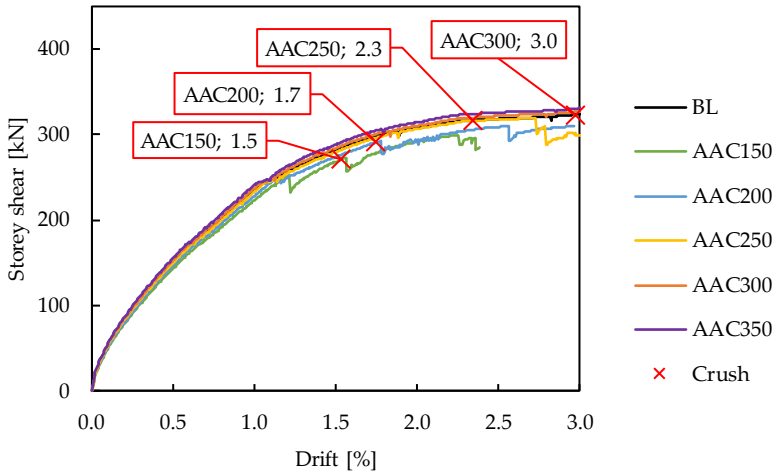

Figure 2.39: Identification of the first crushing for different thicknesses of the infill made of AAC.

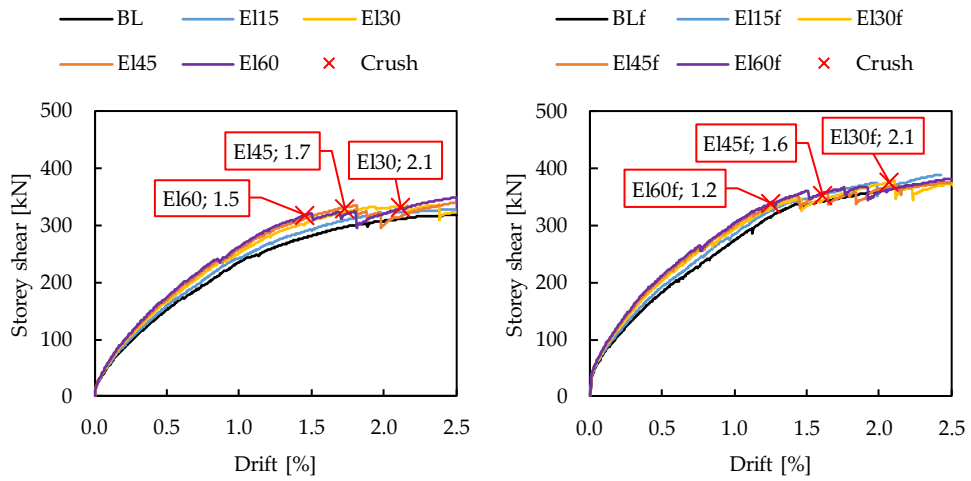

a) Lat. Joint stiffness, top gap *b) Lat. Joint stiffness, gap filled*

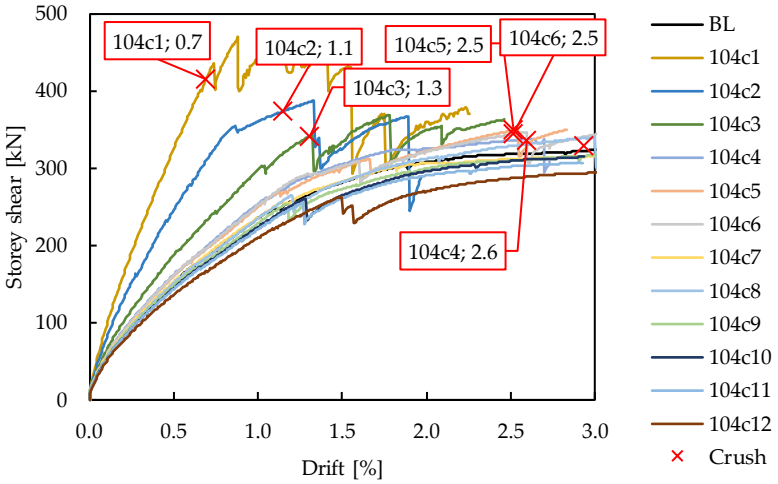

c) Number and configuration of sliding joints

Figure 2.40: Identification of the first local crushing of the subpanels in the parametric analysis. Identification of the model and the respective drift at the reaching of the local crushing.

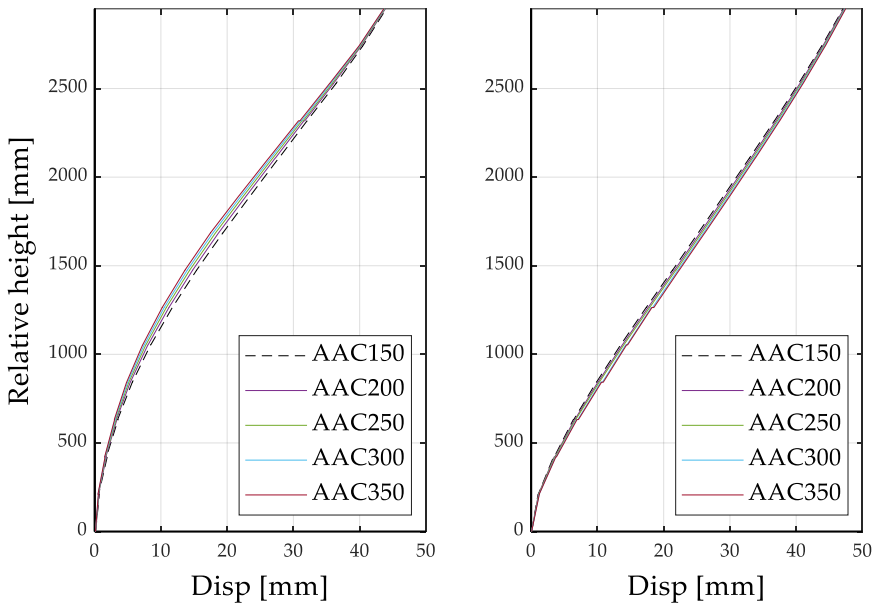

Figure 2.41: Deformation profiles of the windward a) and leeward b) columns for different thicknesses of the infill made of AAC.

2.3.4 *Summary of the results and design suggestions*

The parametric analyses conducted allow for investigating the influence of the infilled frame response on some significant design parameters. The effect on the global lateral force drift response, on the column shear action, and on the drift capacity at the first local crushing of the sub-panel corners is discussed.
The absence of the sliding joint at the base does not modify the global response; locally, a redistribution of the shear action between the columns and its inversion at the base of the windward column is observed.
The presence of plaster on the sliding joints adds an initial strength and stiffness that led to an initial peak strength before the activation of the sliding.
The contact of the infill with the top beam adds a significant contribution to the lateral strength due to the vertical confinement exerted by the top beam on the infill in the sway mechanism, which increases as the top joint stiffness or the infill length increases, while the shear action on the columns is not significantly affected. The influence of the stiffness of the lateral joints is reduced.
The increase in the number of sliding joints allows for a reduction in the lateral strength of the infill and shear action on the columns. Two sliding joints are sufficient for ductile behaviour; three sliding joints are required to postpone the masonry crushing after 2.5% drift.
The stiffness of the lateral joints modifies the lateral strength and the maximum shear acting on the columns for both the configurations with and without the top gap. This parameter governs the first local crushing at the corners of the subpanels. As the stiffness increases, crushing is anticipated.
If the masonry panel is sufficiently rigid and strong, local crushing does not occur, but a higher interaction with the frame is exhibited. The masonry panels characterised by a very low stiffness, for example, in earthen masonry, do not exhibit crushing. Masonry properties of intermediate stiffness and weak compressive strength are more susceptible to anticipated corner crushing, as in the case of aerated autoclaved concrete masonry.
The infill damage could be preliminary limited by controlling the ratio between the lateral joint stiffness, E_{lat}, and the compressive peak strength, f_m, of the masonry in the horizontal direction. A preliminary design proposal to protect the subpanel from corner crushing is derived by imposing a strength hierarchy along the contact length between the lateral joints and the masonry. If an elastic contact material is considered for the lateral joint at the column interface, no stress cup is ensured by the contact material. Thus, assuming a pendular frame with rigid columns, the difference in displacement between the two opposite corners of the subpanel is given by Eq. (2.3-1), where δ is the clear interstorey drift and h is the height of the subpanel (Figure 2.42 left). If no friction along the sliding joints is considered, this relative

displacement is assumed to be equally subdivided on the windward and leeward sides. This assumption means that the neutral axis of the contact area is assumed to be equal to half of the subpanel height. If the masonry is markedly stiffer than the contact material, the deformation of the latter is negligible, and the average strain of the contact material is derived by subdividing the local relative displacement, previously evaluated, by the thickness, s_{lat}, of the lateral contact material. It is noteworthy that if the stiffness of the masonry and that of the lateral contact material are comparable, the deformation of the masonry could not be neglected. The strain multiplied by the elastic modulus of the deformable material, E_{lat}, allows for evaluating the maximum stress, $\sigma_{c,lat}$, transmitted to the masonry (Eq. (2.3-2)). The crushing of the masonry at the corners could be avoided if the stress transmitted to the masonry is lower than its peak compressive strength in the horizontal direction, f_{md}. Consequently, a limit to the ratio between the elastic stiffness of the lateral contact material and the masonry compressive strength could be defined as in Eq. (2.3-3) to prevent crushing until a defined drift level δ.

$$d_h = \delta \cdot h \tag{2.3-1}$$

$$\sigma_{c,lat} = \frac{\delta \cdot h}{2} \cdot \frac{1}{s_{lat}} \cdot E_{lat} \tag{2.3-2}$$

$$\left(\frac{E_{lat}}{f_{md}}\right)_{lim} = \frac{2 \cdot s_{lat}}{\delta \cdot h} \cdot \tag{2.3-3}$$

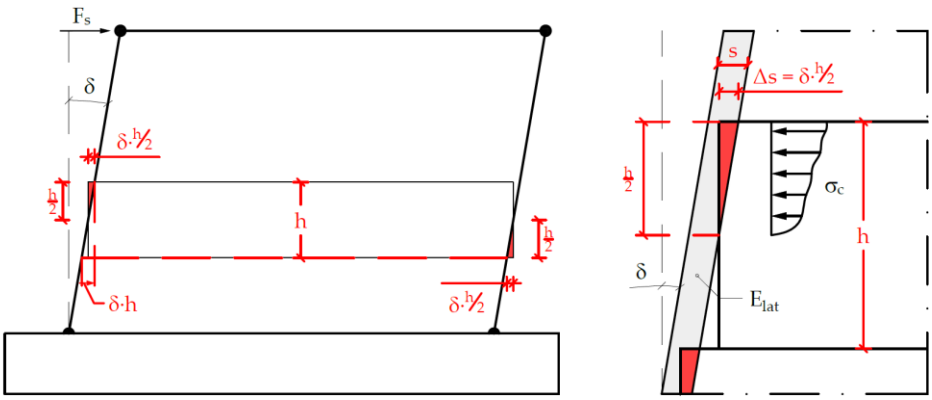

Figure 2.42: Schematic representation of the distribution of the crushing between windward and leeward sides (left) and detail of the contact between the infill and the lateral joints (right).

Despite the linear deflection hypothesised, in real behaviour, the constraints at the extremes of the columns allow for a nonlinear displacement profile that exhibits a nonlinear demand on the infill along its height. At the contact forces acting along the columns correspond the columns outer deflection since their stiffness is not unlimited; a higher crushing is expected at the windward side given by the friction along the sliding joints that opposes the subpanel slide and concentrates the deformation at the windward side. Given all the hypotheses, the proposed equation results in a preliminary formulation aimed at giving a simplified indication.
To better test the proposal, a parametric analysis of the stiffness of the lateral joints was also conducted for the AAC200 masonry. Figure 2.43 compares the analytical limit proposed to the drift at the activation of the first crushing numerically obtained. The parametric analyses of the lateral joint stiffness of the baseline model and the AAC200, and the parametric analyses conducted for different thicknesses of the AAC masonry are considered. Other materials are not considered since they do not reach the crushing stage. The proposed limit allows for the definition of an upper domain for the analyses considered, except for AAC150. It is clearly visible that for very low E_{lat}/f_m ratios, the first crushing tends to occur at high drift levels. It is worth noting that the equation is a first proposal, and its direct applicability must be tested by extensive parametric analyses of different frame geometry, infill thickness, materials, and relative stiffness between the infill and the frame.

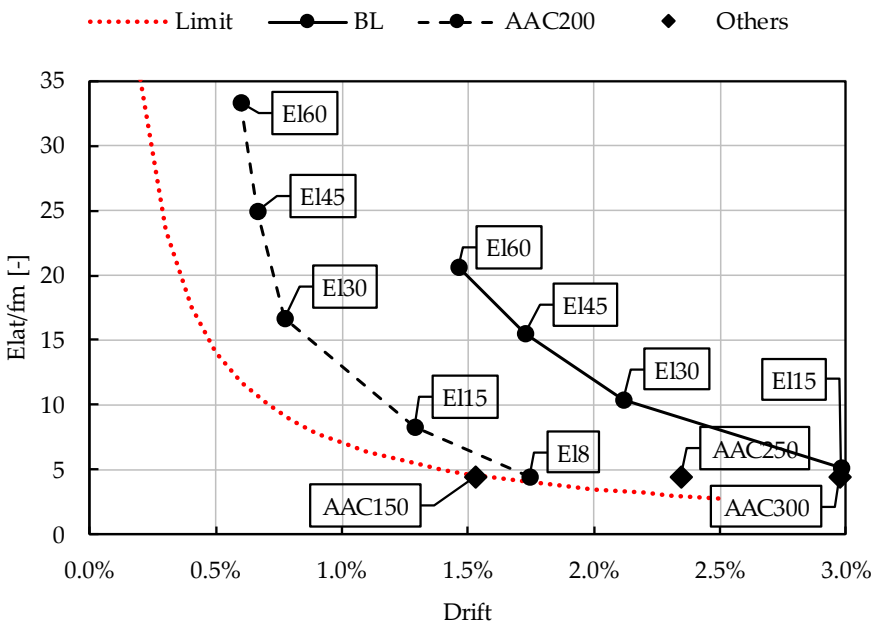

Figure 2.43: Comparison of the proposed equation to limit the crushing of the infill and the activation of the crushing detected in the parametric study.

2.4 Analytical prediction

2.4.1 *Introduction*

The analytical model proposed in Preti et al. (2019) [33] to describe the ductile infill tested at the University of Brescia and described in Preti et al. (2015) [15] is here modified to account for the elastic response of the lateral joints.
The recalled analytical model was built to describe the in-plane behaviour of infills partitioned by horizontal sliding joints, separated from the top beam by a gap, connected to the base beam by a sliding joint, and having lateral vertical joints with a plastic yielding plateau lower than the masonry compressive strength. The estimation of the in-plane behaviour considers the superposition of the effects of the bare frame and infill resistance: the contribution of the infill to the lateral strength is separately evaluated, referring to a pendular frame with rigid elements, and it is successively added to that of the bare frame.
The benchmark is the numerical baseline model described in §2.2.4; the modifications introduced to represent the experimental test are not considered. As highlighted in Figure 2.24 of §2.2.5, in the presence of a sliding joint at the base of the infill, the contact forces are similar along the height of the column; consequently, the assumption of equal contact forces made in the analytical model is applicable. Vice versa, in its absence, high concentration occurs at the windward side of the first subpanel, and no contact force is exerted at the base of the leeward side, providing an irregular distribution of the contact forces. Furthermore, if the top gap is filled, the contribution of the force directly transmitted by the top beam to the infill must be added to the infill-columns interaction mechanism. Figure 2.44 shows each contribution to lateral strength.

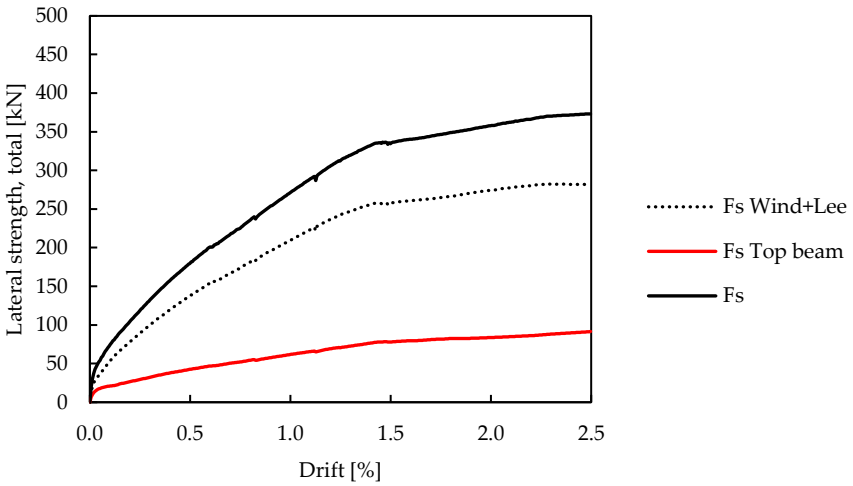

Figure 2.44: Identification of the contributions to the lateral strength in the numerical model (model baseline with top gap filled, "noGap")

Since the capacity backbone of the bare frame has a non-regular trend given by drops, the evaluation of the infill contribution to the lateral strength by subtracting the capacity backbone of the bare frame from that of the infilled frame is only a simplification; its effective contribution to the lateral strength is not known. In the following, the infill contribution to lateral strength is quantified as the sum of the shear action at the top of the columns (Eq. (2.4-1)), evaluated on a pinned column subjected to the horizontal and vertical contact forces (Eqs. (2.4-2) and (2.4-3)). The reference scheme is represented in Figure 2.45.

$$F_s = V_{top}^{Win} + V_{top}^{Lee} \tag{2.4-1}$$

$$V_{top}^{Win} \cdot H = \sum_{i=1}^{N} \left[R_{h,i}^{Win} \cdot Z_i + \frac{1}{2} R_{v,n}^{Win} \cdot b_c \right] \tag{2.4-2}$$

$$V_{top}^{Lee} \cdot H = -\sum_{i=1}^{N} \left[R_{h,i}^{Lee} \cdot Z_i + \frac{1}{2} R_{v,n}^{Lee} \cdot b_c \right] \tag{2.4-3}$$

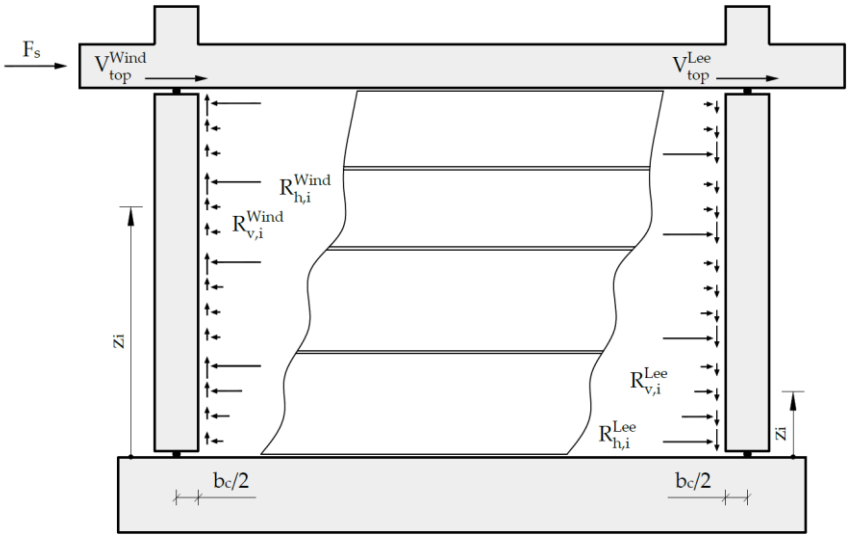

Figure 2.45: Scheme adopted for the evaluation of the infill contribution to the lateral strength.

The contribution of the infill evaluated as previously defined is compared in Figure 2.46 for the baseline model to the infill contribution evaluated as the difference between the capacity backbone of the infilled frame and the bare one. The two profiles are close between them; consequently, the application of the superposition of the effect is possible despite the highly nonlinear mechanisms that govern the behaviour.

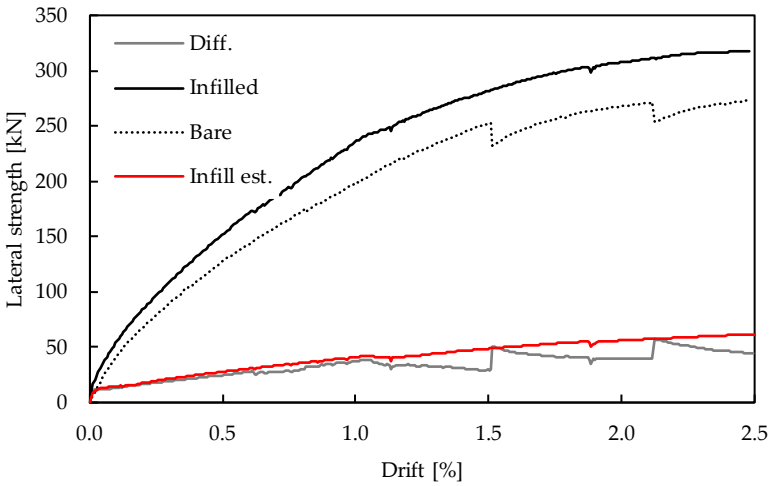

Figure 2.46: Comparison of the contribution of the infill to the lateral strength evaluated as the difference ("Diff.") between the capacity backbone of the infilled frame and the bare one and estimated ("Infill est.") through the procedure previously described.

2.4.2 *Modifications to the analytical model*

The original analytical model proposed in Preti et al. (2019) [33] considers the resultants of the horizontal and vertical contact forces of each subpanel acting on the columns; the shear action at the top of the columns is evaluated by equilibrium on the pendular system; and, consequently, the infill contribution to the infilled-frame lateral strength is derived.

Firstly, the horizontal contact forces at the leeward side are evaluated by a strut mechanism, and then the horizontal forces at the windward side are derived by adding the friction contribution. The vertical force on the leeward side is calculated from the horizontal component, accounting for the strut inclination assumed to be equal to the sub-panel diagonal. On the windward side, relative sliding between the infill and the lateral vertical boards is considered, and the vertical component is derived from the horizontal one by applying the friction coefficient that characterises the surface infill-lateral joints. The only unknown is the horizontal contact force at the leeward side, and it is derived by the integration of a simplified stress block distribution of the contact stresses, characterised by a stress level equal to the compressive strength of the contact material. The neutral axis depth is empirically calibrated considering the average numerical contact force acting on the leeward side and a stress-block distribution. In the analytical model, the following simplifications are considered: the same height (average height), the same neutral axis depth, and the same contact force for each subpanel. For further details, refer to §2.1.2.

In the new application, the elastic or pseudo-elastic material for the lateral contact joint adds an issue. A yielding cup to the contact stresses does not occur; thus, they depend on the strain demand imposed by the frame deformation and the infill-frame interaction. Some simplifications are here introduced. The same hypotheses adopted in §2.3.4 to evaluate the maximum stress imposed on the masonry are considered: linear deformation profile of the columns; inclination of the deformation profile equal to the drift; deformation of the masonry negligible; linear strain profile of the lateral joint in the contact area. In the design proposal in §2.3.4, a neutral axis depth equal to half of the subpanel height was derived from geometrical considerations for rigid elements. In this case, a more detailed estimation is required, and it is empirically calibrated. The maximum contact stress, $\sigma_{c,max}$, is evaluated as in Eq. (2.4-4).

Consequently, the original expression for the horizontal reaction at the leeward side (Eq. (2.1-11)) is modified as in Eq. (2.4-5) to account for a linear distribution of the stresses. Remember that, in the analytical model, firstly the strut contribution in the absence of friction is evaluated. The horizontal reaction is evaluated at the leeward column. Successively, it is assumed applied also to the windward column and the friction contribution is added.

$$\sigma_{c,max} = \frac{\delta \cdot \overline{X}_n^{Lee}}{s_{lat}} \cdot E_{lat} \tag{2.4-4}$$

$$R_{h,n}^{Strut} = 0.5 \cdot t \cdot \overline{X}_n^{Lee} \cdot \frac{\delta \cdot \overline{X}_n^{Lee}}{s_{lat}} \cdot E_{lat} \tag{2.4-5}$$

The neutral axis depth (or contact length) is derived empirically from the parametric analysis; a complete description will be given in the following section.
Since a linear distribution of the stresses is assumed, the resultants are applied at one third of the neutral axis depth. The schematic representation is reported in Figure 2.47

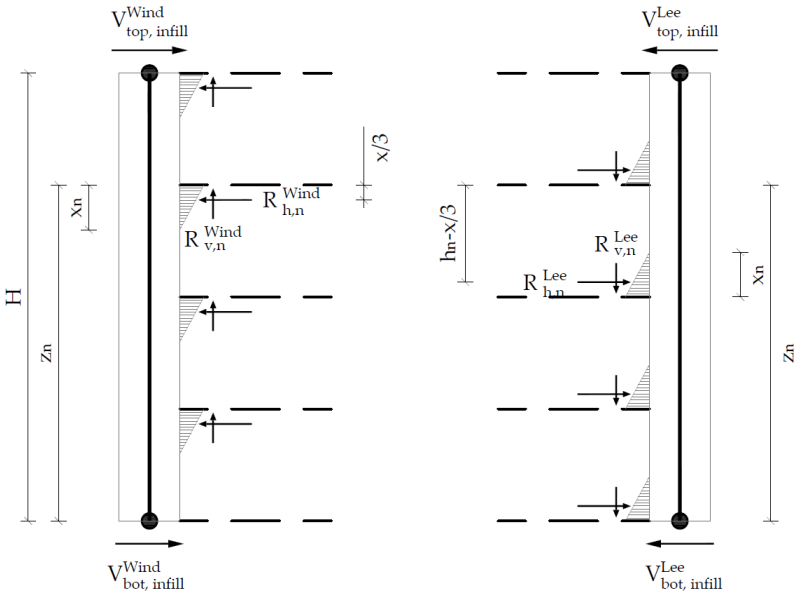

Figure 2.47: Schematic representation used for the equilibrium on the windward and leeward columns.

The equations of the equilibrium on the columns expressed in Eqs. (2.1-9) and (2.1-10) are modified according to Eqs. (2.4-6) and (2.4-7).

$$\Delta F_s^{Win} = V_{top}^{Win} = \frac{1}{H} \cdot \sum_{n=1}^{N} \left[R_{h,n}^{Win} \cdot \left(Z_n - 1/3 \cdot \overline{X}_n^{Win} \right) + \frac{1}{2} R_{v,n}^{Win} \cdot b_c \right] \tag{2.4-6}$$

$$\Delta F_s^{Lee} = V_{top}^{Lee} = -\frac{1}{H} \cdot \sum_{n=1}^{N} \left[R_{h,n}^{Lee} \cdot \left(Z_n - h_n + 1/3 \cdot \overline{X}_n^{Lee} \right) - \frac{1}{2} R_{v,n}^{Lee} \cdot b_c \right] \quad (2.4\text{-}7)$$

Following the same steps reported in §2.1.2, Eq.s (2.1-15), (2.1-16), and (2.1-17) are modified in Eq.s (2.4-8), (2.4-9), and (2.4-10) to obtain the shear acting at the top of columns and the lateral strength given by the strut mechanism. The same neutral axis depth and the same horizontal force is assumed for all the subpanels.

$$\Delta F_s^{strut,wind} = V_{top}^{strut,wind} = R_{h,n}^{strut} \cdot \left[\frac{N+1}{2} - \frac{1}{3h} \left(\overline{X}^{Lee} - \frac{3}{2} \mu_c \cdot b_c \right) \right] \quad (2.4\text{-}8)$$

$$\Delta F_s^{strut,lee} = V_{top}^{strut,lee} = -R_{h,n}^{strut} \cdot \left[\frac{N-1}{2} + \frac{1}{3h} \left(\overline{X}^{Lee} - \frac{3}{2} tan\,\alpha \cdot b_c \right) \right] \quad (2.4\text{-}9)$$

$$\Delta F_s^{strut} = R_{h,n}^{strut} \cdot \left[\left(1 - \frac{2}{3} \cdot \frac{\overline{X}^{Lee}}{h} \right) + \frac{b_c}{2h} (\mu_c + tan\,\alpha) \right] \quad (2.4\text{-}10)$$

On the windward side, the contribution of the friction mechanism to the shear at the top of the column (Eq. (2.1-19)) must be added. The total lateral strength is given by the sum of Eq. (2.4-10) and the friction contribution evaluated as in the original work (Eq. (2.1-19)) with a modification in the friction coefficient between the contact material and the masonry panel that will be described in the following §2.4.3.
It is important to highlight that the here proposed model is representative of the range of elastic modulus of the contact material here analysed (7.5-60MPa) and until a drift level of 3.0%.

2.4.3 *Empirical calibration of the strut inclination on the windward side*

In the original work, vertical contact forces on the windward side are evaluated by assuming that the vertical sliding between masonry and contact material mobilises the friction. Given the high deformability of the contact material, a deformable response is also expected in the tangential direction. Numerical analysis shows that the relative sliding at the lateral joints is prevented by the shear deformation of the deformable material. Thus, the inclination of the strut at the windward contact can be expected to be limited within the inclination of the subpanel diagonal, α, and the angle corresponding to the friction coefficient of the infill-to-lateral joint interface, μ_c (Figure 2.48).

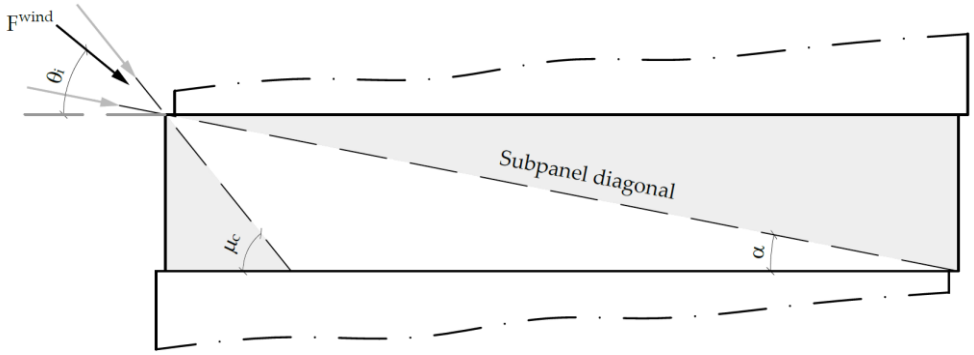

Figure 2.48: Indication of the range of the strut inclination.

The analytical assessment of such an inclination is non-trivial since the compatibility of the displacements at the lateral joints must be considered. In this study, the inclinations of the sub-panel internal struts at the windward and leeward column interfaces are numerically evaluated as the ratio of the resultants of the vertical and horizontal components of the contact forces. The results are reported in Figure 2.49. By varying the design parameter (elastic stiffness of the contact material), the results show that the inclination at the leeward side (dotted line) remains close to the inclination of the subpanel diagonal, while at the windward side (continuous line) it is higher, and it varies from a minimum value equal to about 0.36 for the baseline case to 0.6 for the stiffer case. Starting from a stiffness equal to 30 MPa, the sudden drop corresponds to the local crushing of the masonry, after which the redistribution of stresses does not allow a clear reading of the strut inclination, so those values are disregarded.

The trend of variation of the inclination of the strut at the windward side given by the elastic stiffness of the lateral joints could be represented by an exponential expression, but a simpler linear relationship function of the elastic stiffness of the lateral contact material is proposed (Eq. (2.4-11)). The proposal is compared to the

numerical one in Figure 2.50. The proposed strut inclination is quantified in the analytical equations as an equivalent friction coefficient for the lateral joints.

$$\theta^{wind} = 0.3 + 0.005\, E_{lat}(MPa) \qquad (2.4\text{-}11)$$

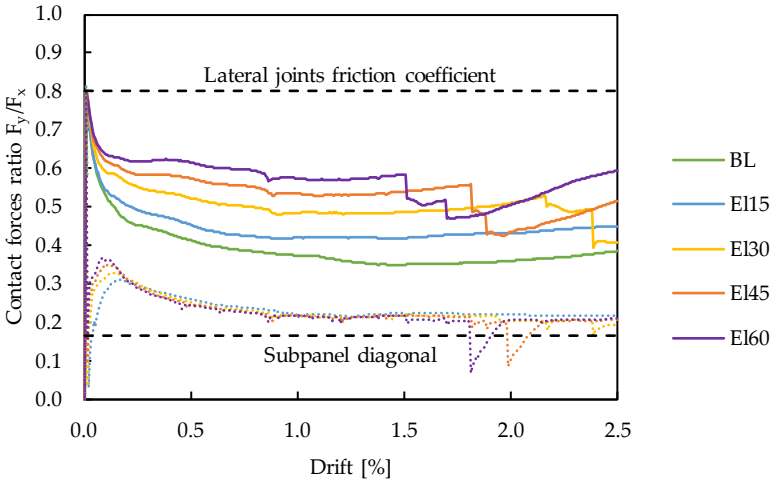

Figure 2.49: Ratio between the resultant of the vertical contact forces and horizontal contact forces at the windward (continuous) and leeward (dotted) sides, as a function of the interstorey drift and for different values of the elastic stiffness of the contact material at the column interfaces. The lower (subpanel diagonal) and upper (friction of the surface at the lateral joints) limits are also represented.

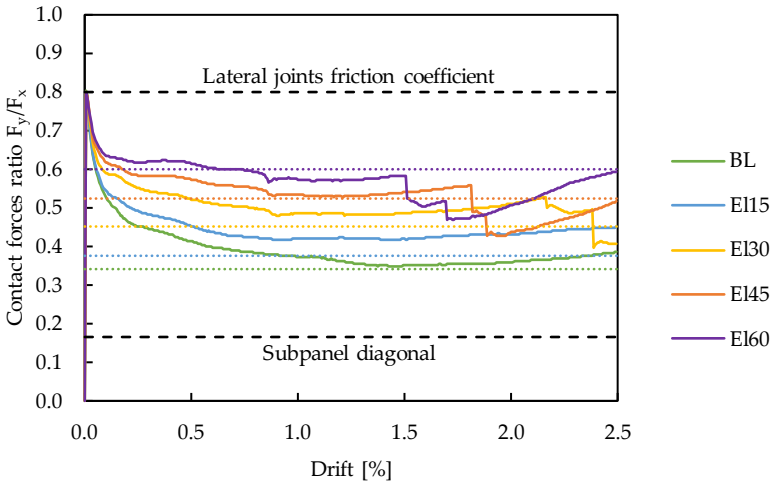

Figure 2.50: Comparison of the proposed inclination of the strut at the windward side (dotted line) to the numerical one (continuous line) for different stiffnesses of the lateral joints.

2.4.4 *Empirical calibration of the contact length*

The average contact length obtained in the numerical analysis, $\overline{X}_{num}^{Lee}$, is adopted to calibrate an empirical predictive equation. To this end, the mean value, $R_{h,\text{mean}}$, of the horizontal contact forces of each subpanel on the leeward side is first calculated. Then the contact length, $\overline{X}_{num}^{Lee}$, is evaluated by Eq. (2.4-12), which is the inversion of Eq. (2.4-5). Eq. (2.4-13) provides the empirical representation of the numerical neutral axis: a linear equation modified by an exponential variation to account for the influence of the stiffness of the lateral joints. The comparison of the proposal and the numerical results for different stiffnesses of the lateral joints is reported in Figure 2.51.

$$\overline{X}_{num}^{Lee} = \sqrt{\frac{2 \cdot R_{h,\text{mean}} \cdot s_{lat}}{t \cdot E_{lat} \cdot \delta}} \qquad (2.4\text{-}12)$$

$$\overline{X}_{appr}^{Lee} = h_{mean} \cdot E_{lat}^{-0.37}\left(0.95 - 0.1 \cdot \delta(\%)\right) \qquad (2.4\text{-}13)$$

Where E_{lat} is expressed in MPa and h_{mean} is the mean subpanel height.

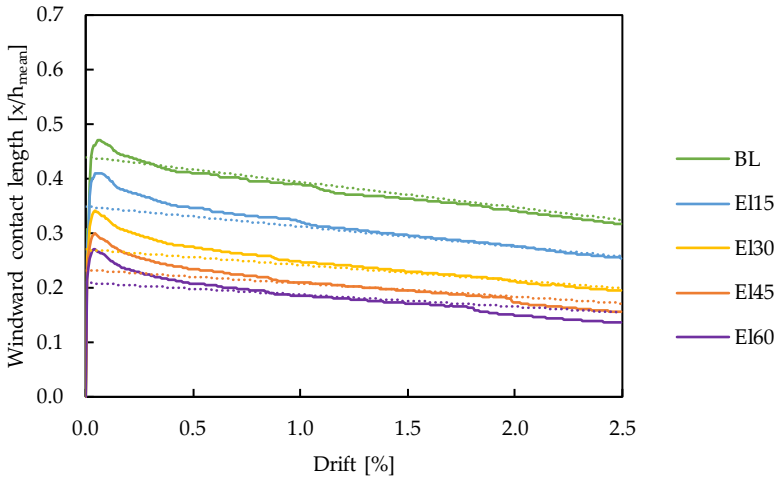

Figure 2.51: Comparison of the proposed neutral axis depth at the leeward side (dotted line) to the numerical one (continuous line) for different stiffnesses of the lateral joints.

2.4.5 *Validation of the analytical model*

The modifications to the analytical model previously defined are here applied to the parametric analyses conducted on the stiffness of the lateral joints and the infill length. In the following, only its application to the baseline model is considered, the results of the other models are reported in §Appendix A.
The numerical and analytical comparison investigates the normalised contact length at the leeward column (Figure 2.53a), the horizontal resultant of the contact forces along the two columns (Figure 2.53b) and the shear action at the two extremes of the columns (Figure 2.53c-d). Finally, the infill contribution to the lateral strength is examined (Figure 2.52).
The comparisons of all the results considered in the parametric analysis are schematically represented in Figure 2.54 and Figure 2.55 for different stiffnesses of the contact material and infill lengths, respectively. The shear action at the top of the windward column and at the base of the leeward column and the contribution of the infill to the lateral strength are considered. The overall good agreement seems acceptable. Note that the comparison loses its meaning when the local crushing of the corners of the subpanels occurs. This typically occurs for stiffnesses higher than 30MPa at large drift levels, as predicted by equation 2.4-5.

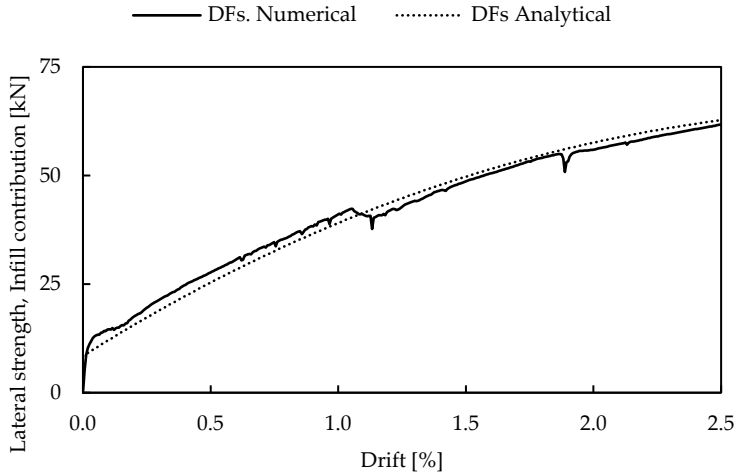

Figure 2.52: Comparison of the numerical and analytical contribution of the infill to the lateral strength on the baseline model, that is characterised by a stiffness of lateral joints equal to 8 MPa.

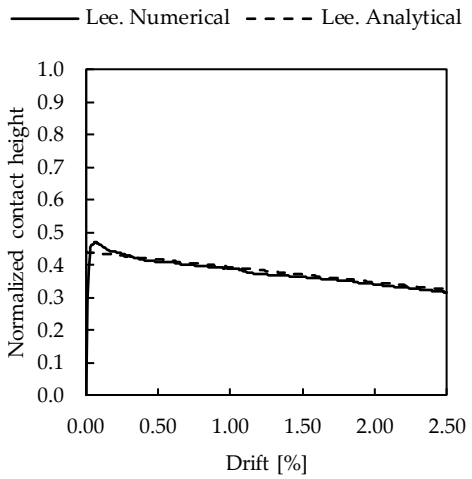

a) Normalized contact length

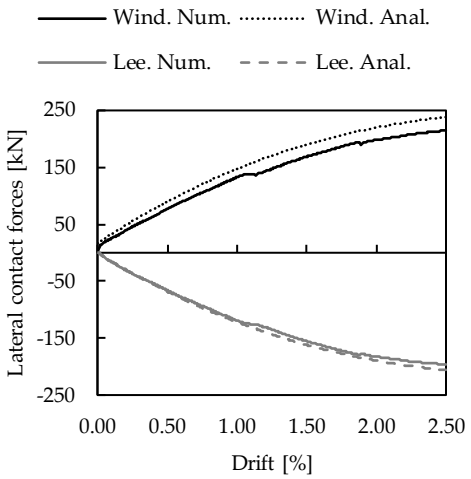

b) Horizontal contact forces

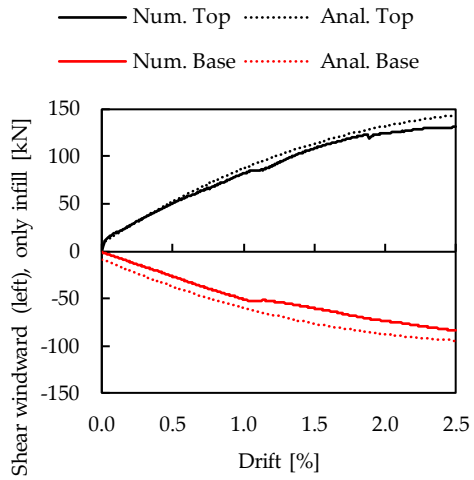

c) Shear actions on the windward column

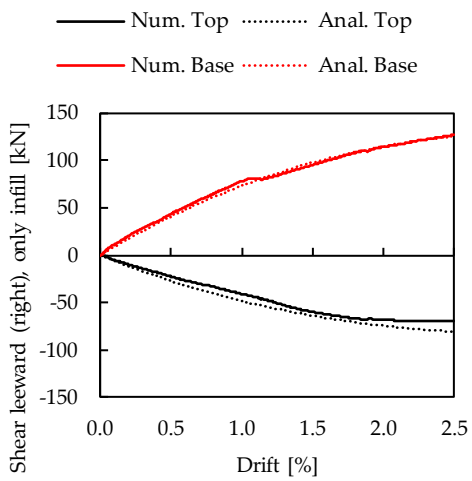

d) Shear action on the leeward column

Figure 2.53: Comparison of the numerical and analytical results of the baseline model, that is characterised by a stiffness of lateral joints equal to 8 MPa.

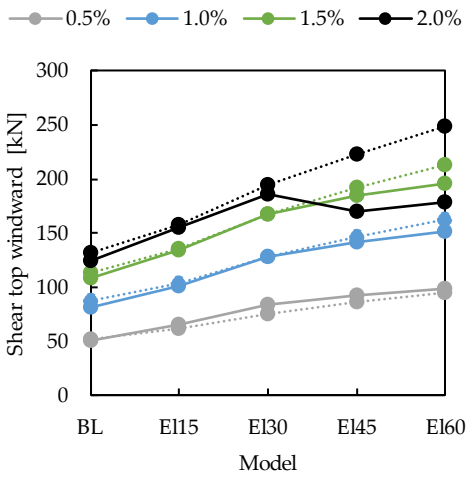

a) Shear action at the top of the windward column

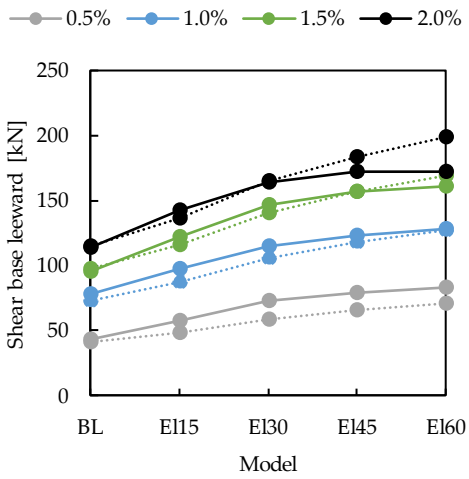

b) Shear action at the base of the leeward column

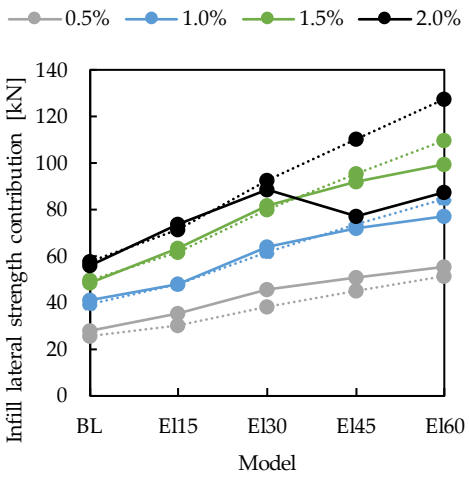

c) Infill contribution to the lateral strength

Figure 2.54: Comparison, at different interstorey drift levels (0.5%, 1.0%, 1.5%, and 2.0%), of the numerical and analytical results for the model studied in the parametric analysis on the stiffness of the lateral joints.

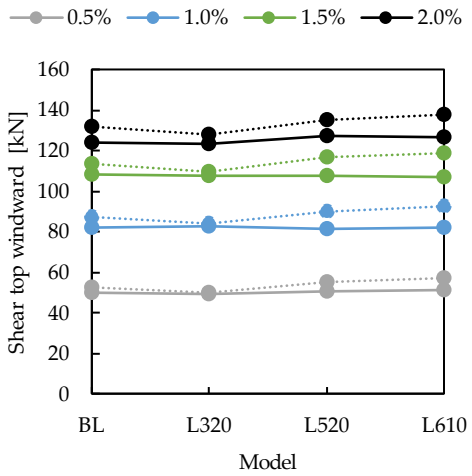

a) Shear action at the top of the windward column

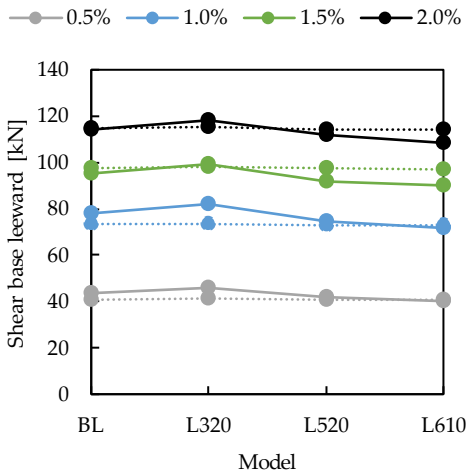

b) Shear action at the base of the leeward column

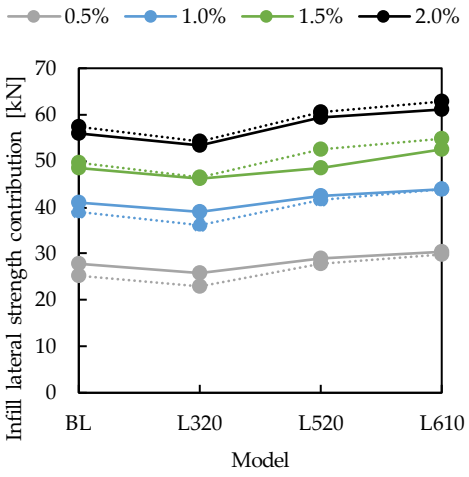

c) Infill contribution to the lateral strength

Figure 2.55: Comparison, at different interstorey drift levels (0.5%, 1.0%, 1.5%, and 2.0%), of the numerical and analytical results for the model studied in the parametric analysis on the length of the infill.

3 MODELLING OF THE GLOBAL RESPONSE OF RC FRAME STRUCTURES WITH SLIDING JOINT INFILLS

The influence of ductile infills on the global behaviour of RC frame structures and the ability of different analysis typologies to predict the seismic demand at all limit states are explored.

A bidimensional frame designed according to three different ductility levels and infilled with ductile infills of three different responses (different stiffness and strength due to different thicknesses) is analysed by means of response spectrum analysis (RSA), nonlinear static analysis (pushover, PO), and nonlinear time history analysis (NLTHA). A simplified approach to account for the infill contribution in linear dynamic analyses is proposed and tested. The ductile infill typology considered in this study is the one originally proposed in the literature by Preti et al. (2015) [15], discussed in the previous chapters.

NLTHA results are taken as the target response; firstly, the ability of the other analyses to estimate the seismic demand is tested for the frames in the bare configuration. Recognising that the NTLHA results are obtained from a single septuple of accelerograms, the efficiency of the predictions of simpler analyses for the infilled configuration is evaluated by comparison to those obtained in the bare configuration.

A specific, brief literature review about some of the main phenomena that influence the deformation mechanisms of RC frames, and their numerical modelling is discussed in Section §3.1. A similar description of the literature for the simplified modelling of ductile infills is also reported.

Section §3.2 describes the numerical framework built to manage the input files, run nonlinear static and dynamic analyses on columns and regular bidimensional frames, and post-process their results.

Modelling choices of RC frames at both local and global levels in the static nonlinear field are discussed in Section §3.3, and they are tested by comparison with experimental tests on RC columns and portal frames available in the literature. Mass discretization and damping modelling in the dynamic field are also investigated by testing different choices on an auxiliary frame derived from the literature. The modelling choices for the nonlinear cyclic response of ductile infills are discussed, with some variations to the calibrations proposed in the literature. A simplified approach to account for this type of infill in linear dynamic analyses is also proposed.

The frames that will be used in the analyses are described in Section §3.4. Gravity loads and seismic action, design approach, and hypothesis are fully discussed.

Finally, the results and comparisons of the different types of analysis for the different configurations are discussed in Section §3.4.4. In particular, the ability of RSA to

predict seismic demand is discussed for different infill thicknesses and design ductility levels.

3.1 Literature review on ductile infill-RC frame modelling

3.1.1 *RC frame modelling*

According to Setzler and Sezen (2008) [43], the lateral displacement of a column is the result of the sum of three contributions: flexural deformation, rebar slip at the member ends, and shear deformation (Figure 3.1). The flexural contribution is given by the integration of the elastic and inelastic curvatures along the member.
In the following, the flexural response is modelled through a fibre approach based on distributed plasticity. Different models have been proposed in the literature. A comparison between some of the most popular modelling approaches is reported in the following. Because the flexural response was found to be strongly influenced by the rebar slip beyond the element end cross-section (in the foundation or in the joints between elements), a discussion of some available approaches for the modelling of the strain penetration is included in the discussion. The confining effect of the transverse reinforcing stirrups is accounted for in the modelling. The shear contribution of slender elements can be sufficiently small to be neglected, and it is not considered here.

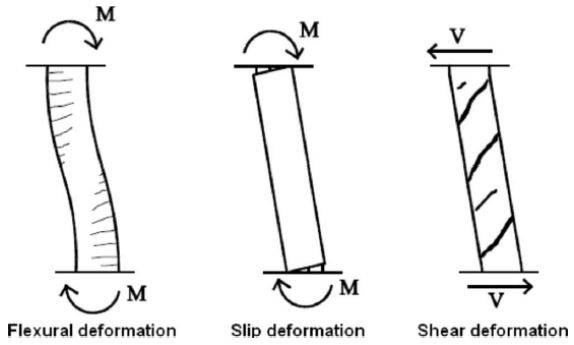

Figure 3.1: Components of lateral deformation in a reinforced concrete column [43].

3.1.1.1 Flexural contribution

A clear description of the nonlinear response of flexural-dominated RC members can be found in Paulay and Priestley (1992) [44] and Priestley et al. (2008) [45], and it is graphically represented in Figure 3.2.

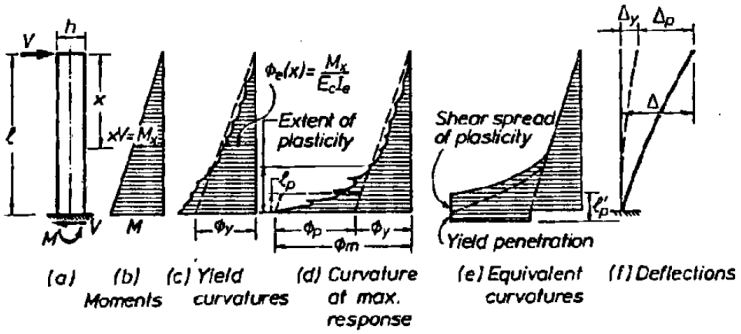

Figure 3.2: Moment, curvature, and deflection profiles for a RC column [44].

The element cross-section rotation and the resulting deflection can be obtained by integrating the curvature developing along the element length. This approach cannot completely reproduce the experimental force-displacement behaviour if some phenomena, such as the tension shift or the rebar slip and strain penetration, are neglected, as discussed in Priestley et al. (2008) [45].

The numerical modelling of the flexural behaviour in frame structures typically adopts beam-column elements, accounting for a distributed or concentrated plasticity approach. The representation of the sections by a fibre model allows to directly account for the interaction of bending moment and axial load by performing the sectional analysis at each time step with the updated value of the axial load applied to the element section. So, the non-linear behaviour of the materials at the sectional level is accounted for. Spacone et al. (1996) [46] proposed a force-based non-linear element; the sectional forces are interpolated with respect to the basic forces, and the equilibrium of the bending moment and axial forces is ensured along the elements. Then, an iterative procedure evaluates the sectional curvature. Several solutions for the curvature integration are proposed in the literature, with different weights and locations for the integration sections to better capture the real structure deflection. In the force-based approach [46], the classic solution obtains the deflection by integrating the curvature over the geometric tributary length of each integration section. So, an accurate discretization of the structure and choice of the position and number of the integration sections need to be adopted based on the expected distribution of plasticity in the structure. As an alternative, the beam with hinges approach proposed by Scott and Fenves (2006) [47], uses modified locations of

integration sections and integration lengths that are calibrated by applying the concept of the plastic hinge. In this case, the curvature integration can also account for phenomena that physically occur outside the element (e.g., strain penetration) by a fictitious extension of the plastic hinge length.
Both approaches are suitable to obtain an accurate representation of a frame element response. In the following paragraph, a comparison of selected different modelling solutions for the prediction of the cyclic pseudo-static response of some test specimens is reported.

3.1.1.2 Strain penetration contribution

When a plastic hinge occurs at the element end cross section, the strains of the longitudinal reinforcement reach their peak values and penetrate along the anchored bars into the connecting elements (e.g. beam column joints, foundation elements). The result is the relative slip of the anchorage with respect to the concrete block and a consequent local rotation of the element, as schematically represented in Figure 3.1. This local deformation contributes to increasing the lateral displacement capacity of the structure, and the residual displacement under cyclic loads enhances energy dissipation, as discussed in Sritharan et al. (2000) [48].
The study conducted by Sritharan et al. (2000) [48] on bridge joint systems shows that neglecting the strain-penetration contribution leads to satisfactory global force-displacement behaviour. The overestimated resultant forces due to the concentration of strains in the longitudinal reinforcement and in the concrete at the interface are compensated by a reduced lever arm, leading to an acceptable column moment resistance. The strain penetration contribution to the overall displacement is compensated by higher strains in the column rebars. On the other hand, at the local level, an unrealistic overestimation of the sectional curvatures and the damage at the member ends may be obtained. An accurate modelling of the interface crack and the anchorage slip is required to represent the hysteretic response of the structure.
For a cantilever column, an approximated way to account for the strain penetration into the foundation consists in defining a fictitious plastic hinge length, which is empirically calibrated to obtain the experimentally measured top displacement. This approach allows for a simplified consideration of all the deformation mechanisms through the flexural one. The Eurocode 8 part-3 [49] suggests the expression in Eq. (3.1-1) for the equivalent plastic hinge length, L_{pl}.

$$L_{pl} = 0.1 \cdot L_v + 0.17 \cdot \mathrm{h} + 0.24 \cdot \frac{d_{bl} f_y}{\sqrt{f_c}} \qquad (3.1\text{-}1)$$

Where L_v is the shear length, h the cross-section height, and d_{bl} the mean rebar diameter.

Alternatively, Paulay and Priestley (1992) [44] proposed to evaluate the strain penetration effect by extending the column-element into the foundation by a length equal to the length of the yield penetration, L_{pj}, defined as in Eq. (3.1-2). The effective stiffness of the moment-curvature bilinear curve can be considered for the link element [50].

$$L_{pj} = 0.022 \cdot d_{bl} f_y \tag{3.1-2}$$

Thus, the elastic contribution to the top displacement is evaluated on an elongated element. The plastic contribution is evaluated considering a plastic length evaluated according to Eq. (3.1-3) [44], which must be greater than two times the yield penetration length if one wants to account for its effect also on the element side of the interface crack [50].

$$L_{pj} = 0.08 \cdot l + 0.022 \cdot d_{bl} f_y \geq 0.044 \cdot d_{bl} f_y \tag{3.1-3}$$

These approaches are empirically based. In the literature, many authors have proposed different approaches to explicitly account for the strain penetration contribution.

Focusing on fibre-based modelling approaches, Zhao and Sritharan (2007) [51] used a zero-length section element [52] to account for the end-rotation due to the bond slip. The use of a fibre section has the advantage of modifying the location of the neutral axis as a function of the axial load and the load direction. Two overlapped nodes are connected by a fibre section defined by a zero length, which governs the relative rotation and the axial displacement, while the transversal degree of freedom is fixed unless the shear behaviour is considered (the schematic representation of the model is represented in Figure 3.3). Working at the element level instead of the sectional one, the fibre axial deformations are formulated in terms of displacement.

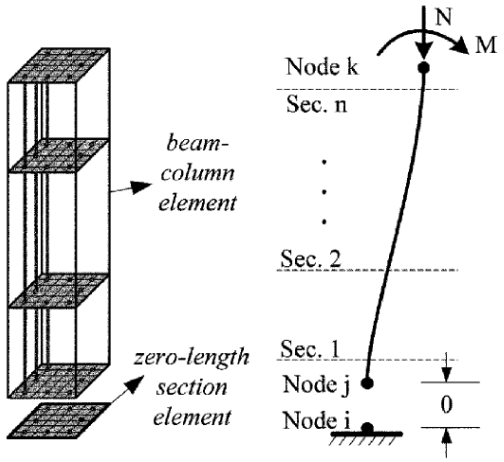

Figure 3.3: Fibre-based modelling of strain penetration effects [51].

In this model, the steel fibres of the section represent the stress-slip behaviour of the anchorage at the interface. If the column-to-foundation joint is considered, the generic model is based on the measured slip of a rebar anchored in a concrete block when subjected to an axial load at its head. In the case of an interior beam-to-column joint, the condition is different because the bar crossing the joint is simultaneously subjected to push-in and pull-out at the opposite joint sides, and the cyclic loading condition leads to the progressive degradation of the bond stresses and to the progressive slip of the rebar. This condition was not considered in the referred paper. Zhao and Sritharan (2007) [51] proposed, for fully anchored rebars, the bar-slip relationship graphically represented in Figure 3.4; it is characterised by a linear branch until the rebar yielding, followed by a non-linear curve. The main parameters required to build the curve are the slip of the loaded end at the rebar yielding (s_y) and at the ultimate stress (s_u), and the stiffness reduction factor (b).

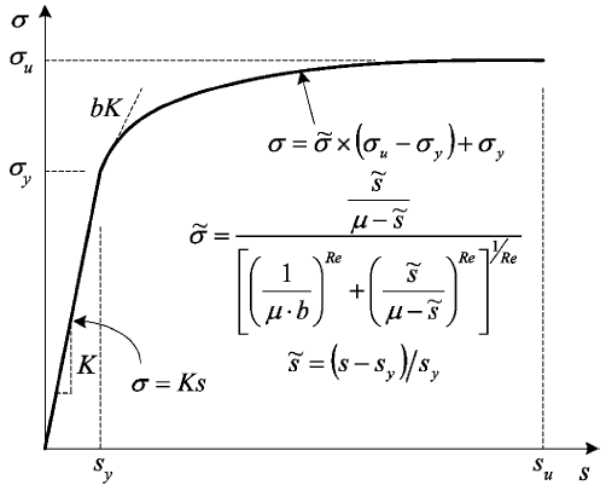

Figure 3.4: Envelope curve for bar stress versus loaded-end slip relationship [51].

The simulation of two concrete cantilever columns and a bridge tee-joint system highlighted that if strain penetration is ignored, the force resistance at a given lateral displacement is overestimated and the hysteretic loops are enlarged. At the local level, the steel strain and the section curvature, which indicate the extent of structural damage, were grossly overestimated.

Ghannoum and Moehle (2012) [53] noticed that the previous described model produces a discontinuity in the neutral axis depth between the fibre section that describes the bar-slip effect and the first fibre section of the connected frame-member (column or beam). To avoid this problem, the two sections must be geometrically the same, and the materials of the zero-length section must be defined by uniformly scaling the constitutive laws used to define the materials of the element fibre section. In the representations in Figure 3.5, the fibre section of the element and the slip element are subjected to the same loading condition. The fibre section curvature K_{fe} is given by the ratio between the steel strain ε_s and the distance c' of the longitudinal bar to the neutral axis (Eq. (3.1-4)), while the bar-slip section rotation O_{bs} is given by the ratio between the rebar slip S_s and the same c' (Eq. (3.1-5)). The imposition of the same c' leads to a relationship between the section curvature and the section rotation (Eq. (3.1-6)). Consequently, the strains of concrete and steel at the bar-slip element must be related to the ones at the frame-element side by the ratio r between the sectional rotation and curvature (Eq. (3.1-7)).

$$K_{fe} = \frac{\varepsilon_s}{c'} \tag{3.1-4}$$

$$O_{bs} = \frac{S_s}{c'} \tag{3.1-5}$$

$$O_{bs} = K_{fe}\frac{S_s}{\varepsilon_s} \tag{3.1-6}$$

$$r = \frac{O_{bs}}{K_{fe}} = \frac{S_s}{\varepsilon_s} \tag{3.1-7}$$

The rebar slip, S_s, at the interface section is evaluated by the integration of the axial strains developed by the anchorage when subjected to the axial load. Assuming a bi-uniform bond-stress distribution for the elastic and post-elastic parts of the rebar, the required anchor length, the stress profile, and then the strain profile are calculated by equilibrium considerations on the anchorage. A parabolic curve is obtained in both elastic and plastic regions. It is, then, bi-linearized, and only the slip S_y at the rebar yielding and the hardening ratio b are required for its definition. In the following, the effective strain penetration depth l_{sp} and the slip at the rebar yielding are calculated according to Eqs. (3.1-8) and (3.1-9) following the steps previously described.

$$l_{sp} = \frac{f_y \cdot d_b}{4 \cdot u_e} \tag{3.1-8}$$

$$S_y = \frac{\varepsilon_y \cdot l_{sp}}{2} = \frac{\varepsilon_y \cdot f_y \cdot d_b}{8 \cdot u_e} \tag{3.1-9}$$

Where:

- f_y is the rebar yielding stress.
- ε_y is the rebar yielding strain.
- d_b is the rebar diameter.
- u_e is the elastic bond stress.

b is taken to be equal to 0.01 according to the hardening ratio of the longitudinal steel rebar.

Ghannoum and Moehle (2012) [53] proposed to use an elastic bond stress u_e equal to $1.0\sqrt{f_c}$ $[MPa]$ according to the indications of Lehman and Moehle (1998) [54]; while NIST GCR 17-917-46v3 guidelines [55] suggested to assume a value equal to $0.8\sqrt{f_c}$, for all beams and columns interfaces.

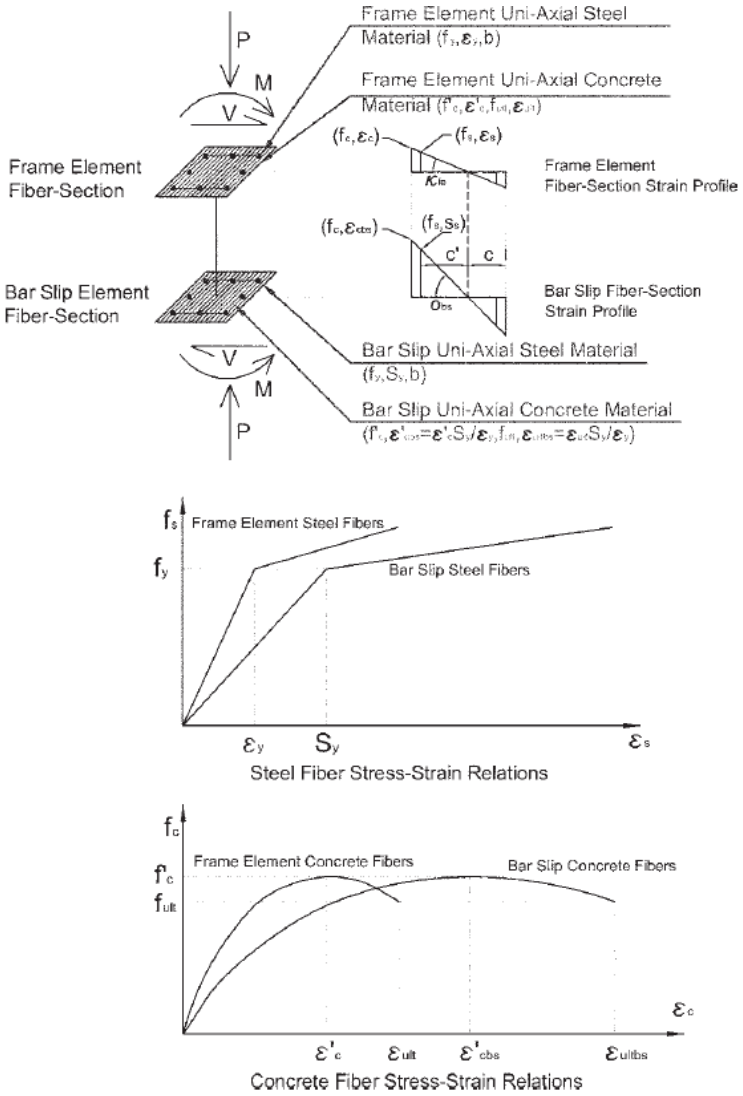

Figure 3.5: Bar-slip fibre-section equilibrium, strain profiles, and materials [53].

3.1.1.3 Confinement effects

Hoops or crossties can enhance the ductility and strength of a compressed concrete material. By increasing the sectional curvature of a reinforced concrete section, when the unconfined concrete cover reaches its peak strain, it is spalled. If enough transversal reinforcement is provided, the confined concrete core may reach higher loads and strains, allowing a large curvature capacity. The stress-strain model of the confined concrete can be evaluated according to Mander (1983) [56] and Mander et al. (1988) [57].

The confined concrete behaves similarly to the unconfined one for low axial stresses, but once the compressive strength is attained, internal cracking appears, the concrete spreads out, and the axial strain of the transversal reinforcement rises. Thus, the transverse reinforcement acts as passive confinement.

As far as rectangular hoops are concerned, effective confinement action is provided at the intersection of the restrained longitudinal reinforcements and the transverse ones. The effectively confined area A_e is delimited by natural arches in the transversal plane, between two constrained longitudinal reinforcements, and in the longitudinal direction, between two consecutive transversal reinforcements, which stand at the intersection of retained longitudinal and transversal reinforcements. A representation of the arching mechanism is reported in Figure 3.6.

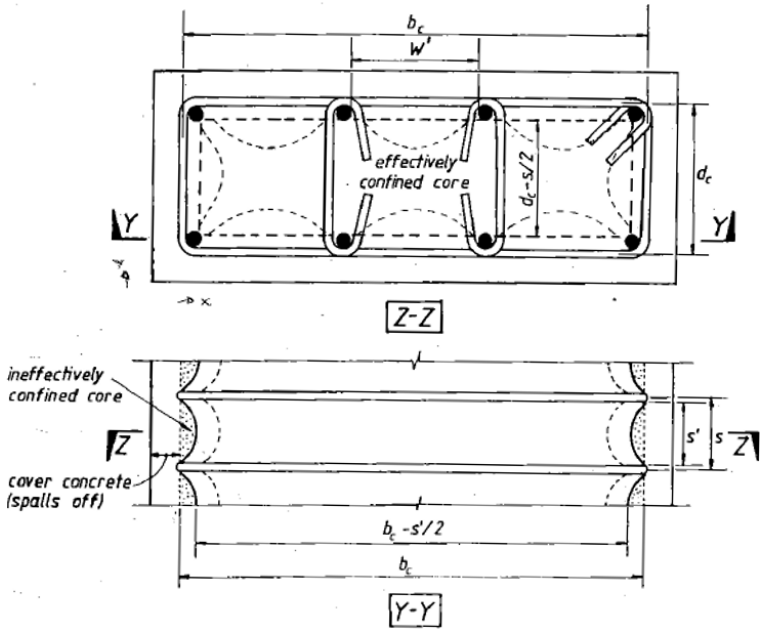

Figure 3.6: Assumed arching mechanism between hoops for rectangular columns [56].

The net concrete core area A_{cc} is the area included in the stirrup centreline $A_c = b_c \cdot d_c$ reduced by the longitudinal reinforcement area (Eq. (3.1-10)). The effectively confined core A_e (Eq. (3.1-11)) at the midspan between two consecutive stirrups is evaluated by applying the reduction factors α_n and α_s for the arching effect in the cross-section plane (Eq. (3.1-12)) and the longitudinal direction (Eq. (3.1-13)), respectively.

$$A_{cc} = b_c \cdot d_c \cdot (1 - \rho_{cc}) \tag{3.1-10}$$

$$A_e = A_c \cdot \alpha_n \cdot \alpha_s \tag{3.1-11}$$

$$\alpha_n = 1 - \sum_{i=1}^{n} \frac{(w'_i)^2}{6 \cdot b_c \cdot d_c} \tag{3.1-12}$$

$$\alpha_s = \left(1 - \frac{s'}{2b_c}\right) \cdot \left(1 - \frac{s'}{2d_c}\right) \tag{3.1-13}$$

Where ρ_{cc} is the longitudinal reinforcement ratio with respect to the confined area A_c.

The effect of the transversal reinforcement is the application to the confined core A_c of a confining pressure f_l (Eq. (3.1-14) and (3.1-15)), which increases the compressive axial strength with respect to the unconfined one f'_{c0} by a factor k_1. The average confinement pressure (Eqs. (3.1-16) and (3.1-17)) given by the two directions is considered.

$$f_{lx} = \frac{A_{sx} \cdot f_{ys}}{s' \cdot d_c} = \rho_{sx} \cdot f_{ys} \tag{3.1-14}$$

$$f_{ly} = \frac{A_{sy} \cdot f_{ys}}{s' \cdot b_c} = \rho_{sy} \cdot f_{ys} \tag{3.1-15}$$

$$f_l = \frac{1}{2}(f_{lx} + f_{ly}) = \rho_s \cdot f_{ys} \tag{3.1-16}$$

$$\rho_s = \frac{1}{2}(\rho_{sx} + \rho_{sy}) \tag{3.1-17}$$

Where f_{ys} is the yielding stress of the stirrups.
The global axial load capacity P_{cc} is evaluated on the net concrete core, A_{cc}. Consequently, the concrete core A_{cc} has unconfined concrete strength f'_{c0}, while the effectively confined core has an additional strength accounted for in equation (3.1-18).

$$P_{cc} = f'_{c0} \cdot A_{cc} + (k_1 \cdot f_l) \cdot A_e \tag{3.1-18}$$

The increased compressive strength f'_{cc} is evaluated by averaging the axial load capacity over the concrete core area.

$$f'_{cc} = \frac{P_{cc}}{A_{cc}} = f'_{c0} \cdot + (k_1 \cdot f_l) \cdot \frac{A_e}{A_{cc}} \tag{3.1-19}$$

By defining the confinement effectiveness coefficient k_e, the effective lateral confining pressure f'_l is derived.

$$k_e = \frac{A_e}{A_{cc}} = \frac{A_e}{A_c \cdot (1 - \rho_{cc})} \tag{3.1-20}$$

$$f'_l = k_e \cdot f_l = k_e \cdot \rho_s \cdot f_{ys} \tag{3.1-21}$$

Referring to Figure 3.7, the strain ε_{cc} and the stress f'_{cc} at peak strength are evaluated as follows.

$$f'_{cc} = f'_{c0} \cdot \left(-1.254 + 2.254 \cdot \sqrt{1 + \frac{7.94 \cdot f'_l}{f'_{c0}}} - 2 \cdot \frac{f'_l}{f'_{c0}} \right) \tag{3.1-22}$$

$$\varepsilon_{cc} = \varepsilon_{c0} \cdot \left[1 + 5 \cdot \left(\frac{f'_{cc}}{f'_{c0}} - 1 \right) \right] \tag{3.1-23}$$

The ultimate compressive strain is evaluated through the relationship proposed by Paulay and Priestley (1992) [44].

$$\varepsilon_{ccu} = \varepsilon_{cu} + 1.4\frac{\rho_s \varepsilon_{sm} f_{yk}}{f'_{cc}} \qquad (3.1\text{-}24)$$

Where ε_{sm} is the stirrups steel strain at maximum tensile stress.

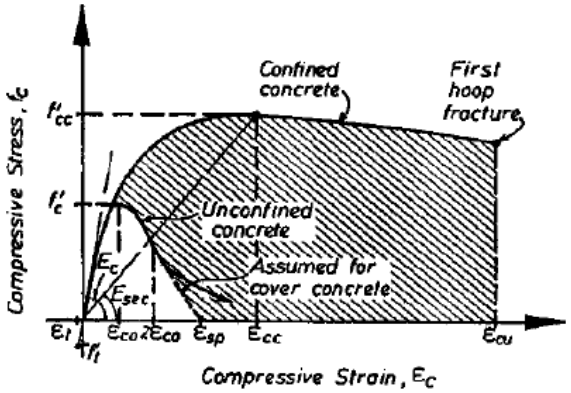

Figure 3.7: Stress-strain relationship of confined and unconfined concrete [57]

Italian [58] and European [59] technical codes define as in Eqs. (3.1-25) and (3.1-26) the effective lateral confining pressure and the ultimate compressive strain of the confined concrete.

$$f_l = \sqrt{f_{lx} \cdot f_{ly}} \qquad (3.1\text{-}25)$$

$$\varepsilon_{ccu} = \varepsilon_{cu} + 0.2\frac{f'_l}{f'_{c0}} \qquad (3.1\text{-}26)$$

3.1.2 *Simplified modelling of ductile infills*

The analytical model reported in §2.1.2 can be used to represent ductile infills by means of simplified strut macro-models. In the studies reported in Bolis et al. (2017) [60] and Preti et al. (2019) [33, p. 209], a compression-only truss element per infill diagonal is adopted to model the infill lateral behaviour.
Three parallel non-linear springs, whose monotonic and cyclic behaviour is represented in Figure 3.8, simulate both the friction and the strut contributions:

- Spring 1 represents the friction contribution due to the self-weight by means of a rigid-perfect plastic curve (first part of Eq. (2.1-19)).
- Spring2 represents, by means of a slip bilinear hysteretic curve, the hardening effect of the frictional contribution (second part of Eq. (2.1-19)); initial and unloading rigid branches characterise the behaviour.
- Spring 3 represents the strut contribution (Eq. (2.1-17)) by means of a slip-bilinear curve.

The cyclic characteristics are derived from phenomenological considerations; no direct experimental evidence is available for their individual calibration.
Concentric or eccentric struts are proposed to represent the infill. The second configuration allows to represent not only the lateral strength versus interstorey displacement global behaviour but also the shear action on the columns at a specific drift level by calibrating the eccentricity. The static schemes of the two solutions are represented in Figure 3.9.
The translation of the global lateral strength versus horizontal displacement curve, $\Delta F_s - \Delta$, to the axial one of the inclined struts, $N_A - \Delta d_A$, is obtained according to equations (3.1-27) and (3.1-28) (referring to Figure 3.9).

$$N_A = \Delta F_s \cdot \sqrt{1 + \left(\frac{H}{L}\right)^2} \qquad (3.1\text{-}27)$$

$$\Delta d_A = \Delta \cdot \cos\vartheta \qquad (3.1\text{-}28)$$

The proposals were tested by the simulation of the experimental test described in Preti et al. (2015) [15]. Both solutions provided an efficient representation of the experimental response.

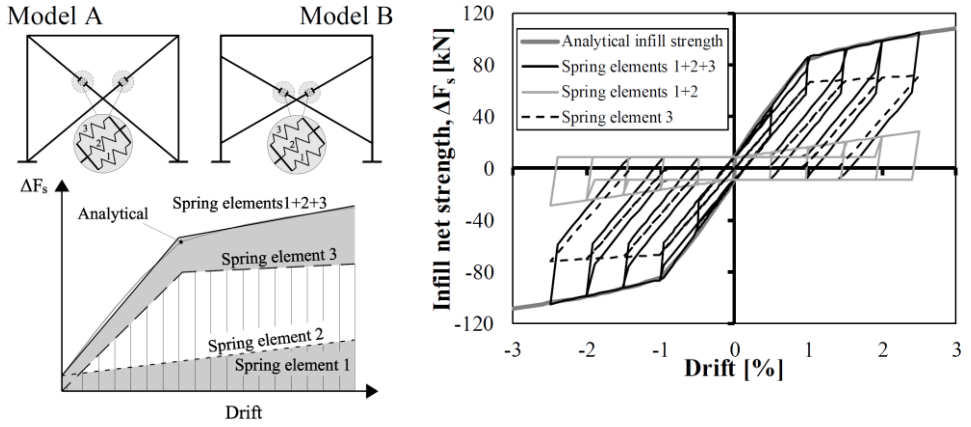

a) *b)*

Figure 3.8: Monotonic response and spring elements layout a) and cyclic representation of the nonlinear responses of three springs representing the infill b), depicted from Bolis et al. (2017) [60].

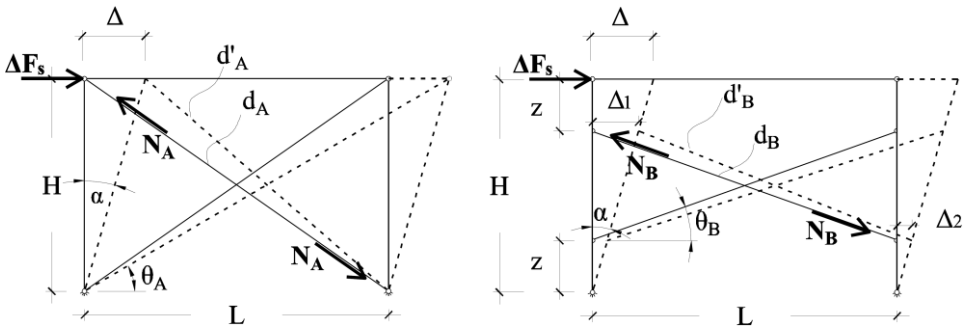

a) *b)*

Figure 3.9: Representation of the concentric a) and eccentric b) models of the infill, depicted from Bolis et al. (2017) [60].

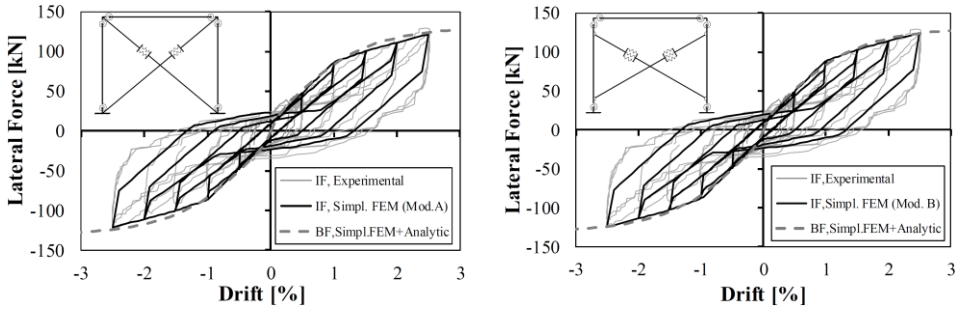

a) *b)*

Figure 3.10: Application of the concentric a) and eccentric b) numerical models to the experimental test described in Preti et al. (2015) [15], depicted from Bolis et al. (2017) [60].

The proposed modelling approach was applied to the simulation of multistorey and multi-bay RC infilled frames. The macro model was shown to capture the global response of the frame. As for the local response of the columns, the shear action obtained by the superposition of the analytical estimate of the shear contributions due to the infill thrust to the shear action calculated on the bare frame offered a good agreement with the results obtained with the detailed modelling of the infilled frame, both on the windward and leeward columns.

3.2 *Case study numerical framework*

The nonlinear analyses are executed using the "OpenSees" Finite Element Analysis software [52]. An automated process makes use of the "Matlab" [61] software to write the input file necessary to run the analyses, to run OpenSees, and, finally, to post-process the results. All the calculations required to evaluate geometry, material properties, and all the other properties are directly and automatically done by means of specific Matlab scripts. The procedure is briefly represented in the tree chart in Figure 3.11. The same scheme is applied to automatically generate RC columns or bidimensional regular RC frames.

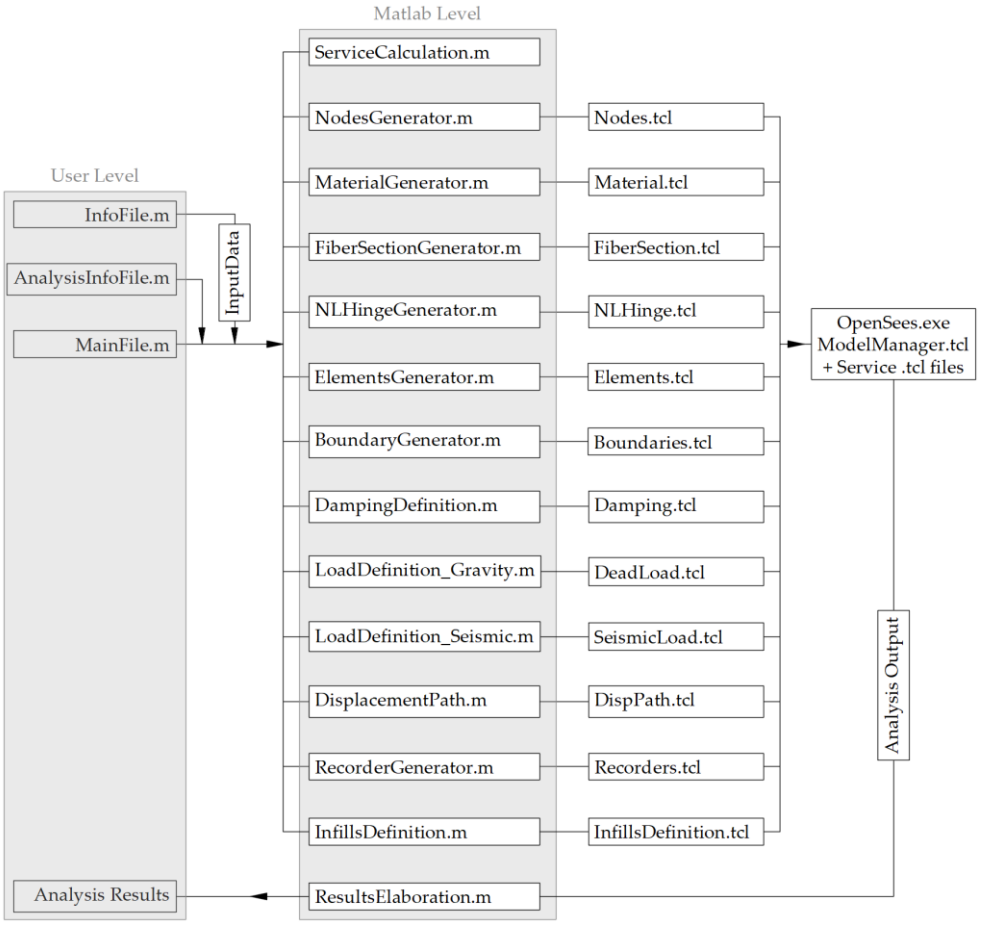

Figure 3.11: Tree chart of the numerical framework.

Specifically, the main steps required by the user can be summarised as follows:

- Define the geometrical and mechanical properties of the specimen and the applied loads by running the "InfoFile.m" script.
- Define in the "AnalysisInfoFile.m" script the analysis information: modelling approach, analysis typology, damping model and characteristics, and all the other information required to define the specific analysis.
- Run the "MainFile.m" script, which automatically does the following steps:
    - Run the "AnalysisInfoFile.m" script to load and store the analysis information.
    - Run the "ServiceCalculation.m" script to do all the auxiliary service calculations, like, for example, the evaluation of the confined properties of the concrete material.
    - Run the "NodesGenerator.m" script: given the input geometry, it directly writes the OpenSess instructions to define the nodes and the service nodes of the model in the "Nodes.tcl" file.
    - Run the "MaterialGenerator.m" script: given the input geometry, the mechanical properties, and properties evaluated in the "ServiceCalculation.m" script, it directly writes the OpenSess instructions in the "Material.tcl" file to define all the materials that will be used in the model.
    - Run the "FiberSectionGenerator.m" script: given the input geometry and the materials previously evaluated, it directly writes the OpenSess instructions in the "Sections.tcl" file to define all the fibre sections of the elements and of the strain-penetration elements.
    - Run the "NLHingeGenerator.m" script: it directly writes the OpenSess instructions in the "NLHinge.tcl" file to define the zero-length section elements that simulate the strain-penetration contribution.
    - Run the "ElementsGenerator.m" script; it directly writes the OpenSess instructions in the "Elements.tcl" file to define the elements of the model.
    - Run the "BoundaryGenerator.m" script; it directly writes the OpenSess instructions in the "Boundaries.tcl" file to define the node constraints.
    - Run the "DampingDefinition.m" script; it writes in the "Damping.tcl" file the information required to define damping, such as the selected damping model, the damping

level, and the elements to attribute damping, and defines the command for OpenSees.

- Run the "LoadDefinition_Gravity.m" script; it evaluates the elements and nodes gravity loads, and it writes the OpenSess instructions in the "DeadLoad.tcl" file.
- Run the "LoadDefinition_Seismic.m" script; it writes the "SeismicLoad.tcl" where the lateral load distribution of pushover analyses or the ground motion acceleration of the NLTH analyses are defined.
- Run the "DisplacementPath.m" script; it writes the displacement path of PO analyses in the "DispPath.tcl" file.
- Run the "RecorderGenerator.m" script; it directly writes the OpenSess instructions in the "Recorders.tcl" file to define all the output that the analysis has to return.
- Run the "InfillsDefinition.m" script; it evaluates the properties of each infill and writes "InfillsDefinition.tcl", where materials, elements, and recorders of the infills are defined.
- Automatically run the "OpenSees.exe" software by giving in input a "modelManager.tcl" file, which assembles all the previously defined ".tcl" files. To this end, other ".tcl" files are defined, but here they are not reported for conciseness.
- Run the "ResultsElaboration.m" script, which is a post-processor that reads all the output files and creates all the required graphs.

The potentiality of the described procedure is that it easily allows for the direct analysis of columns or bidimensional regular frames without the use of manual calculations. Based on geometry and material properties defined in the input file, all the calculations are automatically managed until the complete definition of the analyses, the successive runs, and the elaboration of the results. Another advantage is that parametric analyses or multiple analyses on the same structure, such as nonlinear time history analyses considering sets of input ground motions, can be directly handled.

3.3 *Case study modelling choices*

3.3.1 *Modelling scheme*

The frame elements are modelled using force-based fibre-section beam-column elements [46]. Each column is subdivided into three elements: two end portions defined by a length equal to the cross-section height and a central part, so different confined properties can be adopted depending on the specific stirrup spacing. As in Ghannoum and Moehle (2012) [53], the Lobatto integration method with two integration sections is used for the exterior elements to account for a plastic hinge length equal to half of the column cross-section height. The Lobatto integration method locates integration sections at the end of the element, where the bending moment reaches its peak values (in the absence of applied loads along the element). Vice versa, if an integration method that locates integration sections only along the element is used, fictitious higher values of the bending action with respect to the yielding one may occur at the element ends. Five integration sections are considered for the interior element.

Strain-penetration deformability is explicitly modelled where plastic hinges are expected to occur, at the extremes of the beams and at the base of the columns. This modelling choice neglects the pre-yield deformability in the other sections of the columns to avoid an excessive estimation of the structure deformability.

At the column-to-foundation interfaces, two overlapped nodes are connected by a zero-length section, which explicitly represents the strain penetration contribution. Instead, this contribution is not considered at the column-to-joint interfaces.

The same modelling scheme is adopted for beams, where the strain penetration is explicitly modelled at each end of the elements. Since the central part of the beam (outside the confined lengths) is expected to not undergo inelastic deformations, it is modelled by means of a linear elastic element. The moment of inertia, here, is reduced by a factor equal to 0.35, according to Paulay and Priestley (1992) [44], to account for the cracking of the element.

As described in Ghannoum and Moehle (2012) [53], the bar-slip phenomenon accounts for the greatest contribution of the joint deformability. Anyway, panel joint deformability is implicitly modelled by extending beams and columns into the joints with an elastic link having the reduced elastic stiffness of the cracked beam and no stiffness reduction on the column side.

The schematic representation of the model is reported in Figure 3.12.

"P-Delta" geometric transformations are adopted for beams and columns.

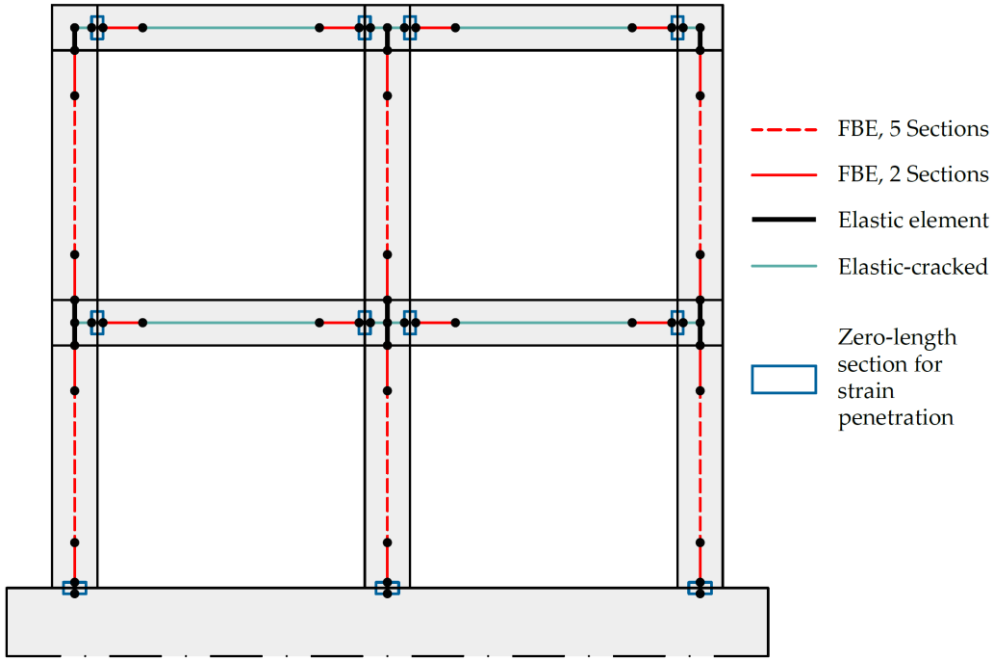

Figure 3.12: Modelling scheme represented for a two-bay and two-storey frame ("FBE" = Force based element, "5 Sections" = 5 integration sections assumed for the element, "2 Sections" = 2 integration sections assumed for the element, "Elastic-cracked" = Elastic element characterised by the stiffness of the cracked section).

3.3.2 *Materials model definition*

The concrete behaviour adopted in the numerical simulation is "Concrete04" [52] which adopts the Mander et al. (1988) [57] envelope curve. The mean concrete cylindrical strength is assumed as the peak stress, and the values of 0.002 and 0.004 are considered for the peak and the ultimate strains, respectively. Since new structures are the target, concrete mean compressive strength is evaluated from the characteristic one using the relation proposed at Section §11.2.10.1 of the Italian Code [58], by adding $8MPa$.
According to Priestley et al. (2008) [45], concrete elastic stiffness is evaluated as $E_c = 5000\sqrt{f_c}$. The tensile strength is calculated as proposed by Paulay and Priestley (1992) [44] for concrete in flexural tension, $f_{ct} = 0.75\sqrt{f_c}$. The same elastic stiffness is adopted for both tension and compression loads.
The properties of the confined concrete of the columns are evaluated according to Section §3.1.1.3, by assuming an only axially loaded section. For the beams, the flexural loading condition is accounted for by following the indications by Fardis (2009) [62] (reference to Figure 3.13):

- The neutral axis depth in the loading direction is considered instead of the size of the confined core.
- The reduction for the arches in the cross-section plane is evaluated only for the external sides: the base and the two lateral compressed depths.
- The reduction between two consecutive stirrups is considered only for the compressed area, excluding the inner side along the neutral axis.

The modified equations (3.1-12) and (3.1-13) are reported in (3.3-1) and (3.3-2).
A conventional constant ratio between the neutral axis depth and the confined depth (b_{xo} in Figure 3.13) equal to 0.2 is considered for beams.

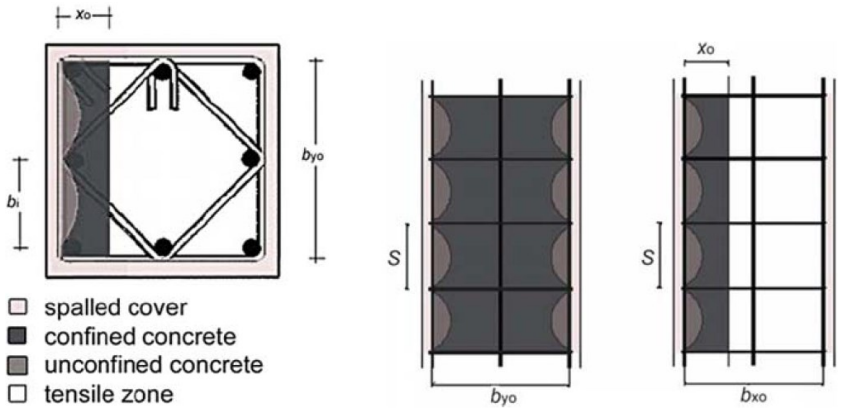

Figure 3.13: Calculation of confinement effectiveness in the compression zone of the confined core of a member in flexure, depicted from Fardis (2009) [62].

$$\alpha_n = 1 - \sum_{i=1}^{n} \frac{(w'_i)^2}{6 \cdot b_c \cdot x_0} \tag{3.3-1}$$

$$\alpha_s = \left(1 - \frac{s'}{2b_c}\right) \cdot \left(1 - \frac{s'}{4x_0}\right) \tag{3.3-2}$$

The steel behaviour is numerically represented by the "Steel02" material [52], which considers the Giuffrè-Menegotto-Pinto model. An elastic modulus equal to 205000 MPa and a strain hardening ratio equal to 0.02 are assumed. The steel mean yielding tensile stress is evaluated by multiplying the characteristic one by the factor 1.15, as proposed at §4.10.4 of Fardis (2009) [62]. The transition from elastic to plastic branches is regulated by the R0, cR1, and cR2 parameters; R0 is assumed to be equal to 18.5, according to Di Trapani et al. [34], while cR1, and cR2 are assumed to be equal to 0.925 and 0.15, respectively, according to Filippou et al. (1983) [63] and Menegotto and Pinto (1973) [64].
Examples of the hysteresis of the two numerical models adopted for the concrete and steel fibres are represented in Figure 3.14.

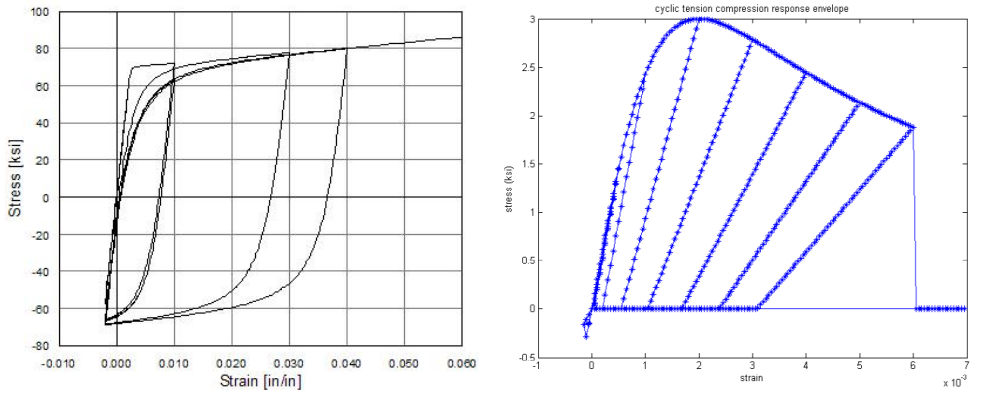

a) *b)*

Figure 3.14: Example of the hystereses of the Steel02 [52] a) and Concrete04 [52] b) models adopted for the steel and concrete fibres, respectively. Depicted from the OpenSees [52] website manual.

3.3.3 *Strain penetration modelling*

The strain-penetration contribution to the structure deformation is explicitly accounted for using zero-length sections located at the beam-to-column and column-to-foundation interfaces using the model proposed by Ghannoum and Moehle (2012) [53], as briefly reported in §3.1.1.2. In the original proposal, the stress-slip law of the rebar is bi-linearized, and the resulting curve is mainly defined by the slip at the rebar yielding. A constant scale factor, r_y, is evaluated at the rebar yielding as expressed by Eq. (3.1-9) and recalled in Eq. (3.3-3).

$$r_y = \frac{S_y}{\varepsilon_y} = \frac{l_{sb}}{2} \tag{3.3-3}$$

At the exterior beam-column joint and at the column-foundation joint, the anchorage is characterised by a straight length, l_b, followed by a bent. If the effective strain penetration depth, l_{sp} (Eq. (3.1-8)), is larger than the available straight length, the rebar bent is considered a rigid constraint, and the slip at the rebar yielding is evaluated as expressed in Figure 3.15 by Eqs. (3.3-4) and (3.3-5). This simplification leads to stiffer behaviour because the slip contribution of the bent is neglected.

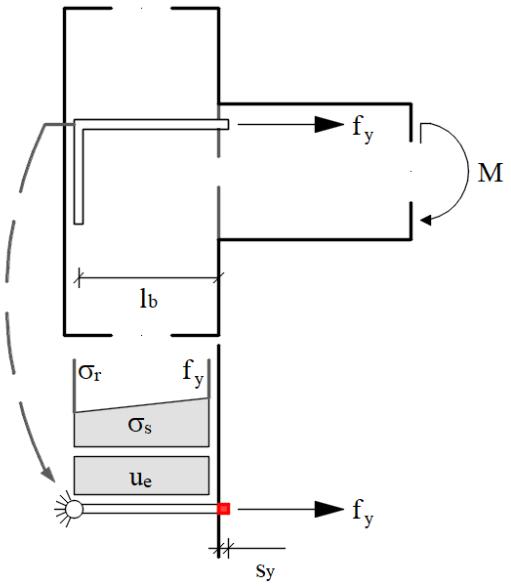

$$l_{sp} > l_b$$

$$S_y = \left(2f_y - \frac{4 \cdot u_e \cdot l_b}{d_b}\right) \cdot \frac{l_b}{2E_s} \tag{3.3-4}$$

$$r_y = \frac{S_y}{\varepsilon_y} = l_b - \frac{2 \cdot u_e \cdot {l_b}^2}{d_b \cdot f_y} \tag{3.3-5}$$

Figure 3.15: Evaluation of the slip when the required anchorage length is larger than the straight length.

At the interior joints, the rebar is simultaneously pulled and pushed at the two sides of the joint (see Figure 3.16), and the cyclic load condition gradually degrades the bond stresses between the rebar and the surrounding concrete. No limit to the anchorage length in the joint is considered because the pulled bar continues to the opposite side of the joint. Consequently, the original definition, Eq. (3.3-3), is adopted.

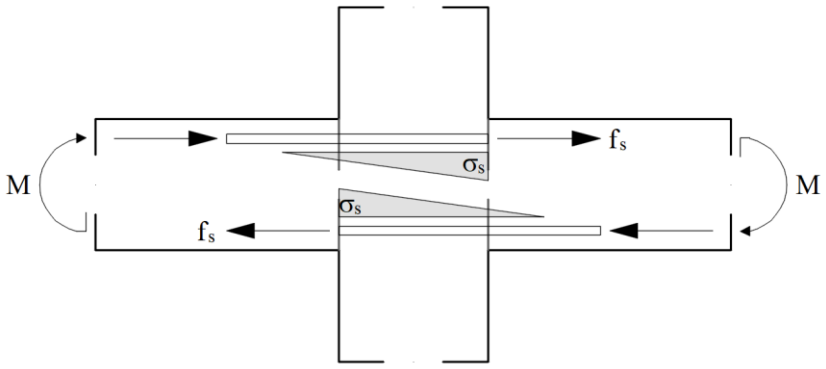

Figure 3.16: Scheme adopted for the evaluation of the strain penetration depth at the interior beam-column joint.

According to Ghannoum and Moehle (2012) [53], the elastic bond stress, u_e, is considered to be equal to $1.0\sqrt{f_c}$ for column-foundation interfaces, while it is assumed to be equal to $0.8\sqrt{f_c}$ for beam-column interfaces, as suggested by NIST.GCR.17-917-46v3 [55]. These values are in accordance with Section §7.4.3.2 of Model Code (2010) [65], which indicates a mean bond stress equal to $\sqrt{f_c}$.
The strain penetration depth is evaluated considering the mean yielding stress and diameter of the rebars that intercept the considered interface.
The material hystereses described in §3.3.2 for the frame elements (Steel02 [52] and Concrete04 [52] for steel and concrete fibres, respectively) are adopted and modified to derive the concrete and steel hystereses of the materials used for the zero-length section that represent the strain penetration effect. To guarantee compatibility between the neutral axis depth evaluated at the zero-length section and the one at the element side, the stress-strain hystereses are amplified in the strain domain by the r_y factor to convert it into the stress-displacement domain. The scale factor multiplies the strain parameters that define the hysteresis, while it divides the stiffness parameters. Also, the parameters that define the transition from elastic to plastic branches of the steel must be modified with respect to those assumed for the frame elements. For columns, comparing the steel hysteresis red at the first section at the element side with those red at the zero-length section side allows for calibrating the parameters that ensure their better fit. R0 is modified from a value equal to 18.5

to 19.5, while cR1 and cR2 remain unchanged. Steel numerical hysteresis is strain-unlimited (possible strain collapse is evaluated a posteriori). Concrete material hysteresis is characterised by a cut-off at the ultimate compressive strain. Since the zero-length section and the first fibre section of the element behave in series, which of them crushes is uncertain. To convey the damage on the element side, no displacement limit for the unconfined concrete material is considered at the zero-length level. After the crushing, compatibility of the neutral axis depth at the column-to-foundation interface is lost.

3.3.4 *Beam and column fibre section*

The reinforced concrete cross-section is numerically represented in the OpenSees [52] environment by a "fibre section", and the discretized scheme is graphically represented in Figure 3.17. Concrete sections and steel rebars are modelled by means of discretized fibres defined by an area and a stress-strain law.
The concrete section is discretized into fibres using the "patch rect" command [52], which defines a rectangular patch based on the input coordinates of the two opposite vertexes and the number of the discretization fibres in the two principal directions. The confined concrete core and the external unconfined concrete cover are divided by the centreline of the stirrups, according to the confinement model presented in §3.1.1.3. A 10 mm discretization in the loaded direction is assumed, while only 3 fibres are defined in the other one since a straight bending action is considered.
The steel rebars are defined using the "fiber" command [52]. Since a bidimensional model is considered, the total area of each different reinforcement material is lumped into the same fibre. The central steel layers are defined using the "layer straight" command [52], which defines a number of fibres uniformly distributed between two input coordinates.

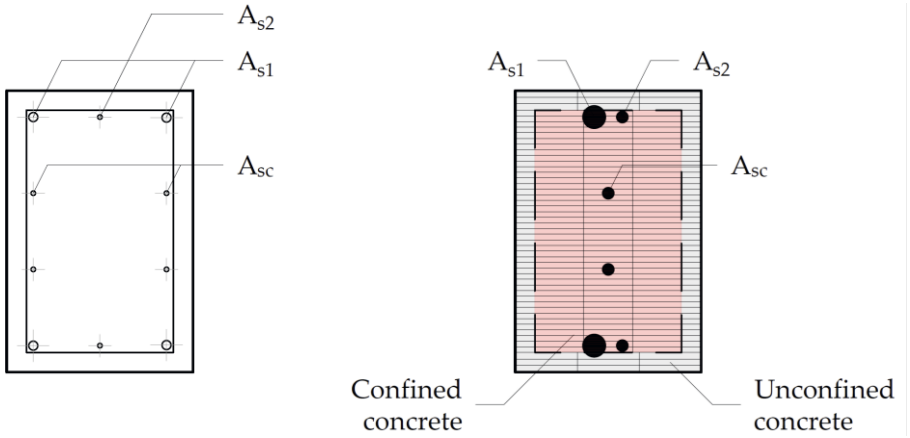

Figure 3.17: Typical reinforced concrete cross-section a) and its fibre section schematization b). A_{s1} and A_{s2} fibres are separately drawn for better clarity; in the numerical model, they are overlapped.

3.3.5 *Modelling approach validation*

In this sub-section, the results of the modelling scheme previously described are compared with some experimental responses of columns and portal frames taken from the literature. Furthermore, a comparison between the results obtained by adopting different modelling schemes for the simulation of cantilever columns is presented. As discussed at Section §3.3.3, at the column-to-foundation interface, the zero-length section that represents the strain penetration contribution and the first integration section (at the base) of the element that simulates the column are two in-series sections, and the compatibility of the deformations between them is an issue. The numerical simulations on the columns allow us to discuss their mutual behaviour.

3.3.5.1 Columns tests

The experimental tests considered are those reported in Di Ludovico et al. (2014) [66] and Meda et al. (2014) [67]. Square and rectangular columns were tested under monotonic and cyclic loading conditions. A vertical load was applied at the column top by means of a base-oriented hinged system, minimising the P-Δ effect, and a monotonic or cyclic horizontal displacement was imposed at the height of the ideal shear span of the frame column (about half of the storey height). The scheme of the numerical model of the test is reported in Figure 3.18.
The main geometrical and mechanical characteristics of the considered columns are reported in Table 3.1. Note that specimens were designed without seismic details for ductility. The comparison mainly focuses on the evaluation of the ability of the modelling scheme to capture the pre-peak response of the experimental test until it reaches a drift target of about 2.5%. To capture post-peak at larger drift, phenomena exhibited by non-detailed structure (stirrups opening, anticipated rebar buckling, concrete crushing at small deformations) require specific calibrations and are beyond the scope of the work.

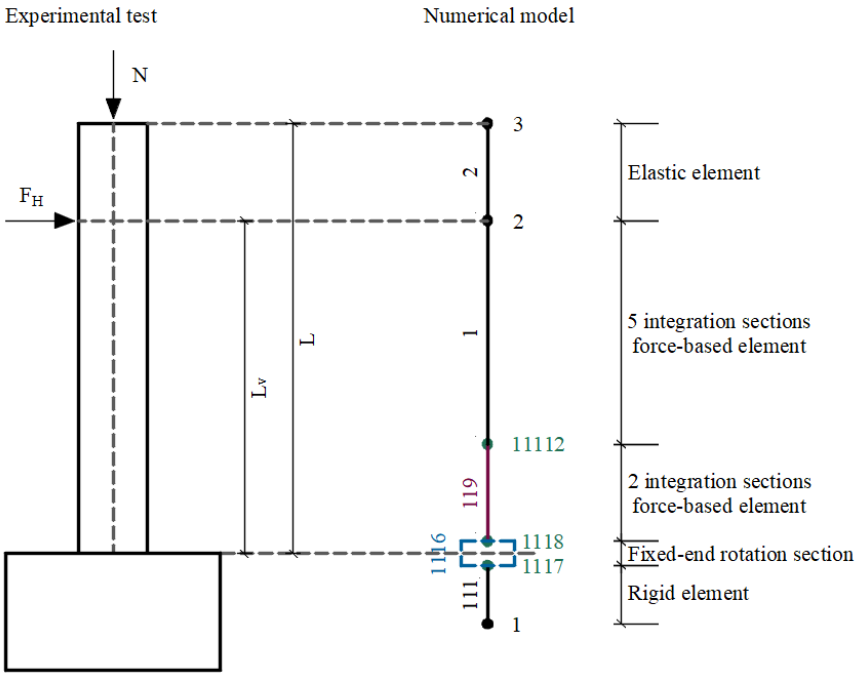

Figure 3.18: Experimental test and its numerical schematization.

Author	ID	B	H	L_v	L	f_c	f_y	A_s	A_{sc}
Di Ludovico et al. (2014) [66]	S300D-m	300	300	1500	1945	18.8	520	3ϕ12	2ϕ12
Di Ludovico et al. (2014) [66]	S300D-c	300	300	1500	1945	18.8	520	3ϕ12	2ϕ12
Di Ludovico et al. (2014) [66]	R300D-c	500	300	1500	1945	18.8	520	5ϕ12	2ϕ12
Di Ludovico et al. (2014) [66]	R500D-c	300	500	1500	1945	18.8	520	3ϕ12	6ϕ12
Meda et al. (2014) [67]	-	300	300	1500	1800	19.0	520	3ϕ16	-

Excitation = Type of applied horizontal load
B = Section base
H = Section height
L_v = Shear span
L = Column total height
f_c = Concrete cylindrical strength
f_y = Steel yielding stress of the longitudinal rebars
A_s = Rebars configuration in tension and compression sides
A_{sc} = Central rebars configuration
Stirrups consisted in 2ϕ8/150mm and 2ϕ8/300mm for Di Ludovico and Meda specimens, respectively.

Table 3.1: Main geometrical and mechanical properties of the considered columns reported in Di Ludovico et al. (2014) [66] and Meda et al. (2014) [67].

3.3.5.1.1 Numerical model description and comparison of different modelling schemes

The numerical model described in §3.3.1 is modified to account for the specific characteristics of the experimental tests, as schematically represented in Figure 3.18 and in Figure 3.19 as "Scheme 1". At the base, two service nodes are overlapped at the column-to-foundation interface; at the top of the column, two nodes are located at the points of application of the horizontal and vertical loads. Two fibre-based elements are used to represent the plastic length at the base and the central part of the element, while a classical elastic element connects the two upper nodes.
The results of the modelling scheme adopted are compared to those of alternative modelling strategies that were investigated in the decision-making process. Referring to Figure 3.18, the following will be considered:

- Scheme "0", extends the lumped plasticity approach described by Priestley et al. (2008) [45] to evaluate the top displacement of a cantilever column. This is a lumped plasticity model based on the fibre-section approach. A "beam with hinges" [52] element models the column member, while an elastic element, with cracked section stiffness, elongates the column into the foundation by a length equal to the strain penetration depth evaluated according to Eq. (3.1-2). The plasticity due to the spread of inelasticity into the foundation not modelled by the elastic link is accounted for by adding its contribution to the definition of the plastic length of the base column element. The use of the "HingeEndPoint" integration method allows to model the plastic hinge with a single integration section located at the base of the element; consequently, the dominating bending moment is directly the one at the column base.
- Scheme "1" is the modelling approach previously described and the one that will be used in the following of this work.
- Scheme "2", like scheme "1", is a lumped plasticity model based on the fibre section approach. The difference is that the strain penetration contribution into the foundation is accounted for in the definition of the plastic hinge length according to Eq. (3.1-1) of the code suggestions. The link element to the foundation is rigid, and a horizontal constraint is added at the element base. The "HingeEndPoint" quadrature rule is adopted.
- Scheme "3" is a mixed method. A "beam with hinges" element accounts for the element plasticity; the use of the "HingeRadauTwo" quadrature rule enables better integration of the curvature along the member. The fixed-end rotation due to the strain penetration contribution is explicitly accounted for, like in scheme "1".

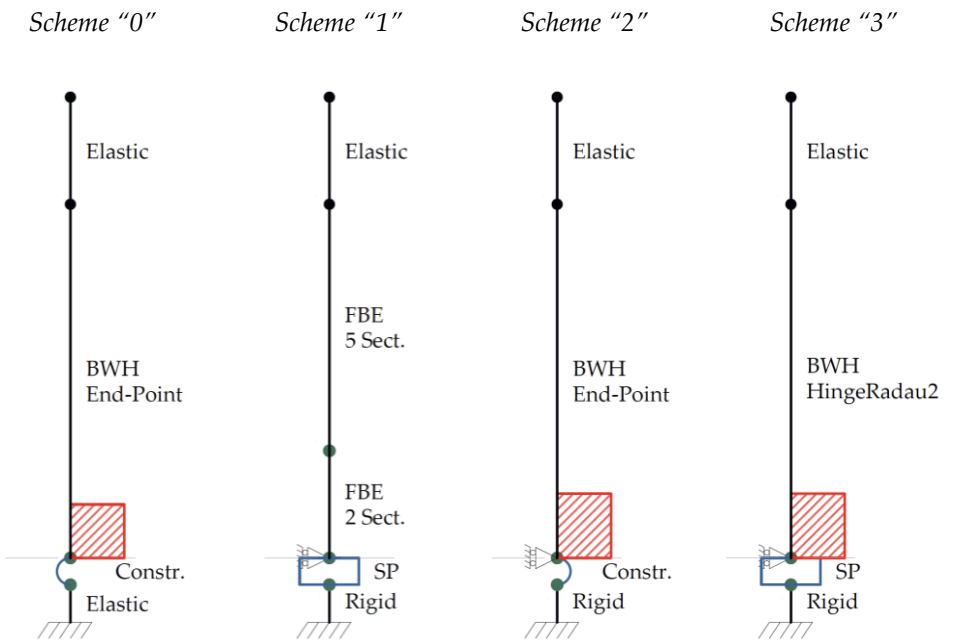

Figure 3.19: Modelling schemes adopted for the comparison of the results obtained by different modelling approaches. ("Elastic" = elastic element, "Rigid" = rigid element "BWH" = beam with hinges element, "End-Point" = use of the "HingeEndPoint" quadrature rule, "HingeRadau2" = use of the "HingeRadau2" quadrature rule, "FBE" = force-based beam-column element, "5 Sect" = use of a "Lobatto" quadrature rule with 5 integration sections, "2 Sect" = use of a "Lobatto" quadrature rule with 2 integration sections, "FE" = zero length section that represents the strain-penetration (or fixed-end rotation) contribution, "Constr." = rigid constrain between the two nodes).

To compare the modelling schemes, their force-drift responses are compared to those of the experiments previously cited. Figure 3.20 to Figure 3.25 show the results for both monotonic and cyclic tests. All the predictions follow similar behaviour and are in good agreement with each other. Only "scheme 3" leads to a little wider hysteresis, mostly at the load reversal.
In the next section, the results of the adopted modelling scheme are discussed in further detail.

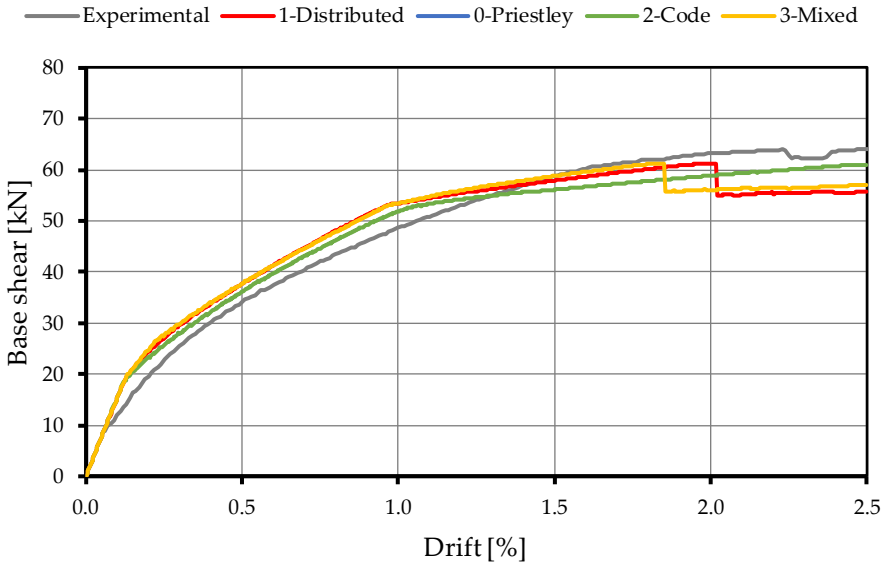

Figure 3.20: Comparison of the experimental and numerical monotonic capacity backbone of the "S300D-m" [66] specimen.

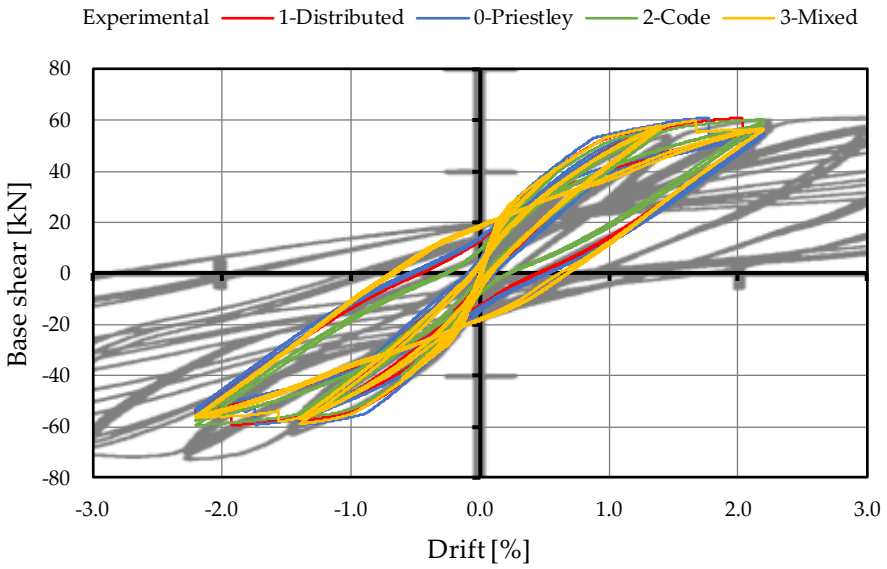

Figure 3.21: Comparison of the experimental and numerical cyclic capacity backbone of the "S300D-c" [66] specimen.

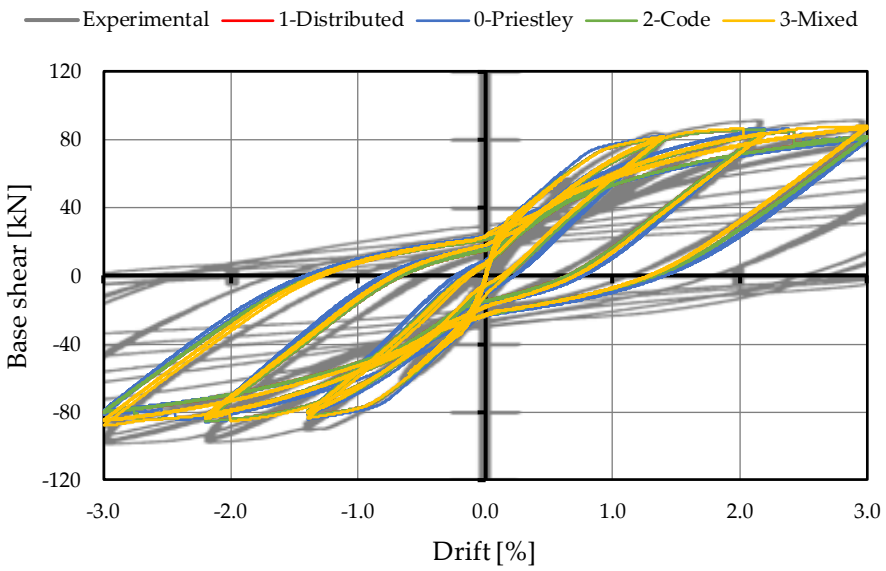

Figure 3.22: Comparison of the experimental and numerical cyclic capacity backbone of the "R300D-c" [66] specimen.

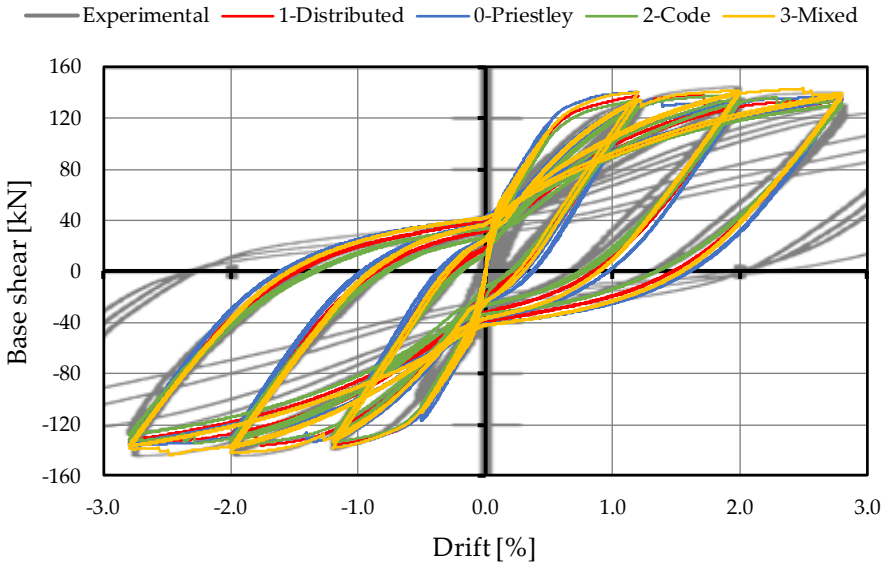

Figure 3.23: Comparison of the experimental and numerical cyclic capacity backbone of the "R500D-c" [66] specimen.

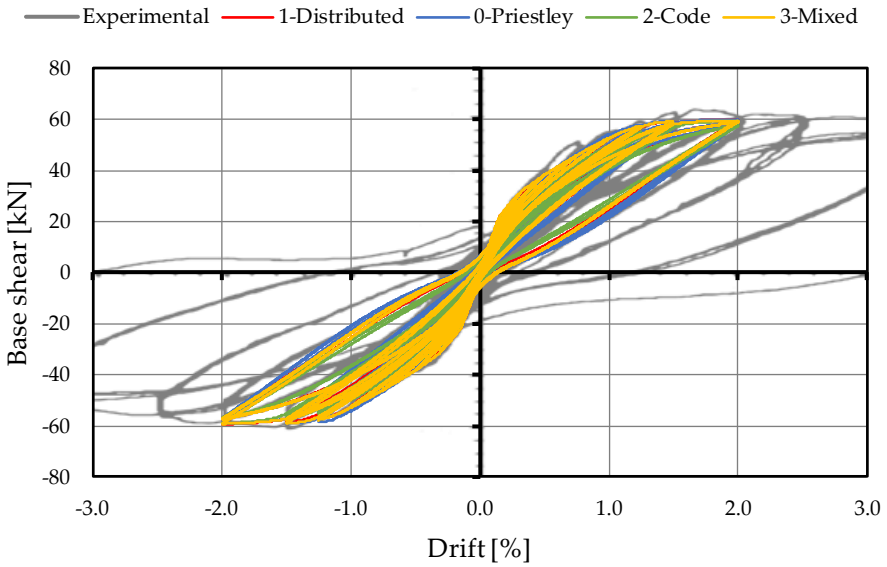

Figure 3.24: Comparison of the experimental and numerical cyclic capacity backbone of the Meda et al., 2014 [67] specimen.

3.3.5.1.2 Monotonic experimental and numerical results comparison

In Figure 3.25, the comparison between the monotonic experimental results of the specimen "S300D-m" [66] and its numerical simulation is reported. The global behaviour, described by the base shear versus the drift response, is well captured, both in terms of stiffness and strength. As previously described, the numerical simulation explored a maximum drift level equal to 2.5%.
In Figure 3.26, the hysteresis of the external confined and unconfined concrete fibres and of the steel fibres is reported, both for the right (leeward) and left (windward) section sides. Negative values refer to compressive strains and stresses. Figure 3.27 shows the hysteresis of the fibres at the zero-length section that simulates strain penetration. Since a zero-length section is considered, the deformations refer to displacements rather than strains.

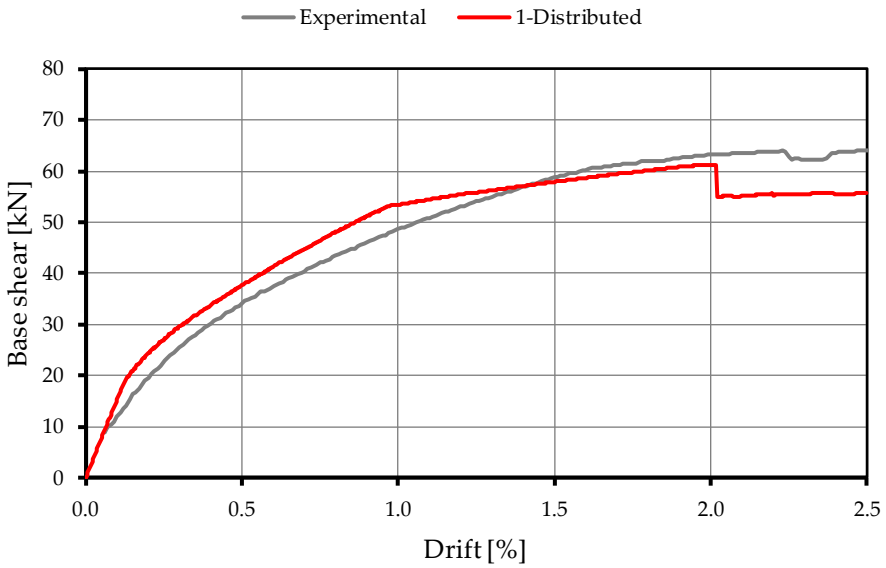

Figure 3.25: Comparison of the experimental and numerical monotonic capacity backbone of the "S300D-m" [66] specimen.

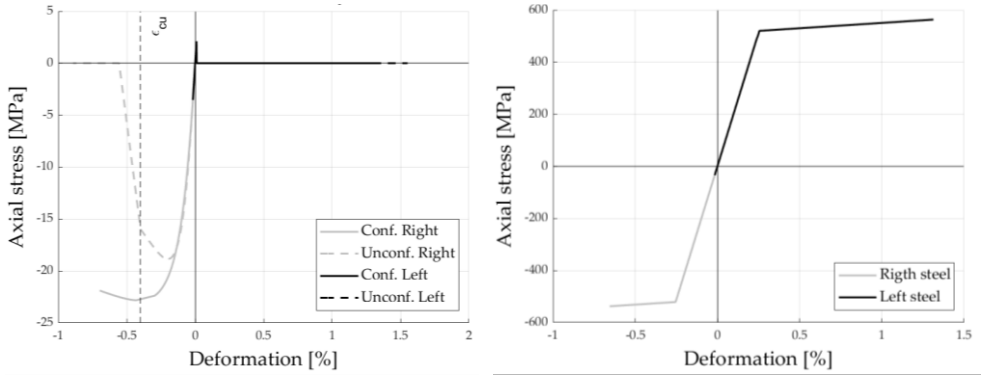

a) *b)*

Figure 3.26: Stress-strain relationships of the concrete a) and steel b) external fibres in the first integration section (interface column-to-foundation) of the element ("Right" corresponds to the external fibre on the leeward side, "Left" corresponds to the external fibre on the windward side).

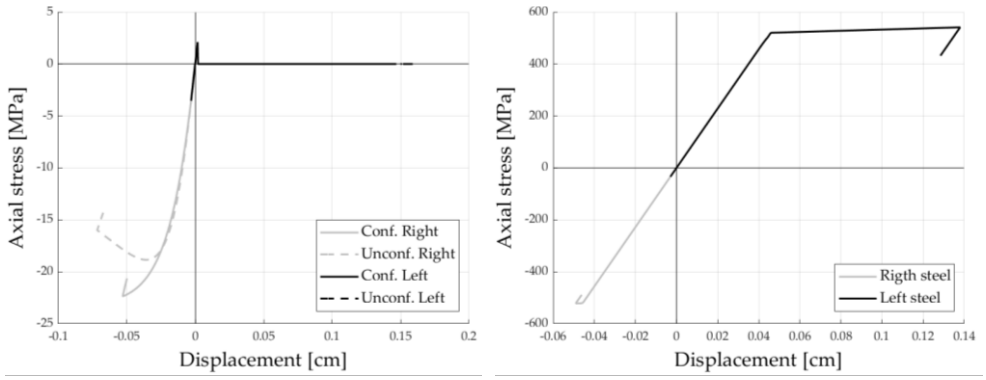

a) *b)*

Figure 3.27: Stress-strain relationships of the concrete a) and steel b) external fibres of the zero-length section that represents the strain penetration contribution ("Right" corresponds to the external fibre on the leeward side, "Left" corresponds to the external fibre on the windward side).

The numerical gap exhibited in Figure 3.25 at a drift level of about 2.0% is given by the numerical crushing of the unconfined concrete cover at the base on the element side. This is clearly visible in the axial strain history reported in Figure 3.28 (lower graph), where the external unconfined concrete fibre at the right side of the cross section reaches the ultimate compressive strain of 0.4%. At this step, both the strains

on the compressive and tensile sides increase. At the fixed-end section, instead, the displacement suddenly decreases (Figure 3.29). In fact, Figure 3.30 represents the moment-curvature and the curvature time-history of the base section of the column element and the equivalent ones of the zero-length section that represents the strain penetration contribution. When the external fibre that represents the unconfined concrete fibre at the element side reaches the crushing, the bending moment suddenly decreases, and the curvature suddenly increases. At the same time, at the zero-length section, crushing is not permitted and the section remains fully reactive; consequently, at the bending moment reduction due to the crushing at the base section of the element, corresponds a reduction in the equivalent curvature. The equivalent curvature is evaluated by subdividing the zero-length section rotation by the scale factor r_y (Eqs. (3.3-3) and (3.3-5) used to define the material properties. The deformation concentrates at the element side, where the curvature (Figure 3.30 right) and the neutral axis depth (Figure 3.31) increase, while at the zero-length section, after the stress drop, they start to be constant. This is also visible in the materials hystereses of the zero-length section, which exhibit an unloading trend.
This test validates the proposal of Ghannoum and Moehle (2012) [53] (§3.1.1.2). Until the crushing of the unconfined concrete, the neutral axis depth at the zero-length section and the first element integration section overlaps.

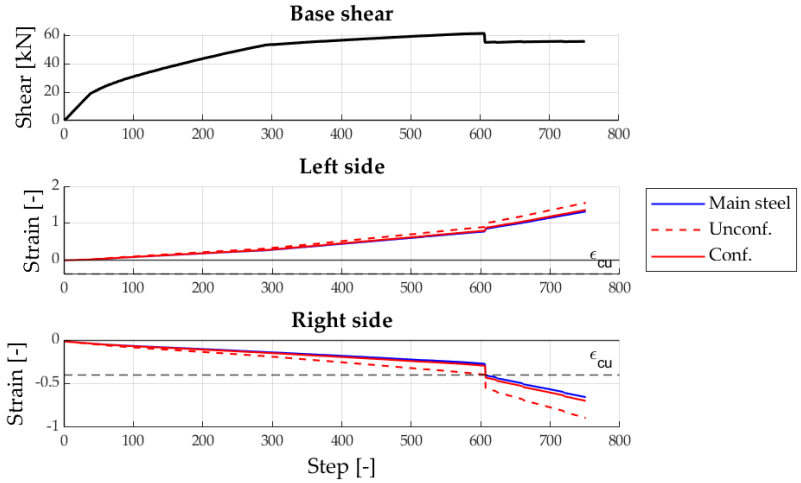

Figure 3.28: Axial strain history of the main materials at the first integration section of the beam-column element.

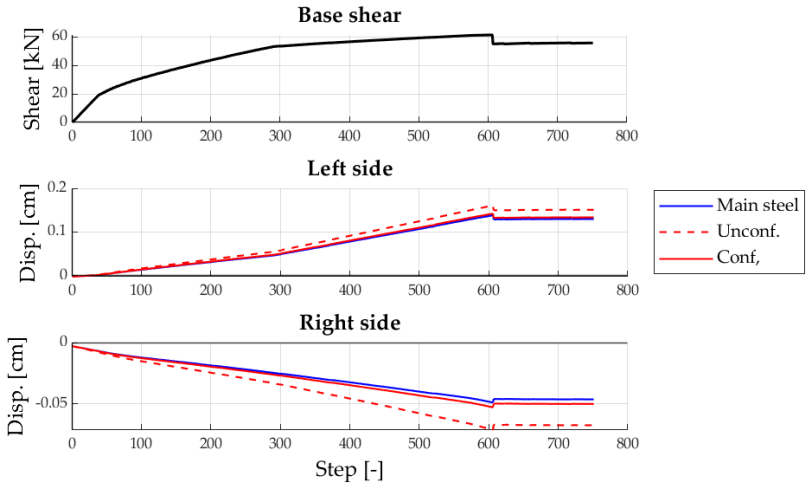

Figure 3.29: Axial strain history of the main materials at the zero-length section that represents the strain penetration effect.

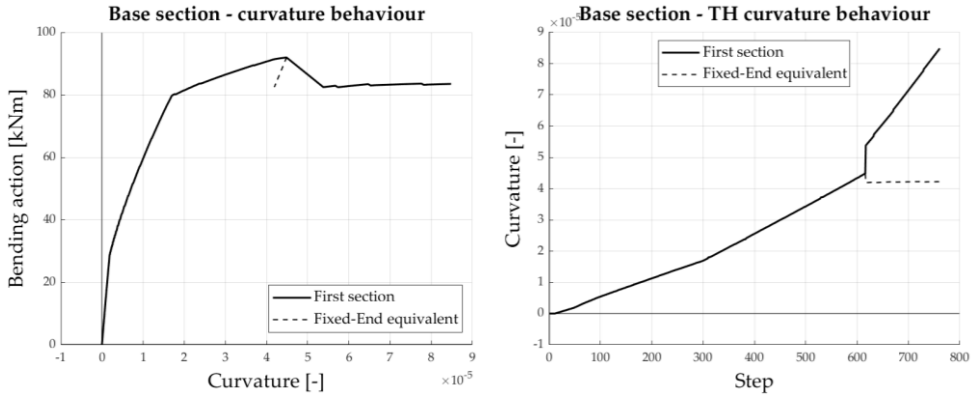

a) *b)*

Figure 3.30: Base section and zero-length section curvatures comparison as a function of the bending action a) and the time step in the analysis b).

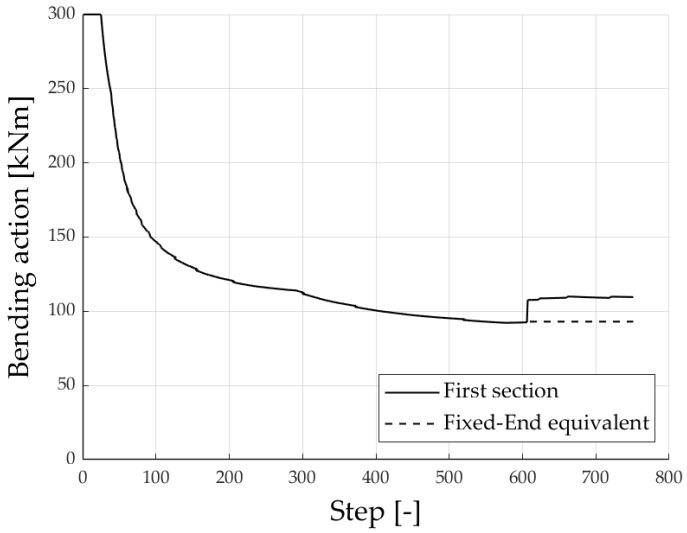

Figure 3.31: Comparison of the neutral axis depth at the zero-length section and at the first integration section of the beam-column element.

3.3.5.1.3 Cyclic experimental and numerical results comparison

A column similar to that previously tested under monotonic loading is here discussed under the cyclic test. The global behaviour is represented in Figure 3.32, with the numerical simulation capable of reasonably capturing the test results. The initial stiffness, the strength, and the unloading branch are well captured. An asymmetry is clearly visible, and it is motivated by the authors because of a non-symmetric concrete cover in the specimen.
The considerations about the interaction between the base integration section at the element side and the zero-length section that represents the strain penetration effects described for the monotonic tests in §3.3.5.1.2 are here confirmed. In the following Figure 3.33 and Figure 3.34, the cyclic hystereses of the materials for the two sections are reported. Despite unconfined concrete at the element side crushes, this never occurs in the zero-length section. Referring to Figure 3.35, the equivalent curvature at the zero-length section overlaps the one of the base fibre section at the element side until the crushing of the unconfined concrete in the latter; after that, the curvature concentrates at the element side, where it suddenly increases, while it suddenly reduces at the zero-length section. The same behaviour is exhibited by the neutral axis depth (Figure 3.36). This confirms that after crushing, the deformation concentrates on the element side, as desired.

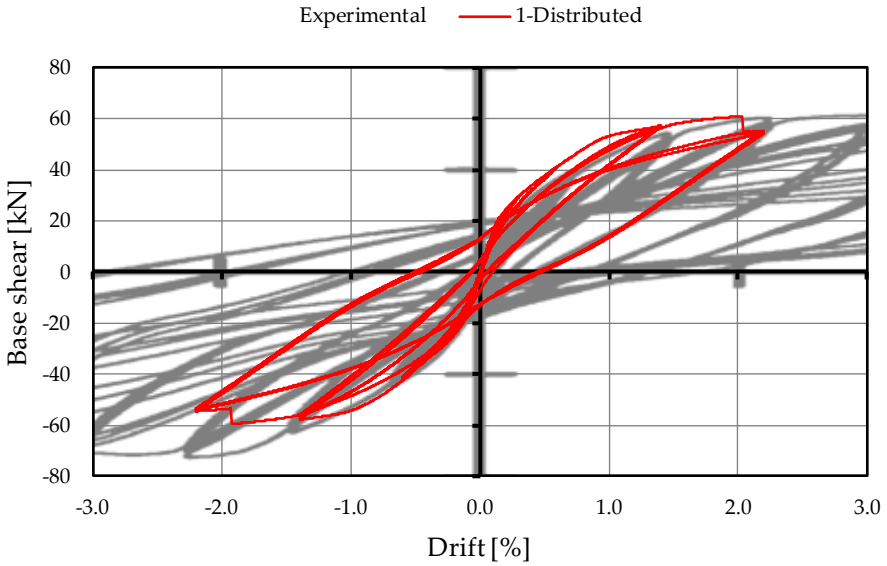

Figure 3.32: Comparison of the experimental and numerical cyclic capacity backbone of the "S300D-c" [66] specimen.

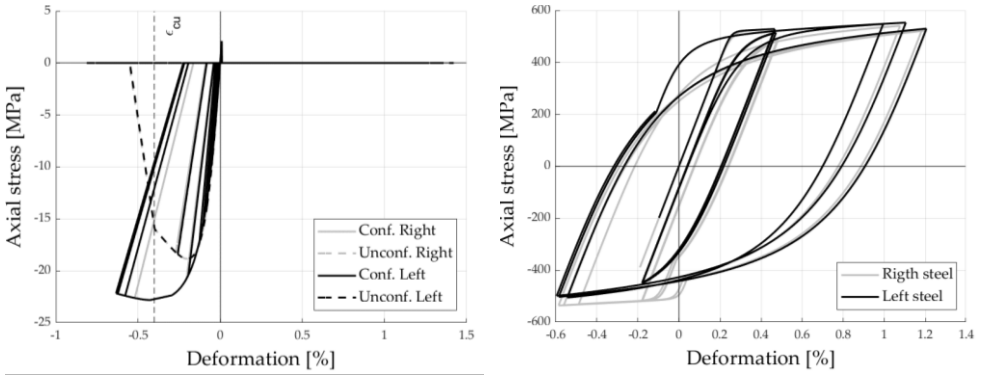

a) *b)*

Figure 3.33: Hysteresis of the concrete a) and steel b) external fibres in the base section of the beam-column element ("Right" corresponds to the external fibre on the leeward side, "Left" corresponds to the external fibre on the windward side).

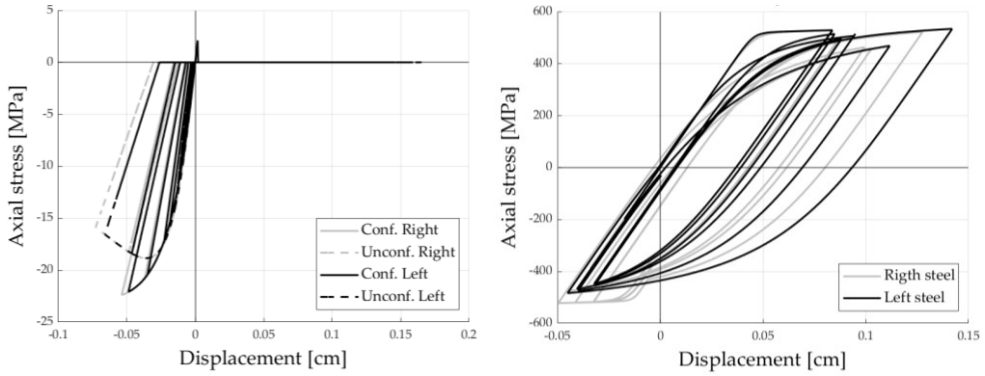

a) *b)*

Figure 3.34: Hysteresis of the concrete a) and steel b) external fibres of the zero-length section that represents the strain-penetration contribution ("Right" corresponds to the external fibre on the leeward side, "Left" corresponds to the external fibre on the windward side).

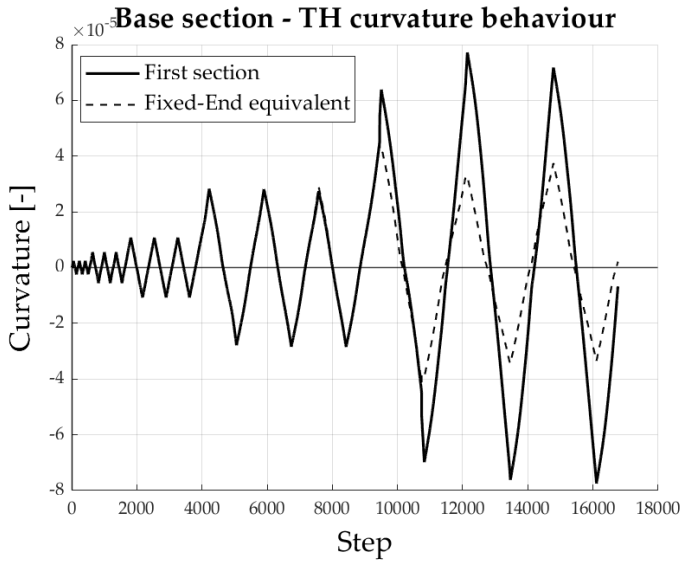

Figure 3.35: Base section of the beam-column element and zero-length section curvatures comparison.

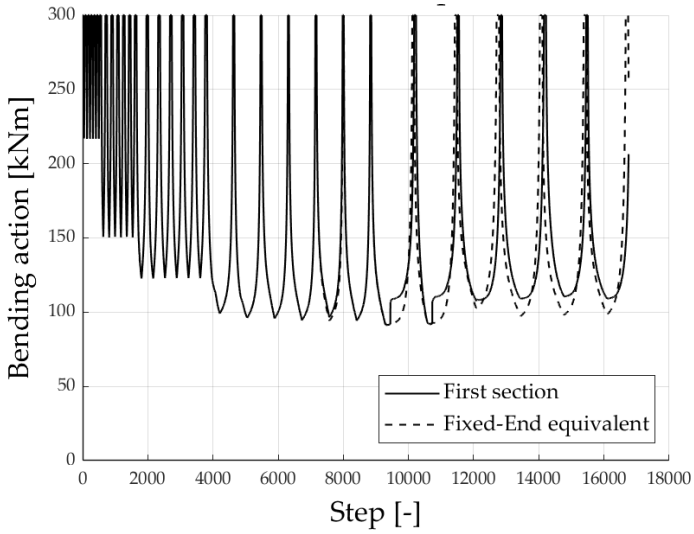

Figure 3.36: Comparison of the neutral axis depth at the zero-length section and at the first beam-column element integration section.

The same authors [66] tested two rectangular columns with 300 [mm] by 500 [mm] cross-section sizes, respectively, in the weak ("R300D-c") and strong ("R500D-c") directions. The comparisons reported in Figure 3.37 and Figure 3.38 confirm the results previously described. Finally, the results of the tests performed by Meda et al. (2014) [67] are reported in Figure 3.39.

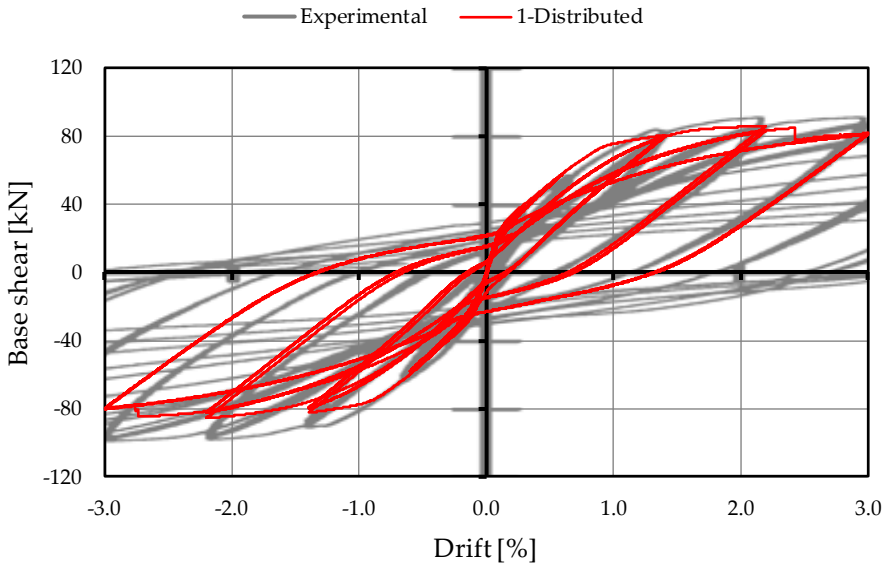

Figure 3.37: Comparison of the experimental and numerical cyclic capacity backbone of the "R300D-c" [66] specimen.

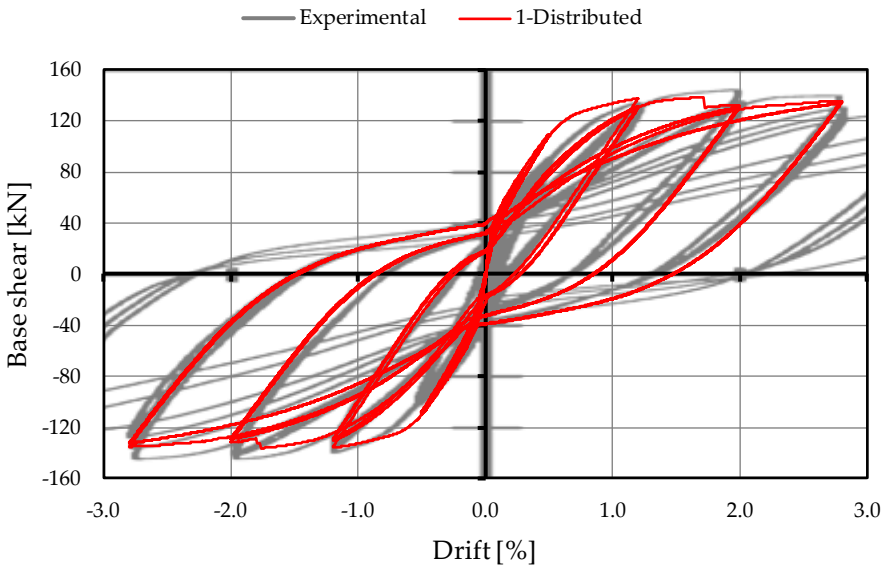

Figure 3.38: Comparison of the experimental and numerical cyclic capacity backbone of the "R500D-c" [66] specimen.

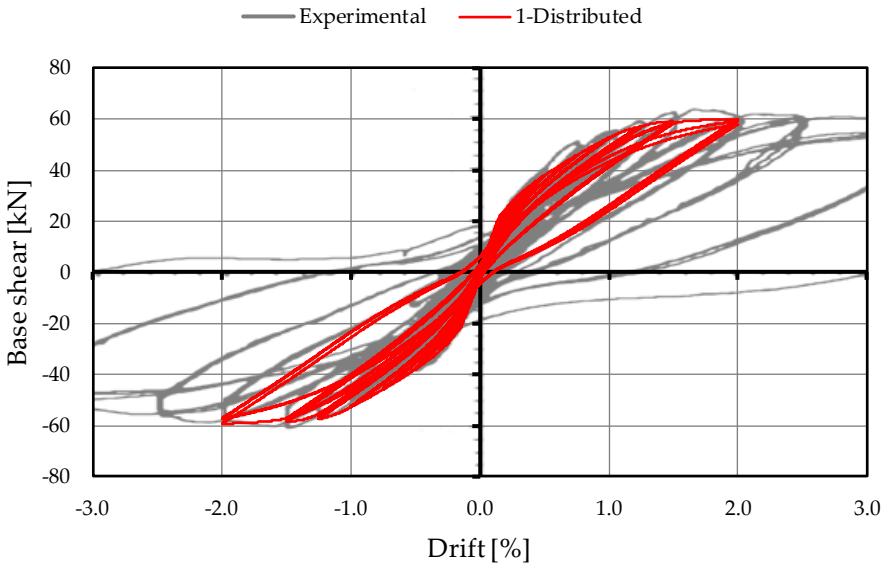

Figure 3.39: Comparison of the experimental and numerical cyclic capacity backbone of the specimen tested in Meda et al. (2014) [67].

3.3.5.2 Frame tests

The RC bare frame tested by Morandi et al. (2018) [68] is numerically simulated, and the results are here discussed.
The structure is a one-bay, one-story frame subjected to vertical loads applied at the top of the columns and to a cyclic horizontal displacement history imposed at the top beam. The numerical model adopts the modelling scheme described in §3.3.1.
In Figure 3.40, the force-drift experimental behaviour is compared with the numerical monotonic response. The initial stiffness, the stiffness decay, and the maximum strength are well captured. The cyclic numerical simulation presented in Figure 3.41 highlights the good agreement for both the unloading and loading branches.

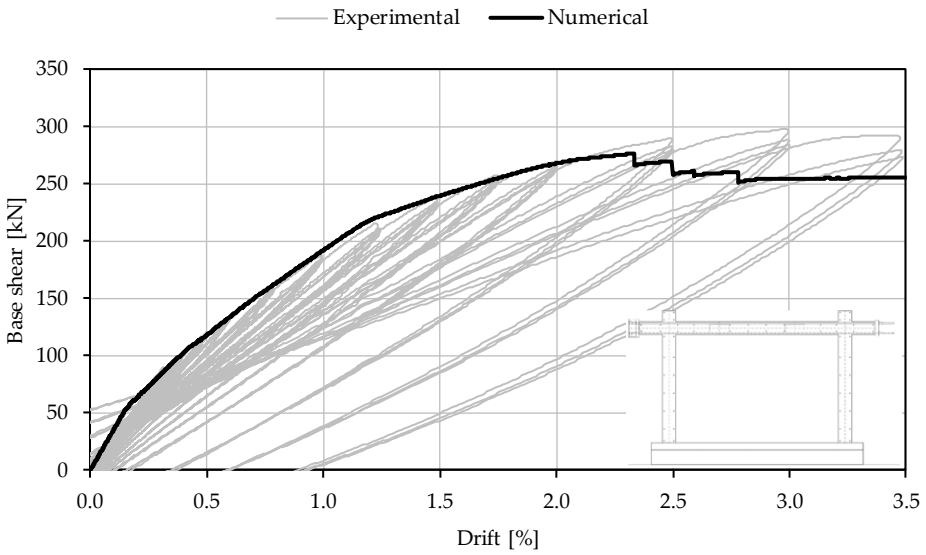

Figure 3.40: Comparison of the cyclic experimental force -drift results of the portal frame tested by Morandi et al. (2018) [68] with its monotonic numerical simulation.

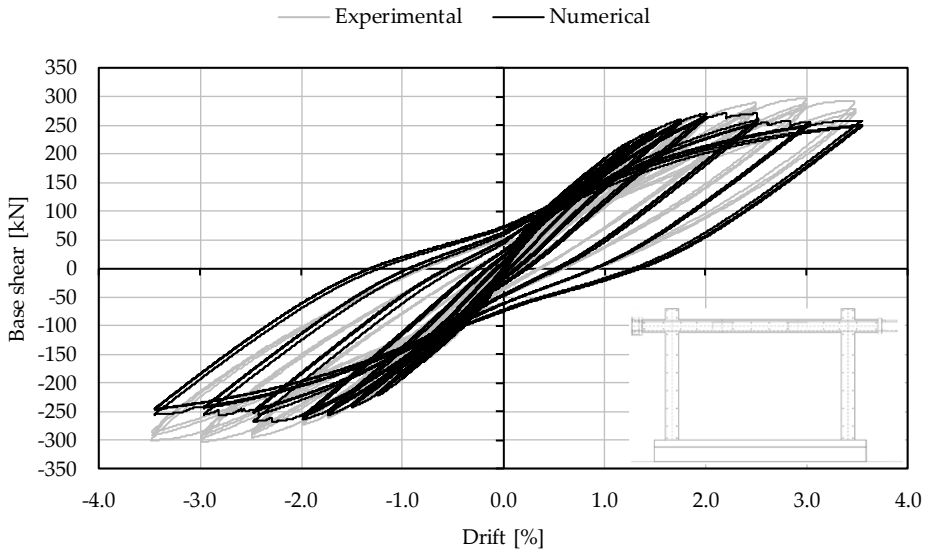

Figure 3.41: Comparison of the cyclic experimental force -drift results of the portal frame tested by Morandi et al. (2018) [68] with its cyclic numerical simulation.

3.3.6 *Mass discretization*

The mass discretization may follow different approaches. In the presence of a rigid diaphragm, floor masses can be lumped, and the discretization is simplified. On the other hand, the rigid diaphragm imposes that all the nodes of each floor have the same horizontal degree of freedom; no relative horizontal displacement is allowed between two nodes of each element. As a consequence, when fibre-section-based elements are used, their axial deformation is prevented, the section could be forced to rotate around the mean axis, and, consequently, unreal internal actions may occur in the beams with the consequent global overstrength.
In light of that, diaphragms are not considered rigid in this work, and the choice of mass discretization for the nodes of the floors is discussed by investigating the responses obtained by different discretization schemes (Figure 3.42):

- I) A single mass for each floor located in its centre. If an even number of spans characterises the frame, the mass is concentrated at the central axis node; otherwise, mass is equally subdivided between the two internal nodes of the middle beam (those that divide the end lengths from the central one). In this configuration, their horizontal degree of freedom is constrained (model "SING").
- II) Mass is equally distributed to all the internal nodes of the beams (model "MD").
- III) Mass is equally distributed to all the beam nodes aligned with the axis of the columns (Model "MDN").
- IV) Mass is equally distributed to all the nodes of the beams ("MDF").

The sensitivity analysis is performed by means of nonlinear dynamic analyses on the five-story, three-bay frame described and numerically tested in Di Trapani et al. (2020) [34], subjected to the ground motion represented in Figure 3.43. The Rayleigh damping model, characterised by 2% and 5% of the critical damping in the first and third modes, respectively, is assumed. More details about damping modelling choices are discussed in the next section.

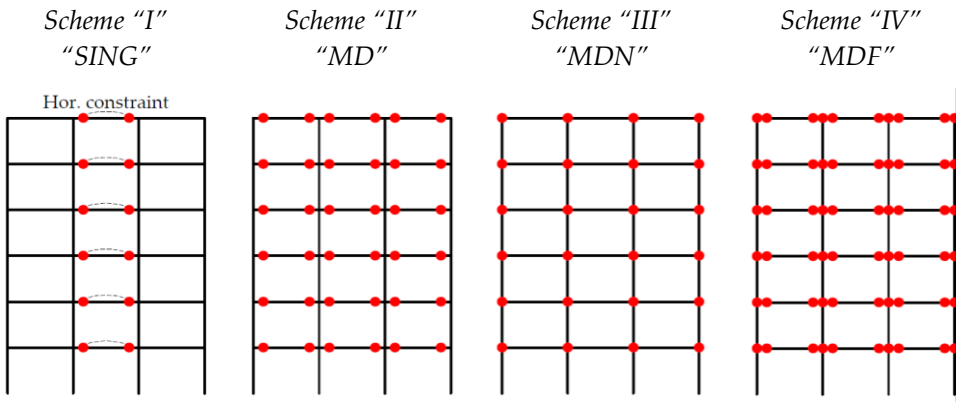

Figure 3.42: Schemes of the different mass discretization investigated applied to a five-story, three-bay frame.

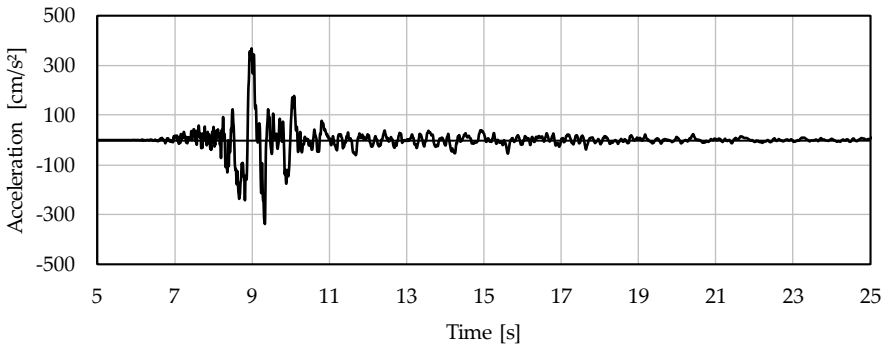

Figure 3.43: Ground motion (ID Itaca: EMSC-20160824_0000006) used in the NLTHA to evaluate the influence of the discretization scheme of the nodal masses.

The time histories of the global drift and the base shear are compared for different scale factors applied to the ground motion (Figure 3.44 to Figure 3.46). The initial part of the response, characterised by the peak displacement and base shear, is the same for all the discretization schemes. After that, the responses exhibited by the analyses with the mass distributed to the nodes are very similar. A small amplification is shown moving from the configuration with masses distributed in the beams only (MD), in the beams and column axis nodes (MDF), and in the column axis nodes only (MDN), progressively. With a lumped mass for each floor, the response amplitude is slightly reduced for both the global drift and the base shear with respect to the other mass discretization layouts. The same trend is exhibited for the lower intensity of the ground motion (scale factor equal to 0.5, Figure 3.44) and for the design one (scale factor equal to 1, Figure 3.45). When the structure largely enters the plastic field (scale

factor 2.0, Figure 3.46), the differences reduce, and the oscillation occurs around a residual displacement.

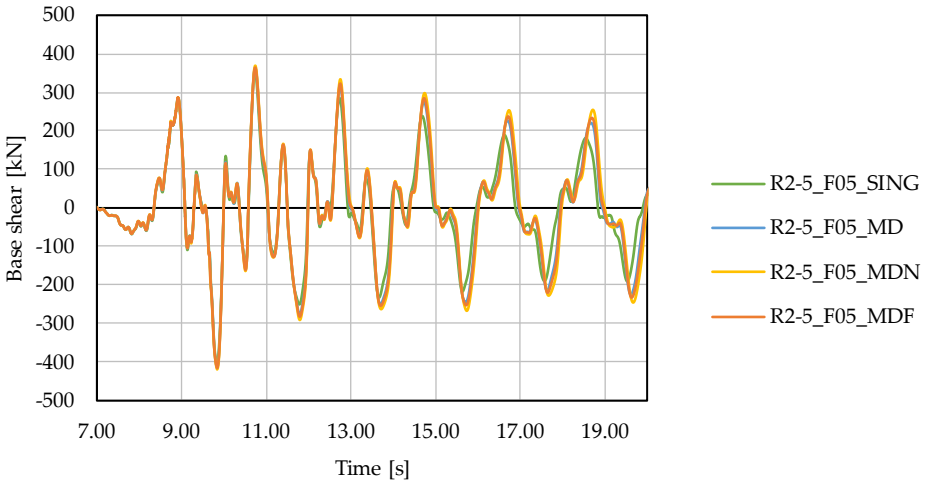

a)

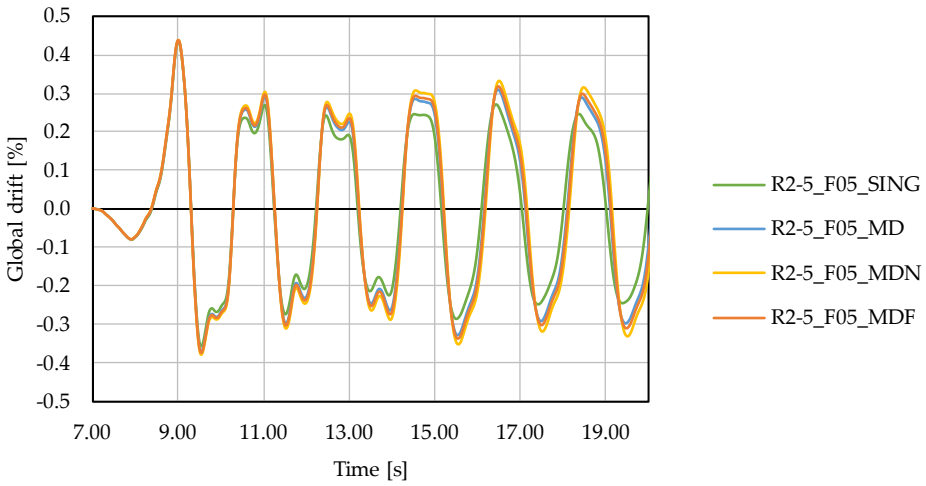

b)

Figure 3.44: Base shear a) and the global drift b) time history plot for a scale factor applied to the ground motion equal to 0.5.

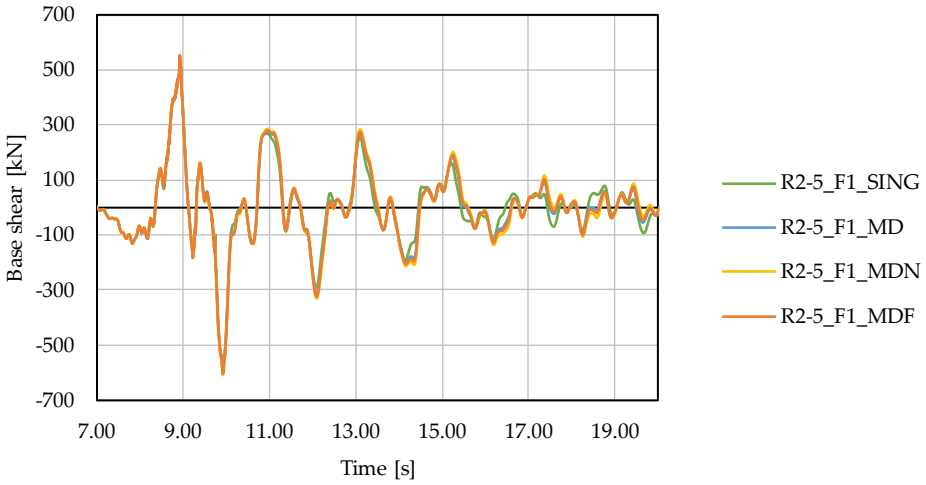

a)

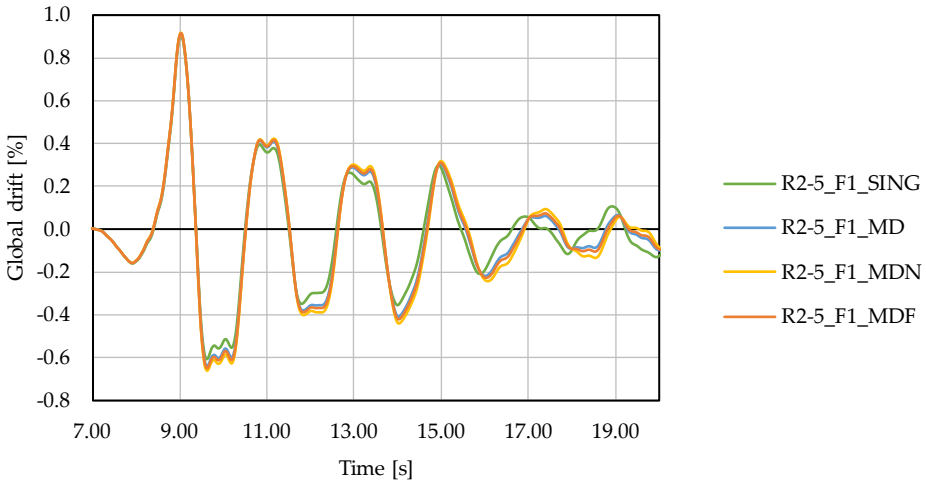

b)

Figure 3.45: Base shear a) and the global drift b) time history plot for a scale factor applied to the ground motion equal to 1.0.

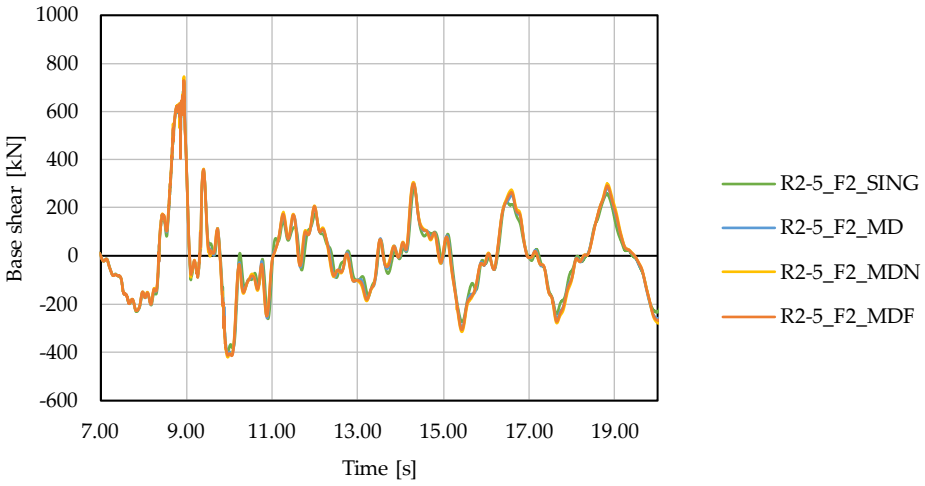

a)

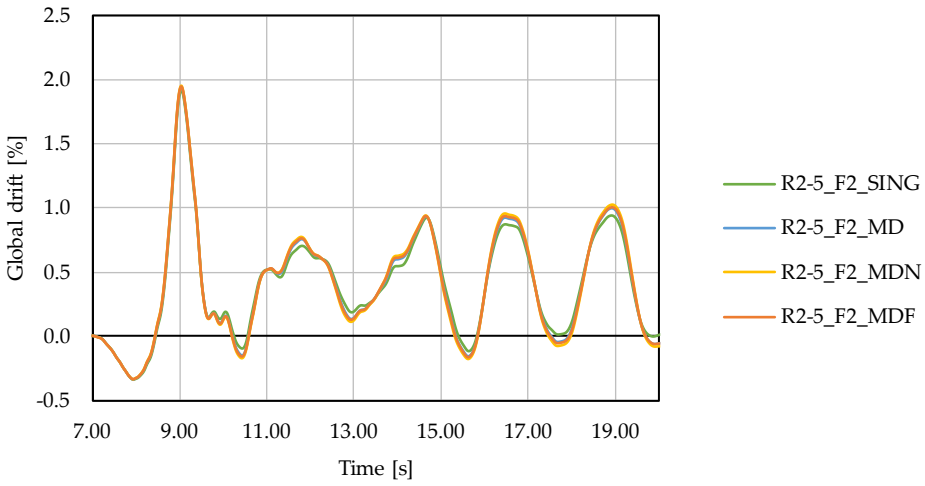

b)

Figure 3.46: Base shear a) and the global drift b) time history plot for a scale factor applied to the ground motion equal to 2.0.

Since the masses of the floors are not constrained to undergo the same degrees of freedom, different displacements, velocities, and accelerations could be read on the masses. Despite a basically coincident history of displacements experienced by all the nodes on the same floor, different accelerations are highlighted. For example, Figure 3.47 shows the accelerations of the masses on the last floor for the

discretization scheme MDN, in the case of a ground motion scale factor equal to 1. The black line represents their average value. In order to understand the disturbance induced by the mass discretization on the reading of the floor acceleration, an additional structure layout is analysed, characterised by the introduction of an "artificial diaphragm" by means of an elastic truss that connect the beam end nodes. Such trusses are characterised by the same cross section of the beam and an elastic modulus which is one half that of the concrete of the beam. Figure 3.48 shows the different responses in terms of base shear and global mean drift of the structure with and without the introduction of the artificial diaphragm.
In Figure 3.47, the acceleration recorded in the model with the simulation of the diaphragm is represented by the red line. The comparison shows that the average acceleration (black) in the model without the artificial diaphragm is very close to the one (red) in the model with the additional trusses that simulate the diaphragm effect. The two accelerations are only slightly amplified when, instead, the base shear history shows a significant difference because of the additional strength offered by the introduction of the artificial diaphragm.
In this work, mass is equally distributed to all the beam nodes aligned with the axis of the columns (Model "MDN").

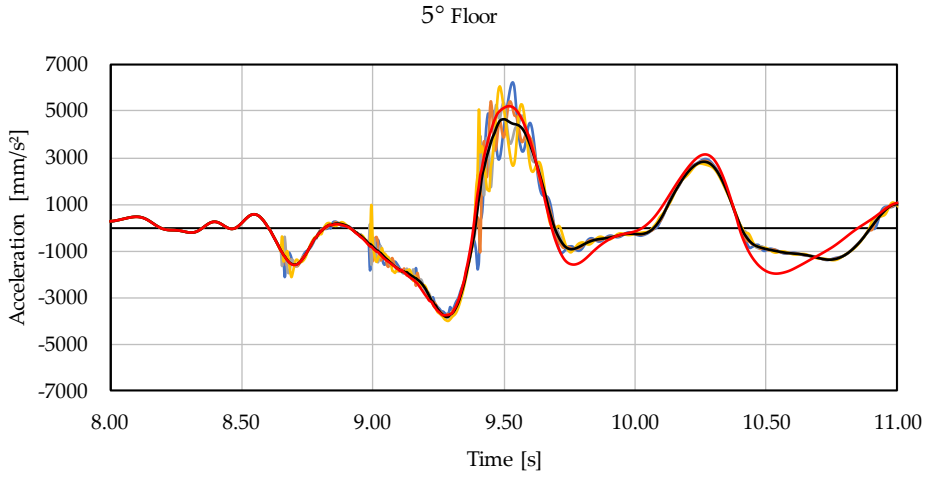

Figure 3.47: Acceleration of the nodes of the top floor and representation of their average value by the black line, for a scale factor applied to the ground motion equal to 1. Red line represents the average acceleration if a fictitious diaphragm is simulated by connecting the nodes with elastic trusses.

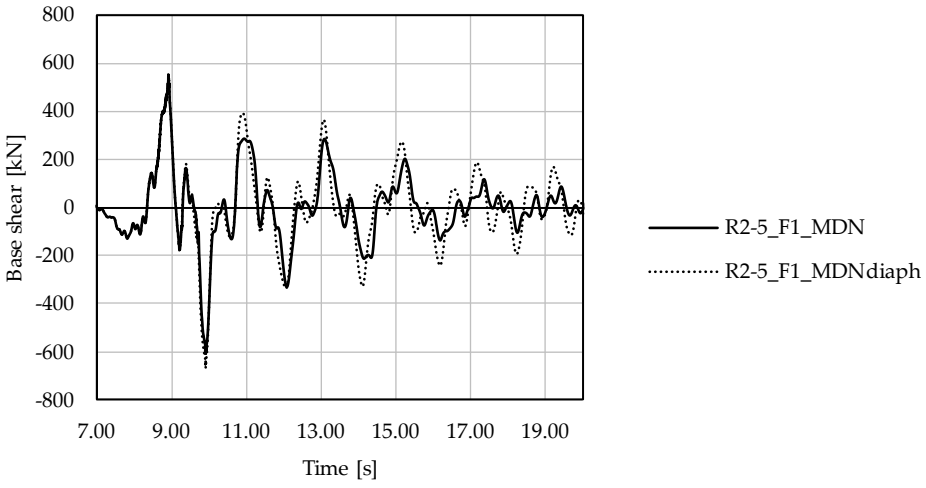

a)

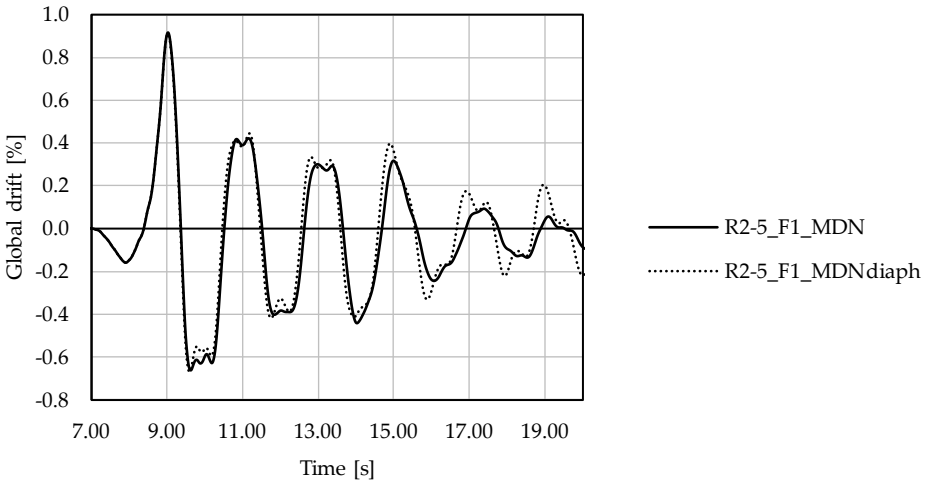

b)

Figure 3.48: Comparison of the base shear a) and the global drift b) time history obtained with the MDN scheme (continuous line, "MDN") and the ones obtained by simulating the diaphragm through elastic trusses (dotted line, "MDNdiaphr) (scale factor applied to the ground motion equal to 1.0, "F1", and Rayleigh damping with 2% and 5% critical damping ratios, "R2-5").

3.3.7 *Damping model*

The damping modelling in the elastic field has an important role in non-linear dynamic analyses. The paragraph discusses the results obtained by adopting two damping models with different damping ratios to the same case study previously used for the discussion of mass discretization.
The first model considered is the Rayleigh damping model. Modal damping matrix is mass and stiffness proportional with two proportionality constants, according to Equation (3.3-6).

$$\mathbf{C} = \alpha_m \mathbf{M} + \beta_k \boldsymbol{K} \tag{3.3-6}$$

The critical damping ratio, ν_i, of the i-th mode can be evaluated considering the i-th equation (Eq. (3.3-7) of system (3.3-6), and it can be written (Eq. (3.3-8)) as a function of the i-th natural frequency of the system.

$$\mathrm{C}_i = \alpha_m M_i + \beta_k K_i \tag{3.3-7}$$

$$\nu_i = 0.5 \cdot \left(\frac{\alpha_m}{\omega_i} + \beta_k \omega_i \right) \tag{3.3-8}$$

By observing Eq. (3.3-8), ν_i is linear with respect to ω if only stiffness contribution is considered, while hyperbolic if only mass contribution is considered. The constants α_m and β_k are evaluated by the system of equations (3.3-9) and (3.3-10) by imposing two critical damping ratios ν_i and ν_j at two frequencies, ω_i and ω_j.

$$\alpha_m = 2 \frac{\nu_i \omega_j - \nu_j \omega_i}{\omega_j^2 - \omega_i^2} \omega_i \omega_j \tag{3.3-9}$$

$$\beta_k = 2 \frac{\nu_j \omega_j - \nu_i \omega_i}{\omega_j^2 - \omega_i^2} \tag{3.3-10}$$

Damping at frequencies lower than ω_i rapidly increases, while at frequencies higher than ω_j increases without boundary.
OpenSees software allows for the definition of the proportionality to different stiffness matrixes. Current tangent stiffness $K_{current}$, initial tangent stiffness K_{init}, or last-committed stiffness $K_{last\ commit}$ can be selected as described in Eq. (3.3-11).

$$\mathbf{C} = \alpha_m \mathbf{M} + \beta_k \boldsymbol{K_{current}} + \beta_{k,init} \boldsymbol{K_{init}} + \beta_{k,commit} \boldsymbol{K_{last\ commit}} \quad (3.3\text{-}11)$$

Charney (2008) [69] claims that the use of Rayleigh damping in nonlinear systems suffers from problems when the tangent stiffness matrix changes and, consequently, when the stiffness of the structure changes at global or local levels. The current tangent stiffness choice adopts the stiffness matrix of each iteration, and it could change significantly, so it is not recommended. On the other hand, the use of an initial stiffness matrix generates high spurious damping forces when the structure yields, since the damping matrix is proportional to the initial stiffness of the structure, which remains constant. The problem is also exhibited at a local level when concentrated plastic hinges are defined. Damping moments are related to rotational velocity and rotational stiffness; when yielding occurs, fictitious high initial stiffness (as common in lumped plasticity models) can generate excessively high spurious damping moments, and high errors can be made. The easier solution is to not provide stiffness-proportional damping to these elements. If tangent stiffness is used and damping coefficients are evaluated on the initial system, the artificial damping generated is reduced. While updating the proportional coefficients based on the tangent stiffness, no artificial damping is provided.
Chopra and McKenna (2016) [70] highlighted some conflicts regarding the use of the tangent stiffness matrix from the physics point of view. Since elements are provided by a force-deformation hysteresis, damping force velocity exhibits hysteresis. Damping can become negative when the structural stiffness becomes negative at large displacements with gravity load effects. Furthermore, the constant damping principle is violated. Modal damping, as described below, is suggested as a solution. The authors clarify that the problems are mainly correlated with the use of lumped plasticity models. If distributed plasticity models are used, the Rayleigh damping model gives acceptable results. Hall (2016) [71] discussed that it is not true, but also that distributed plasticity models suffer from this drawback when deformation rates are high, and the structure enters a collapse mechanism. A detailed discussion can also be found in Hall (2016) [71] and Chopra and McKenna, (2016) [72], where a focus is placed on the physical representativeness of the damping models. Moreover, it is discussed that damping must not be defined for penalty elements, elements that work as constraints, such as at the contacts or at the plastic hinges.
In this work, a distributed-plasticity model is adopted, mixed with the use of concentrated zero-length sections that simulate the strain penetration contribution. Following the previous discussion, the stiffness proportional damping is defined only for the beam and column elements, and the last committed tangent stiffness is used at each step. Moreover, mass-proportional damping is applied only to the nodes where mass is assigned. No damping is provided to the zero-length elements that

represent the strain penetration contribution; regardless, they do not have an initial rigid stiffness and do not suffer from the issues previously discussed. Rayleigh damping coefficients are evaluated based on the dynamic characteristics of the structure before the non-linear dynamic excitation and after the nonlinear analysis conducted for gravity loads.

The results of three different damping ratio calibrations are reported, namely: 2% damping ratio for the 1st and 3rd vibration frequencies (R2), 5% damping ratio for the 1st and 3rd vibration frequencies (R5), and 2% and 5% damping ratio for the 1st and 3rd vibration frequencies, respectively (R2-5). Figure 3.49 represents the Rayleigh damping ratio functions for the three different assumptions (evaluated from Eq. (3.3-8)).

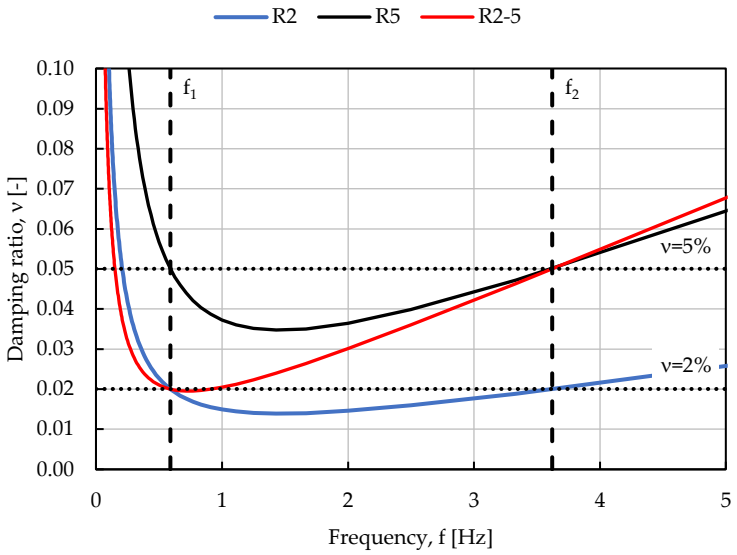

Figure 3.49: Representation of the Rayleigh damping functions for the different adopted models.

Figure 3.50 and Figure 3.51 show the structure response by applying the ground motion used to investigate the influence of the mass discretization scheme with scale factors equal to 0.5 and 1, respectively. As expected, higher frequencies are not in phase with respect to the main one, and they are represented by a secondary oscillation around the first one; consequently, they can amplify or reduce the response given by the main frequency. If higher modes are overdamped (R5 and R2-5), the oscillation becomes smoother with time. For low excitation, for which the structure remains close to the elastic field (Figure 3.50), the model R5 shows a reduction of the secondary oscillation around the main one with respect to R2 and R2-5. The equivalent period of oscillation is not modified since the damping in the

first mode is not changed. The higher mode effect is more visible in the base shear, where the secondary oscillation and the local peaks are more pronounced. Higher damping in the first mode significantly reduces these peaks, allowing for a smoother trend. For R5, the response reduces faster, appears smoother, and exhibits a little reduction in the equivalent period of vibration.
The same behaviour is exhibited for the design ground motion (scale factor equal to 1.0, Figure 3.51).

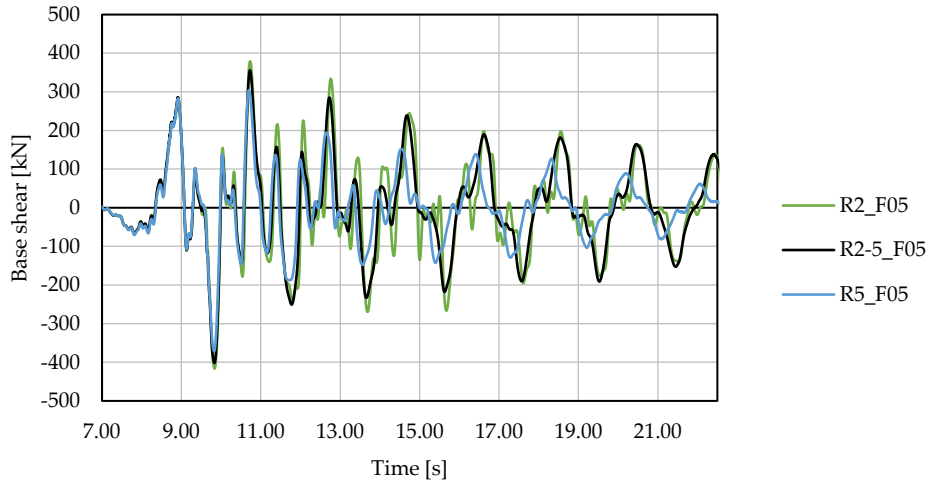

a)

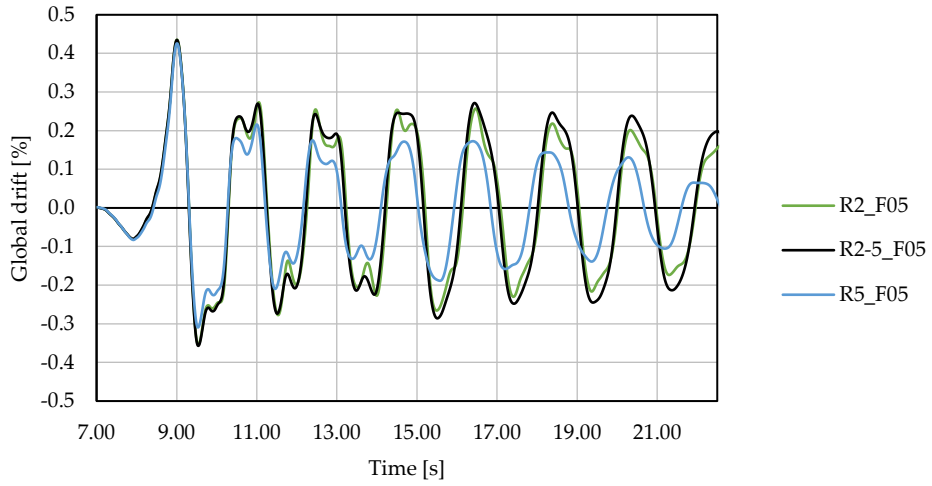

b)

Figure 3.50: Base shear a) and global drift b) time history plot for different damping ratio choices of the Rayleigh damping model for a scale factor applied to the ground motion equal to 0.5, "F05". R2 = 2% damping at the first and third frequencies, R2-5 = 2% at the first frequency and 5% at the third one, and R5 = 5% at the first and third frequencies.

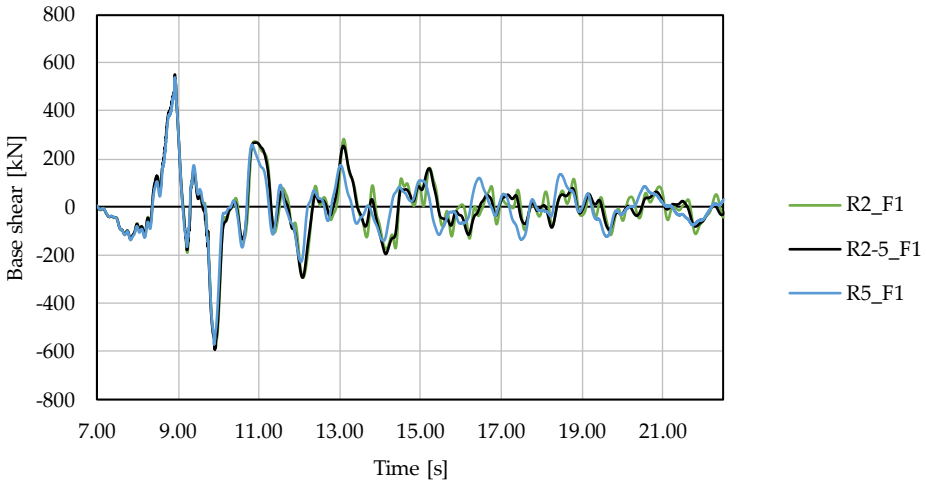

a)

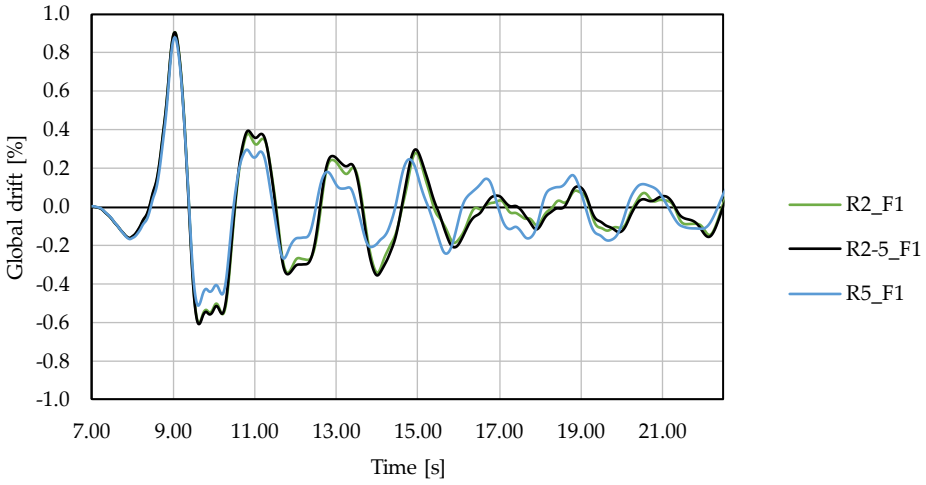

b)

Figure 3.51: Base shear a) and global drift b) time history plot for different damping ratio choices of the Rayleigh damping model for a scale factor applied to the ground motion equal to 1, "F1". R2 = 2% damping at the first and third frequencies, R2-5 = 2% at the first frequency and 5% at the third one, and R5 = 5% at the first and third frequencies.

The second test analyses the response of the structure with the adoption of the Modal damping model. According to the literature [70], [73], the modal damping model avoids some issues of the Rayleigh damping model given by its proportionality to the stiffness matrix. With the Modal damping model, specific damping ratios are directly assigned to each vibration mode of the structure, while the Rayleigh approach allows one to choose the ratio of two modes of vibration only, and the others are consequently derived. Its application is here tested for a low intensity of the ground motion (scale factor equal to 0.5) under the following three conditions: a damping ratio equal to 2% for all the modes (M2), 2% for the first and 5% for all the other modes (M2-5), and 5% for all the modes (M5). The results show that just for a damping ratio equal to 2%, the displacement history became smoother, and the effect of the second mode disappeared quicker than in the Rayleigh damping model (Figure 3.52). The base shear history exhibits less pronounced local peaks. A first observation is that the damping coefficient assigned to the second mode is higher with respect to the one obtained with the Rayleigh model. In fact, if 2% and 5% of critical damping are imposed in the Rayleigh model for the first and third modes, respectively, a damping ratio lower than 5% for obtained at the second one. This is clearly visible in Figure 3.49. As the damping increases, the same considerations highlighted for Rayleigh damping apply to the Modal damping model responses.

A direct comparison of the application of the Rayleigh and the modal damping models is reported in Figure 3.53 for different scale factors of the ground motion. The Rayleigh damping model with 2% and 5% critical damping assigned to the first and third modes, respectively, and modal damping with 2% and 5% assigned to the first and all the other modes, respectively, are compared. The latter is chosen according to the proposal of Smyrou et al. (2011) [73]. The displacement history is very similar; it is smoother in the case of modal damping. While the base shear history exhibited an initial similar response, it is quicker reduced if modal damping is concerned, especially for low values of the scale factor applied to the ground motion.

The overall trend is very similar for all the scale factors considered. The first peak is practically the same; the following response obtained by the modal approach led to lower base shear (Figure 3.53 to Figure 3.55). As for displacement, the differences increase as the earthquake intensity increases, with a trend of Rayleigh damping producing larger residual drifts (Figure 3.55).

Concluding, in the present study, the Rayleigh damping model is applied with 2% and 5% of the critical damping assigned to the first and third frequencies, respectively.

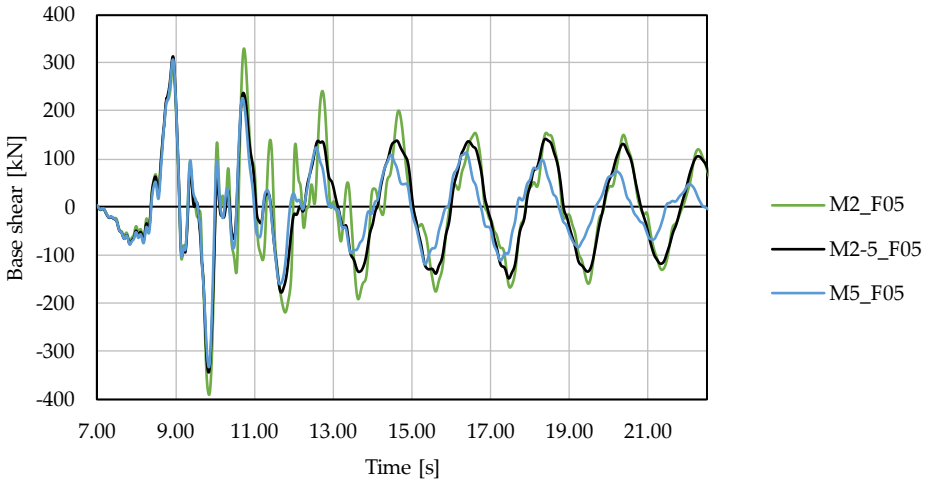

a)

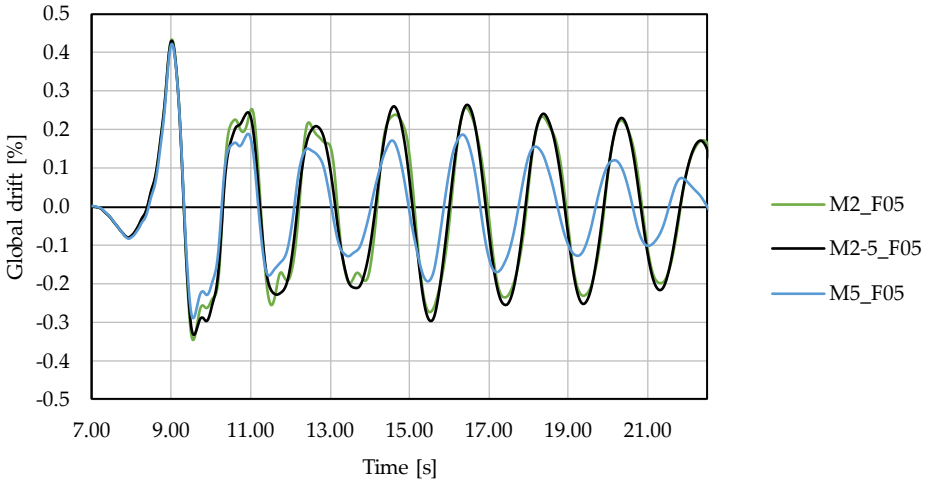

b)

Figure 3.52: Base shear a) and global drift b) time history plot for different damping ratio choices of the modal damping model for a scale factor applied to the ground motion equal to 0.5, "F05". M2 = 2% damping at all the modes; M2-5 = 2% at the first mode and 5% at the other; and M5 = 5% at all the modes.

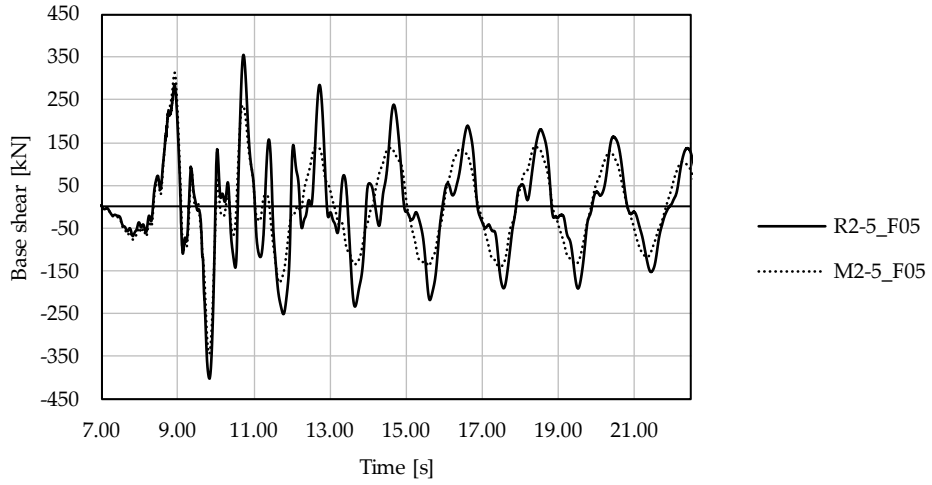

a)

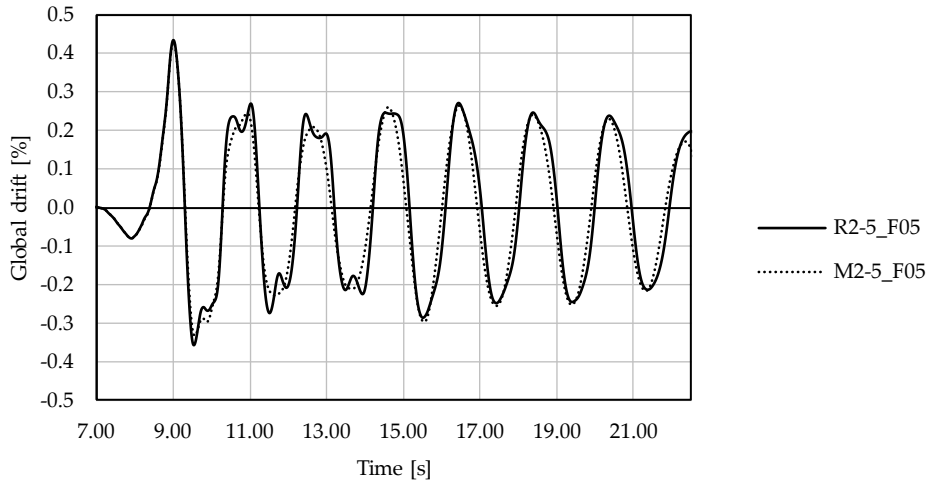

b)

Figure 3.53: Comparison of the base shear a) and global drift b) time history plots for a scale factor applied to the ground motion equal to 0.5, "F05", for the Rayleigh damping model with 2% and 5% critical damping assigned to the first and third modes (R2-5), respectively, and modal damping with 2% and 5% assigned to the first and all the other modes (M2-5), respectively.

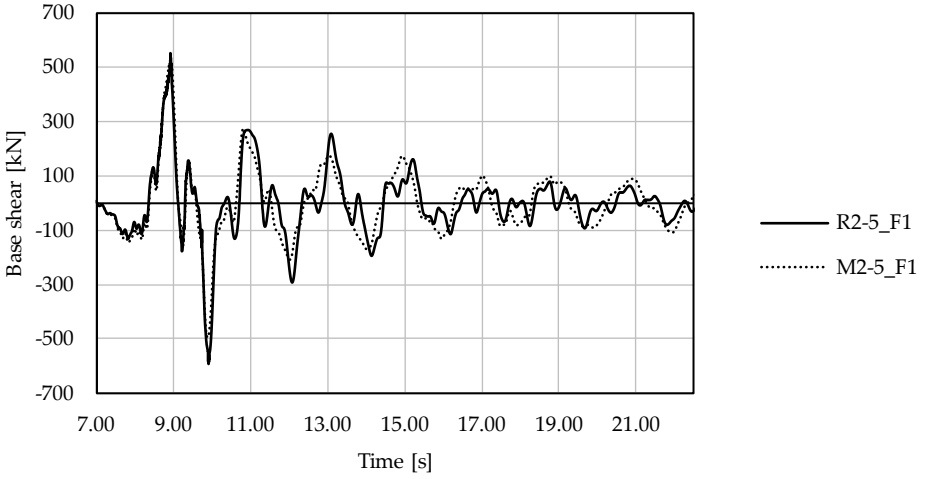

a)

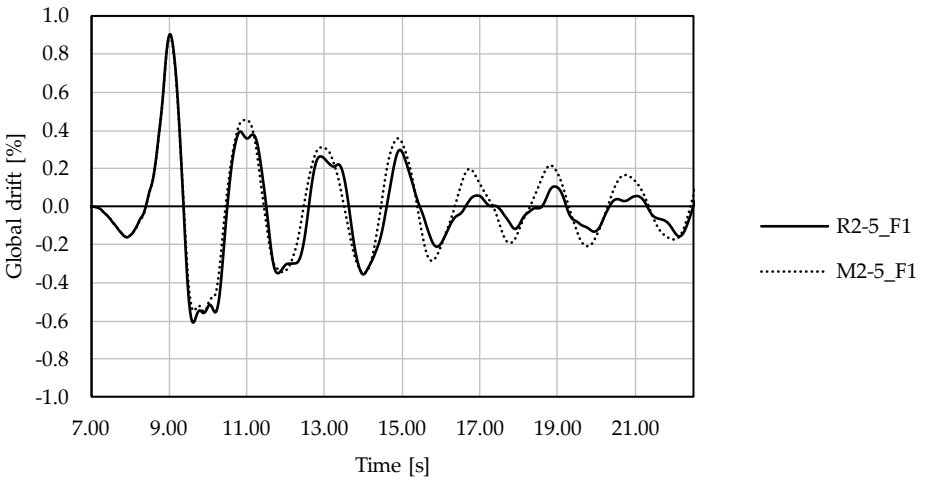

b)

Figure 3.54: Comparison of the base shear a) and global drift b) time history plots for a scale factor applied to the ground motion equal to 1.0, "F1", for the Rayleigh damping model with 2% and 5% critical damping assigned to the first and third modes (R2-5), respectively, and modal damping with 2% and 5% assigned to the first and all the other modes (M2-5), respectively.

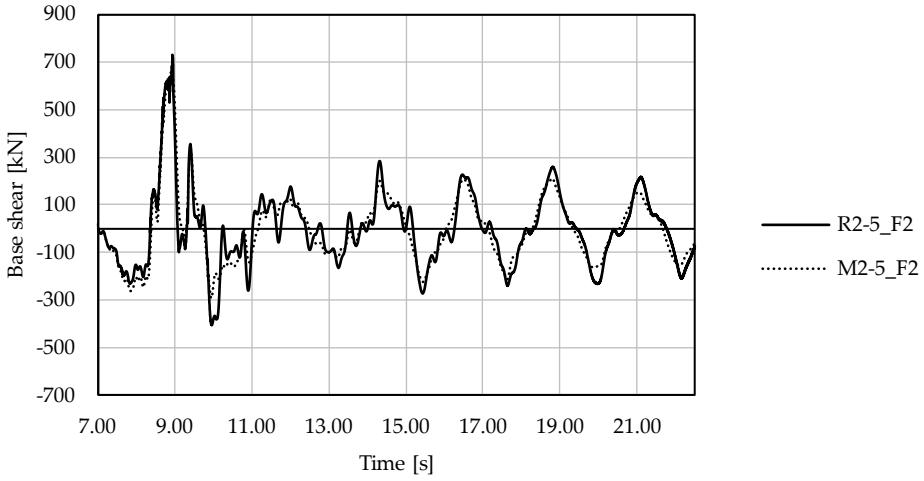

a)

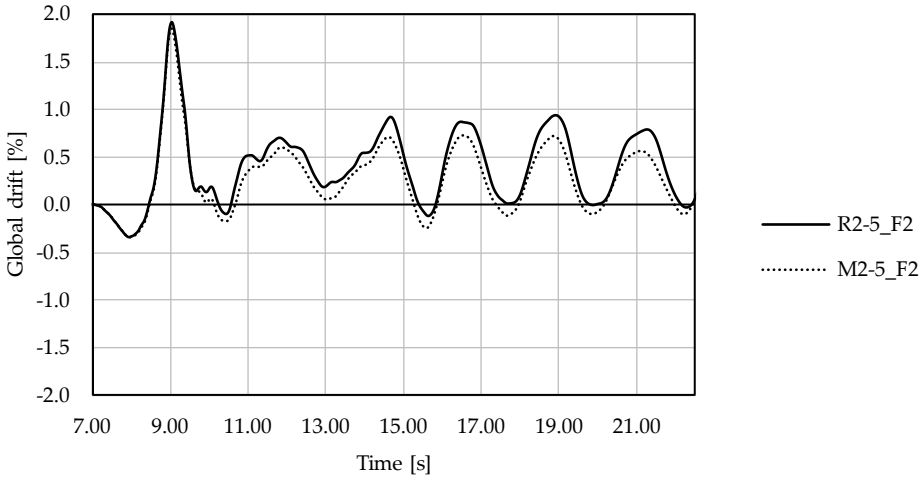

b)

Figure 3.55: Comparison of the base shear a) and global drift b) time history plots for a scale factor applied to the ground motion equal to 2.0, "F2", for the Rayleigh damping model with 2% and 5% critical damping assigned to the first and third modes (R2-5), respectively, and modal damping with 2% and 5% assigned to the first and all the other modes (M2-5), respectively.

3.3.8 *Modelling of ductile infills*

Ductile infills are modelled in nonlinear analyses through the simplified macromodel approach proposed in Bolis et al. (2017) [60] and Preti et al. (2019) [33] and briefly reported in §3.1.2. Each infill is represented by a couple of concentric equivalent struts calibrated (Figure 3.58) to reproduce the global lateral strength versus interstorey drift response.
In this work, the use of OpenSees software [52] allows for some modifications to the cyclic calibration with respect to the proposal of previous studies, based on phenomenological considerations.
Each strut works only in compression, and to reproduce the different cyclic behaviour of the mechanisms, three overlapped "twoNodeLink" elements [52] represent:

- The constant friction contribution given by the self-weight of the infill (Figure 3.59, left) by means of rigid-plastic behaviour characterised by rigid reloading at the displacement inversion. In the deformed state of the infill, at the inversion of the displacement, the strut that was previously compressed loses all of its load, and the strut that was previously in tension (unloaded) rigidly loads to provide the initial friction force needed to trigger the sliding. The reload occurs at each displacement inversion.
- The hardening friction contribution induced in each subpanel by the internal strut mechanism (Figure 3.59, central). A bilinear backbone with a slope change at 1% drift and a secant reloading from zero displacement represents the increasing contribution of the friction force.
- The strut contribution (Figure 3.59, right). A bilinear backbone is characterised by a slope change at 1% drift and slip reloading to account for the local crushing of the masonry at the corners.

The constant friction contribution is directly evaluated by the analytical model. The slope change points of the bilinear backbone curves are evaluated by considering the strength contributions derived by the analytical model at a drift level equal to 1%. The ultimate point of the bilinear shape is evaluated at a drift equal to 3%. The rigid unloading is simulated by defining a fictitious initial rigid branch. The analyses of frames described in this second part of the work refer to the infill typology described in Preti et al. (2015) [15] and its analytical representation described in Preti et al. (2019) [33]. Figure 3.56 represents the comparison of the monotonic analytic force-drift curve (applied to the 200mm thickness infill of the frame "DCH" that will be described in the following sections) and the envelope of the linearized curve assumed in the numerical model.
"Hysteretic" uniaxial material [52] is used to represent the two friction contributions, while "ElasticPPGap" [52] is used to represent the strut mechanism. Reloading of the

hardening friction contribution at zero displacement is obtained by setting to 0.5 the strain pinching factor ("pinchx"), a simplified assumption accepted by post-analysis checks.

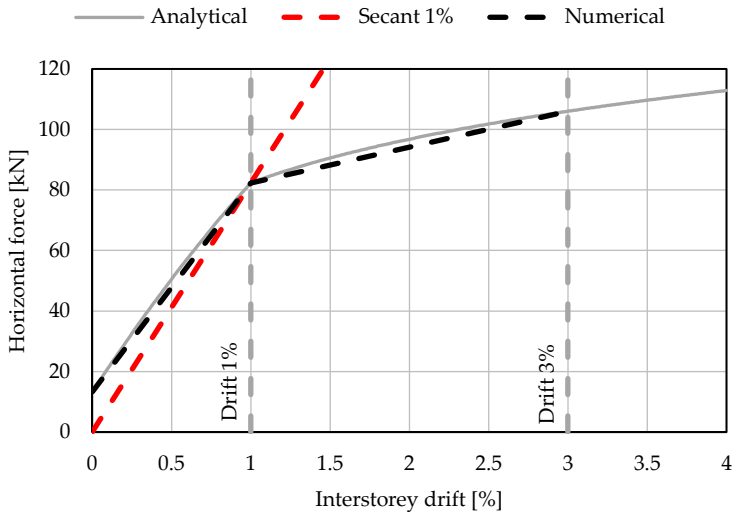

Figure 3.56: Representation of the horizontal force vs. interstorey drift analytical curve (grey line), the envelope of the linearized curve assumed in the numerical model (black line), and the secant one to 1% drift adopted in the elastic analyses (red line).

The applicability of the proposed modelling choices for the infill is validated by comparison of the model results with the test results on an infilled steel frame [15] considered in the reference study of Preti et al. (2019) [33] to calibrate the proposal. The steel frame of the experimental test is realised by means of commercial steel profiles. The connection of the columns to the top beam consisted of plastic hinges made of thin steel plates. Initially, the calibration of the behaviour of the bare frame is required; columns and beams are simulated by means of elastic elements characterised by the properties of the profiles. Plastic hinges are simulated by a zero-length fibre section characterised by the cross section of the plate; steel material is represented by a "Steel02" uniaxial material [52] with a reduced elastic stiffness to account for the degradation of the plastic hinges due to their previous use. The comparison of the experimental result and its numerical representation is represented in Figure 3.57.

Once the bare frame response is calibrated, the complete infilled frame is simulated. A near-concentric model is considered: a couple of three "twoNodeLink" elements connect the base of a column to the top of the other one. To better represent the experimental test, the upper connection is below the plastic hinge, in correspondence

with the lower interface of the beam. The schematic representation of the numerical model is reported in Figure 3.58, while the cyclic behaviour of each nonlinear spring that models the infill is represented in Figure 3.59. The numerical result is compared to the experimental one in Figure 3.60.

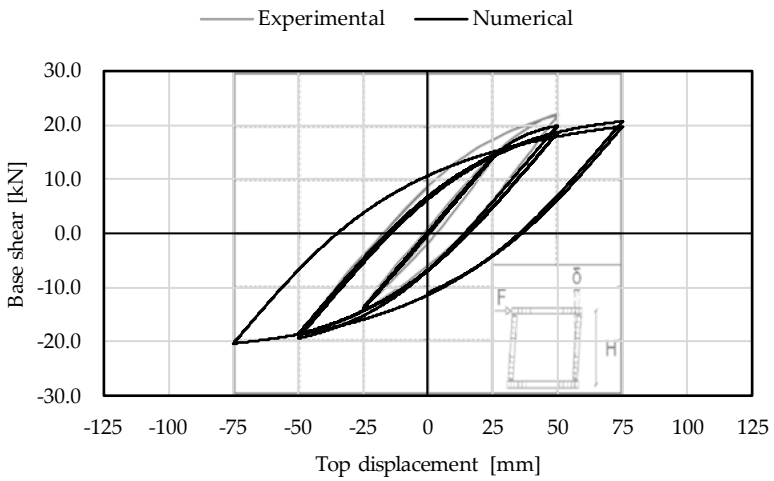

Figure 3.57: Numerical simulation of the steel bare frame tested in Preti et al. (2015) [15].

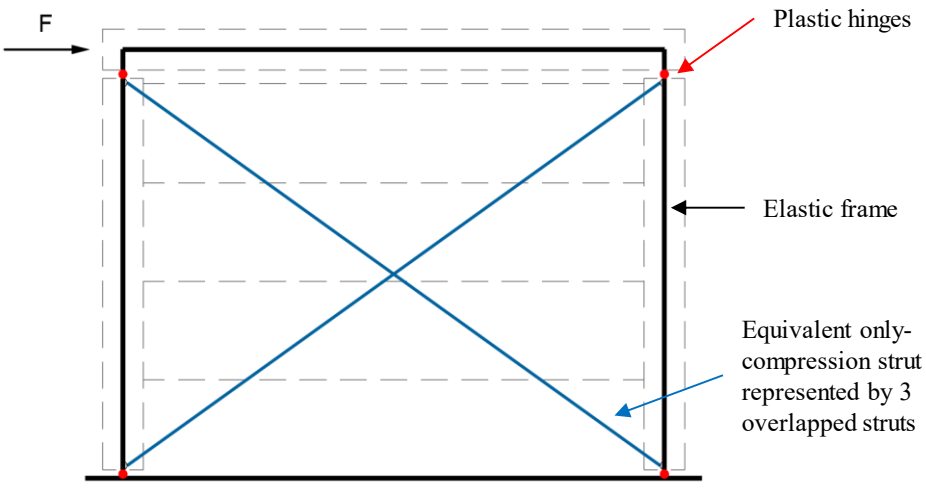

Figure 3.58: Schematic representation of the numerical model.

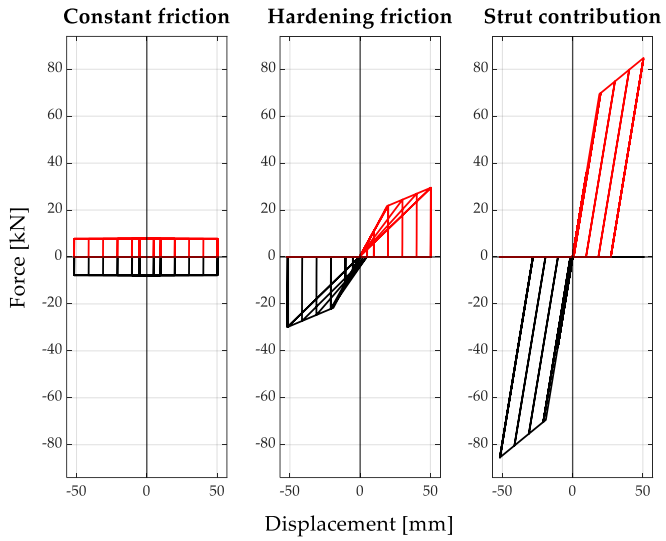

Figure 3.59: Hysteresis of the three overlapped struts representing the three contributions. The black and red lines correspond to the two cross struts.

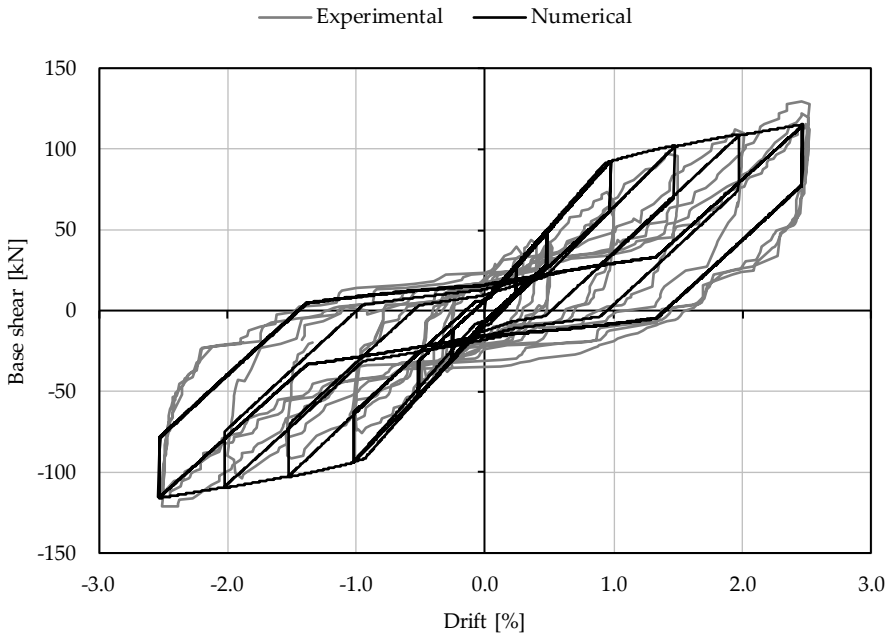

Figure 3.60: Numerical simulation of the infilled frame tested in Preti et al. (2015) [15].

In the following, the concentric strut model of the infill is adopted, postponing the evaluation of the infill thrust on the column to a posteriori analysis. This choice avoids concentrated forces on the columns that could lead to altered internal action distributions and localised, fictitious plasticization. In fact, a single strut represents all the lateral strength of the infill, exerting a single force on the columns instead of a set of forces distributed over them. Furthermore, uncontrolled interaction of the deformation between the struts and the columns is avoided. These aspects require further investigation.

One of the goals of the work is to propose a methodology to represent ductile infills in elastic models, as in response spectrum analysis, to represent the displacement and deformation demands due to the seismic action. In this context, the use of bidiagonal elastic trusses characterised by a secant stiffness at 1% drift of the infill backbone curve is suggested. The representation of the adopted stiffness is represented in Figure 3.56 (red line), where the line secant to 1% drift is compared to the calibration curve derived by the analytical model (calculated for the 200mm thickness infill of the frame "DCH").

Given that elastic models consider the stiffness of the diagonals both in compression and in tension, the single strut stiffness needs to be halved for both diagonals to match the response of the single reacting diagonal in the compression-only non-linear modelling.

The proposed representation is not able to represent the internal actions due to the seismic demands; the strut that works in tension influences the frame internal actions. Consequently, this approach is not feasible for the design phase.

In the following sections, the proposed approach is tested by comparison to the results of nonlinear static and dynamic analyses.

3.4 *Case study*

3.4.1 *Reference structures*

The case study is a residential building in the Municipality of Cosenza (CS), located in an Italian high-seismicity region. The structure is a tridimensional RC frame characterised by five spans in the main direction, three in the transversal one, and five floors (Figure 3.61), designed according to Italian [58] code. Soil type "C" and topography category "T1" are considered. The main materials are C35/45 concrete and B450C steel.

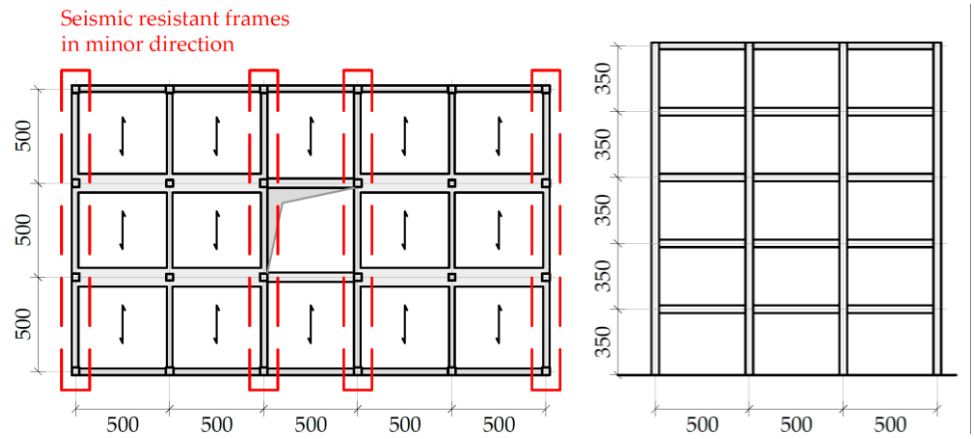

a) *b)*

Figure 3.61: Representation of the RC structure in plan a) and elevation b), with focus on the considered external frame in the minor direction (lengths are expressed in cm).

The design gravity loads are reported in Table 3.2. The infills are located on the perimeter and on the two inner frames near the central hole, parallel to the short length of the building. The case study frame analysed is one of the two external planar frames oriented along the short length. In this direction, only the four frames stiffened by the infills are considered primary elements. The remaining columns are considered secondary elements and are designed for gravity loads only.
The design for seismic resistance is performed by response spectrum analysis (RSA). The elastic spectra of the construction site are represented in Figure 3.62.
Linear analyses and structural design are made using the commercial software MidasGen 2024 [74].

Floor type	G_1 [kN/m²]	G_2 [kN/m²]	Q [kN/m²]
Floors	3.55	3.60	2.00
Roof	3.55	3.30	0.50
Linear loads			
Infills load	7.56 [kN/m]		

Table 3.2: Loads on the structure.

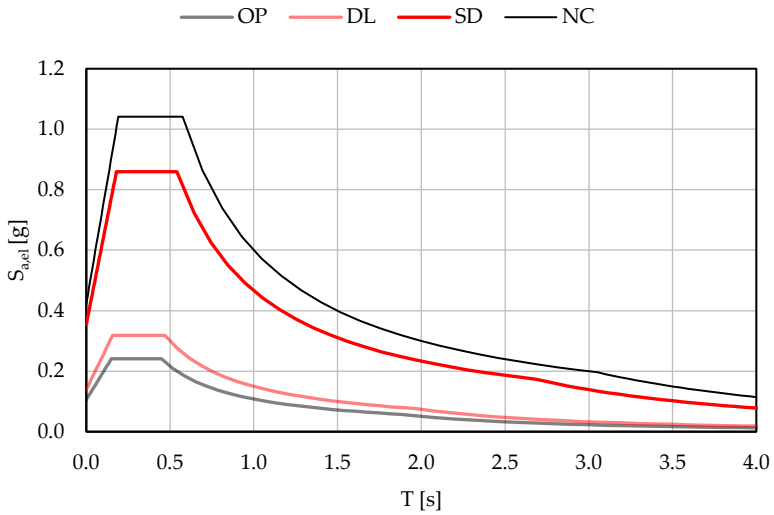

Figure 3.62: Elastic spectra in the horizontal direction used for the design of the building.

The bidimensional design of the frame makes use of the indication of the Italian code at §7.4.4.2.1 [58]. The flexural checks can be conducted in a simplified way by considering that, for each main direction of the seismic action, the uniaxial strength of the columns is reduced to 70%. Capacity design and hierarchy of strengths principles are guaranteed. The cracked stiffness of the members is considered by applying a uniform stiffness reduction factor equal to 0.5 to both columns and beams, which is equal to the lower coefficient allowable by the Italian Code (§7.2.6 [58]). The low axial stress acting on the columns justifies the use of this value. At the serviceability limit states, the interstorey drift limits indicated by the code for ductile infills are considered: δ_{DLLS}=1.0% and δ_{OPLS}=2/3 δ_{DLLS}.
Three ductility levels are followed in the design of the frame to obtain three prototype frames with different flexibility. The design is made according to both "high" (DCH) and "medium" (DCM) ductility classes, adopting a behaviour factor equal to 4.9 for DCH and 3.9 and 2.7 for DCM. The behaviour factor in the DCH class design is reduced with respect to the maximum allowable, equal to 5.85, because at the fundamental period of the structure, the resulting spectrum is characterised by ordinates lower than the minimum spectral acceleration equal to 0,2 a_g indicated by the Italian code at §3.2.3.5 [58] and the European one at §3.2.2.5 [75]. The third frame

is designed according to DCM for a behaviour factor equal to 2.7 to limit the plasticization at the serviceability limit states, which is possible if a high behaviour factor is assumed. The design behaviour factors of each frame are reported in Table 3.3. The details of the main sections of frame "DCH" are represented in Figure 3.63 and Table 3.4, while the details of the other two frames are reported in §B.1.1 and §B.1.2.

Table 3.5 shows the fundamental period that characterises the frames by considering uncracked and cracked sections. As expected, the period increases as the design ductility level increases. The effective cracked stiffness of beams (that are subjected to low axial stress levels) is lower than half of the full one, as suggested by the code. When discussing the seismic demand on the frames, for a reliable comparison of the results to those of nonlinear analyses, a reduction factor equal to 0.3 is assumed in the RSA analyses that will be discussed in the following. In the same table, the corresponding fundamental periods are reported.

Frame code	**Ductility class**	q_0	α_u/α_1	**q**
DCH	DCH	4.5	1.3	5.85→4.9
DCM	DCM	3.0	1.3	3.90
DCM_2	DCM	N.D.	N.D.	2.70

Table 3.3: Frame structures designed, ductility class [58], and corresponding behaviour factors assumed.

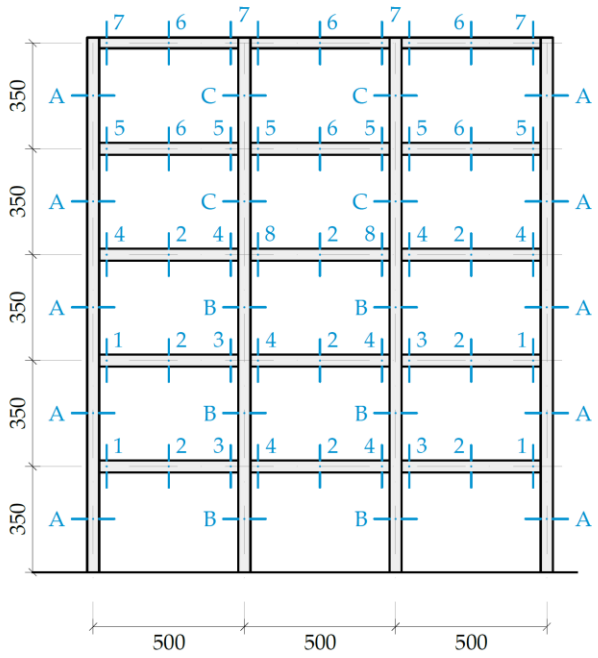

Figure 3.63: Indication of the main sections of beams and columns of frame "DCH".

Beams reinforcement					
Sect.	**B [mm]**	**H [mm]**	**Reinf. Upper**	**Reinf. Low**	**Stirrups**
1	350	400	3ϕ16+2ϕ20	4ϕ16	ϕ10/8
2	350	400	3ϕ16	3ϕ16	ϕ10/24
3	350	400	5ϕ16	4ϕ16	ϕ10/8
4	350	400	5ϕ16	3ϕ16	ϕ10/8
5	350	350	4ϕ16	3ϕ16	ϕ10/7
6	350	350	3ϕ16	3ϕ16	ϕ10/24
7	350	350	3ϕ16	3ϕ16	ϕ10/7
8	350	400	4ϕ16	3ϕ16	ϕ10/8
Columns reinforcement					
Sect.	**B [mm]**	**H [mm]**	**Reinf. Vertex**	**Reinf. Sides**	**Stirrups Conf. / Inner**
A	400	400	4ϕ16	8ϕ16	4ϕ10/10 / 4ϕ10/15
B	400	400	4ϕ20	8ϕ16	4ϕ10/10 / 4ϕ10/15
C	400	400	4ϕ16	8ϕ16	4ϕ10/10 / 4ϕ10/15

Table 3.4: Reinforcement details of frame "DCH".

Structure	T_1 Uncracked	T_1 Design	T_1 Comparisons
DCH	1.27s	1.79s	2.09s
DCM	1.03s	1.46s	1.70s
DCM_2	0.79s	1.11s	1.29s

Table 3.5: Fundamental periods of the frames in the three configurations: full stiffness ("Uncracked"), cracked section assumed in the design ("Design"), and cracked section assumed for the comparison to the other analysis types ("Comparison").

Frames will be investigated in four configurations: bare and infilled, with three different thicknesses of infill. Since the only test of the ductile infills under consideration where the net contribution of the infill is directly available is the one described in Preti et al. (2015) [15], the original form of the analytical model (briefly discussed in §2.1.2 and §3.1.2) is considered. The mechanical properties and characteristics assumed in the models are reported in Table 3.6. The difference between the three typologies is only the infill thickness and the effective contact thickness.

Parameter	Description	Value
t_{jt}	Top joint thickness	50 mm
t	Infill thickness	(200-250-300) mm
t_{eff}	Effective contact thickness	(128-178-228) mm
N_i	Number of infill subpanels	4
σ_c	Contact material strength	2.2 MPa
γ	Infill specific weight	14 kN/m^3
μ_c	Sliding joints friction coefficient	0.50
μ_j	Lateral joints friction coefficient	0.42

Table 3.6: Mechanical properties and characteristics of the infills used in the analyses.

3.4.2 *Ground motions selection*

Nonlinear dynamic analyses require a rational selection of the input ground motions. The Italian code imposes spectrum-compatible conditions based on the deviation of the mean spectrum of the selected ground motions with respect to the design spectrum of the specific construction site. A tolerance on the matching of the ordinates of the spectrum equal to +30% and -10% is imposed on a range of periods of interest for the dynamic properties of the structure.
Seven natural ground motions for the four design limit states are selected through the RexelWeb online service [76]. The target design spectra of the case study refer to the specific site characteristics: Cosenza city (Lat. 39.293°, Long. 16.256°), "C" soil type, and "T1" topography category. The spectrum matching is assumed on a range of periods equal to 0.15-2.5s, which includes the fundamental periods derived by the eigenvalue analysis and the equivalent periods derived by the pushover analyses, up to the 3rd mode of vibration for the structures considered. The tolerance for the matching of the ordinates is restricted to ±10%. The identification data of the selected ground motions at the severe damage limit state (SDLS) are reported in Table 3.7, while their representation is visible in Figure 3.64. The corresponding pseudo-acceleration spectra, their mean spectrum, the design spectrum, and the period and tolerance considered in the accelerogram selection are represented in Figure 3.65. The same data for the operational, damage, and collapse limit states are reported in §B.1.3.

Code	Recorder ID	ID ITACA	Scale factor
SD1	IT.NOR.00.HG.EMSC-20161026_0000077	EMSC-20161026_0000077	E: 2.210
SD2	IT.MTR.00.HG.EMSC-20160824_0000006	EMSC-20160824_0000006	E: 4.395
SD3	IT.SAN0.00.HN.IT-2012-0011	IT-2012-0011	N: 1.605
SD4	IT.MRN.00.HN.IT-2012-0008	IT-2012-0008	E: 1.352
SD5	IT.SAN0.00.HN.IT-2012-0011	IT-2012-0011	E: 2.035
SD6	IT.NOR.00.HG.EMSC-20161026_0000095	EMSC-20161026_0000095	N: 2.939
SD7	IV.T0819..HN.IT-2012-0010	IT-2012-0010	E: 1.374

Table 3.7: Ground motions selected for the SD limit state.

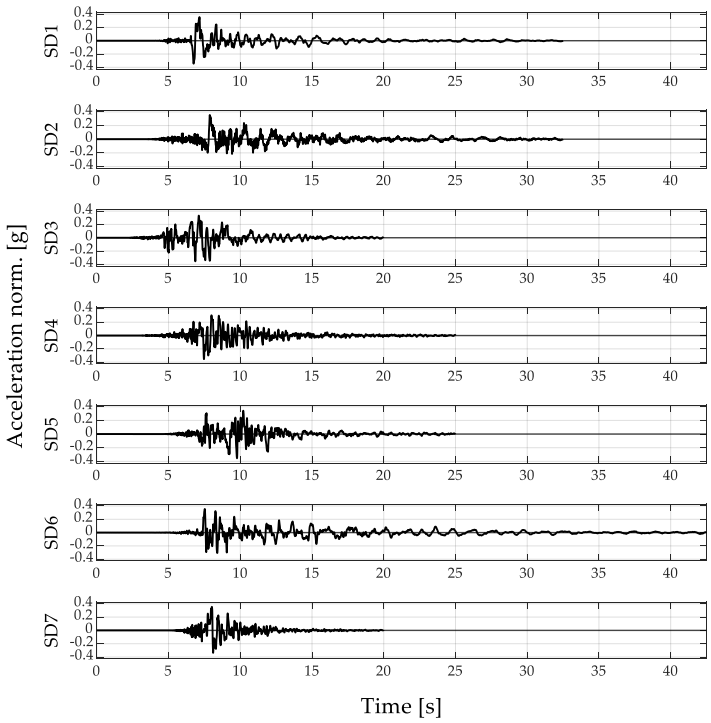

Figure 3.64: Time history of the ground motions considered at the SD limit state.

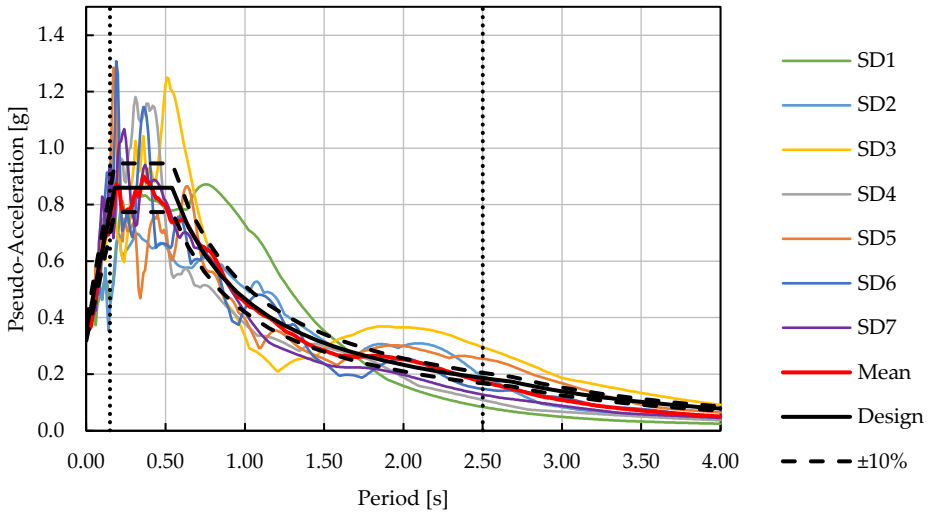

Figure 3.65: Pseudo acceleration spectra of the ground motions at SD limit state, average spectrum, design spectrum, and period and ordinates limit for the spectrum-compatibility evaluation.

3.4.3 *Limit state identification*

The Near Collapse Limit State (NCLS) is identified at a global and local level as follows:

- Local level:
  - Ultimate curvature. Since fibre-section elements are adopted in the model, material hystereses are directly monitored instead of chord rotation limits. The ultimate sectional rotation is defined as the reaching of the ultimate compressive strain of the confined concrete or a tensile strain of the steel rebars equal to 4.00%, according to Italian code [58].
  - Ultimate shear-compressive strength of the columns. In the presence of infills, the shear action increases due to the infill thrust, and it is evaluated in the post-processing phase. Tensile-shear strength is not considered a NCLS since the shear contribution due to the infill thrust is not considered in the design phase and the transversal reinforcement can be specifically increased. More details can be found in the following §3.5.5, where the shear safety checks are conducted for the pushover analyses at SDLS capacities.
- Global level:
  - Global strength reduction equal to 15%, only for static nonlinear analysis.
  - 4.0% interstorey drift. This limit is not provided by the code, but it is indicated by NIST GCR 17-917-46v3 guidelines [55]. Furthermore, it is imposed to prevent ductile infills from crushing and overturning. The available tests did not explore such a drift limit, but the absence of significant damage at 3% drift (Figure 1.10 and Figure 1.14) suggests a larger limit for collapse, arbitrarily chosen to be equal to 4%.

Regarding the Significant Damage (SDLS) or Life Safety Limit State, following the indication provided by the code to identify the chord rotation limit at SDLS as ¾ the one at the ultimate condition, it is identified at the reaching of ¾ times of the strain limits set for steel and concrete at the NCLS. Regarding the infills, 2.5% of interstorey drift is assumed to be the reaching of SDLS. In fact, as shown in Figure 1.10 and Figure 1.14, experimental tests reached this drift level without significant damage. Particularly, the infill solution described in Preti et al. (2015) [15] after the in-plane test at 2.5% drift was subjected to an out-of-plane test without collapse. After that,

the in-plane test was continued until a drift level of 3.0% was reached without collapse. While the infill described in Morandi et al. (2018) [14], after the in-plane test up to a 3.0% drift level, did not experience severe damage in the out-of-plane dynamic test [27].

During the design phase, interstorey drift limits equal to 0.67% and 1.00% were assumed for Fully Operational (OPLS) and Damage Limitation (DLLS) limit states, respectively. Based on experimental evidence [14], [15], in this work, the limits of 0.50% and 1.25% are assumed at OPLS and DLLS, respectively.

3.4.4 *Modelling approach in linear analysis and geometric nonlinearities*

The more diffuse seismic analysis used in the design of structures is the response spectrum analysis (RSA); firstly, the dynamic behaviour of the structure in the elastic field is investigated through the eigenvalue analysis, then the seismic actions are evaluated by referring to the design spectrum and combining the response to each mode of vibration. In elastic models, nonlinearities due to cracking and plasticization are accounted for by reducing the elastic stiffness of the members. According to the literature, the stiffness reduction factors applied to beams and columns depend on the axial stress level and the ductility requested.
The structures here considered are characterised by a low axial stress level; consequently, in the design of the frames, the lower code admissible stiffness reduction factor equal to 0.5 is used for all the members. Since this work aims to compare the deformation demand resulting from RSA to those of more advanced nonlinear analyses based on fibre-section beam elements, some precautions are required to represent the reduced stiffness of the members due to cracking, which latter are explicitly modelled in the non-linear analysis; if there is a very low level of axial load stress on the elements, such as beams, the stiffness of the cracked section is lower than half of the stiffness of the uncracked one. For the comparisons, in the RSA, the seismic demands are evaluated on an auxiliar elastic model where the stiffness of the beams is reduced by a factor equal to 0.3.
When high ductility levels are adopted in the design of the structure, as for the "DCH" frame in this work, the column slenderness may increase, and second-order effects may become important in the estimation of the seismic effects. Their relevance can be assessed as required by the Italian code (§7.3.1) by evaluating, at each interstorey, the ϑ-factor as described in Eq. (3.4-1):

$$\vartheta = \frac{P \cdot d_{Er}}{V \cdot h} \qquad (3.4\text{-}1)$$

Where P and V are, respectively, the global vertical load and the horizontal interstorey design shear action, d_{Er} is the mean interstorey displacement at SDLS, and h is the interstorey height.
According to the code, geometric non-linearities can be neglected if ϑ is lower than 0.1; they can be accounted for by amplifying the seismic effects by the factor $1/(1-\vartheta)$ when ϑ is comprised in the range 0.1-0.2; nonlinear analyses are required if it falls within the range 0.2-0.3; and values higher than 0.3 are not allowed.
In this study, the ϑ-factor is evaluated for all three frames designed in both the bare and infilled configurations and for all four limit states on the auxiliar models characterised by the reduced elastic stiffness of the beams. Since the fundamental period of the structure is higher than the T_C, the equal displacement principle applies

($\mu_\Delta = q$), and interstorey drifts can be directly evaluated considering the elastic spectra. The modification in the stiffness of the beams and the exploration of different limit states with respect to the design complicate the evaluation of the design interstorey shear; the design behaviour factor may not be representative of the response, and an effective one is required. To overcome the problem, the effective behaviour factor is evaluated, as in Eq. (3.4-2), by the ratio between the elastic base shear of the auxiliar model, $V_{b,el}$, and the design base shear, $V_{b,design}$.

$$q_{eff} = \frac{V_{b,el}}{V_{b,design}} \tag{3.4-2}$$

Consequently, the interstorey shears, $V_{s,i}$, are evaluated from the elastic spectra, and then they are uniformly scaled by the specific effective behaviour factor of the considered limit state as described by Eq. (3.4-3).

$$V_{s,i,d} = \frac{V_{s,i,d}}{q_{eff}} \tag{3.4-3}$$

If the elastic base shear is lower than the design one, such as at the serviceability limit states, the elastic interstorey shears are directly considered.
In the infilled configurations, the effective behaviour factor prediction is non-trivial; in fact, both the elastic seismic action and the base shear resistance increase due to the stiffening and strengthening effect of the infills. Arbitrarily assuming the infill yielding at 1% drift, the design strength of the infilled RC frame is here quantified as the sum of the structure design strength, $V_{b,design}$, plus the contribution of the ground-storey infills strength evaluated at 1% drift, $\Sigma R_{infills,1\%}$. The effective behaviour factor is evaluated by Eq. (3.4-4).

$$q_{eff} = \frac{V_{b,el}}{V_{b,design} + \sum R_{infills,1\%}} \tag{3.4-4}$$

Equation (3.4-4) is here applied for the evaluation of ϑ when the interstorey drift at the first level is larger than 1% drift. For stiffer frames or for lower seismic action, the P-Δ effect is negligible.
ϑ-factor is evaluated at each interstorey, and Figure 3.66 represents the higher values calculated for each case analysed. ϑ shows a uniform reduction from the NCLS to the SDLS. At the SLSs, the value estimated for the bare frames is lower than 0.10. For the same frame, it strongly reduces as the infills are introduced, and a little variation is visible as the infill thickness increases. As the frame becomes stiffer, reducing the design behaviour factor, the ϑ-factor shows significant variation just for the bare frame; it progressively increases with the design behaviour factor, resulting in a

value lower than 0.1 for q=2.7, in between 0.1 and 0.2 for q=3.9, and larger than 0.2 for q=4.9. All the infilled configurations fall into the range lower than 0.1 at the ULSs. The same trend is exhibited at the NCLS and SDLS. In light of the results presented, the bare frame "DCH" (q=4.9) requires nonlinear analysis; for the bare frame "DCM" (q=3.9) the simplified approach is admissible, while for the bare frame "DCM_2" (q=2.7) geometric nonlinearity can be neglected. Infilled frames do not require specific considerations.

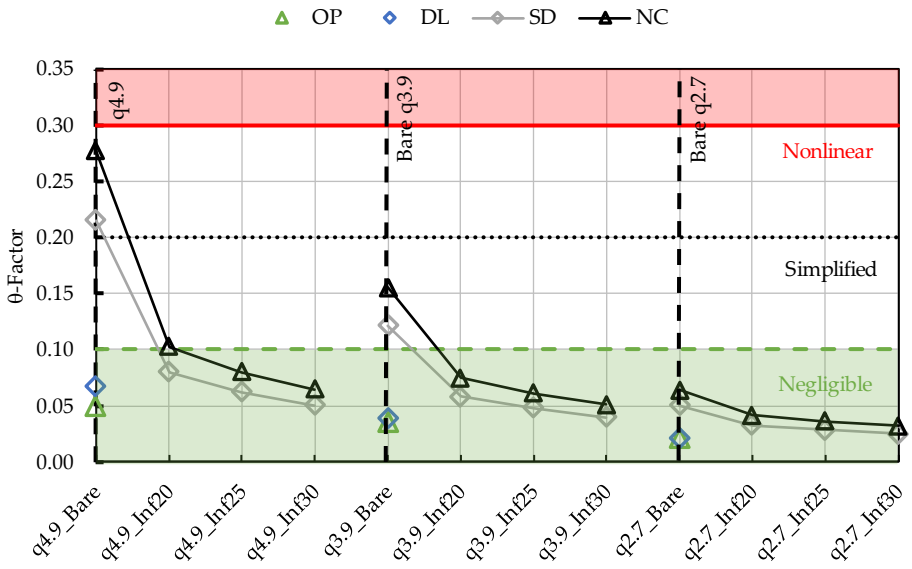

Figure 3.66: ϑ-factor evaluation for bare frames and infilled frames at different limit states.

In the simplified approach, P-Δ effects can be accounted for by amplifying the seismic action effects at each interstorey, considering the specific ϑ factor. A safe-side approach that allows for maintaining equilibrium is to amplify the effects by considering the maximum ϑ factor between all the interstories. This approach does not anyhow consider the period lengthening.
When specific nonlinear analyses are required, the elastic stiffness matrix of columns must be reduced by subtracting the linearized geometric stiffness matrix that accounts for the axial load in the element. When elastic analyses using the design spectrum are used, the geometric stiffness matrix must be multiplied by the displacement ductility factor to convert the elastic displacements to the inelastic ones. More details can be found in Fardis (2009) [62]. An alternative approach admissible when diaphragms can be considered rigid was proposed in Rutenberg (1982) [77]; adjacent floors are connected by shear and torsional link elements characterised by negative stiffness. These methods reduce the elastic stiffness of the frame; consequently, the period lengthening is captured.

In this work, response spectrum analyses at the SLS do not consider the P-Δ effects, while at the ULS they are always accounted for regardless of the range in which the ϑ factor falls. In MidasGen software, geometric nonlinearities are evaluated by introducing the geometric stiffness matrix. The seismic load combination of the gravity loads is considered and amplified by the displacement ductility factor, which is considered equal to the behaviour factor since the fundamental period is higher than T_c.

Figure 3.67 represents the displacement profiles and the interstorey drift profiles evaluated in the analyses of the bare and the infilled (thickness of the infills equal to 20cm) configurations of frame "DCH", characterised by the higher values of ϑ-factor. In the graphs, only NCLS is represented. RSA without second-order effects and RSA with second-order effects (called "RSA PD") are compared. Both the interstorey drifts and the displacements are amplified, especially at the first levels where the deformation is concentrated. As expected, in the infilled configuration, the variability is negligible, validating the low value of the ϑ factor. Consequently, infills help to reduce seismic deformation and the effects of geometric nonlinearities. In the same graph, the estimation of the interstorey drift profile evaluated through the simplified approach is represented; interstorey drifts are amplified by $1/(1-\vartheta_i)$, where ϑ_i (Eq. (3.4-1)) is the factor evaluated at the specific interstorey. This approach led to higher predictions; the increment due to the second-order effect is about twice that of using the geometric stiffness matrix.

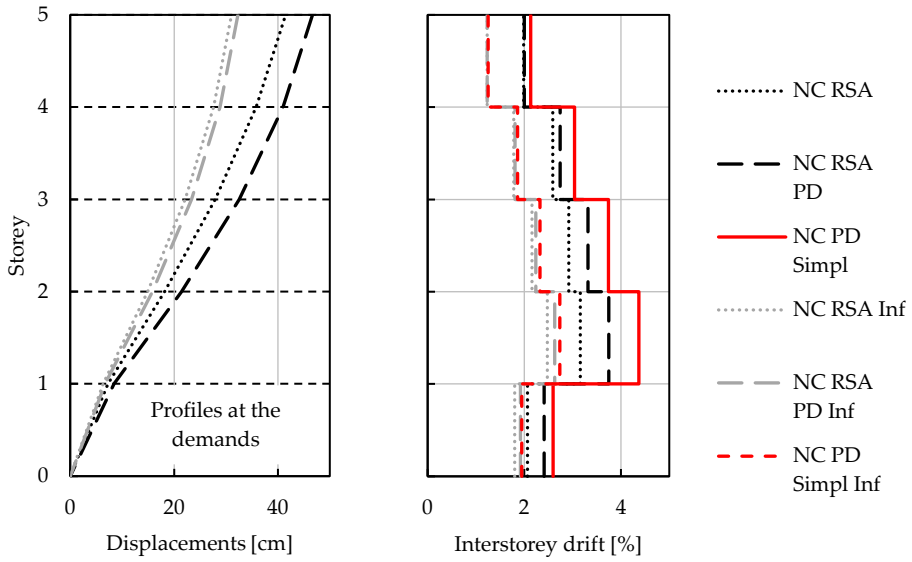

a) *b)*

Figure 3.67: Floor displacement a) and interstorey drift b) profiles at NCLS obtained by the response spectrum analysis on the elastic model by considering ("NC RSA PD") or not ("NC RSA") the geometric nonlinearities on the bare and the infilled ("Inf") configurations. Representation of the profiles obtained by the simplified approach ("Simpl").

Figure 3.68 and Figure 3.69 show the displacement and interstorey drift demands at NCLS derived from the RSA by considering or not second-order effects; the deviation is higher in the bare configuration, especially in the frame designed for the higher ductility level. In the infilled configurations, the differences are negligible.
In the comparisons presented in the following sections, geometric nonlinearities are accounted for in reducing the elastic stiffness matrix. Specific analyses are conducted for each frame configuration and for each limit state by considering the effective behaviour factor to amplify the vertical loads in the nonlinear analyses required to evaluate the stiffness matrix.

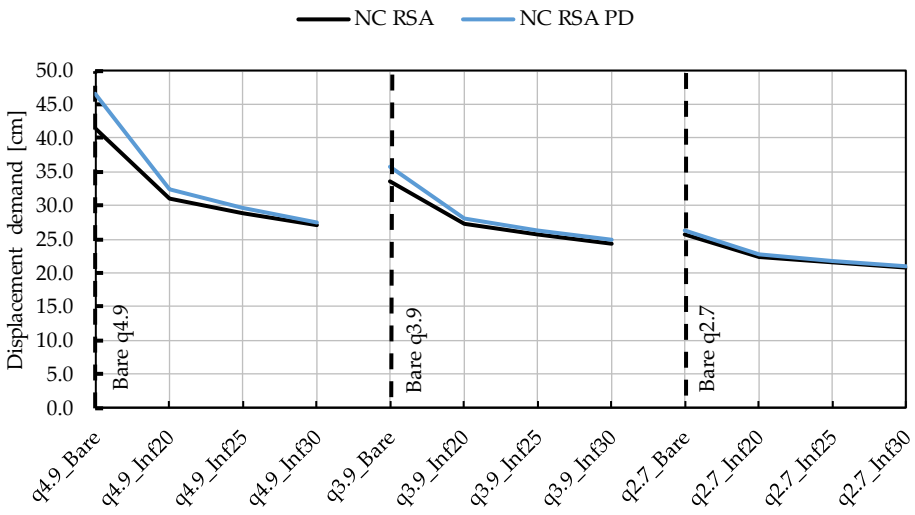

Figure 3.68: Displacement demand at NCLS by RSA with ("NC RSA PD") and without ("NC RSA") considering P-Δ effects.

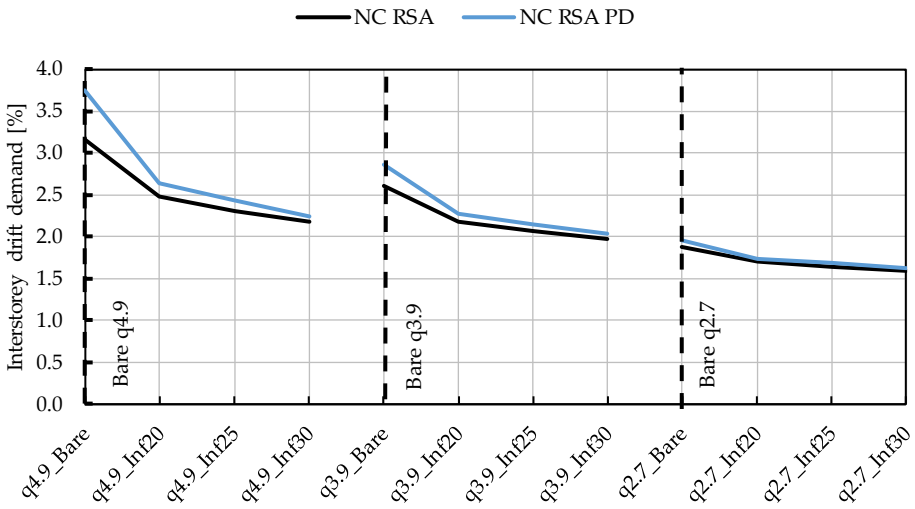

Figure 3.69: Interstorey drift demand at NCLS by RSA with ("NC RSA PD") and without ("NC RSA") considering P-Δ effects.

3.5 Numerical results

The three frames designed for different levels of ductility are modelled in linear and nonlinear fields. Linear elastic RSAs are conducted using the commercial software MidasGen [74], while nonlinear static and dynamic ones are performed using the OpenSees software [52].

In this section, a detailed description of the results obtained by different analysis types of the bare frame "DCH" and the comparison between them is presented. Then, the impact of the presence of infills in the 200mm thickness configuration is discussed.

The influence on the seismic demands of the frame flexibility and design behaviour factor and the infill thickness is studied by means of the NLTHA results.

The applicability of the N2-method [78], an approach proposed by Fajfar (2000) normally used to estimate seismic demands from PO analyses, is evaluated by comparing the predicted demands to the NLTH demands. Finally, the proposed approach to represent ductile infills in linear analyses is verified on all the analysed configurations, and the consequences of the choices taken in the design phase are discussed.

3.5.1 *Description of the results for different analysis types for the bare frame designed for DCH*

In this paragraph, a description of the results obtained in the different analyses for one case study configuration is given as an example. The following paragraphs will synthesise the results for different case studies.

3.5.1.1 Response Spectrum Analysis (RSA)

Figure 3.70 represents the profiles of the displacements and the interstorey drifts due to the seismic actions for the four limit states, while Table 3.8 reports the top displacement, the max interstorey drift, and the elastic base shear values. The higher interstorey drift always occurs at the second level because of the fixed-end restraint of the column at the base. The drift progressively decreases in the upper storeys.

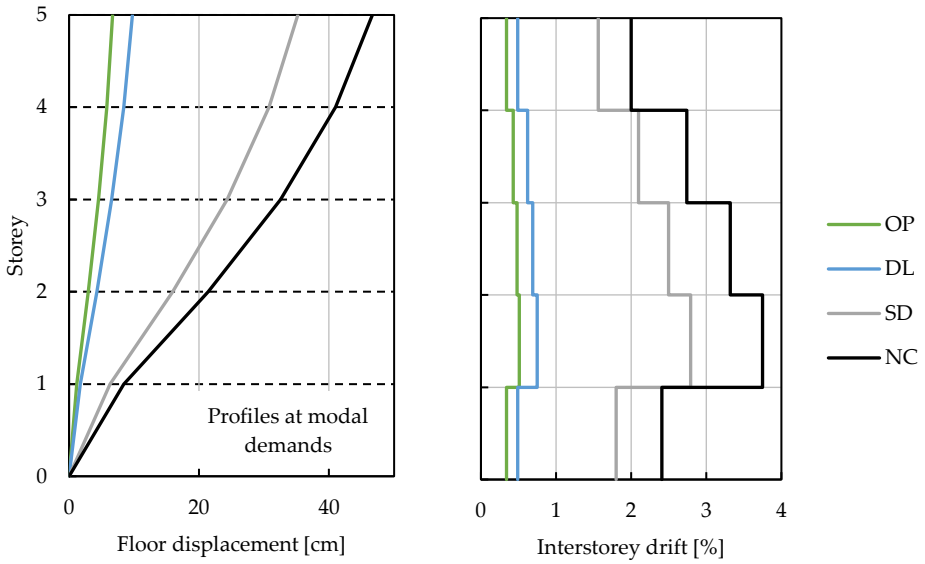

a) *b)*

Figure 3.70: Floor displacement a) and interstorey drift b) profiles obtained by the response spectrum analysis on the elastic model by applying the design elastic action referred to each limit state.

Limit state	OP	DL	SD	NC
Displacement [cm]	6.72	9.77	35.18	46.67
Max local drift [%]	0.51	0.74	2.79	3.75
Elastic base shear [kN]	211	301	971	1247

Table 3.8: Estimation of the max displacement and max interstorey drift demands at the limit states.

3.5.1.2 Push-Over analyses

The push-over analyses consider two different load distributions: a first-mode proportional distribution and a mass proportional distribution. Since no rigid diaphragm is modelled, floor forces are equally subdivided among the nodes at the intersection of beams and columns. In such a way, the complete compression or tension of all the beams of the floor due to the concentration of the applied forces on one node is avoided. Figure 3.71 represents the global hysteresis in terms of top displacement versus base shear. The curve related to the mass proportional analysis is stiffer and stronger due to the lower location in height of the lateral load resultant. The capacity of the structure (reaching the near collapse limit state, NCLS) is limited in both cases by the achievement of an interstorey drift equal to 4%, reached at the second storey. Given the higher stiffness, the displacement demand at the collapse limit state for the mass proportional distribution (mass PO) is lower than the one for a modal distribution of lateral forces (modal PO).
In Figure 3.72, the displacement demand evaluated by applying the N2-method [78] is compared to the corresponding displacement capacity for each limit state. The SDLS demand of the modal distribution is slightly higher than the corresponding capacity. Note that the drift limitation at SDLS that governs the capacity in this case is not required by the codes.
Figure 3.73 and Figure 3.74 represent the limit state reached by each infill and the structural mechanism (identification of the plasticized sections) at the reaching of the limit state capacity by the structure. The maximum interstorey drift always occurs at the second level and decreases in the upper storeys. The structural mechanism starts with the yielding of the beams at the damage limit state (DLLS), reaching the yielding of the base section of the columns at the severe damage limit state (SDLS), and ending with the yielding of some of the top sections of the columns at the near collapse limit state (NCLS). If the mass-proportional distribution is considered, the yielding is more concentrated in the lower part of the structure, and the yielding at the base of the columns is anticipated.
Figure 3.75 shows the displacement and the interstorey drift profiles that were calculated during the pushover analysis at the step where the limit state demands were reached for both push-over analyses. Profiles obtained by the two load

distributions are different; mass PO exhibits a concentration of the deformations at the first two levels.
Table 3.9 summarises the top displacement, the maximum interstorey drift, and the elastic base shear on the equivalent SDOF at the demands.

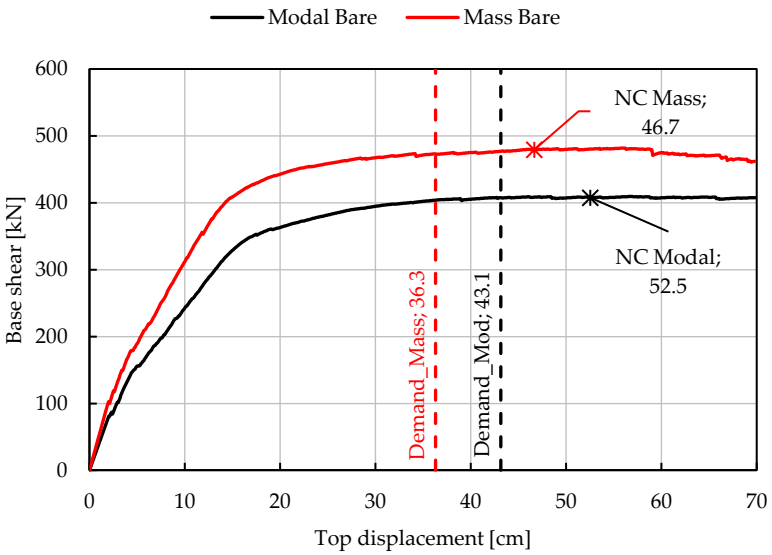

Figure 3.71: Comparison of capacity vs. demand at NC limit state for the two load distributions of the pushover analyses.

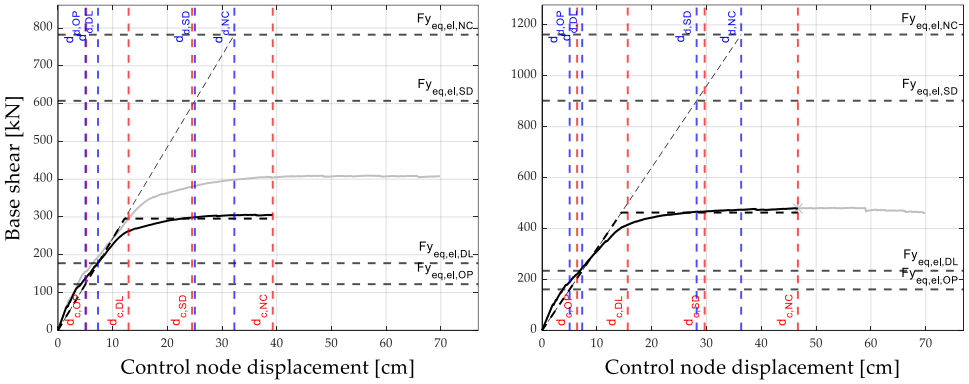

a) Modal distribution *b) Mass distribution*

Figure 3.72: Capacity curve of the MDOF system, capacity curve of the equivalent SDOF system, its bilinearization, and comparison of the estimated seismic demand by the N2-method

and the corresponding capacity at different limit states, for the modal load distribution a) and mass-proportional distribution b).

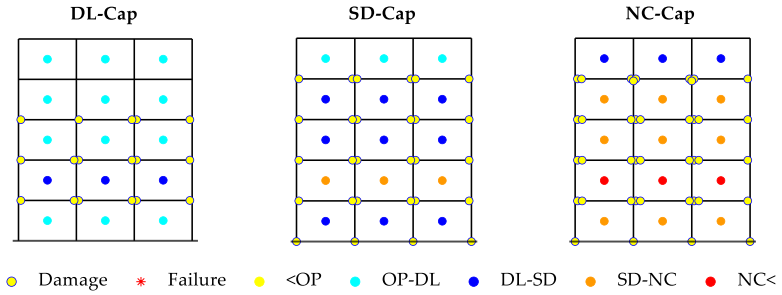

Figure 3.73: Mechanism and interstorey drift level indication at the reaching of the different limit states for the modal load distribution. For the beam, two control sections are considered: at the beam-column interface and at a depth equal to the critical length far from the previous one section.

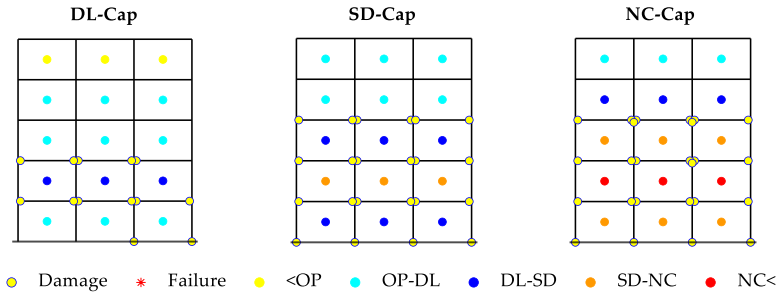

Figure 3.74: Mechanism and interstorey drift level at the reaching of the different limit states for the mass proportional load distribution.

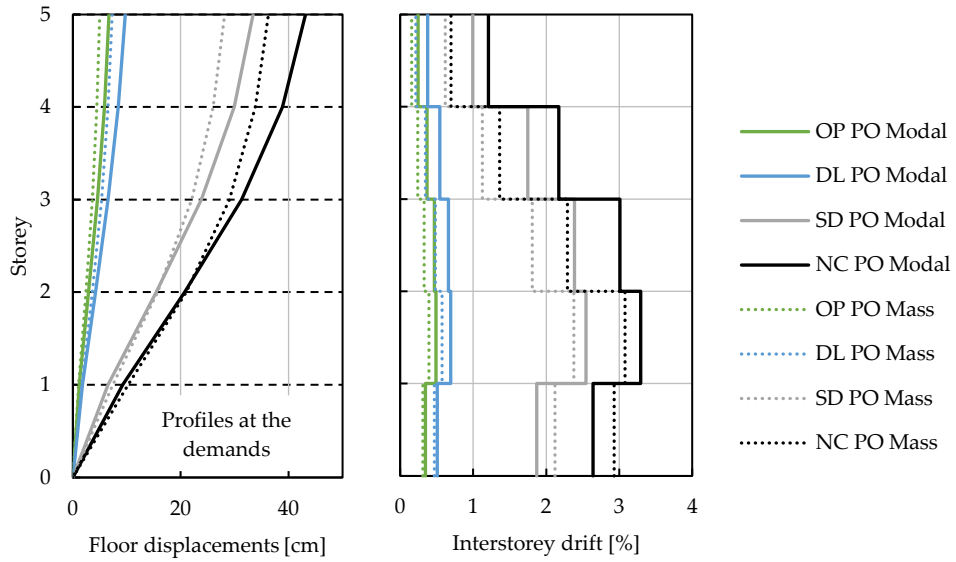

a) *b)*

Figure 3.75: Displacement a) and interstorey drift b) profiles at the demands evaluated for each limit states for the two load distributions.

Limit state	OP	DL	SD	NC
Modal - displacement [cm]	6.74	9.80	33.49	43.14
Modal - Max local drift [%]	0.49	0.69	2.55	3.29
Modal – Elastic shear demand [kN]	163.39	237.61	812.31	1046.35
Mass - displacement [cm]	5.04	7.32	28.19	36.31
Mass - Max local drift [%]	0.39	0.57	2.38	3.08
Mass – Elastic shear demand [kN]	161.22	234.45	902.33	1162.31

Table 3.9: Estimation of the max displacement and max interstorey drift demands at the limit states. The elastic shear demand on the equivalent SDOF is also reported.

3.5.1.3 Nonlinear time-history analyses

Figure 3.76 represents an example of the hysteresis of the structure subjected to SDLS input ground motion. The first plasticization of beams and columns is indicated. For each limit state, seven ground motions are considered. The main information is recorded during the analyses to monitor the structural state. The results show the reaching of the NCLS interstorey drift limit at the second level, despite the fact that SDLS ground motion is considered. This is caused by the fact that the single record selected resulted in the most severe of the seven records considered. Figure 3.77 represents the same results for another record where the interstorey drifts do not reach the SDLS limit. On the right side of the figures, the mechanisms at the end of the analysis are represented. The damage occurred at the beam ends and the column bases; only some of the top sections of the columns underwent rebar yielding or concrete cover spalling. Figure 3.78 represents the deformation profiles and the deformed shape at the main step of the analysis, such as at the reaching of the maximum displacement in the negative and positive directions and at the reaching of the maximum local interstorey drift.

For each ground motion of the considered limit state, the peak floor acceleration, floor displacement, and interstorey drift are calculated to obtain the envelope profiles. Their mean values give the envelope profiles at the demand level for each limit state. The symmetry of the structure allows for considering the absolute values between the negative and positive directions. An example is represented in Figure 3.79 and Figure 3.80, where the profiles of each input ground motion are plotted together with the mean profile that will be considered the limit state demand. The mean profiles for all the limit states investigated are represented in Figure 3.81 and Figure 3.82. The peak values are summarised in Table 3.10.

The displacement profiles (Figure 3.81a) at the two serviceability limit states and the two at the ultimate limit states are very similar. The same result is visible for the interstorey drift profile (Figure 3.81b) and the maximum floor acceleration (Figure 3.82). The peak interstorey drift occurs at the third level; it is relatively uniform in the other storeys, and the lower value is recorded at the base. The maximum floor acceleration is similar to the maximum base acceleration.

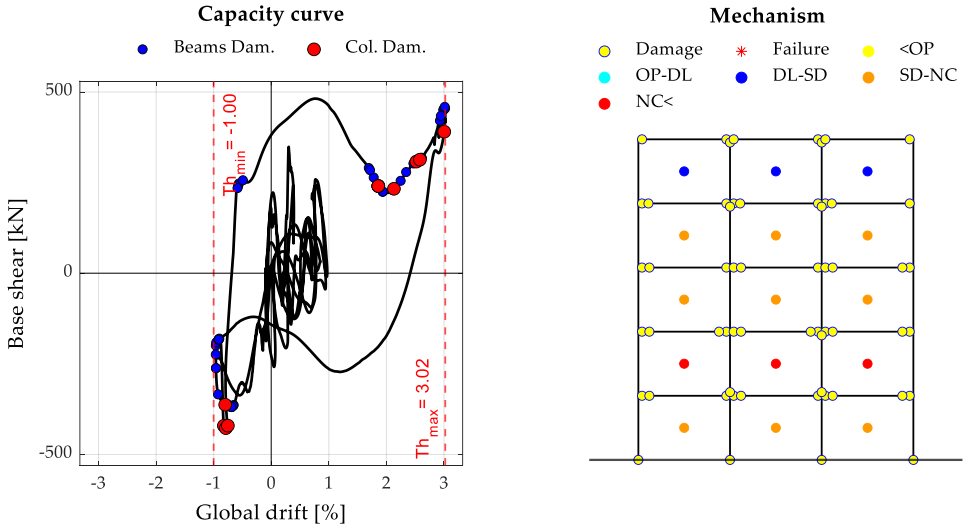

Figure 3.76: Hysteresis of the time history SD3 and corresponding mechanism at the end of the analysis. The yellow circles on the hysteresis represent the plasticization of beam sections, while the blue circles represent the columns. The yielded sections are schematically represented on the frame on the right side of the figure.

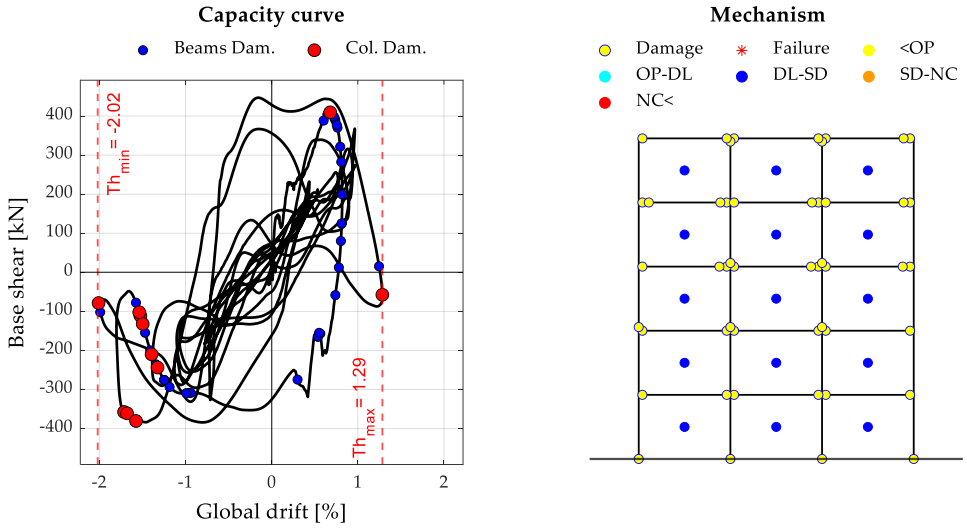

Figure 3.77: Hysteresis of the time history SD2 and corresponding mechanism at the end of the analysis.

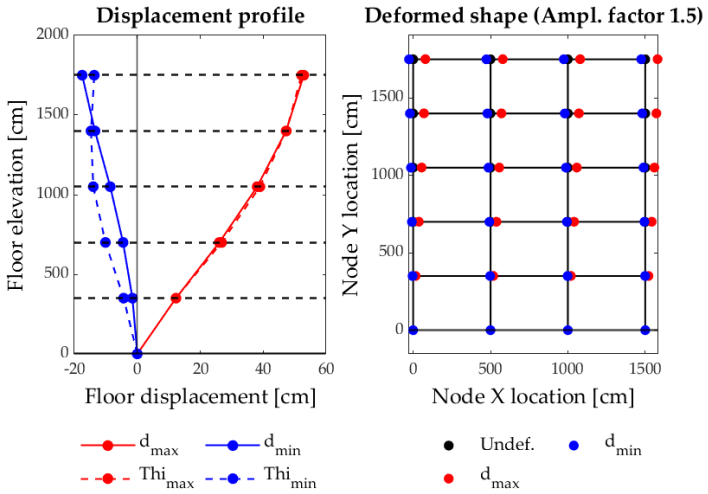

Figure 3.78: Floor displacement profiles and deformed frame at different time steps of the ground motion SD3: maximum displacement (d_{max}), minimum displacement (d_{min}), max interstorey drift (Thi_{max}), and minimum interstorey drift (Thi_{min}).

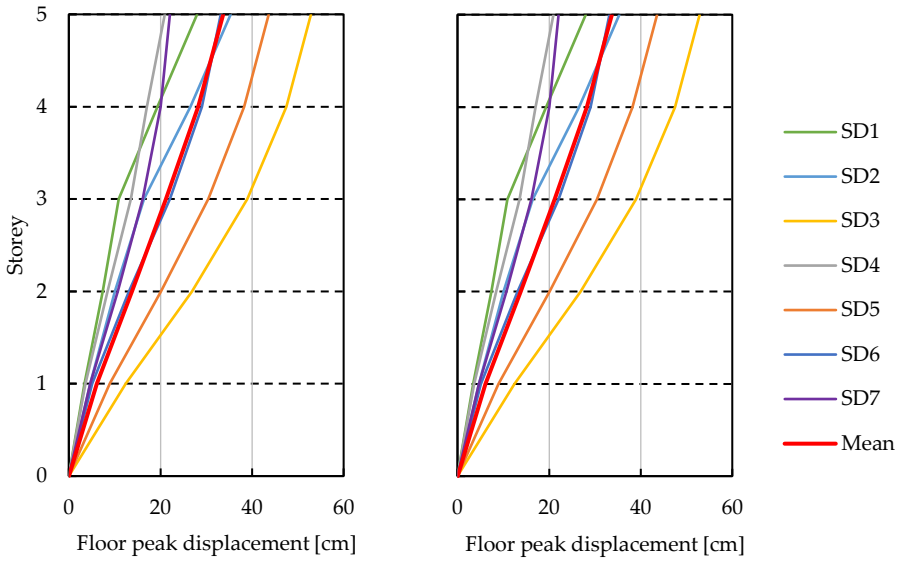

a) *b)*

Figure 3.79: Floor displacement a) and interstorey drift b) envelope profiles obtained by each design ground motion at SD limit state and corresponding mean profiles.

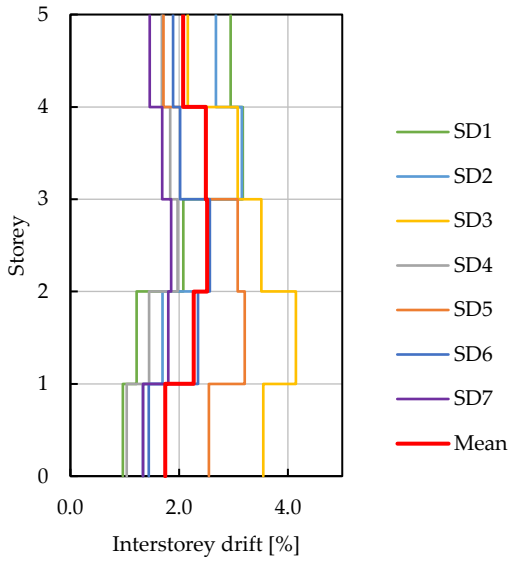

Figure 3.80: Floor max acceleration for each ground motion at SD limit state and mean profile.

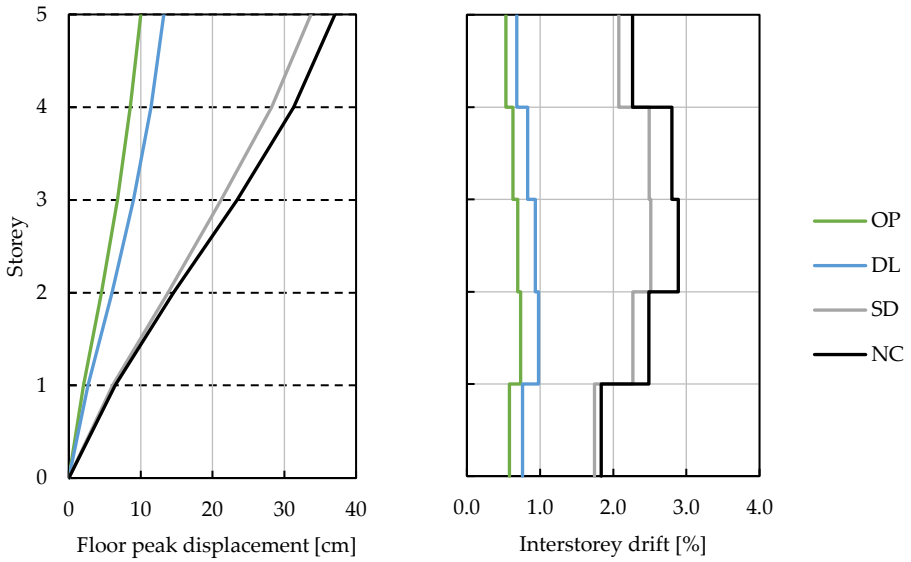

a) *b)*

Figure 3.81: Mean floor displacements a) and interstorey drift b) profiles for the limit states.

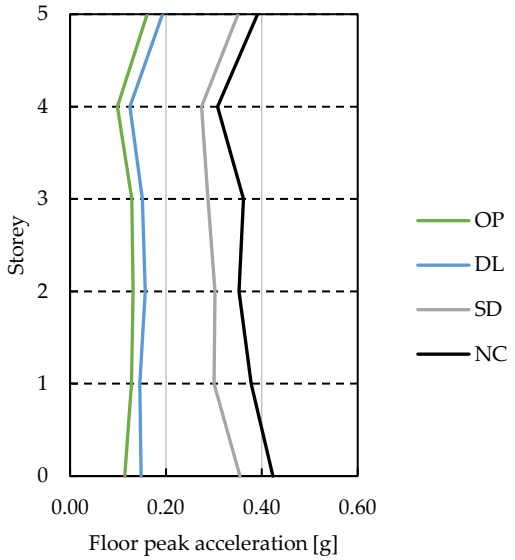

Figure 3.82: Envelope of the floor acceleration for each limit state.

Limit state	OP	DL	SD	NC
Mean max displacement [cm]	10.0	13.2	33.7	37.1
Mean max local drift [%]	0.76	1.02	2.87	3.06
Mean max base shear [kN]	302.91	340.77	480.69	502.84

Table 3.10: Main mean quantities derived by the nonlinear time-history analysis.

3.5.1.4 Comparison of the seismic demands estimated by the different analysis types

In this section, the results obtained by the three analysis types previously described are compared in terms of top displacement and max interstorey drift demand for the different limit states. An example of comparison is represented in Figure 3.83, where the four demands at the life-safety limit state (SDLS) are plotted on the push-over curves. In the same graph, the demands of each time history analysis are represented by a point indicating the maximum displacement and the maximum base shear recorded in the analysis.

The full summary of the limit states investigated is reported in Table 3.11, together with the normalised deviation with respect to the results of the NLTH analyses, assumed as s benchmark. At the ULS, the results of RSAs account for the P-Δ effects. In general, the estimation of displacement and interstorey drift demands of modal-PO analysis is close to the NLTHA results, except at the NCLS, where a better fit is observed for the mass PO. The deviation with respect to the NLTH analyses is at most about 35% at the serviceability limit states and 20% at the ultimate limit states for both the top displacement and maximum interstorey drift. Generally, NLTHAs led to higher deformation demands than the other analysis types at all the limit states, except for the NCLS.

The results of the RSAs are in good agreement with the results of the PO modal analysis.

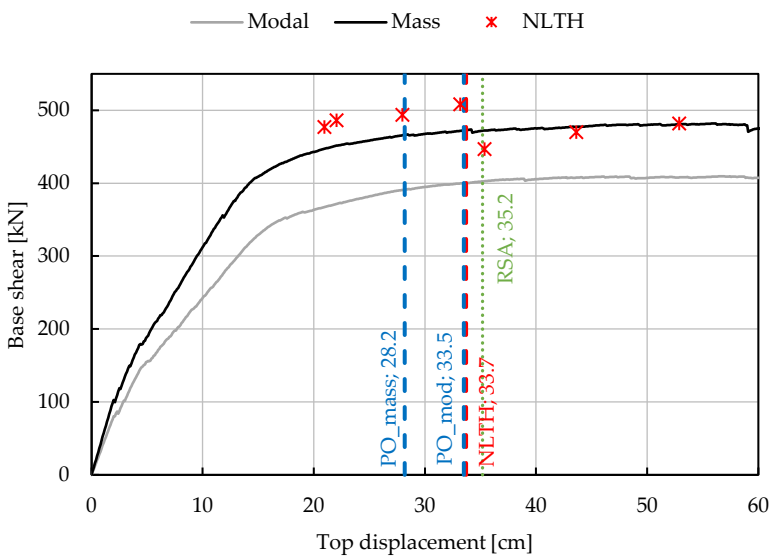

Figure 3.83: Comparison of the demands estimated by the different analyses for the SD limit state: modal analysis (RSA), Push-Over modal distribution (PO_mod), Push-Over mass distribution (PO_mass), single NLTH demand (star points), and NLTH mean value (NLTH).

		RSA	RSA / NLTH	RSA / PO_mod	PO_{mod}	PO / NLTH	PO_{mass}	PO / NLTH	NLTH
OP	d [cm]	6.72	67%	100%	6.74	67%	5.04	50%	9.99
	δ [%]	0.51	67%	104%	0.49	64%	0.39	52%	0.76
DL	d [cm]	9.77	74%	100%	9.80	74%	7.32	55%	13.20
	δ [%]	0.75	74%	108%	0.69	68%	0.57	56%	1.02
SD	d [cm]	35.18	104%	105%	33.49	99%	28.19	84%	33.71
	δ [%]	2.79	97%	110%	2.55	89%	2.38	83%	2.87
NC	d [cm]	46.67	126%	108%	43.14	116%	36.31	98%	37.06
	δ [%]	3.75	122%	114%	3.29	108%	3.08	101%	3.06

Table 3.11: Comparison of the seismic demands (d = max top displacement, δ = interstorey drift) evaluated from the different analysis types. For the RSA, the difference with respect to the NLTHA and the First mode PO are reported.

Assuming the demands evaluated by the nonlinear time-history analyses as the benchmark, the displacement and drift profiles evaluated with the PO analyses at the step corresponding to a top displacement equal to the one estimated by the NLTHAs are compared to the envelopes evaluated by the NLTHA in Figure 3.84 for the DLLS and NCLS. The floor displacements along the height are overestimated by the PO analyses, with a higher amplitude for the mass PO. The interstorey drift distribution

is altered. In fact, the POs exhibit a peak at the second interstorey with a decrease at the upper levels, while the NLTH exhibits a peak at the third level and a lower reduction at the upper levels. It means that the PO analyses exhibit a concentration of the drift demand at the first levels, while the NLTH analyses show a uniform distribution of the drift along the upper levels. Nevertheless, the peak value is similar and overestimated in the modal PO. Concluding, modal PO offers the best fit to the NLTHA results.

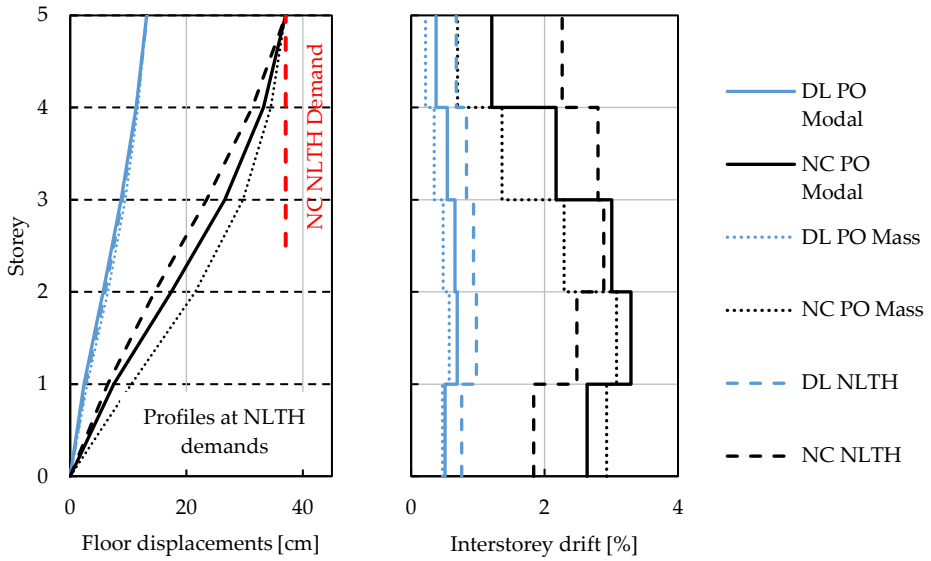

a) *b)*

Figure 3.84: Displacement a) and interstorey drift b) profiles for DL and NC limit states evaluated by the Push-Over analyses and the nonlinear time history analyses.

As shown in Figure 3.85, comparing the linear dynamic to the modal PO, the displacement profile and the interstorey drift profile evaluated at the demands have the same shape. At the DLLS, the curve of the RSA is completely overlapped with the one of the PO. The NLTH response exhibits higher displacement and drift demands. At the near collapse (NC) limit state, the profiles of the RSA slightly overestimate the floor displacements and the interstorey drift of the PO analysis. Both analyses overestimate the displacement and drift demands of the NLTHA. The interstorey drift profile of the NLTH has a completely different shape; the peak is reached at the third level instead of the second one. Despite this, the peak drift recorded at the third level is aligned with all the analyses; RSA appears conservative.

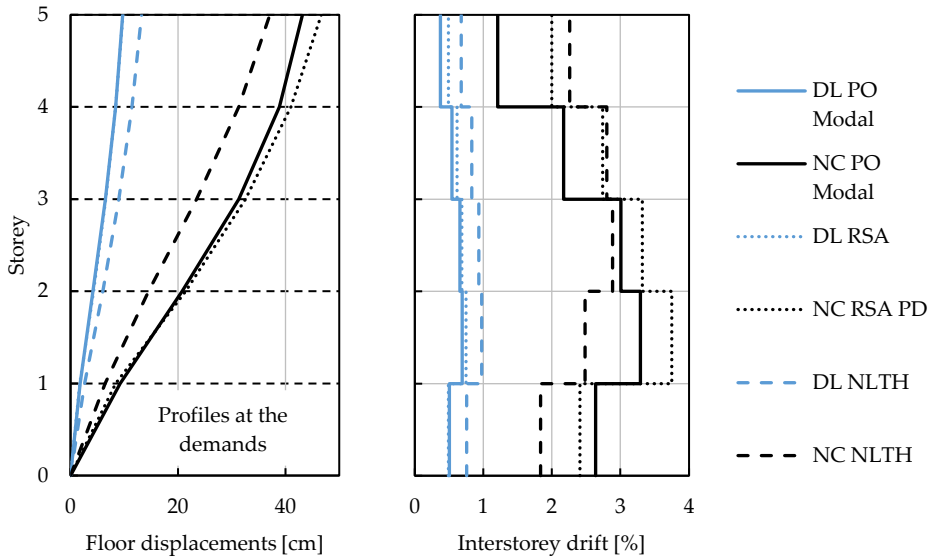

a) *b)*

Figure 3.85: Displacement a) and interstorey drift b) profiles for the main limit states evaluated by the RSA, the modal PO, and the NLTHA.

Consequently, the PO analyses are able to represent the peak displacement and the peak interstorey drift profile of the NLTHA, but not the drift profile or the location of the maximum interstorey drift. RSA, accounting for a reduced stiffness of the beams equal to 0.3, has the same capability to predict the max top displacement, the interstorey drift, and the displacement profile as the PO analysis.

3.5.2 *Influence of the infills in the response of the frame designed for "DCH"*

3.5.2.1 Modal analyses

Infills in the elastic analysis are modelled by means of equivalent elastic struts, as described in §3.3.8.
In Figure 3.86, the displacement and drift profiles evaluated at the response spectrum analysis demands for the bare frame and the infilled configurations are compared. The infilled configuration exhibits the same-shaped curves but with a reduced amplitude; a lower drift reduction is exhibited at the first interstorey. Also in the infilled configuration, the RSA shows the peak interstorey drift at the second interstorey, and it progressively reduces at the upper levels.
The summary of the elastic demands derived from the response spectrum analysis for the different limit states is reported in Table 3.12. At the reduction of the fundamental period, increased base shear, reduced top displacements, and interstorey drifts occur. The periods indicated refer to the elastic period at the SLS; they do not account for the lengthening due to the second-order effects.

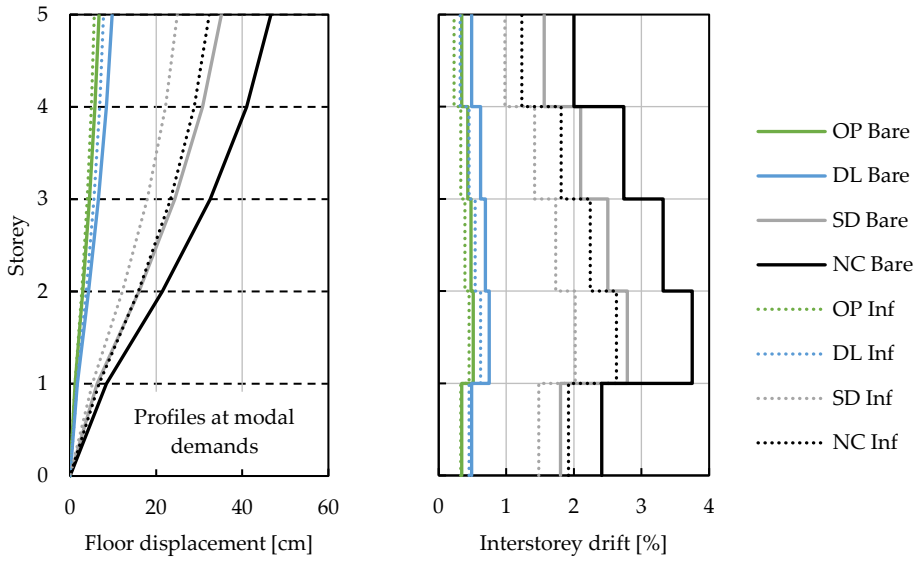

a) *b)*

Figure 3.86: Floor displacement a) and interstorey drift b) profiles obtained by the response spectrum analysis on the elastic model by applying the design elastic action referred to each limit state.

		OP	DL	SD	NC
Bare	T_1	2.09s			
	$V_{b,el}$ [kN]	211	301	889	1108
	d_{el} [cm]	6.72	9.77	35.18	46.67
	δ_{el} [%]	0.51	0.75	2.79	3.75
Infilled	T_1	1.60s			
	$V_{b,el}$ [kN]	293	406	1219	1543
	d_{el} [cm]	5.60	7.76	24.89	32.32
	δ_{el} [%]	0.45	0.62	1.93	2.48

Table 3.12: Comparison of the elastic demands (T_1 = frame fundamental period considering cracked stiffness, $V_{b,el}$ = elastic base shear, d_{el} = elastic top displacement, δ_{el} = elastic max interstorey drift) obtained by the response spectrum analyses for the bare and infilled configurations at different limit states.

Figure 3.87 represents the top displacement and the base shear points evaluated by the RSA for the different limit states. Consideration of second-order effects at ULS leads to nonlinear backbones. It is clear that the stiffness (equivalently represented by the secant line to the demand point) is increased in the infilled configuration. The base shear demand is increased at all the limit states, while the top displacement is reduced. In the same graph, the design shear action (correlated to the elastic model used in the design of the structure and characterised by a higher value of cracked stiffness of the beams, equal to half of the full section one) is represented.

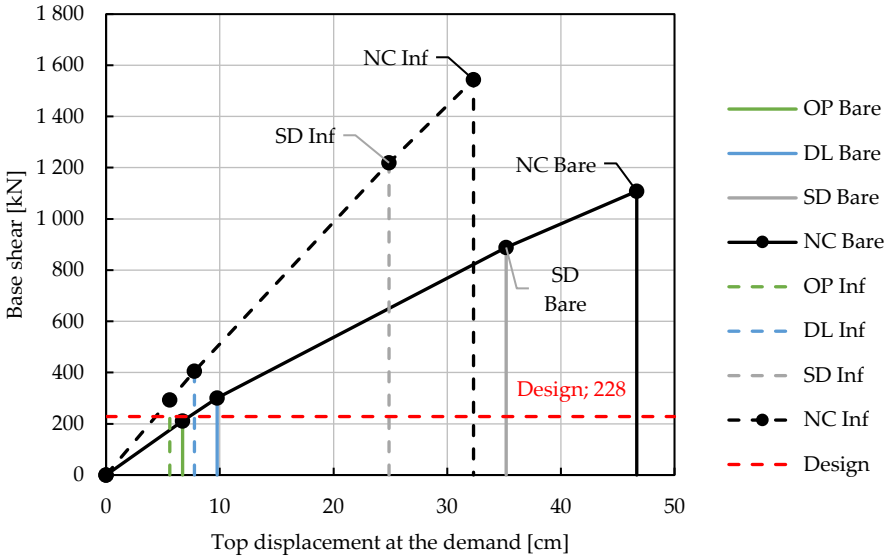

Figure 3.87: Displacement and respective base shear demands evaluated from the RSA for the bare and infilled configurations.

3.5.2.2 *Push-Over analyses*

Figure 3.88 represents the comparison between the two push-over analyses on the bare and infilled configurations. The same considerations highlighted for the bare frame apply here. As expected, the infills contribute to the global lateral strength. Dashed lines represent the shear contribution of the frame in the infilled configuration, which is very similar to the capacity curves of the bare frame. In all the configurations, the collapse limit state is governed by the 4% interstorey drift limit chosen for the infill collapse. The fact that the NCLS reaching is governed by interstorey drift and that in the infilled configuration is anticipated suggests that there is a concentration of interstorey drift at an interstorey level.

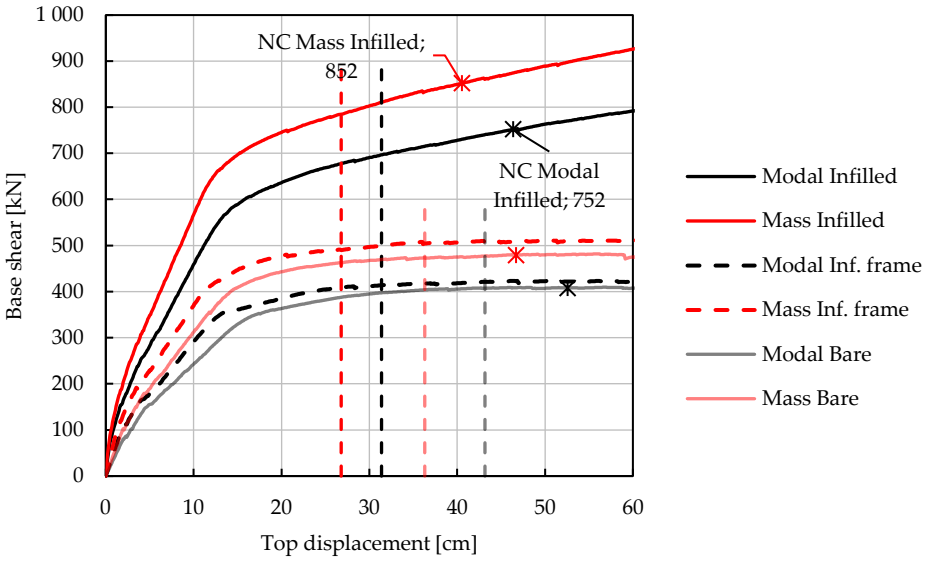

Figure 3.88: Comparison of the capacity curves of the push-over analyses on the infilled and bare configurations. The star points represent the NC capacity, and the vertical dashed lines represent the corresponding demands. Dashed curves represent the shear action adsorbed by the frame in the infilled configuration.

Table 3.13 summarizes the main data that characterize the PO analyses, their SDOF equivalent system, and the corresponding bilinear curve.
In this case, the comparison of the demands evaluated by applying the N2-method [78] with the capacities (Figure 3.89) is satisfied with a large safety margin.
The mechanism evolution is not significantly altered by the presence of the infills until the collapse limit state, as graphically represented in Figure 3.90 and Figure 3.91. The damage involves the beam extremes, the column bases, and only a few columns top sections. No soft storey develops.

	Description	Bare		Infilled	
		Modal	Mass	Modal	Mass
G	Modal participation factor	1.34	1.00	1.31	1.00
m_{SDOF} [ton]	Mass of the equivalent SDOF	288	482	300	482
K_{eq}	Stiffness of the equivalent SDOF	24.25	32.01	46.03	58.73
$T_{1,eq}$ [s]	Fundamental period of the SDOF	2.17	2.44	1.60	1.80
$d_{y,eq}$ [cm]	Yielding displacement of the SDOF	12.19	14.46	11.47	13.45
$F_{y,eq}$ [kN]	Yielding base shear of the SDOF	296	463	528	790
$d_{u,eq}$ [cm]	Ultimate displacement of the SDOF	39.28	46.67	35.26	40.51
$V_{bmax,eq}$ [kN]	Max base shear of the equivalent SDOF	306	480	572	852
$d_{y,eq,el}$ [cm]	Elastic demand displacement of the SDOF at NCLS	32.25	36.31	23.87	26.81
$F_{y,eq,el}$ [kN]	Elastic demand base shear of the SDOF at NCLS	782	1162	1099	1574

Table 3.13: Main parameters of the PO analyses, of the equivalent SDOF system, and of the corresponding bilinear system.

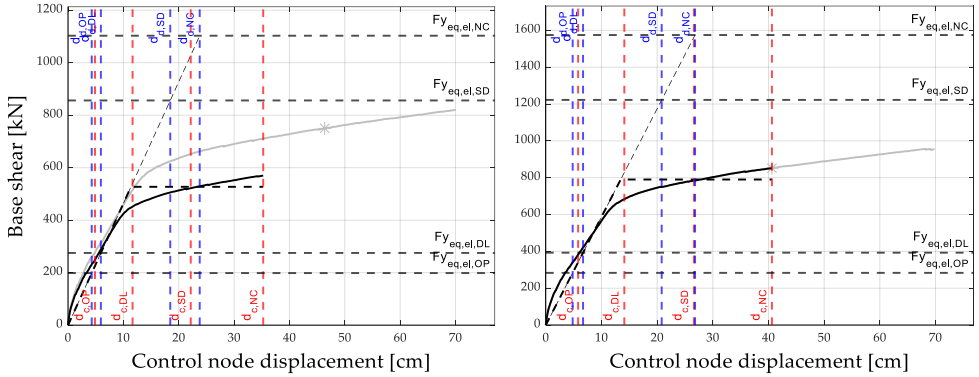

a) Modal distribution *b) Mass distribution*

Figure 3.89: Capacity curve of the MDOF system, capacity curve of the equivalent SDOF system, its bilinearization, and comparison of the estimated seismic demand by the N2-method and the corresponding capacity at different limit states for the modal load distribution a) and mass proportional distribution b).

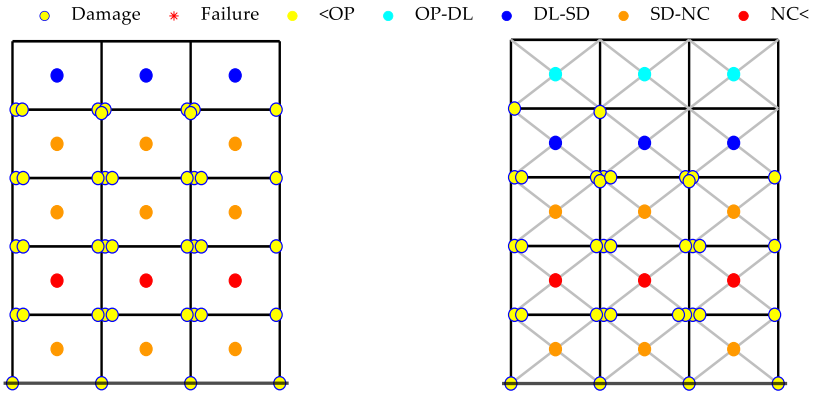

a) Bare frame *b) Infilled frame*

Figure 3.90: Comparison of the mechanisms at the NC limit state capacity of the bare a) and the infilled b) configurations in modal PO.

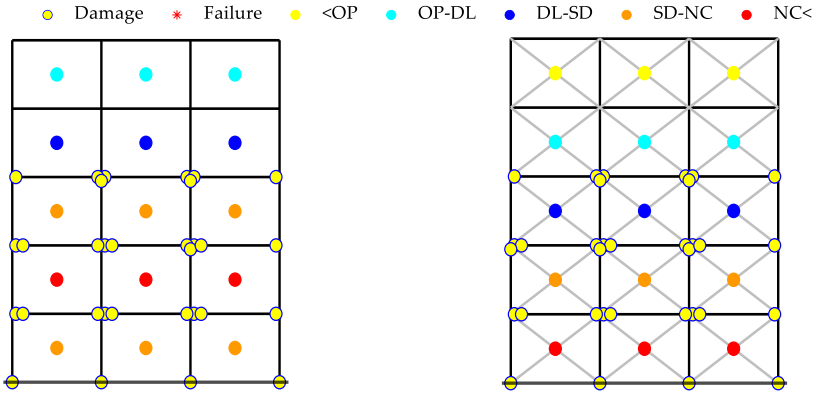

a) Bare frame *b) Infilled frame*

Figure 3.91: Comparison of the mechanisms at the NC limit state capacity of the bare a) and the infilled b) configurations in the mass PO.

Figure 3.92 compares the displacement profiles (left side of the figure) and the interstorey drift profiles (right side of the figure) for different limit states obtained by the two load distributions of the PO (modal in the upper part of the figure and mass in the lower one) for the bare and the infilled configurations. The profiles are simply reduced in magnitude, passing from the bare configuration to the infill configuration, the reduction is lower at the first two levels. The peak of interstorey drift is always reached at the second level in the modal POs and at the first two levels in the mass PO.
Table 3.14 summarises the top displacement and the max interstorey drift at the demands.

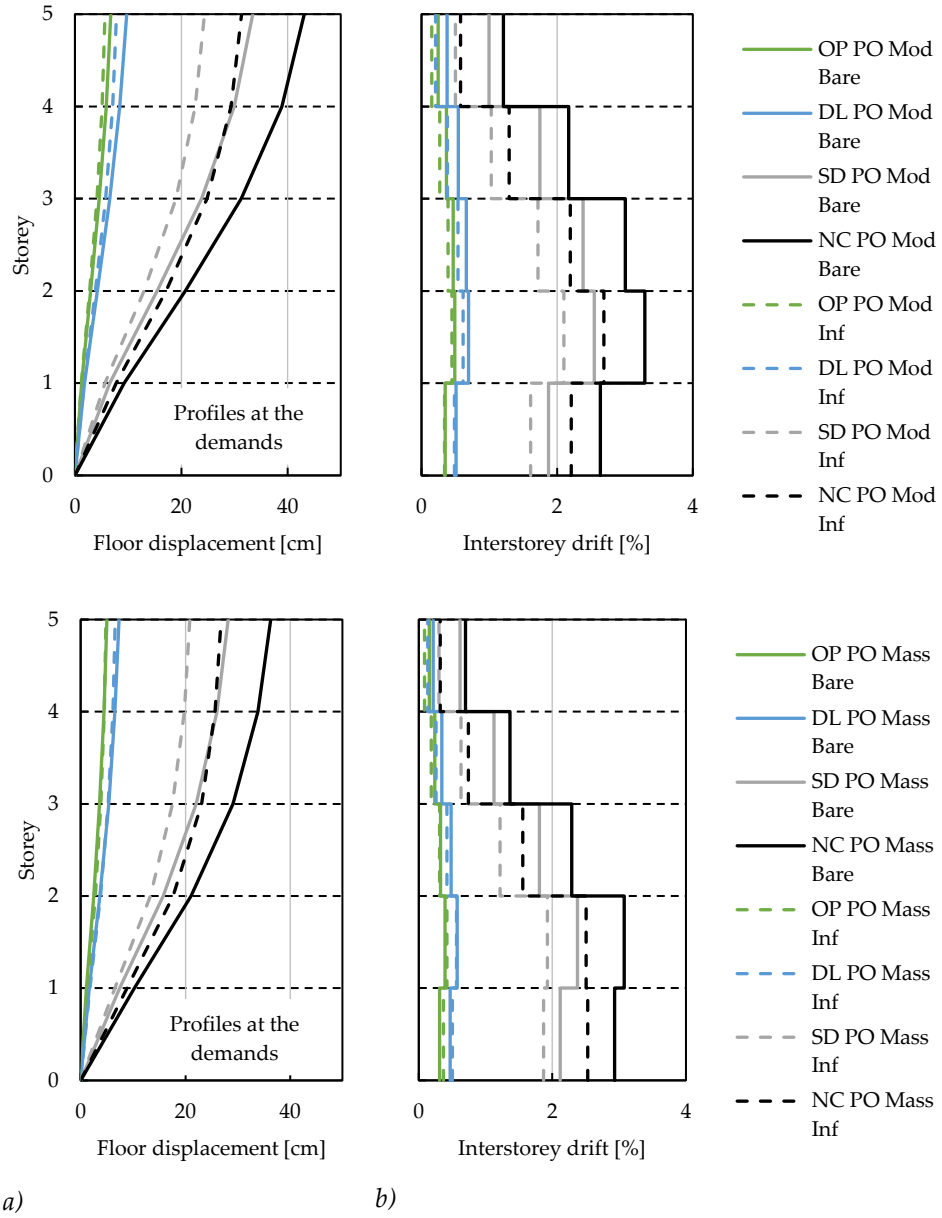

Figure 3.92: Displacement a) and interstorey drift b) profiles at the demands evaluated for each limit states for the two load distributions, modal (upper) and mass (lower).

	OP		DL		SD		NS	
	Bare	Inf.	Bare	Inf.	Bare	Inf.	Bare	Inf.
Modal - displacement [cm]	6.74	5.65	9.80	7.83	33.49	24.37	43.14	31.39
Modal - Max local drift [%]	0.49	0.45	0.69	0.61	2.55	2.10	3.29	2.69
Mass - displacement [cm]	5.04	4.82	7.32	6.69	28.19	20.81	36.31	26.81
Mass - Max local drift [%]	0.39	0.42	0.57	0.56	2.38	1.93	3.08	2.53

Table 3.14: Estimation of the max displacement and max interstorey drift demands at the limit states.

3.5.2.3 *Nonlinear time-history analyses*

Figure 3.93 represents an example of the hysteresis of the infilled configuration, where the triggering of the first damage limit state in beams and columns is highlighted together with the mechanism at the end of the excitation. In the specific case, the damage occurred at the beam ends, the column bases, and only a few top sections of columns of the third storey. Figure 3.94 represents the deformation profiles and the deformed shape at significant steps of the analysis. No localization of the deformations is visible in the infilled configuration.

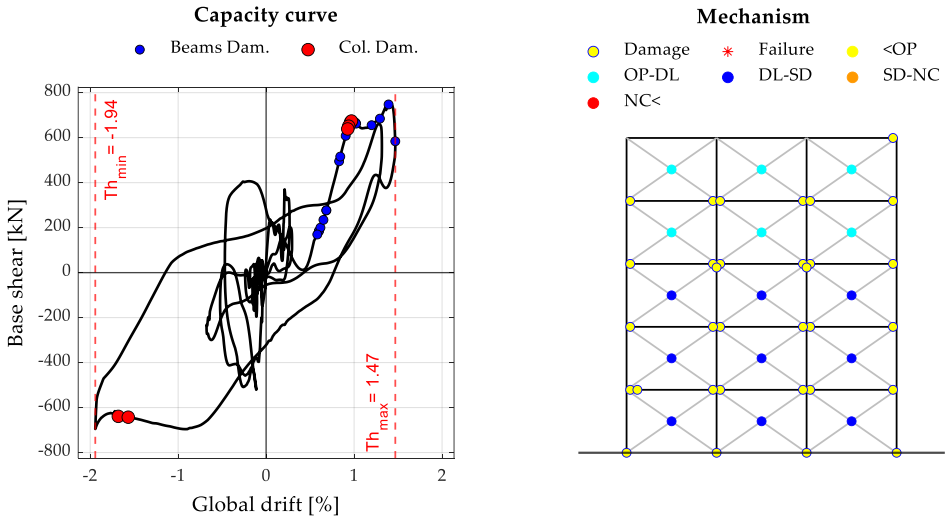

Figure 3.93: Hysteresis of the time history SD3 and corresponding mechanism at the end of the analysis. The yellow circles on the hysteresis represent the plasticization of the beam sections, while the blue circles represent the columns. The yielded sections are schematically represented on the frame on the right side of the figure.

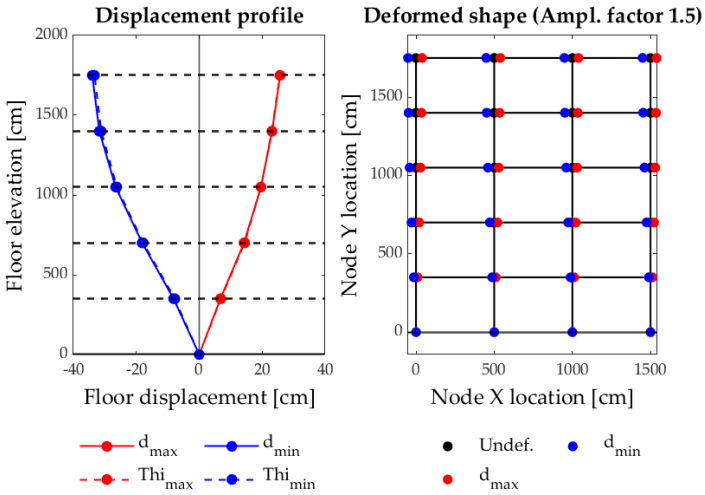

Figure 3.94: Floor displacements profiles and deformed shapes at significant time steps of the ground motion SD3, at the occurrence of maximum displacement (d_{max}), minimum displacement (d_{min}), max interstorey drift (Thi_{max}), and minimum interstorey drift (Thi_{min}).

Figure 3.95 shows how the displacement and interstorey drift profiles change in the infilled configuration. At the serviceability limit states, the profiles have a reduced amplitude but the same trend as the bare frame structure. In fact, the interstorey drifts are simply scaled. At the ultimate limit states, a complete redistribution of the deformation demands occurs. The reduction at the first two levels is progressively lower as the seismic intensity increases, until the NC limit state, where the drift demand at the first two levels is higher in the infilled configuration. At the upper levels, the drift demand is strongly reduced. The shape of the drift profiles becomes similar to the one estimated for the bare frame by simpler analyses, characterised by the peak value at the second level. The final profile at NC limit state is characterised by a similar drift demand at the first three levels where the deformation is concentrated; the corresponding displacement profile passes from a first-mode-like profile to a uniform concavity-shaped one; no soft storey occurs. The numerical details are summarised in Table 3.15.

The peak floor accelerations, as shown in Figure 3.96, are not appreciably changed and are similar to the mean peak ground acceleration. A little amplification is shown on the last floor in the infilled configurations.

Also, in this case, displacement, interstorey drift, and floor acceleration profiles at the OPLS and DLLS and at the SDLS and NCLS are very similar.

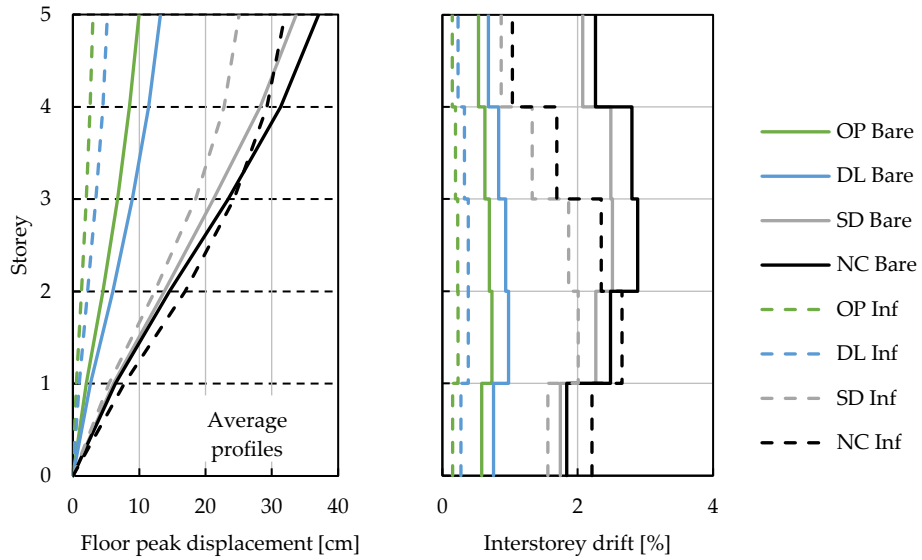

a) *b)*

Figure 3.95: Mean floor displacements a) and interstorey drift b) profiles for the limit states.

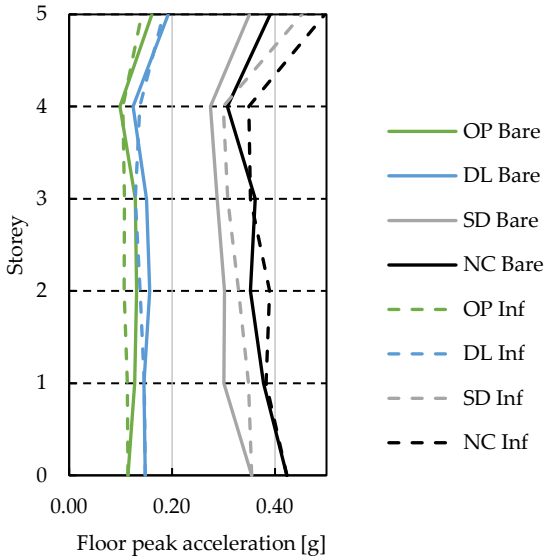

Figure 3.96: Mean profiles of the floor acceleration for each limit state in the bare and infilled configurations.

		OP	DL	SD	NC
Bare	V_b [kN]	302.91	340.77	480.69	502.84
	d [cm]	10.0	13.2	33.7	37.1
	δ [%]	0.76	1.02	2.87	3.06
Infilled	V_b [kN]	209	288	704	736
	d [cm]	3.0	5.2	25.1	32.0
	δ [%]	0.23	0.39	2.10	2.70

Table 3.15: Comparison of the demands (V_b = mean base shear, d = mean top displacement, δ = mean max interstorey drift) derived by the NLTHAs on the bare and infilled frames.

The NLTHAs are used to evaluate the floor spectra. For each analysis, floor acceleration time histories (evaluated by averaging the accelerations of the floor nodes) are recorded. For each of these records, a series of elastic SDOF systems characterised by different periods and a damping ratio equal to 5% are subjected to the acceleration time series. The Newmark method allows for the evaluation of the relative displacement history. The peak relative displacement composes a point of the pseudo-displacement spectrum. Multiplying it by $2\pi/T^2$ the pseudo-acceleration spectrum is constructed. The floor spectra for each limit state are evaluated by averaging the spectra obtained by the seven ground motions.
Figure 3.100 represents the comparison of the floor spectra obtained in the bare and infilled configurations. Bare frame spectra exhibit peaks at 0.7s and 2.2s, corresponding to the first two main periods of vibration shown by the top displacement time history. They are lengthened to 0.8s and 2.6s at the ULS due to the element plasticization. In the infilled configuration, they are anticipated to be about 0.2s and 1.2s at the SLS and 0.6s and 2.0s at the ULS. A reduction, with respect to the bare configuration, of the peak accelerations is shown at the SLS at both main periods, while at the ULS, a decrease occurs at the lower period, but an amplification is visible at the higher one. The peak acceleration of the last floor for the first period (the higher) is about equal to 0.6g at both SLS and ULS. The value decreases at the SLS in the infilled configuration, while it increases to about 0.8g at the ULS. The absolute maximum acceleration of the floor spectra is anyhow reduced by the presence of the infills for all the shaking intensity levels explored.

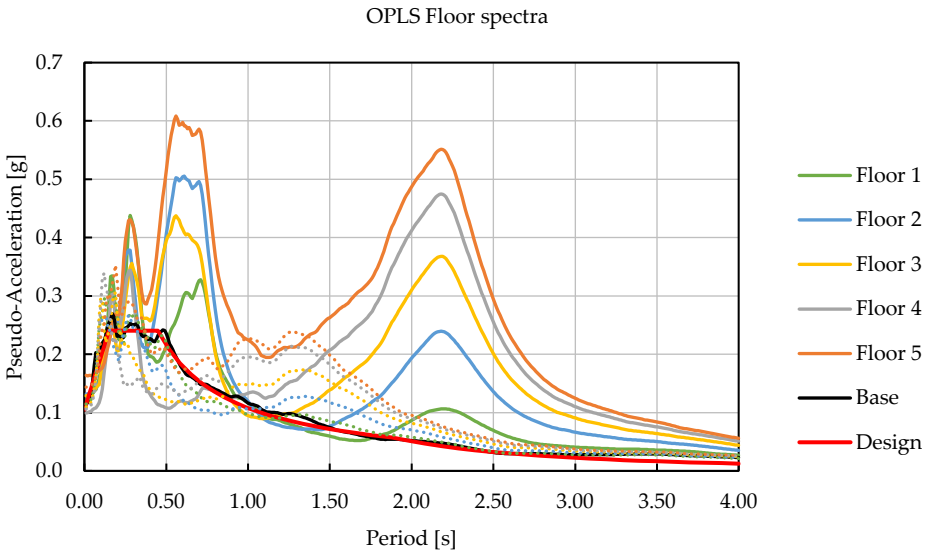

Figure 3.97: Comparison of the floor spectra evaluated for the bare (continuous line) and the infilled (dotted line) frames at the OP limit state.

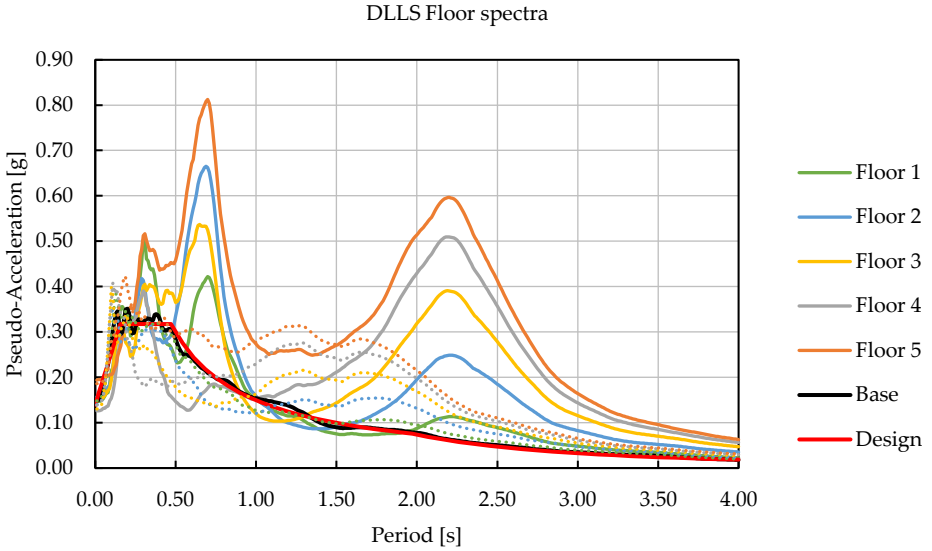

Figure 3.98: Comparison of the floor spectra evaluated for the bare (continuous line) and the infilled (dotted line) frames at the DL limit state.

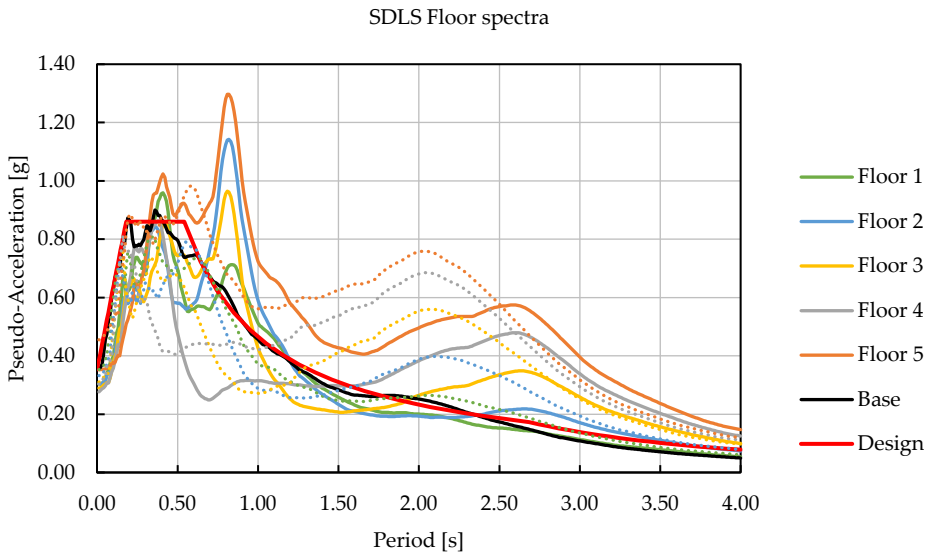

Figure 3.99: Comparison of the floor spectra evaluated for the bare (continuous line) and the infilled (dotted line) frames at the SD limit state.

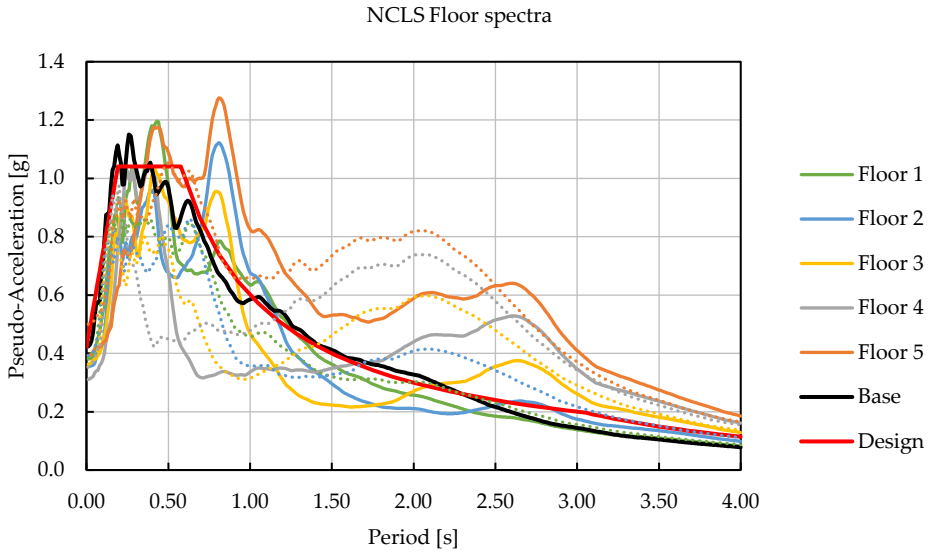

Figure 3.100: Comparison of the floor spectra evaluated for the bare (continuous line) and the infilled (dotted line) frames at the NC limit state.

3.5.2.4 *Comparison of the seismic demands estimated by the different analyses types*

The different analysis types conducted on the infilled configuration are here compared.
Figure 3.101 compares the displacement demands attained with the different types of analysis in the infilled configuration.
The full summary of the limit states investigated is reported in Table 3.11. Looking at the PO nonlinear analyses, the NLTH demands are highly overestimated at the serviceability limit states, while they are slightly underestimated at the ultimate limit states. At the ULS, the modal pushover gives good results.
Also, for the infilled configuration, the results of the RSA are in good agreement with the results of the modal push-over analysis, with a percentile deviation lower than 10% for both displacement and drift demands.
In the infilled configuration, the modal analysis seems to have the same ability to represent the seismic demand estimated by the modal PO analysis as in the bare configuration.

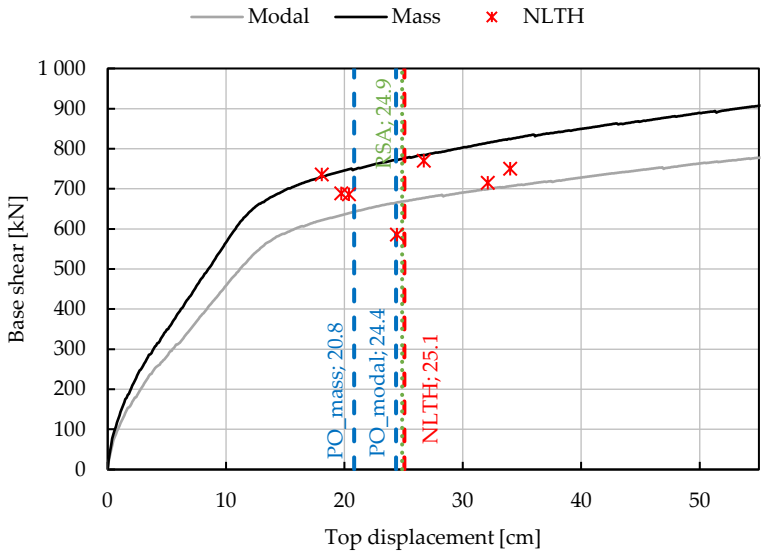

Figure 3.101: Comparison of the demands estimated by the different analyses for the SD limit state: modal analysis (RSA), Push-Over modal distribution (PO_mod), Push-Over mass distribution (PO_mass), NLTH demand points (crosses), and NLTH mean value (NLTH).

		RSA	RSA / NLTH	RSA / PO_mod	PO_{mod}	PO / NLTH	PO_{mass}	PO / NLTH	NLTH
OP	d [cm]	5.60	185%	99%	5.65	187%	4.82	159%	3.03
	δ [%]	0.45	192%	101%	0.45	191%	0.42	180%	0.23
DL	d [cm]	7.76	149%	99%	7.83	150%	6.69	128%	5.22
	δ [%]	0.62	159%	101%	0.61	158%	0.56	145%	0.39
SD	d [cm]	24.89	99%	102%	24.37	97%	20.81	83%	25.06
	δ [%]	2.02	96%	96%	2.10	100%	1.93	92%	2.10
NC	d [cm]	32.32	101%	103%	31.39	98%	26.81	84%	31.98
	δ [%]	2.63	97%	98%	2.69	100%	2.53	94%	2.70

Table 3.16: Comparison of the seismic demands (d = max top displacement, δ = interstorey drift) evaluated from the different analysis types. For the RSA, the difference with respect to the NLTHA and the First mode PO are reported.

Figure 3.102 compares the displacement profiles obtained with the PO analyses with those obtained from the NLTH analyses for the top displacement amplitude calculated with the NLTH analysis. Both infilled and bare frame results are reported for comparison. Mass PO slightly overestimates the floor displacements and exhibits a different drift profile; the drift at the first level is similar to the one at the second level and strongly reduces at the upper levels. The modal PO well represents the displacement profile and the interstorey drift at the lower two levels, while it underestimates the drifts at the upper levels. Modal PO offers the best fit for the NLTHA profiles.

Comparing RSA to the modal PO and the NLTH (Figure 3.103, lower part), the NLTH response exhibits lower displacement and drift demands with respect to the other analyses at the DLLS. RSA results basically match the modal PO ones. At the NCLS, the three displacement profiles are overlapped. The drifts at the lower levels are well predicted by the modal PO and the RSA, while they are underestimated at the upper levels by the modal PO and a little overestimated by the RSA.

Figure 3.102 shows that the best fit between the PO analysis and the NLTH displacement profile is obtained in the infilled configuration. It is important to underline that the envelope profiles of NLTHA here considered are specific to the ground motions selected; nothing excludes different results if a different selection is considered.

Figure 3.103 shows that the RSA has the same ability to represent the results of the modal PO in both bare and infilled configurations. A better agreement between the three analyses is visible in the infilled frame. The interstorey drift shape, the peak value, and its location are better captured in the infilled configuration.

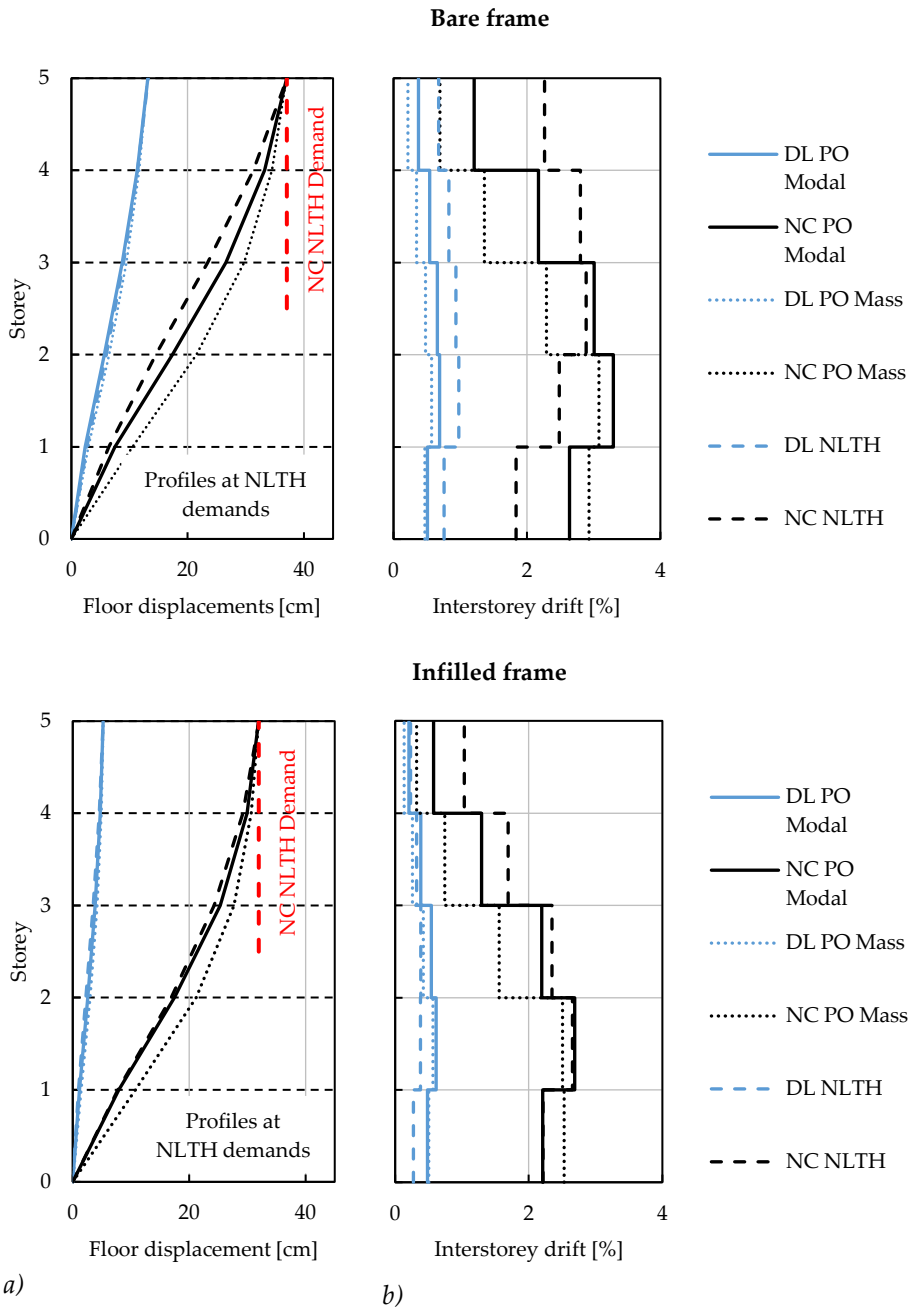

Figure 3.102: Comparison of the displacement a) and interstorey drift b) profiles at the DLLS and NCLS demands from the modal PO and the NLTHA for both the bare and infilled frames.

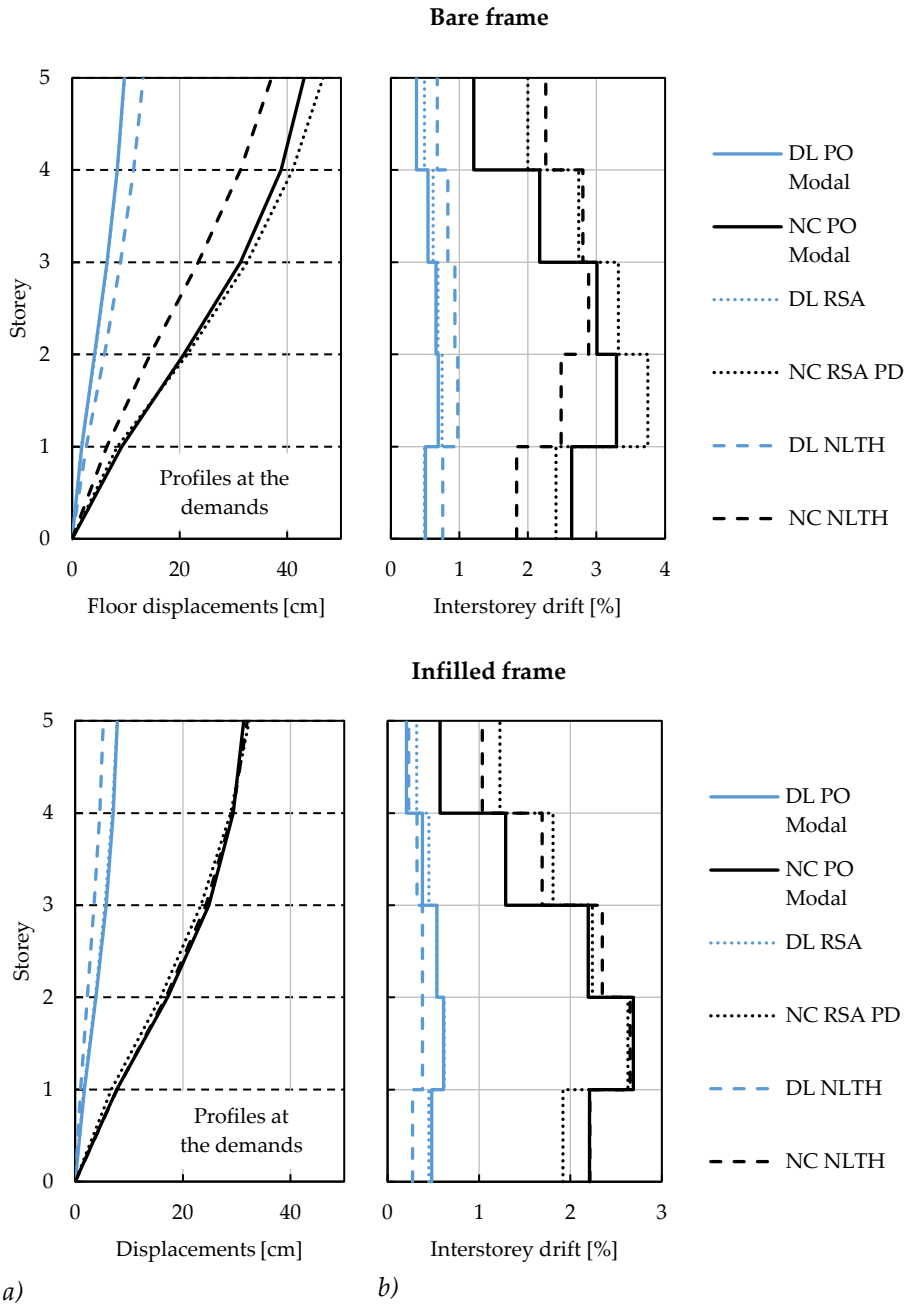

Figure 3.103: Comparison of the displacement a) and interstorey drift b) profiles at the DLLS and NCLS demands from the RSA and the modal PO for both the bare and infilled frames.

3.5.3 *Influence of infill characteristics and ductility level on the NLTH response*

In this section, the influence of some design parameters on the nonlinear dynamic response is discussed.
The ductility level assumed in the design of the frame leads to different levels of flexibility in the structure. As the design behaviour factor becomes higher, the structure becomes slender; the seismic demand in terms of top displacement and interstorey drift increases at the ULSs, but it is constant at the SLSs for infilled configurations. An example of the case of infill thickness equal to 200mm is represented in Figure 3.105. The results of the bare frame and the other infill thicknesses considered are reported in Annex §C.1.1.
By increasing the infill thickness and, especially, the infill contact thickness to the columns, both strength and stiffness of the infill analytical backbone increase, as graphically shown in Figure 3.104. In the graphs, the strength at 1% drift is considered the reference parameter for the comparisons. Figure 3.106 shows the seismic demands on frame "DCH" in the bare configuration and in those with infills. It is clear that when infills are introduced, seismic deformation demands rapidly reduce, and they further reduce as the infill strength increases. The same trend is also shown for the other two frames designed for medium ("DCM") and low ductility ("DCM_2"); those results are reported in §C.1.2. Looking at the displacements and interstorey drift profiles, reported in Figure 3.107, at the DL limit state, they are strongly reduced when infills are introduced. At the NC limit state, the deformations are redistributed: peak drift values exhibited at mid-height levels in the bare configuration move down to the first levels, and the corresponding deformation profile is modified.

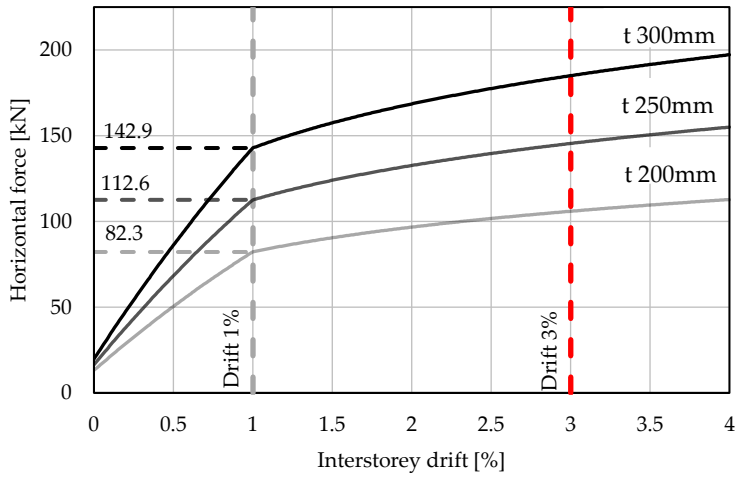

Figure 3.104: Comparison of the infill backbones of different infill thicknesses. Reference to the infills of the first level of frame "DCH". Indication of the strength at 1% drift.

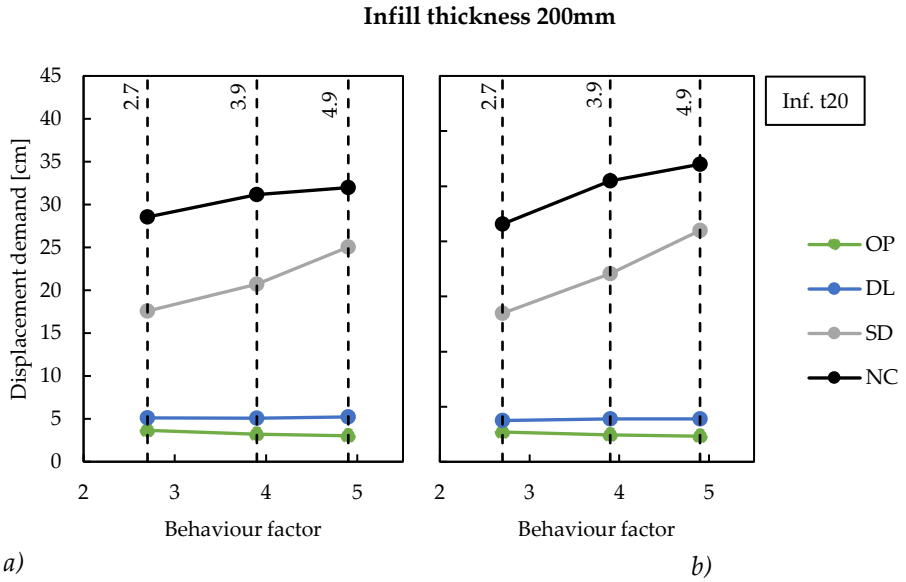

Figure 3.105: Comparison of the top displacement a) and max interstorey drift b) demands at different limit states for different design behaviour factors in the infilled configuration with an infill thickness equal to 200mm.

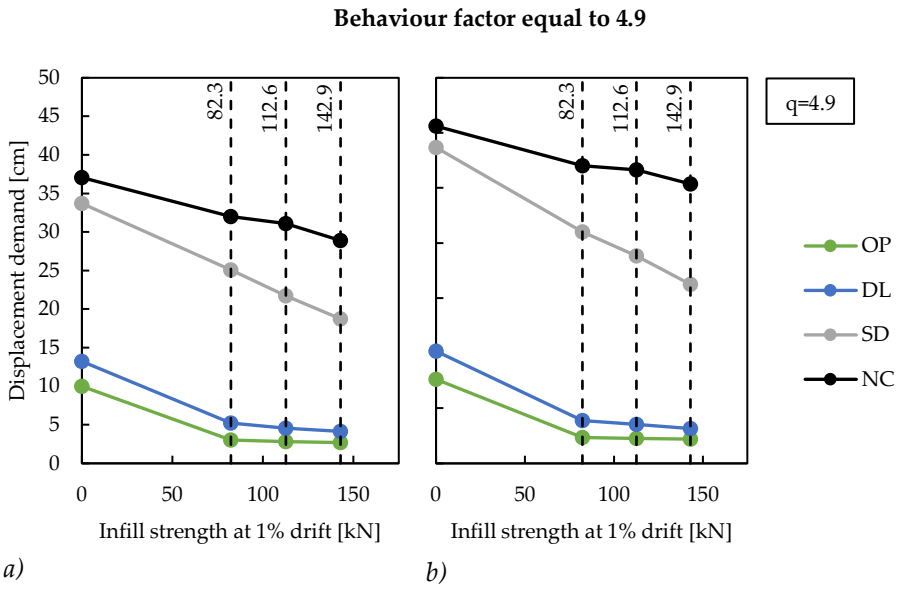

Figure 3.106: Comparison of the top displacement a) and max interstorey drift b) demands at different limit states for different infill characteristics on frame "DCH" (behaviour factor equal to 4.9). The value "0" corresponds to the bare frame.

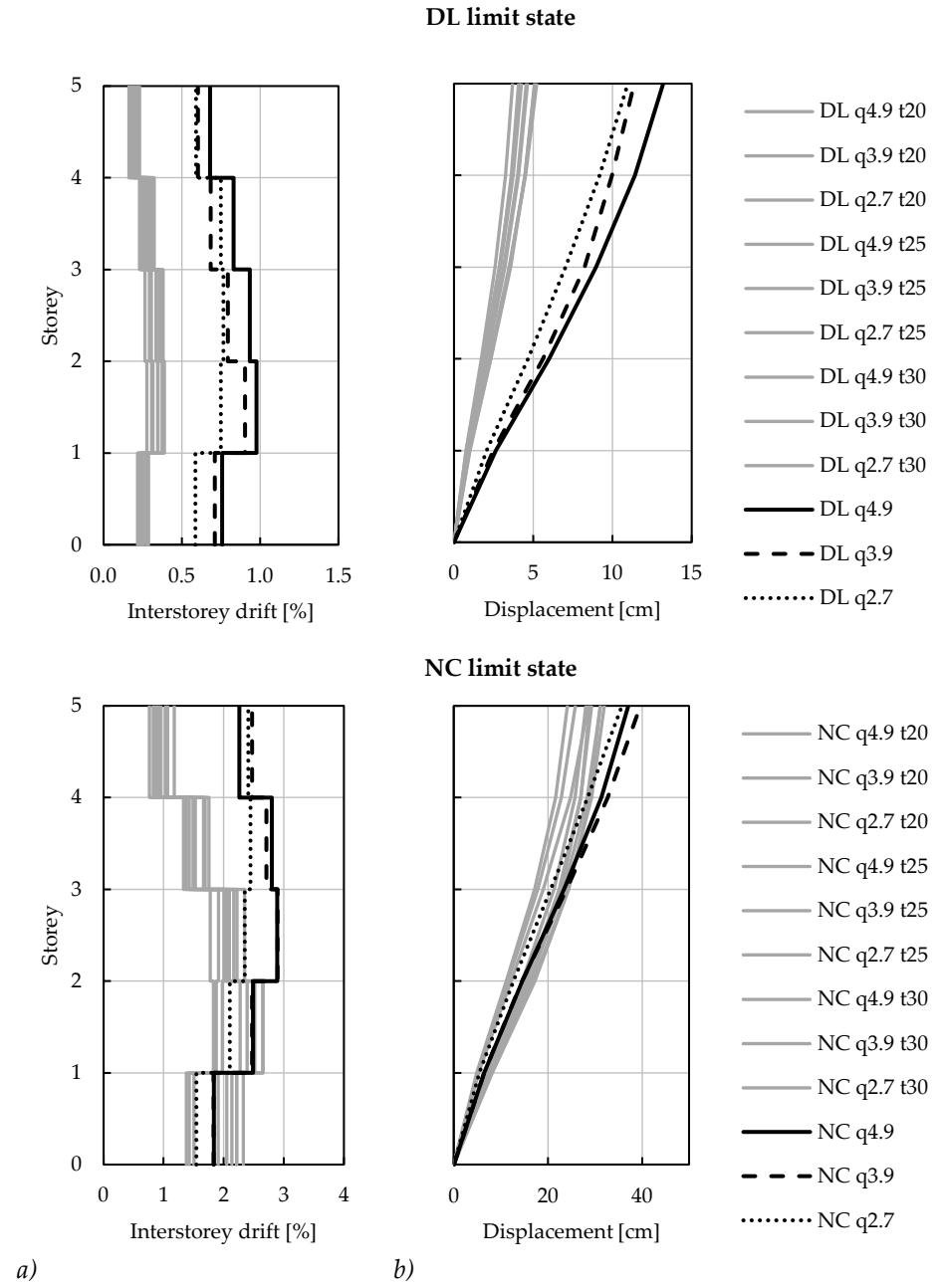

Figure 3.107: Comparison of the displacement a) and interstorey drift b) mean profiles derived by NTLHAs at the DLLS and NCLS for all the analysed structures. Black lines represent the bare frames, while the grey ones represent the infilled structures.

3.5.4 *Infills in Push-Over and Response Spectrum Analyses*

Displacement and interstorey drift maximum values estimated by the modal PO and the RSA are compared to the results of NLTH; the relative deviation, expressed as the ratio with respect to the NLTH demand, is shown in Figure 3.108, referring to the NC limit state. Modal PO is considered since it gives better peak values and displacement profiles compared to NLTH than mass PO. Because NLTH results may depend on the ground motion set selected, the comparison is done in relative terms between infilled and bare frame configurations. The deviation of infilled configurations is lower than the one evaluated in the corresponding bare configuration for all three structures examined, both for top displacement and interstorey drift. Deviation is always lower than 20% in infilled configurations; it increases in bare frame structures. Consequently, for the cases here considered, the N2-method [78] has the same, or better, capacity of predicting the dynamic demands in the infilled configurations as well as the bare ones.
Looking at the RSA, estimations are strictly close to those of the modal PO. The proposed approach to account for infills in linear-elastic analyses is effective in representing PO demands, and both methods seem promising in representing NLTH demands.
At the DLLS (Figure 3.109), modal PO and RSA gave overlapped peak values. Simpler analyses underestimate the NLTH results in the bare frames, while they strongly overestimate the NLTH results in the infilled configuration. Probably this could be justified by the dissipative friction contribution given by the infills, starting from low displacement demands. PO analyses or RSA cannot account for this contribution unless elastic spectra with higher damping are used in the evaluation of the seismic response demands.

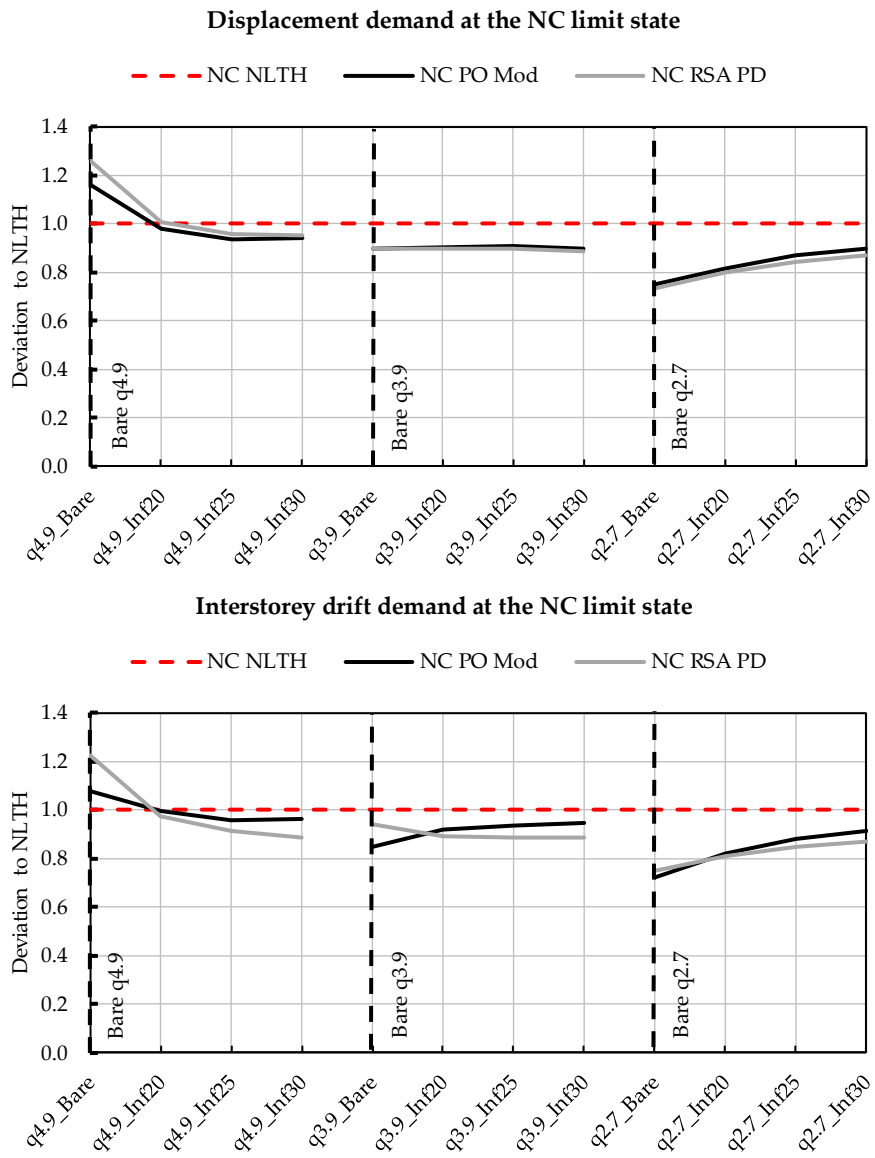

Figure 3.108: Deviation of maximum displacement and interstorey drift demands evaluated by modal PO and RSA to the NLTH at the NC limit state.

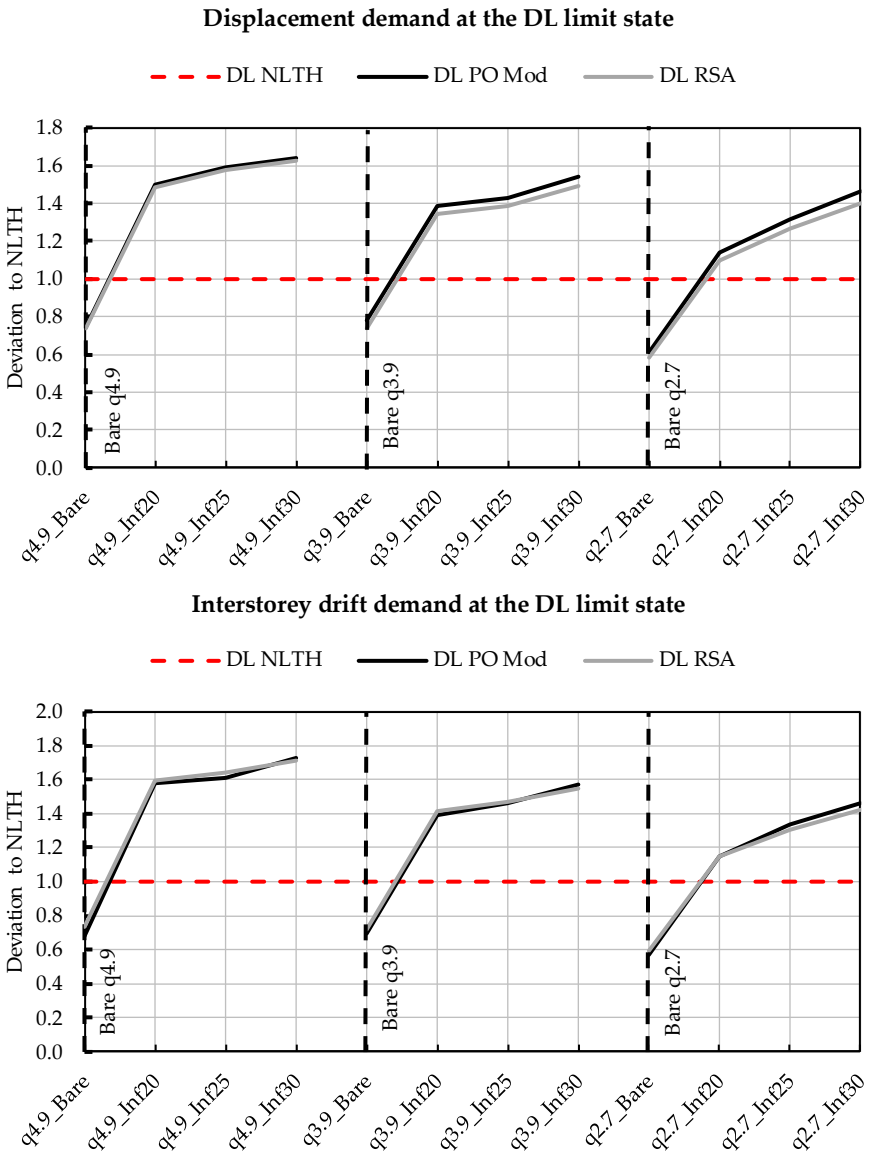

Figure 3.109: Deviation of maximum displacement and interstorey drift demands evaluated by modal PO and RSA to the NLTH at the DL limit state.

3.5.5 *Shear safety checks in Push-Over analyses*

In order to ensure a ductile collapse mechanism for the frame with sliding joint infills, a safety check for shear resistance in the column is necessary. In the following, the comparison of the shear action and resistance at the capacity SD limit state is proposed as a safety verification to avoid premature shear collapse in the structure. During the lateral deformation of the structure, the interaction between infills and columns implies the arise of contact forces along the height of the columns (Figure 3.110). The shear profiles of the columns are always altered, and the maximum shear action always increases in the infilled configuration.

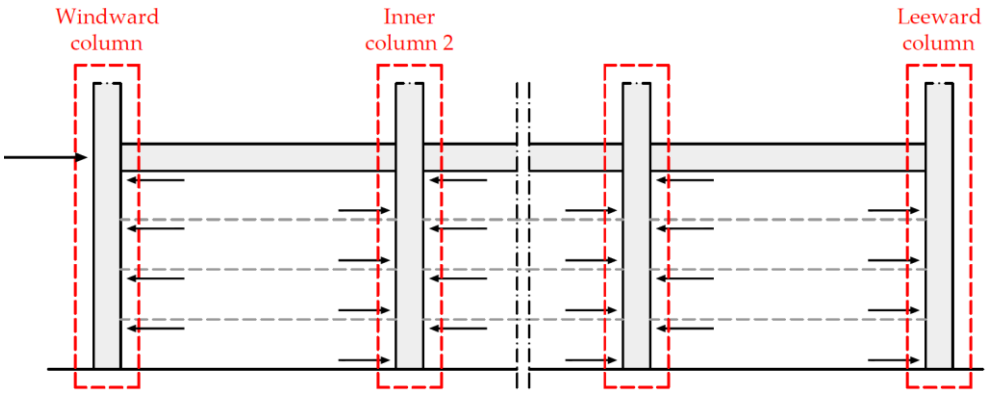

Figure 3.110: Representation of the contact forces exchanged between the infills and the frame in the lateral deformation.

By using concentric struts to represent infills, the shear amplification due to infill-frame interaction is not quantified, so it must be analytically added a posteriori. The analytical model previously described in §2.1.2 allows for evaluating both the infill contribution to the frame lateral strength and the shear action on the column because of the infill interaction as a function of the drift level. Considering a rightward sway mechanism, Figure 3.111 shows the contact forces acting on the windward column (Figure a), on the left inner column (Figure b), and on the leeward column (Figure c) at an interstorey drift equal to 2.0% at the first level (corresponding to 2.5% drift in the second level, corresponding to the reaching of the SD limit state condition for infills) for the case study "DCH" infilled by 200mm infill thickness. The right inner column is not represented for simplicity, but it follows the same trend as the left one. In the figures, the red and blue bars quantify the contact forces on the leeward and windward side of each column, respectively, as obtained from the analytical model (§2.1.2, Eq. (2.1-11) and Eq. (2.1-18)).

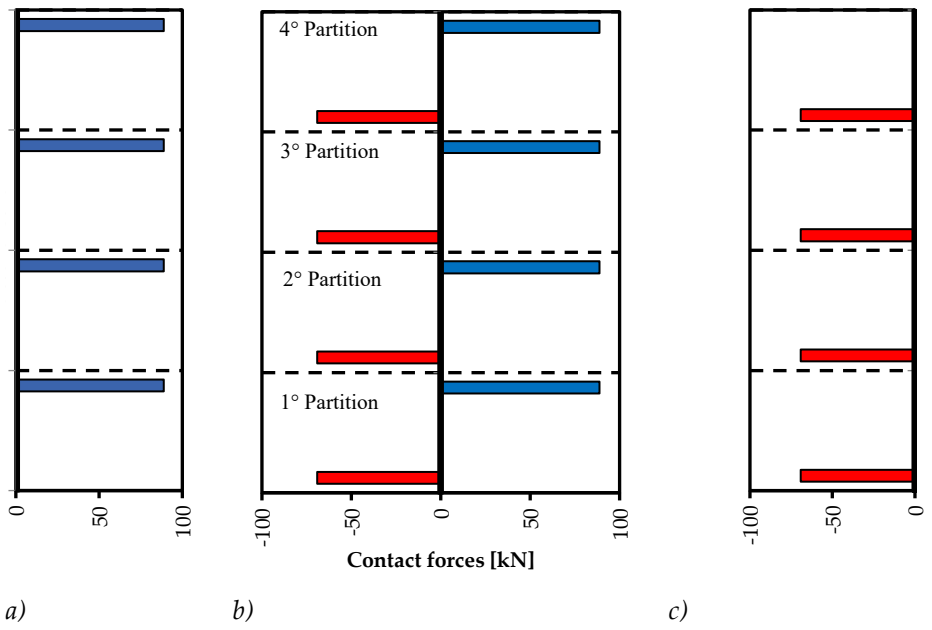

Figure 3.111: Representation of the contact forces exerted by the infills along the windward column a), the left inner column b), and the leeward column c) assuming a rightward sway mechanism at a drift level equal to 2.0% at the first level. Structure DCH with 200mm thick infills.

Figure 3.112 represents the shear action profiles along the same columns. As discussed in §2.1.2, the shear action profile along the column due to the infill is evaluated by equilibrium on the columns subjected to the contact forces (Eqs. (2.1-24) and (2.1-25)). In the inner columns, the shear profile is the result of the contact forces applied on both column sides and is thus obtained by superposition of their effects.
The total shear profiles (continuous blue lines in the figure) are obtained by adding the shear action due to the infill contribution (dotted lines in the figure) and the column shear action read in the analysis (dashed lines in the figure).
The maximum amplification of the shear action occurs at the top of the windward and at the base of the leeward columns. For the external columns, alternatively in the windward and leeward positions in the cyclic response, the safety checks may be governed by the maximum of the two values (Eq. (3.5-1)). For central columns, the maximum shear actions can be evaluated by Eq. (3.5-2), where the subscripts "i" and "j" indicate the infill before and beyond the column in the direction of loading, respectively.

$$V^{External} = max\begin{cases} |V_{frame}^{Wind}| + |V_{infill,top}^{Wind}| \\ |V_{frame}^{Lee}| + |V_{infill,base}^{Lee}| \end{cases} \quad (3.5\text{-}1)$$

$$V^{Central} = |V_{frame}^{Central}| + max\begin{cases} |V_{infill,base}^{Lee,i}| - |V_{infill,base}^{Wind,j}| \\ -|V_{infill,top}^{Lee,i}| + |V_{infill,top}^{Wind,j}| \end{cases} \quad (3.5\text{-}2)$$

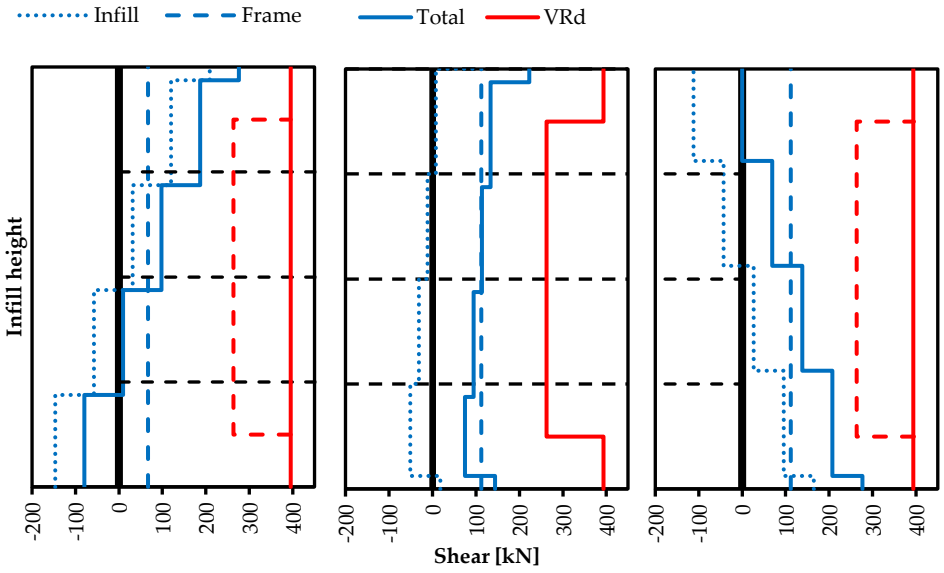

a) *b)* *c)*

Figure 3.112: Representation of the shear profiles along the columns. Dotted and dashed lines represent the infill and the frame shear action contributions, respectively. Continuous blue lines represent the total shear action profile given by their combined effect, while the red continuous lines represent the shear strength. Profile of the windward a), inner left b), and leeward c) columns for the case study "DCH" infilled by 200mm infill thickness.

Moving from the column end, the shear action rapidly decreases after the first concentrated contact force. The check for shear resistance should be done both in the central and the end sections of the columns, which may have different stirrup spacing. The red lines in Figure 3.112 represent the design shear strength profiles along the columns. Note that outside the critical region of the columns (plastic hinges), the stirrups are here designed for the shear action derived by the application of the hierarchy of strength principle to the column plastic mechanism of the bare frame; no action due to the infills is considered in the proportioning. For the external columns, the full height is considered critical length, according to the codes [58], [75].

The following Table 3.17 shows the shear verification ratios obtained for the different case studies. Checks are conducted according to Eurocode 8 [75] at the loading step where the SD limit state capacity condition is reached in the structure, assuming the design characteristics of the materials. Mass-proportional POs analyses govern the design for shear action in the columns. The compressive-shear check is always satisfied. The safety checks show that in frame "DCH", additional shear resistance is required only for the thicker infill typology, for example, by reducing the stirrup spacing or increasing the rebar diameter. For the case study frames designed according to a medium ductility class, an increase in transverse reinforcement is required for all the infill thicknesses. This result is favoured by the use of an overstrength coefficient for the shear action equal to 1.1 instead of 1.3, with the consequent reduction of the design shear action used in the original proportioning of the stirrups. For the case studies under consideration, the minimum required stirrup spacing was $4\emptyset 10/75mm$ for DCH and DCM, while $4\emptyset 12/100mm$ for DCM_2.
Given the above results, in the design of the infilled frame with sliding joint infills, the shear overload on the columns due to the infill thrust must be considered.

Ductility class	**Infill thickness**	**Modal PO**		**Mass PO**	
		V_{Ed}/V_{Rdc}	V_{Ed}/V_{Rds}	V_{Ed}/V_{Rdc}	V_{Ed}/V_{Rds}
DCH	**t20**	0.44	0.71	0.49	0.80
	t25	0.56	0.90	0.61	0.98
	t30	0.69	1.11	0.74	1.19
DCM	**t20**	0.40	0.97	0.47	1.14
	t25	0.48	1.17	0.57	1.37
	t30	0.57	1.39	0.65	1.58
DCM_2	**t20**	0.46	0.96	0.56	1.17
	t25	0.53	1.11	0.63	1.33
	t30	0.59	1.25	0.71	1.48

Table 3.17: Maximum ratio for each analysis of the shear verifications conducted in the PO analyses at the reaching of the SDLS capacity, for the end section of the columns. V_{Ed} = shear action, V_{Rdc} = compressive-shear strength, and V_{Rds} = Tensile-shear strength.

3.5.6 *Infills in the design of the structure*

The previous Section §3.5.4 showed how, in regularly infilled planar frames, the modelling of ductile infills by means of equivalent elastic struts in linear elastic analyses allows for a good prediction of the seismic demand, in terms of displacement and interstorey drift, at the ULS, while a conservative overestimation is shown at the SLS.
The designer normally neglects the presence of infills in the modelling for the structural design. Thus, the possible use of analysis on bare frames instead of analysis on infilled frames is of some interest. Figure 3.113 shows the deviation of RSA demands evaluated on the bare frame with respect to the ones evaluated by means of NLTH analyses on the infilled frame at the DL and NC limit states together with the bare configurations. The prediction of RSA on the bare frame at the NC limit state tends to be conservative in the evaluation of the maximum roof displacement and interstorey drift for the case study "DCH" (q=4.9) and "DCM" (q=3.9) infilled structures. Only for the "DCM_2" (q=2.7) frame, the prediction is slightly unconservative but anyhow closer than the bare frame layout, for which the underestimation is more pronounced. At the DL limit state, the prediction of RSA for the infilled layout is always conservative; conversely, in bare frame configurations, the prediction of RSA underestimates the NLTH one.
Figure 3.114 compares the interstorey drift demands at the SD and NC limit states evaluated by NLTH analyses for all the structures subjected to the same ground motion sets. With respect to the bare configuration, the interstorey drift demands always reduce and stay well below the drift capacity of the specific limit state. Finally, Figure 3.115 compares the interstorey drift profiles evaluated by RSA analyses on the bare frame with those evaluated by NLTH analyses on infilled configurations. The RSA slightly underestimates the NLTH results by 10 to 15% at the NC limit state for the frame "DCM_2" while providing a conservative prediction at the DL limit state. For the other structures, the RSA results for the bare frame configuration offer a safe-sided evaluation of the maximum drift profile. Given the above results, the presence of the infills seems not to make the seismic demand more severe than evaluated on the bare frame. Designing and evaluating the seismic demands on the bare frame seems like a safe approach for evaluating the seismic demands on the frame structures with sliding joint infills. Further studies are needed to widen the set of case studies to test the role of non-regular distribution of the infills in plan and elevation and the effect of openings.

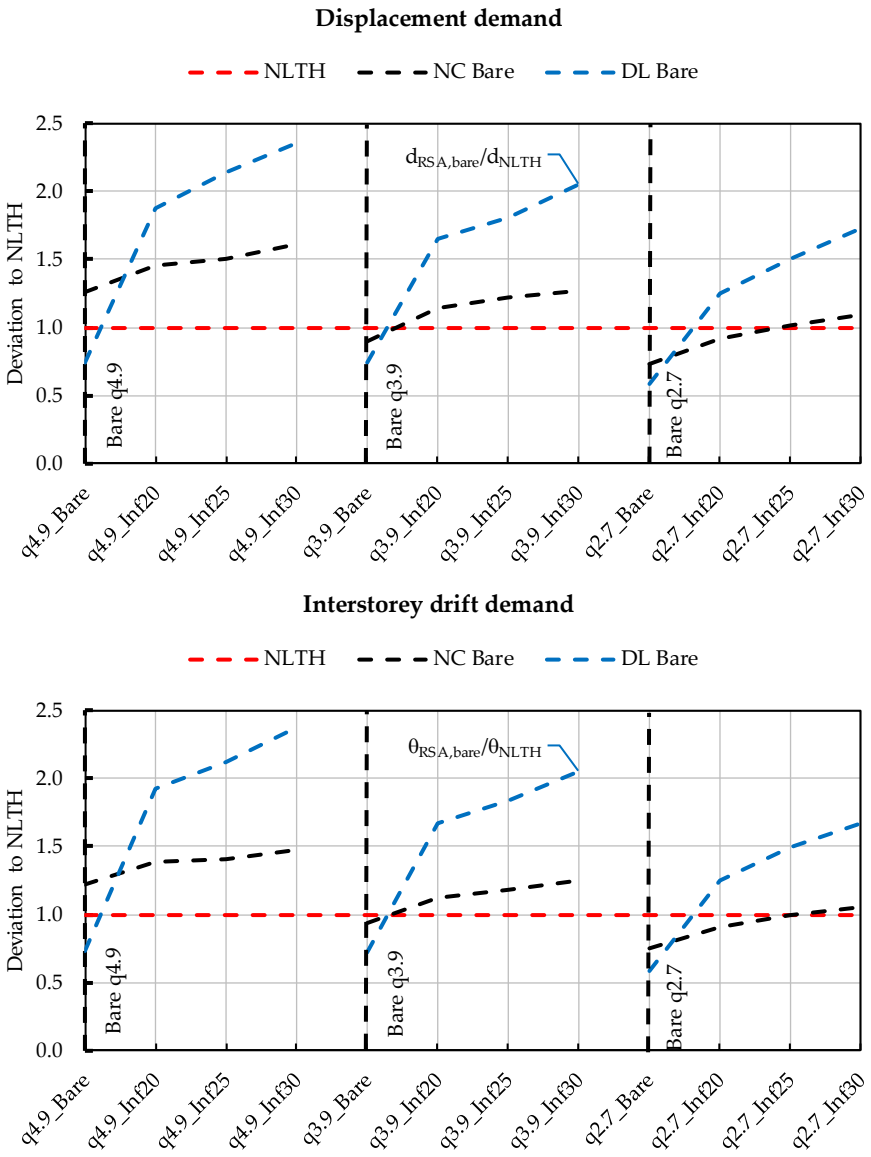

Figure 3.113: Deviation of maximum displacement and interstorey drift demands evaluated by RSA to the NLTH at the DL and NC limit states.

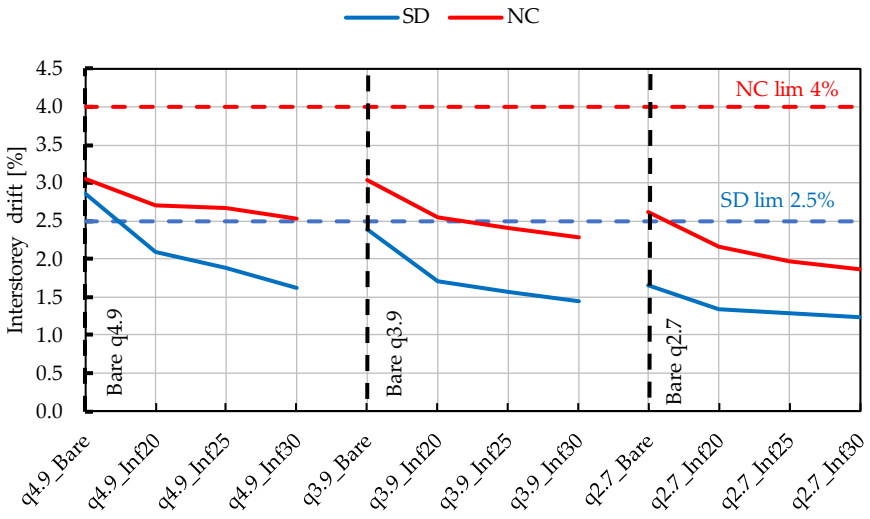

Figure 3.114: Interstorey drift demand evaluated by NLTH analyses and comparison to the interstorey drift limits assumed for ductile infills at the SD and NC limit states.

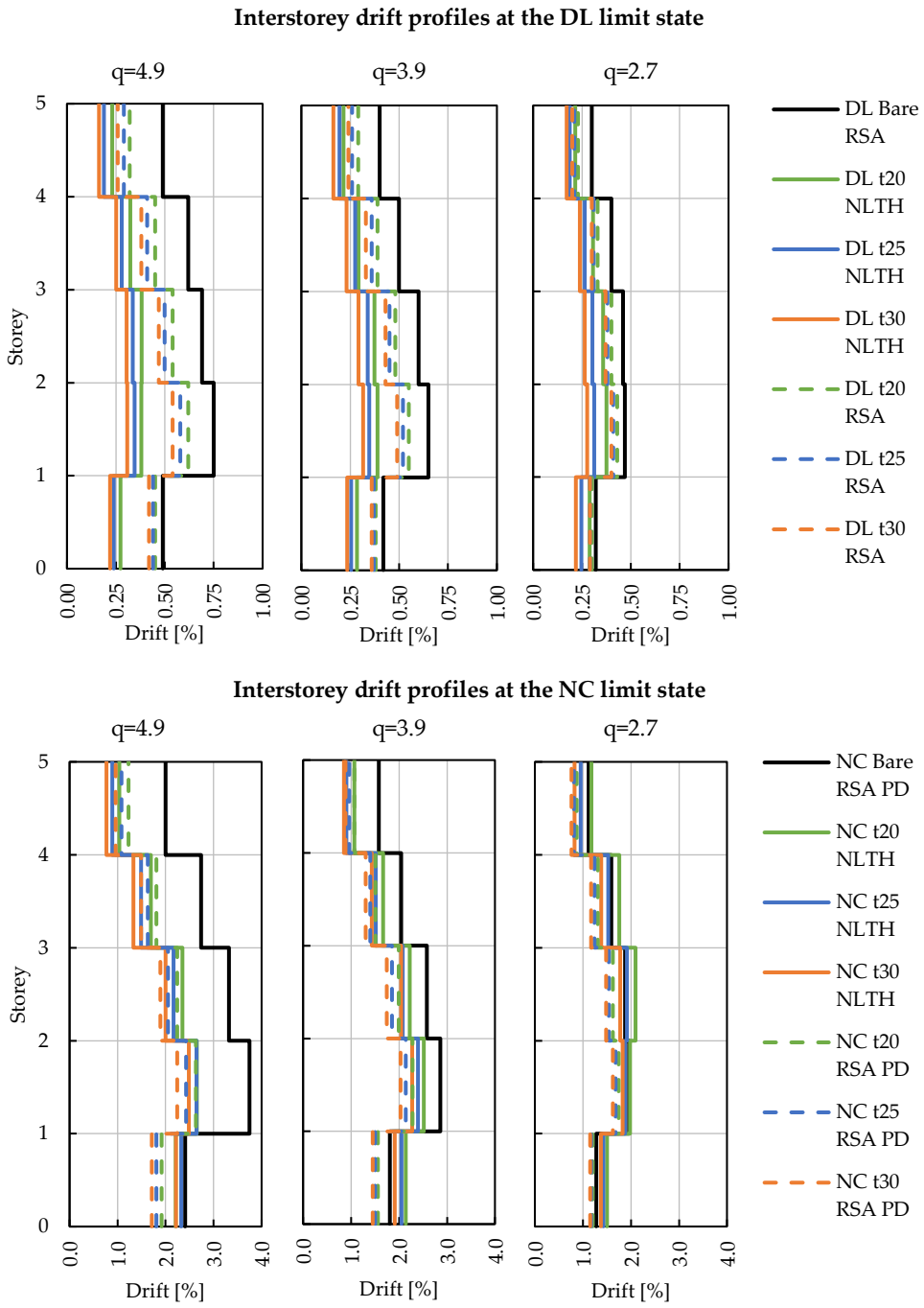

Figure 3.115: Comparison of the interstorey drift profiles evaluated by NLTH analyses to those evaluated on the bare frames by RSAs at DLLS and NCLS for the three frames.

3.5.7 *Behaviour factor*

The role of sliding joint infills in the frame seismic response is here quantified in terms of the capacity-behaviour factor. The behaviour factor is evaluated by accounting for three components, as proposed in the Draft of Eurocode 8 [79], namely the deformation and energy dissipation capacity (q_D), the overstrength due to the redistribution of seismic action effects in redundant structures (q_R), and the overstrength due to other sources (q_S). A specific discussion may address the role of structural period variation when dealing with RSA or PO analyses, but it is beyond the scope of this work. Further details and in-depth analyses on the evaluation of the behaviour factor can be found in Ferraioli (2021) [80], Morandi et al. (2022) [81], and Ricci et al. (2023) [82].
The capacity behaviour factor is evaluated as the product of the following factors. To compare the values of the MDOF to those of the equivalent SDOF, the modal participation factor Γ is adopted.

Overstrength factor, II $$q_{S,II} = \frac{F_{y,design}}{V_{b,d}} \quad (3.5\text{-}3)$$

Overstrength factor, I $$q_{S,I} = \frac{F_{y,mean}}{F_{y,design}} \quad (3.5\text{-}4)$$

Redundancy factor $$q_R = \frac{\Gamma \cdot F_{y,\mathrm{eq}}}{F_{y,mean}} \quad (3.5\text{-}5)$$

Ductility factor $$q_D = \frac{d_{u,eq}}{d_{y,eq}} \quad (3.5\text{-}6)$$

Capacity behaviour factor $$q_c = q_{S,II} \cdot q_{S,I} \cdot q_R \cdot q_D \quad (3.5\text{-}7)$$

It is important to clarify that the $q_{S,II}$ factor was introduced in the definition of the capacity behaviour factor in this work to allow the evaluation of the effective repercussions given by the introduction of ductile infills in a frame structure.

The quantities above recalled are graphically represented in Figure 3.116 on the Modal Push-Over curves and have the following meaning:

- $V_{b,d}$, base shear evaluated in the design of the bare frame, accounting for halved stiffnesses.
- $F_{y,design}$, base shear at the reaching of the first yielding, referring to the design mechanical characteristics f_{cd} and f_{yd}.
- $F_{y,mean}$, base shear at the reaching of the first yielding, referring to the mean mechanical characteristics.
- $F_{y,eq}$, base shear at the yielding of the bilinear backbone associated with the equivalent system.
- $d_{y,eq}$, displacement at the yielding of the bilinear backbone associated with the equivalent system.
- $d_{u,eq}$, ultimate displacement of the bilinear backbone associated with the equivalent system. Evaluated from the MDOF system at the reaching of the conditions explained in §3.4.3.

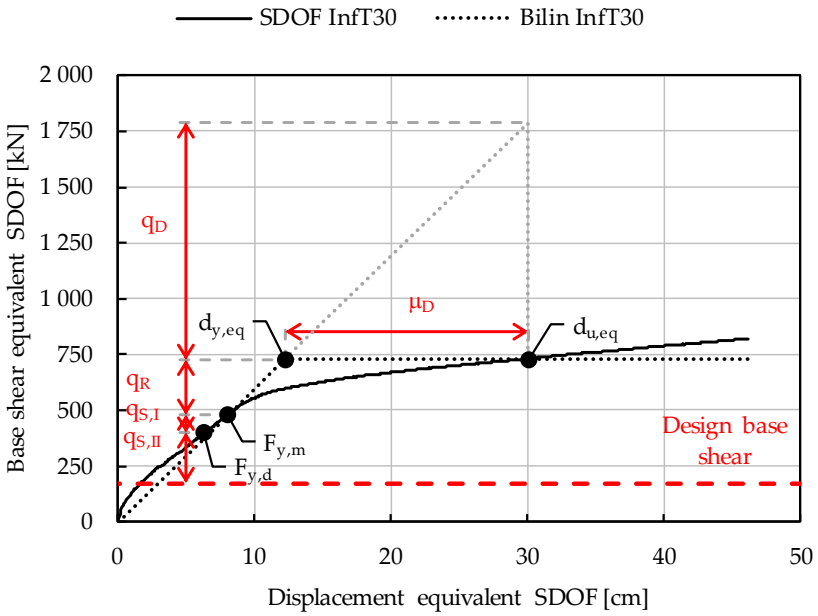

Figure 3.116: Example of significant force and displacement levels for the evaluation of the capacity behaviour factor, represented on the modal Push-Over curve for the case study DCH infilled by 300mm thick infill.

Figure 3.117 represents the variation of each factor contributing to the behaviour factor, as calculated for the case studies analysed. For each case study, two different options are considered for the attainment of the SDLS and NCLS conditions:

accounting (dotted lines) or not (continuous lines) for the interstorey drift limit of 2.5% and 4.0% at SDLS and NCLS, respectively. Note that the overstrength factors $q_{S,II}$ and $q_{S,I}$ are represented by the same curves because they do not depend on displacement capacity of the structure. The graph shows that, in the infilled configurations, the overstrength ratio $q_{S,II}$ (the ratio of the effective design yielding, $F_{y,design}$, to the design base shear, $V_{b,d}$) increases significantly. In fact, infills, by supplying additional lateral strength, increase the action of the first frame plastic hinge activation. This phenomenon is pronounced in the DCH frame, where the share of the infill contribution is larger and increases with the infill strength (thickness). The ductility factors (comparable to q_D) decrease as the infills are introduced. A lower influence is shown if no limit to the interstorey drift is considered.

Figure 3.118 represents the main points considered for the bare frame "DCH" and the one with stronger infills (300mm thickness). The figure highlights the previous consideration. Vice versa, the effect is reduced as the design behaviour factor reduces and the structure becomes stiffer.

Unlike in the literature, for the purposes of this work, the $q_{S,II}$ factor is considered in the evaluation of the behaviour factor to allow the comparison of the seismic performances of the structure when ductile infills are introduced. This term is strictly related to the overstrength of the structure at the first design yielding with respect to the design action. In other words, in the bare frame, it is related to the abundance in the proportioning of the frame. In this specific case, the design of the bare frames is optimised to reach a safety ratio close to 1, as clearly shown in Figure 3.117 by the $q_{S,II}$ factors of the bare frames. Instead, in the infilled configuration, infills act as a seismic-resistant system parallel to the frame, which postpones the plasticization of the frame. This phenomenon can only be considered in the contribution discussed.

Figure 3.119 represents the trend of the capacity behaviour at SD accounting or not, the $q_{S,II}$ factor. If the factor is neglected, the behaviour factor decreases negligibly when infills are introduced, and vice versa, if it is accounted for, the behaviour factor always increases. Figure 3.120 shows the obtained behaviour factors at SD and NC limit states. The global capacity behaviour factors always increase as the infills are introduced and as their thickness increases. The same trend is exhibited by both the limit states considered and by considering or not considering the interstorey drift limits. In the graph, the behaviour factor assumed in the design is also reported. If no limits to the interstorey drift are considered, the capacity behaviour factor is always higher than the design one. When drift limits are considered, the capacity behaviour factor is lower than the design one only in the bare configuration. This is justified because the interstorey drifts do not concern the RC frame, but rather an added condition imposed to preserve the infills.

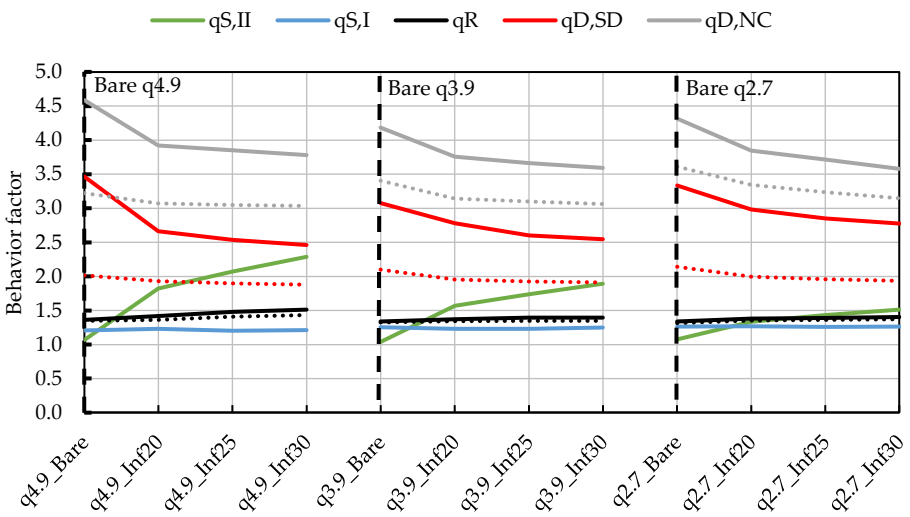

Figure 3.117: Contributions to the capacity behaviour factor. Continuous lines represent the values obtained by neglecting limits for the interstorey drifts. If they are considered, dotted lines represent the results. The overstrength factors $q_{S,II}$ and $q_{S,I}$ are the same for both the cases and the limit states.

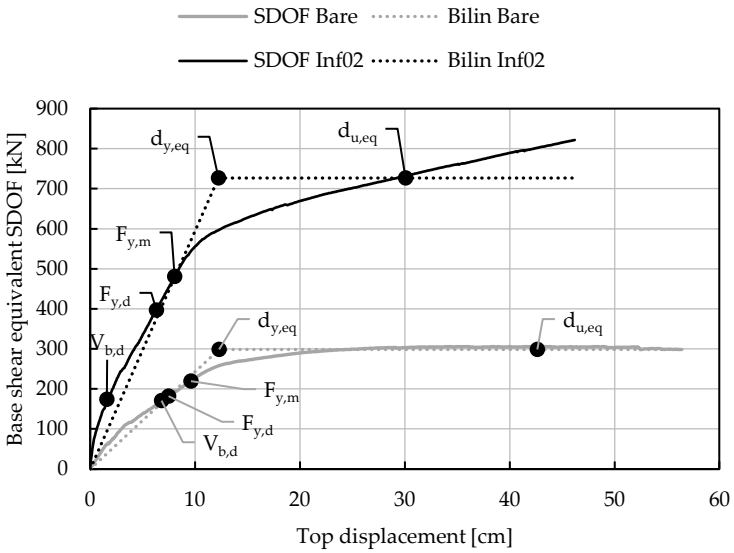

Figure 3.118: Representation of the main points on the SDOF equivalent systems of the bare frame "DCH" and the infilled one with an infill 300mm thick.

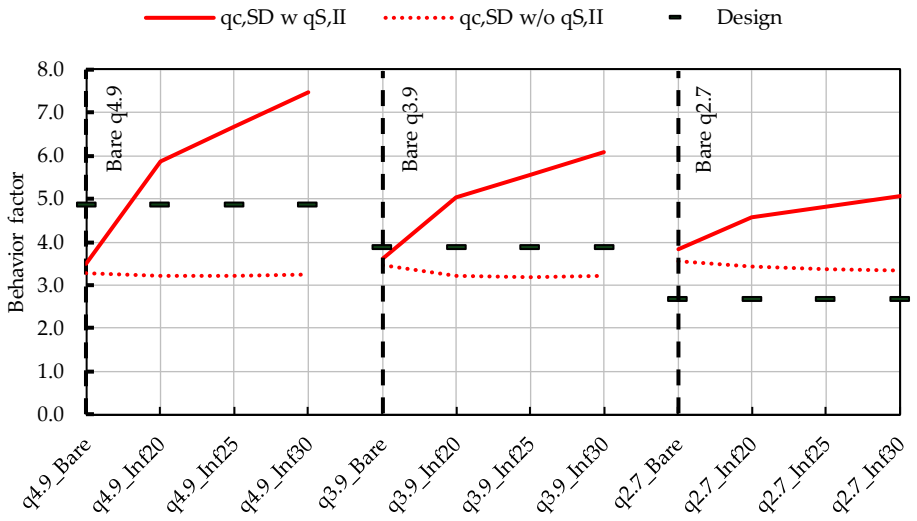

Figure 3.119: Behaviour factor at SD evaluated by considering ("qc,SD w qS,II") or not ("qc,SD w qS,II") the $q_{S,II}$ factor.

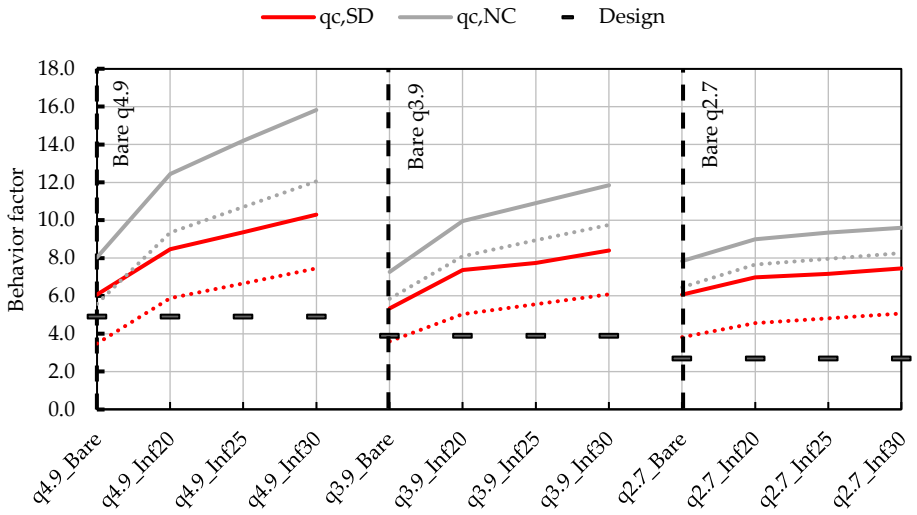

Figure 3.120: Capacity behaviour factor at SDLS and NCLS of the case studies analysed. Continuous and dotted lines represent the values obtained accounting for or not the interstorey drift limits for infilled frame capacity. Dashed lines quantify the behaviour factor adopted in the design of the bare frame structure.

4 CONCLUSIONS AND FURTHER INVESTIGATIONS

4.1 Conclusions

Many construction techniques for non-structural masonry infills have been proposed in the last few years by researchers to reduce the detrimental effect of the infill-frame interaction and mitigate the infill damage. These solutions have been experimentally tested, but indications to design the infill itself and the structure to account for the local interaction of masonry panels are required. Parametric analyses to understand the role of design parameters in both the local and global response are needed to support the definition of design guidelines. This thesis aims to contribute to filling the gap in the deformable infill solution proposed at the University of Brescia. The solution consists of a ductile infill in which the masonry panel is subdivided by horizontal sliding joints where the deformation of the mechanism is concentrated. The insertion of a low-strength material at the contact between the infill and the columns protects the masonry from crushing and limits the infill thrust on the columns. A numerical parametric analysis is presented, which studies the sensitivity of the infilled frame response to the main design parameters and describes feasible alternative construction details. Specifically, the use of a deformable elastic material at the contact between the infill and the surrounding frame instead of a ductile plastic one is investigated. Analytical design equations are proposed that are capable of reasonably capturing the response described by a refined mesoscale FEM analysis, allowing the calibration of strut macromodels to be used in the modelling of global frame structures. It should be noted that the proposal applies to the range of parameters analysed in this work: stiffness of the contact material in the range of 7.5–60 MPa and up to an interstorey drift level of 3.0%.
The following main results are drawn:

- The elastic stiffness of the top joint between the panel and the above beam modifies the lateral strength of the infilled frame, which increases with the stiffness of the top joint. The shear action on the columns and the triggering of the infill damage are not significantly modified by the infill-to-beam contact or by the stiffness of the top joint.
- The elastic stiffness of the lateral joint between the panel and the columns affects the lateral strength of the infilled frame, the maximum shear action in the columns, and the activation of the first damage in the infill in both configurations, with and without panel-to-top beam contact. Larger stiffness of the lateral joint implies higher shear action in the column and the reaching of the first crushing in the masonry corners at lower drift.

- The presence of at least two sliding joints allows for ductile behaviour, but three sliding joints are required to prevent local masonry crushing before 2.5% interstorey drift.
- Regarding the masonry characteristics, the behaviour depends on the combination of thickness, stiffness, and strength. A design limitation of the lateral joint stiffness at the column interface is proposed as a function of the masonry mechanical properties and the target interstorey drift amplitude.

The analytical model previously proposed by Preti et al. for sliding joint infills is here extended to account for the adoption of an elastic contact material in between the infill and the surrounding frame.

- The infill-to-column contact depth at the lateral joints is empirically calibrated as a function of the elastic stiffness of the contact material and of the interstorey drift.
- The use of a deformable material at the contact between the infill and the columns requires the calibration of the inclination of the contact forces on the windward side; an empirical equation is calibrated as a function of the elastic stiffness of the contact material.
- The modified analytical model is tested to evaluate the shear actions due to the infill and the lateral strength of the infill. The parametric analyses of the stiffness of the contact material and the length of the infill are considered.

The second part of the work quantified the contribution of ductile infills to the global structural frame response. In nonlinear analyses, infills are represented by nonlinear equivalent struts. In response spectrum analyses (RSA), a secant stiffness of 1% drift of the analytical backbone of the infill is proposed to represent the infill contribution in the prediction of deformation demands on the structure by means of elastic concentric struts.
The following main results are drawn:

- Static nonlinear analyses show that infills increase both the strength and initial stiffness of the system. The displacement capacity of the structure is slightly reduced, but displacement demands are reduced consistently or even more. The global collapse mechanism is not significantly altered, and no soft storey was observed in the case of a regular infill distribution layout.
- Nonlinear time history analyses show that the seismic demand (top displacement and maximum interstorey drift) is reduced if infills are introduced in the bare frame structural model, with absolute values decreasing as the strength and stiffness of the ductile infill increase.
- Floor spectra are derived for the bare and infilled frame case studies. Maximum amplifications occur at the two main equivalent vibration periods. In the infilled configuration, the peaks are shifted to lower periods. A

reduction, with respect to the bare configurations, of the peak accelerations is shown at the SLS, while an amplification is shown at the first mode at the ULS.

- In the regular planar frames under consideration, the N2 nonlinear analysis method estimates the seismic demands (top displacement and interstorey drift) of the nonlinear time history analyses with at least the same accuracy as for bare frames. At the serviceability limit states, seismic demands are largely overestimated.
- Neglecting infills in the design of structures appears conservative in the estimation of the seismic demands (top displacement and interstorey drift) when ductile infills are present in the structure.
- In the regularly infilled frame examined in this work, the modelling approach proposed to account for infills in linear analyses has been shown to estimate the seismic demand with the same accuracy as the modal pushover analysis.
- Shear overload to the columns due to the infill-frame interaction must be considered in the structure design to avoid brittle failures. Specifically, the shear contribution due to the infill thrust must be added to the shear action of the bare frame.
- The nonlinear static analyses were used to assess the influence of the presence of ductile infills on the capacity-behaviour factor. Ductile infills increase the lateral strength of the structure and postpone its first design yielding at a larger base shear. Consequently, the evaluation of the behaviour factor, as generally conducted, should also consider the overstrength contribution, in terms of base shear, at the reaching of the first design yielding with respect to the design action. The resultant factor does not decrease when infills are introduced.

Consequently, the study highlighted that if deformable infills are introduced, the overall ductile behaviour of the frame is not significantly modified. The seismic demands in terms of maximum displacement and maximum interstorey drift are reduced. The preliminary assessment of the capacity behaviour factor for such structures does not show a reduction due to the ductile infill contribution. For the case study analysed, the modelling of ductile infills by elastic struts in response spectrum analyses allowed for efficient quantification of the displacement demand estimated by nonlinear analyses. If the designer neglects ductile infills in the frame design, the estimated seismic demands seem conservative. The overload shear action must be accounted for in the design of the columns anyway.

4.2 Further investigations

The studies conducted in this work have highlighted some aspects of interest to be further investigated:

- Extend the detailed parametric analysis to account for different infill characteristics (mechanical properties and thickness) and different frame and frame member geometries.
- Upgrade the analytical design equation for the prediction of the infill response to account for the contributions given by the panel-to-top beam contact and the presence of a continuous plaster layer on the infill surfaces.
- Validate the analytical model for different infill and frame characteristics.
- Evaluate the infill-frame interaction in terms of changes in column deformation and the repercussions on the hierarchy of strengths.
- Provide design considerations to account for the shear increase due to the infill thrust in the design phase of the frame.
- Evaluate the energy dissipated and the viscous damping coefficient of the system and compare the results to those of the bare frame and the infilled one with traditional infills.
- Extend the results to existing structures.
- Further studies are needed to widen the set of case studies to test the role of non-regular distribution of the infills in plan and elevation, the effect of openings, and the more accurate definition of the limit for the design behaviour factor.
- Extend the work to account for the out-of-plane behaviour.

5 REFERENCES

[1] F. Braga, V. Manfredi, A. Masi, A. Salvatori, e M. Vona, «Performance of non-structural elements in RC buildings during the L'Aquila, 2009 earthquake», *Bull Earthquake Eng*, vol. 9, fasc. 1, pp. 307–324, feb. 2011, doi: 10.1007/s10518-010-9205-7.

[2] R. Fikri, D. Dizhur, K. Walsh, e J. Ingham, «Seismic performance of Reinforced Concrete Frame with Masonry Infill buildings in the 2010/2011 Canterbury, New Zealand earthquakes», *Bull Earthquake Eng*, vol. 17, fasc. 2, pp. 737–757, feb. 2019, doi: 10.1007/s10518-018-0476-8.

[3] F. Parisi, F. D. Luca, F. Petruzzelli, R. D. Risi, E. Chioccarelli, e I. Iervolino, «Field inspection after the May 20th and 29th 2012 Emilia- Romagna earthquakes».

[4] G. M. Verderame, F. De Luca, P. Ricci, e G. Manfredi, «Preliminary analysis of a soft-storey mechanism after the 2009 L'Aquila earthquake», *Earthq Engng Struct Dyn*, vol. 40, fasc. 8, pp. 925–944, lug. 2011, doi: 10.1002/eqe.1069.

[5] R. Langenbach, «From "Opus Craticium" to the "Chicago Frame": Earthquake-Resistant Traditional Construction*», *International Journal of Architectural Heritage*, vol. 1, fasc. 1, pp. 29–59, mar. 2007, doi: 10.1080/15583050601125998.

[6] M. Mohammadi e V. Akrami, «An engineered infilled frame: Behavior and calibration», *Journal of Constructional Steel Research*, vol. 66, fasc. 6, pp. 842–849, giu. 2010, doi: 10.1016/j.jcsr.2010.01.008.

[7] X. Cheng *et al.*, «A new construction technology suitable for frame partitioned infill walls with sliding nodes and large openings: Test results», *Construction and Building Materials*, vol. 258, p. 119644, ott. 2020, doi: 10.1016/j.conbuildmat.2020.119644.

[8] S. Dorji, H. Derakhshan, e D. P. Thambiratnam, «Experimental investigation of semi-interlocking mortarless masonry-infilled frames», *Structures*, vol. 43, pp. 1913–1931, set. 2022, doi: 10.1016/j.istruc.2022.07.004.

[9] R.-S. Ju, H.-J. Lee, C.-C. Chen, e C.-C. Tao, «Experimental study on separating reinforced concrete infill walls from steel moment frames», *Journal of Constructional Steel Research*, vol. 71, pp. 119–128, apr. 2012, doi: 10.1016/j.jcsr.2011.10.004.

[10] K. Lin, Y. Totoev, H. Liu, e T. Guo, «In-Plane Behaviour of a Reinforcement Concrete Frame with a Dry Stack Masonry Panel», *Materials*, vol. 9, fasc. 2, p. 108, feb. 2016, doi: 10.3390/ma9020108.

[11] H. Lyu, M. Deng, Y. Han, F. Ma, e Y. Zhang, «In-plane cyclic testing of full-scale reinforced concrete frames with innovative isolated infill walls strengthened by highly ductile concrete», *Journal of Building Engineering*, vol. 57, p. 104934, ott. 2022, doi: 10.1016/j.jobe.2022.104934.

[12] M. Marinković e C. Butenweg, «Experimental testing of decoupled masonry infills with steel anchors for out-of-plane support under combined in-plane and out-of-plane seismic loading», *Construction and Building Materials*, vol. 318, p. 126041, feb. 2022, doi: 10.1016/j.conbuildmat.2021.126041.

[13] M. Marinković e C. Butenweg, «Innovative decoupling system for the seismic protection of masonry infill walls in reinforced concrete frames», *Engineering Structures*, vol. 197, p. 109435, ott. 2019, doi: 10.1016/j.engstruct.2019.109435.

[14] P. Morandi, R. R. Milanesi, e G. Magenes, «Innovative solution for seismic-resistant masonry infills with sliding joints: in-plane experimental performance», *Engineering Structures*, vol. 176, pp. 719–733, dic. 2018, doi: 10.1016/j.engstruct.2018.09.018.

[15] M. Preti, L. Migliorati, e E. Giuriani, «Experimental testing of engineered masonry infill walls for post-earthquake structural damage control», *Bull Earthquake Eng*, vol. 13, fasc. 7, pp. 2029–2049, lug. 2015, doi: 10.1007/s10518-014-9701-2.

[16] M. Preti, N. Bettini, e G. Plizzari, «Infill Walls with Sliding Joints to Limit Infill-Frame Seismic Interaction: Large-Scale Experimental Test», *Journal of Earthquake Engineering*, vol. 16, fasc. 1, pp. 125–141, gen. 2012, doi: 10.1080/13632469.2011.579815.

[17] M. Preti e V. Bolis, «Masonry infill construction and retrofit technique for the infill-frame interaction mitigation: Test results», *Engineering Structures*, vol. 132, pp. 597–608, feb. 2017, doi: 10.1016/j.engstruct.2016.11.053.

[18] A. S. Tasligedik e S. Pampanin, «Rocking Cantilever Clay Brick Infill Wall Panels: A Novel Low Damage Infill Wall System», *Journal of Earthquake Engineering*, vol. 21, fasc. 7, pp. 1023–1049, ott. 2017, doi: 10.1080/13632469.2016.1190797.

[19] A. V. Tsantilis e T. C. Triantafillou, «Innovative seismic isolation of masonry infills using cellular materials at the interface with the surrounding RC frames», *Engineering Structures*, vol. 155, pp. 279–297, gen. 2018, doi: 10.1016/j.engstruct.2017.11.025.

[20] M. Vailati, G. Di Gangi, e G. Quaranta, «Thermo-mechanical characterization and hysteretic behavior identification of innovative plastic joint for masonry infills in reinforced concrete buildings», *Journal of Building Engineering*, vol. 65, p. 105803, apr. 2023, doi: 10.1016/j.jobe.2022.105803.

[21] M. Vailati e G. Monti, «Recycled-plastic joints for earthquake resistant infill panels», 2014.

[22] T. Y. P. Yuen, H. Zhang, J. S. Kuang, e Q. Huang, «Shake table tests on RC frame infilled by slitted masonry panels», *Bull Earthquake Eng*, vol. 16, fasc. 9, pp. 4027–4052, set. 2018, doi: 10.1007/s10518-018-0339-3.

[23] C. Zhang *et al.*, «Experimental and numerical studies of improving cyclic behavior of infilled reinforced concrete frame by prefabricated wall panels with

sliding joints», *Journal of Building Engineering*, vol. 77, p. 107524, ott. 2023, doi: 10.1016/j.jobe.2023.107524.

[24] A. Furtado, H. Rodrigues, A. Arêde, e H. Varum, «Experimental tests on strengthening strategies for masonry infill walls: A literature review», *Construction and Building Materials*, vol. 263, p. 120520, dic. 2020, doi: 10.1016/j.conbuildmat.2020.120520.

[25] T. Rousakis *et al.*, «Deformable Polyurethane Joints and Fibre Grids for Resilient Seismic Performance of Reinforced Concrete Frames with Orthoblock Brick Infills», *Polymers*, vol. 12, fasc. 12, p. 2869, nov. 2020, doi: 10.3390/polym12122869.

[26] X. Palios, M. N. Fardis, E. Strepelias, e S. N. Bousias, «Unbonded brickwork for the protection of infills from seismic damage», *Engineering Structures*, vol. 131, pp. 614–624, gen. 2017, doi: 10.1016/j.engstruct.2016.10.027.

[27] R. R. Milanesi, P. Morandi, C. F. Manzini, L. Albanesi, e G. Magenes, «Out-of-plane Response of an Innovative Masonry Infill with Sliding Joints from Shaking Table Tests», *Journal of Earthquake Engineering*, vol. 26, fasc. 4, pp. 1789–1823, mar. 2022, doi: 10.1080/13632469.2020.1739173.

[28] V. Bolis, A. Paderno, e M. Preti, «Experimental assessment of an innovative isolation technique for the seismic downgrade of existing masonry infills», in *Brick and Block Masonry - From Historical to Sustainable Masonry*, 1ª ed., J. Kubica, A. Kwiecień, e Ł. Bednarz, A c. di, CRC Press, 2020, pp. 935–942. doi: 10.1201/9781003098508-133.

[29] P. J. B. B. Lourenço, *Computational strategies for masonry structures*. Delft: Delft Univ. Press, 1996.

[30] V. Bolis, A. Stavridis, e M. Preti, «Numerical Investigation of the In-Plane Performance of Masonry-Infilled RC Frames with Sliding Subpanels», *J. Struct. Eng.*, vol. 143, fasc. 2, p. 04016168, feb. 2017, doi: 10.1061/(ASCE)ST.1943-541X.0001651.

[31] M. Marinković e C. Butenweg, «Numerical analysis of the in-plane behaviour of decoupled masonry infilled RC frames», *Engineering Structures*, vol. 272, p. 114959, dic. 2022, doi: 10.1016/j.engstruct.2022.114959.

[32] P. K. Dhir, E. Tubaldi, B. Pantò, e I. Caliò, «A macro-model for describing the in-plane seismic response of masonry-infilled frames with sliding/flexible joints», *Earthq Engng Struct Dyn*, vol. 51, fasc. 12, pp. 3022–3044, ott. 2022, doi: 10.1002/eqe.3714.

[33] M. Preti, V. Bolis, e A. Stavridis, «Seismic infill–frame interaction of masonry walls partitioned with horizontal sliding joints: analysis and simplified modeling», *Journal of Earthquake Engineering*, vol. 23, fasc. 10, Art. fasc. 10, nov. 2019, doi: 10.1080/13632469.2017.1387195.

[34] F. Di Trapani, V. Bolis, F. Basone, e M. Preti, «Seismic reliability and loss assessment of RC frame structures with traditional and innovative masonry

infills», *Engineering Structures*, vol. 208, p. 110306, apr. 2020, doi: 10.1016/j.engstruct.2020.110306.

[35] A. Stavridis e P. B. Shing, «Finite-Element Modeling of Nonlinear Behavior of Masonry-Infilled RC Frames», *J. Struct. Eng.*, vol. 136, fasc. 3, Art. fasc. 3, mar. 2010, doi: 10.1061/(ASCE)ST.1943-541X.116.

[36] R. L. Taylor e S. Govindjee, «FEAP - - A Finite Element Analysis Program», vol. University of California, Berkeley, p. 705, 2014.

[37] H. R. Lotfi e P. B. Shing, «An appraisal of smeared crack models for masonry shear wall analysis», *Computers & Structures*, vol. 41, fasc. 3, Art. fasc. 3, gen. 1991, doi: 10.1016/0045-7949(91)90134-8.

[38] H. R. Lotfi e P. B. Shing, «Interface Model Applied to Fracture of Masonry Structures», *Journal of Structural Engineering*, vol. 120, fasc. 1, Art. fasc. 1, gen. 1994, doi: 10.1061/(ASCE)0733-9445(1994)120:1(63).

[39] G. M. Calvi e D. Bolognini, «Seismic response of reinforced concrete frames infilled with weakly reinforced masonry panels», *Journal of Earthquake Engineering*, vol. 5, fasc. 2, pp. 153–185, apr. 2001, doi: 10.1080/13632460109350390.

[40] A. Stavridis, «PhD_Th_Stavridis, 2009.pdf», Ph.D. thesis, Univ. of California, 2009.

[41] M. Preti, N. Bettini, L. Migliorati, V. Bolis, A. Stavridis, e G. A. Plizzari, «Analysis of the in-plane response of earthen masonry infill panels partitioned by sliding joints: In-plane Response of Earthen Masonry Infill Panels with Sliding Joints», *Earthquake Engng Struct. Dyn.*, vol. 45, fasc. 8, Art. fasc. 8, lug. 2016, doi: 10.1002/eqe.2703.

[42] R. R. Milanesi, «PhD_Thesis_Riccardo Milanesi», Ph.D. thesis, 2016.

[43] E. J. Setzler e H. Sezen, «Model for the Lateral Behavior of Reinforced Concrete Columns Including Shear Deformations», *Earthquake Spectra*, vol. 24, fasc. 2, pp. 493–511, mag. 2008, doi: 10.1193/1.2932078.

[44] T. Paulay e M. J. N. Priestley, *Seismic design of reinforced concrete and masonry buildings*. New York: Wiley, 1992.

[45] M. J. N. Priestley, G. M. Calvi, e M. J. Kowalsky, *Displacement-Based Seismic Design of Structures*, vol. 24. 2008. Consultato: 1 marzo 2023. [Online]. Disponibile su: http://journals.sagepub.com/doi/10.1193/1.2932170

[46] E. Spacone, F. C. Filippou, e F. F. Taucer, «Fibre beam-column model for non-linear analysis of R/C frames: Part I. Formulation», *Earthquake Engng. Struct. Dyn.*, vol. 25, fasc. 7, pp. 711–725, lug. 1996, doi: 10.1002/(SICI)1096-9845(199607)25:7<711::AID-EQE576>3.0.CO;2-9.

[47] M. H. Scott e G. L. Fenves, «Plastic Hinge Integration Methods for Force-Based Beam–Column Elements», *J. Struct. Eng.*, vol. 132, fasc. 2, pp. 244–252, feb. 2006, doi: 10.1061/(ASCE)0733-9445(2006)132:2(244).

[48] S. Sritharan, M. J. N. Priestley, e F. Seible, «Nonlinear finite element analyses of concrete bridge joint systems subjected to seismic actions», *Finite Elements in Analysis and Design*, 2000.

[49] *EN 1998-3:2005 Eurocode 8: Design of structures for earthquake resistance - Part 3: Assessment and retrofitting of buildings*. 2005.

[50] M. J. N. Priestley, F. Seible, e G. M. Calvi, *Seismic design and retrofit of bridges*. New York: Wiley, 1996.

[51] J. Zhao e S. Sritharan, «Modeling of Strain Penetration Effects in Fiber-Based Analysis of Reinforced Concrete Structures», *ACI Structural Journal*, 2007.

[52] F. McKenna, G. Fenves, e F. C. Filippou, «Open System for Earthquake Engineering Simulation (OpenSees)». 2000.

[53] W. M. Ghannoum e J. P. Moehle, «Dynamic Collapse Analysis of a Concrete Frame Sustaining Column Axial Failures», *SJ*, vol. 109, fasc. 3, 2012, doi: 10.14359/51683754.

[54] D. E. Lehman e J. P. Moehle, «Seismic Performance of Well-Confined Concrete Bridge Columns», Pacific earthquake engineering research center, PEER 1998/01, 1998.

[55] Applied Technology Council, «Guidelines for Nonlinear Structural Analysis for Design of Buildings - Part IIb – Reinforced Concrete Moment Frames», apr. 2017. doi: 10.6028/NIST.GCR.17-917-46v3.

[56] J. B. Mander, «Seismic design of bridge piers», Theses/Dissertations, University of Canterbury. Civil Engineering, University of Canterbury, 1983.

[57] J. B. Mander, M. J. N. Priestley, e R. Park, «Theoretical Stress-Strain Model for Confined Concrete», *J. Struct. Eng.*, vol. 114, fasc. 8, pp. 1804–1826, set. 1988, doi: 10.1061/(ASCE)0733-9445(1988)114:8(1804).

[58] *«D.M. 17/01/2018 - Norme Tecniche per le Costruzioni»*. 2018.

[59] *EN 1992-1-1:2004 Eurocode 2: Design of Concrete Structures - Part 1-1: General Rules and Rules for Buildings*. 2004.

[60] V. Bolis, M. Preti, e A. Stavridis, «Simplified modeling of masonry infill walls with horizontal sliding joints», in *Proceedings of the 6th International Conference on Computational Methods in Structural Dynamics and Earthquake Engineering (COMPDYN 2015)*, Rhodes Island, Greece: Institute of Structural Analysis and Antiseismic Research School of Civil Engineering National Technical University of Athens (NTUA) Greece, 2017, pp. 3367–3379. doi: 10.7712/120117.5651.18605.

[61] «The Math Works, Inc. MATLAB». The MathWorks, Inc., Natick, Massachusetts, 19 giugno 2023. [Online]. Disponibile su: https://www.mathworks.com

[62] M. N. Fardis, *Seismic Design, Assessment and Retrofitting of Concrete Buildings*, vol. 8. in Geotechnical, Geological, and Earthquake Engineering, vol. 8. Dordrecht: Springer Netherlands, 2009. doi: 10.1007/978-1-4020-9842-0.

[63] F. C. Filippou, E. P. Popov, e V. V. Bertero, *Effects of bond deterioration on hysteretic behavior of reinforced concrete joints*. in Report (University of California, Berkeley. Earthquake Engineering Research Center), no. no. UCB/EERC-83/19. University of California: Berkeley, Calif. : Earthquake Engineering Research Center, 1983.

[64] M. Menegotto e P. E. Pinto, «Method of analysis of cyclically loaded RC plane frames including changes in geometry and non-elastic behavior of elements under normal force and bending», presentato al IABSE Symp. on Resistance and Ultimate Deformability of Structures Acted on by Well Defined Repeated Loads, Zurich, Switzerland: International Association for Bridge and Structural Engineering, 1973.

[65] CEB-FIP Model Code, *fib Model Code for Concrete Structures*. 2010, p. 436.

[66] M. Di Ludovico, G. M. Verderame, A. Prota, G. Manfredi, e E. Cosenza, «Cyclic Behavior of Nonconforming Full-Scale RC Columns», *J. Struct. Eng.*, vol. 140, fasc. 5, Art. fasc. 5, mag. 2014, doi: 10.1061/(ASCE)ST.1943-541X.0000891.

[67] A. Meda, S. Mostosi, Z. Rinaldi, e P. Riva, «Experimental evaluation of the corrosion influence on the cyclic behaviour of RC columns», *Engineering Structures*, vol. 76, pp. 112–123, ott. 2014, doi: 10.1016/j.engstruct.2014.06.043.

[68] P. Morandi, S. Hak, e G. Magenes, «Performance-based interpretation of in-plane cyclic tests on RC frames with strong masonry infills», *Engineering Structures*, vol. 156, pp. 503–521, feb. 2018, doi: 10.1016/j.engstruct.2017.11.058.

[69] F. A. Charney, «Unintended Consequences of Modeling Damping in Structures», *J. Struct. Eng.*, vol. 134, fasc. 4, pp. 581–592, apr. 2008, doi: 10.1061/(ASCE)0733-9445(2008)134:4(581).

[70] A. K. Chopra e F. McKenna, «Modeling viscous damping in nonlinear response history analysis of buildings for earthquake excitation», *Earthq Engng Struct Dyn*, vol. 45, fasc. 2, pp. 193–211, feb. 2016, doi: 10.1002/eqe.2622.

[71] J. F. Hall, «Discussion of 'Modelling viscous damping in nonlinear response history analysis of buildings for earthquake excitation' by Anil K. Chopra and Frank McKenna», *Earthq Engng Struct Dyn*, vol. 45, fasc. 13, pp. 2229–2233, ott. 2016, doi: 10.1002/eqe.2761.

[72] A. K. Chopra e F. McKenna, «Response to John Hall's Discussion (EQE-16-0008) to Chopra and McKenna's paper, 'Modeling viscous damping in nonlinear response history analysis of buildings for earthquake excitation'», *Earthq Engng Struct Dyn*, vol. 45, fasc. 13, pp. 2235–2238, ott. 2016, doi: 10.1002/eqe.2762.

[73] E. Smyrou, M. J. N. Priestley, e A. J. Carr, «Modelling of elastic damping in nonlinear time-history analyses of cantilever RC walls», *Bull Earthquake Eng*, vol. 9, fasc. 5, pp. 1559–1578, ott. 2011, doi: 10.1007/s10518-011-9286-y.

[74] «MidasGen». MIDAS Information Technology Co., Ltd., 2023. [Online]. Disponibile su: https://www.midasoft.com/

[75] *EN 1998-1:2013 Eurocode 8: Design of Structures for Earthquake Resistance - Part 1: General Rules, Seismic Actions and Rules for Buildings*. 2013.

[76] S. Sgobba *et al.*, «The online graphical user interface of REXELweb for the selection of accelerograms from the Engineering Strong Motion database (ESM)», presentato al 39° Convegno Nazionale Gruppo Nazionale Geofisica della Terra Solida (GNGTS), giu. 2021.

[77] A. Rutenberg, «Simplified P-Delta Analyses for Asymmetric Structures», *J. Struct. Div.*, vol. 108, fasc. 9, pp. 1995–2013, set. 1982, doi: 10.1061/JSDEAG.0006038.

[78] P. Fajfar, «A Nonlinear Analysis Method for Performance-Based Seismic Design», *Earthquake Spectra*, vol. 16, fasc. 3, pp. 573–592, ago. 2000, doi: 10.1193/1.1586128.

[79] *Final Draft EN1998–1–2 NEN SC8 PT2 2019b–11–08 Draft Eurocode 8: Design of structures for earthquake resistance - Part 1–2: Rules for new buildings*. 2019.

[80] M. Ferraioli, «Behaviour Factor of Ductile Code-Designed Reinforced Concrete Frames», *Advances in Civil Engineering*, vol. 2021, pp. 1–18, feb. 2021, doi: 10.1155/2021/6666687.

[81] P. Morandi, C. Butenweg, K. Breis, K. Beyer, e G. Magenes, «Latest findings on the behaviour factor q for the seismic design of URM buildings», *Bull Earthquake Eng*, vol. 20, fasc. 11, pp. 5797–5848, set. 2022, doi: 10.1007/s10518-022-01419-7.

[82] P. Ricci, M. Di Domenico, e G. M. Verderame, «Behaviour factor and seismic safety of reinforced concrete structures designed according to Eurocodes», *Structures*, vol. 55, pp. 677–689, set. 2023, doi: 10.1016/j.istruc.2023.06.060.

APPENDIX A. ANALYTICAL REPRESENTATION OF THE INFILL

A.1. Stiffness of the lateral joints

A.1.1. Elastic stiffness equal to 15MPa

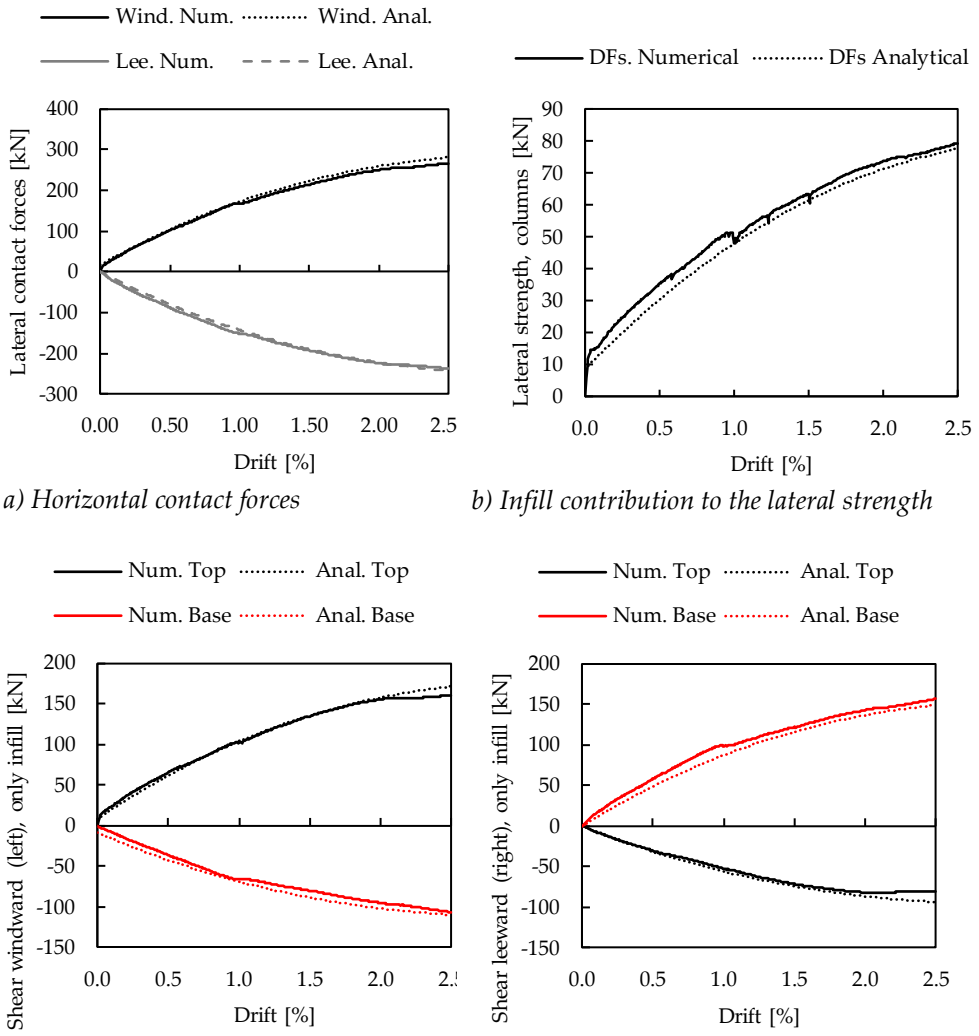

a) Horizontal contact forces

b) Infill contribution to the lateral strength

c) Shear actions on the windward column

d) Shear action on the leeward column

Figure 5.1: Comparison of the numerical and analytical results of the model characterised by a stiffness of lateral joints equal to 15 MPa.

A.1.2. Elastic stiffness equal to 30MPa

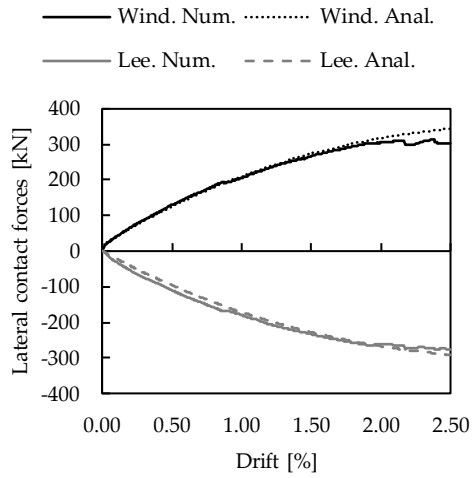

a) Horizontal contact forces

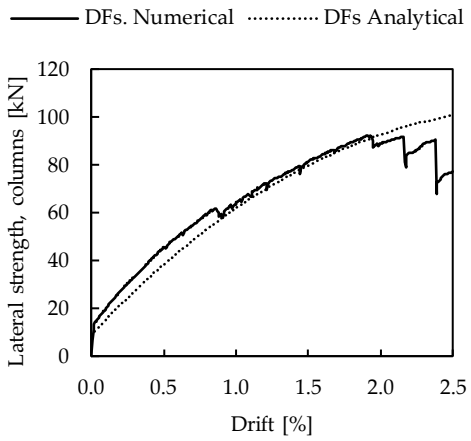

b) Infill contribution to the lateral strength

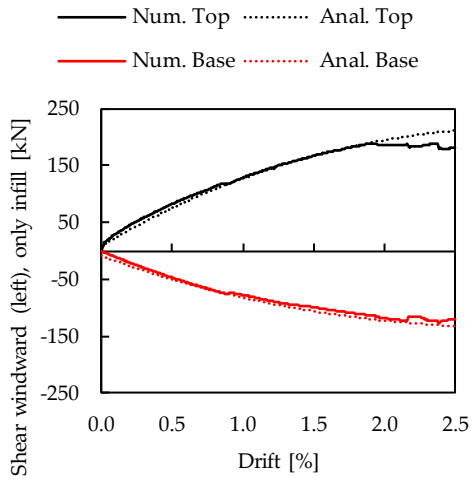

c) Shear actions on the windward column

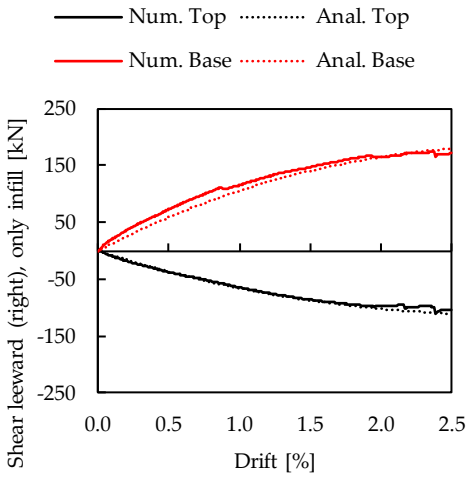

d) Shear action on the leeward column

Figure 5.2: Comparison of the numerical and analytical results of the model characterised by a stiffness of lateral joints equal to 30 MPa.

A.1.3. Elastic stiffness equal to 45MPa

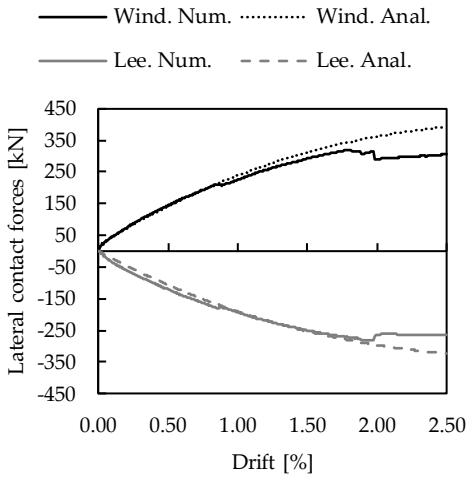

a) Horizontal contact forces

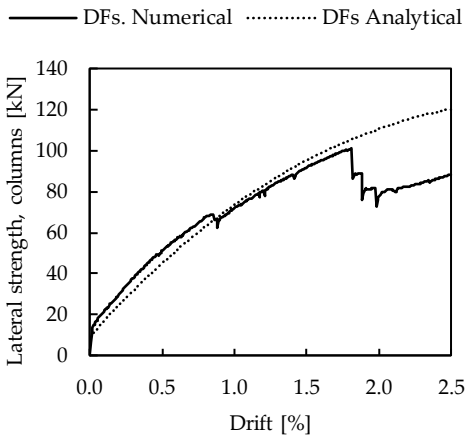

b) Infill contribution to the lateral strength

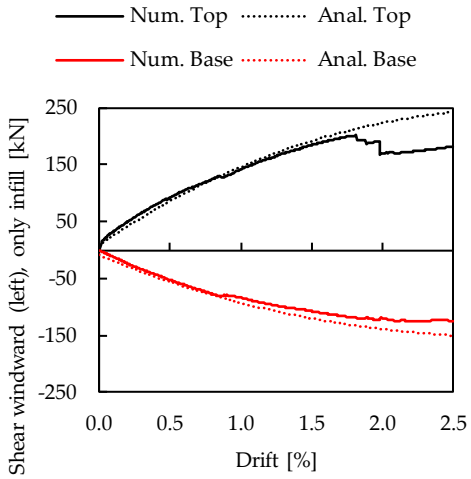

c) Shear actions on the windward column

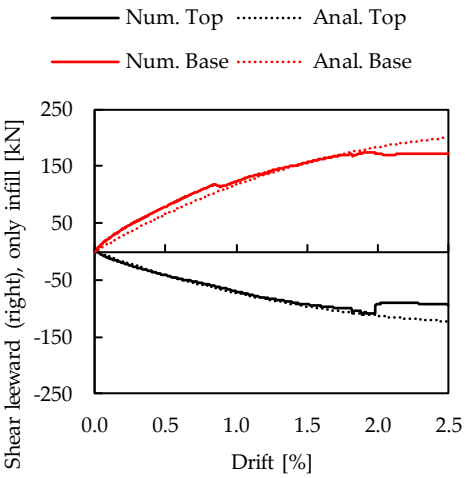

d) Shear action on the leeward column

Figure 5.3: Comparison of the numerical and analytical results of the model characterised by a stiffness of lateral joints equal to 45 MPa.

A.1.4. Elastic stiffness equal to 60MPa

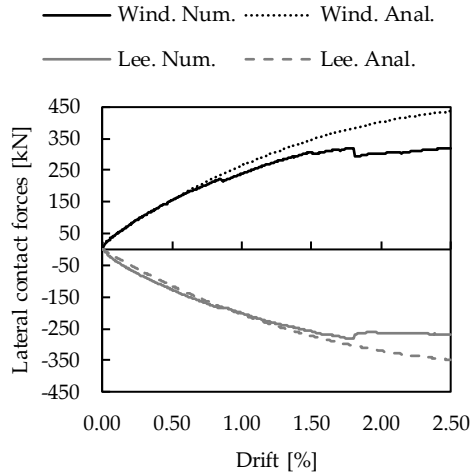

a) Horizontal contact forces

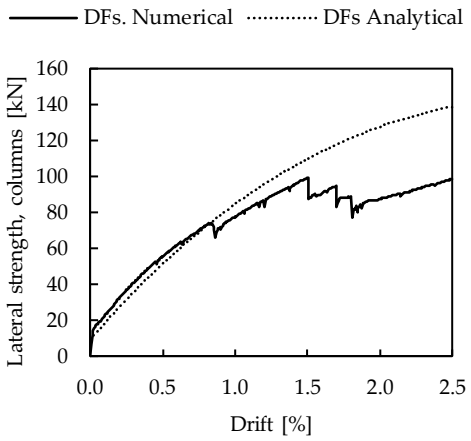

b) Infill contribution to the lateral strength

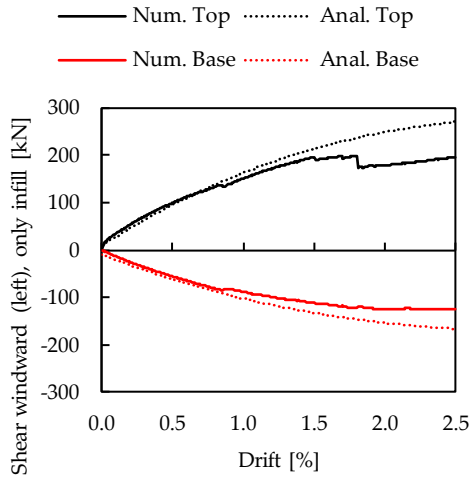

c) Shear actions on the windward column

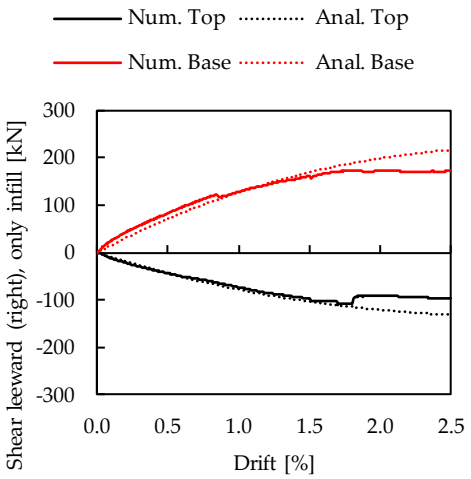

d) Shear action on the leeward column

Figure 5.4: Comparison of the numerical and analytical results of the model characterised by a stiffness of lateral joints equal to 60 MPa.

A.2. Infill length

A.2.1. Infill length equal to 320cm

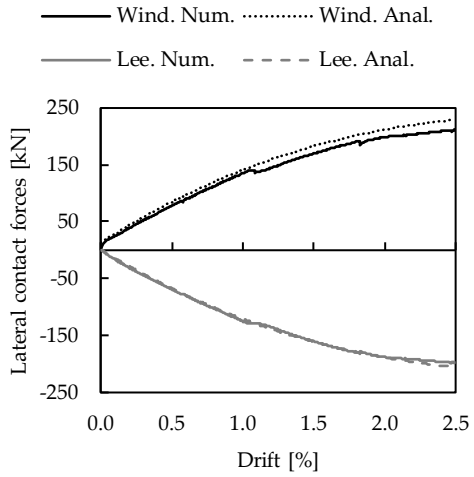

a) Horizontal contact forces

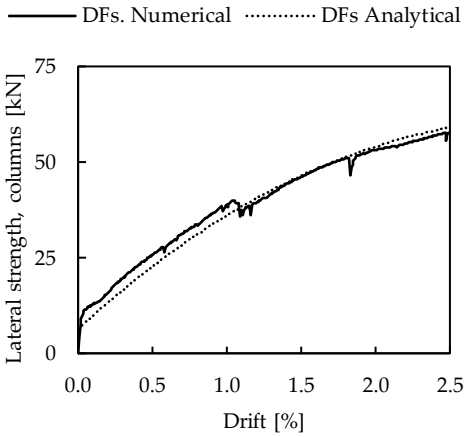

b) Infill contribution to the lateral strength

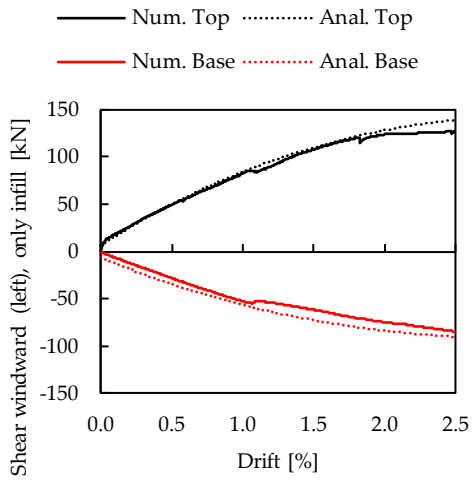

c) Shear actions on the windward column

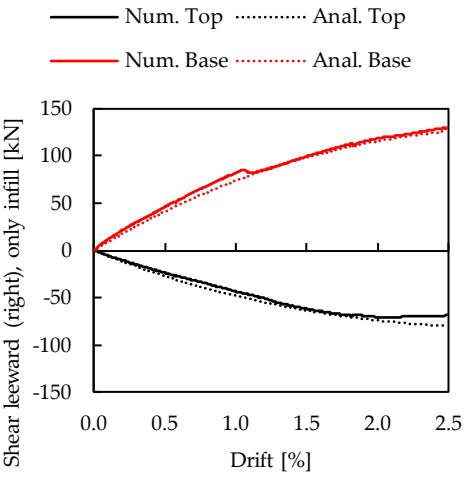

d) Shear action on the leeward column

Figure 5.5: Comparison of the numerical and analytical results of the model characterised by an infill length equal to 320cm.

A.2.2. Infill length equal to 520cm

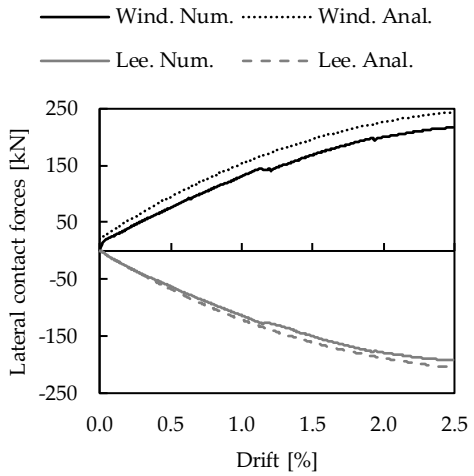

a) Horizontal contact forces

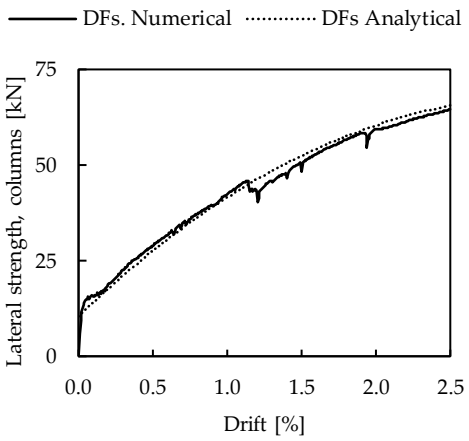

b) Infill contribution to the lateral strength

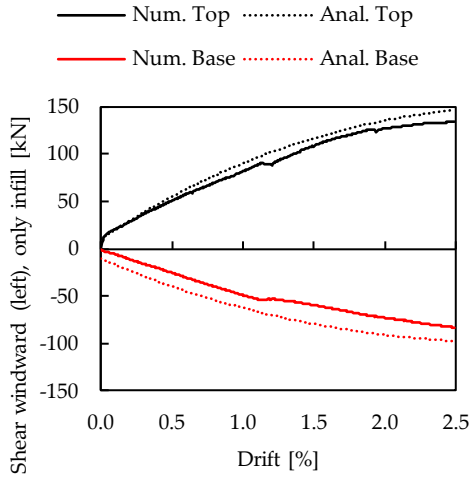

c) Shear actions on the windward column

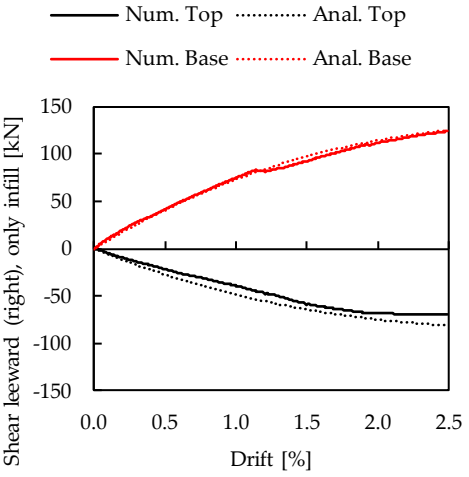

d) Shear action on the leeward column

Figure 5.6: Comparison of the numerical and analytical results of the model characterised by an infill length equal to 520cm.

A.2.3. Infill length equal to 610cm

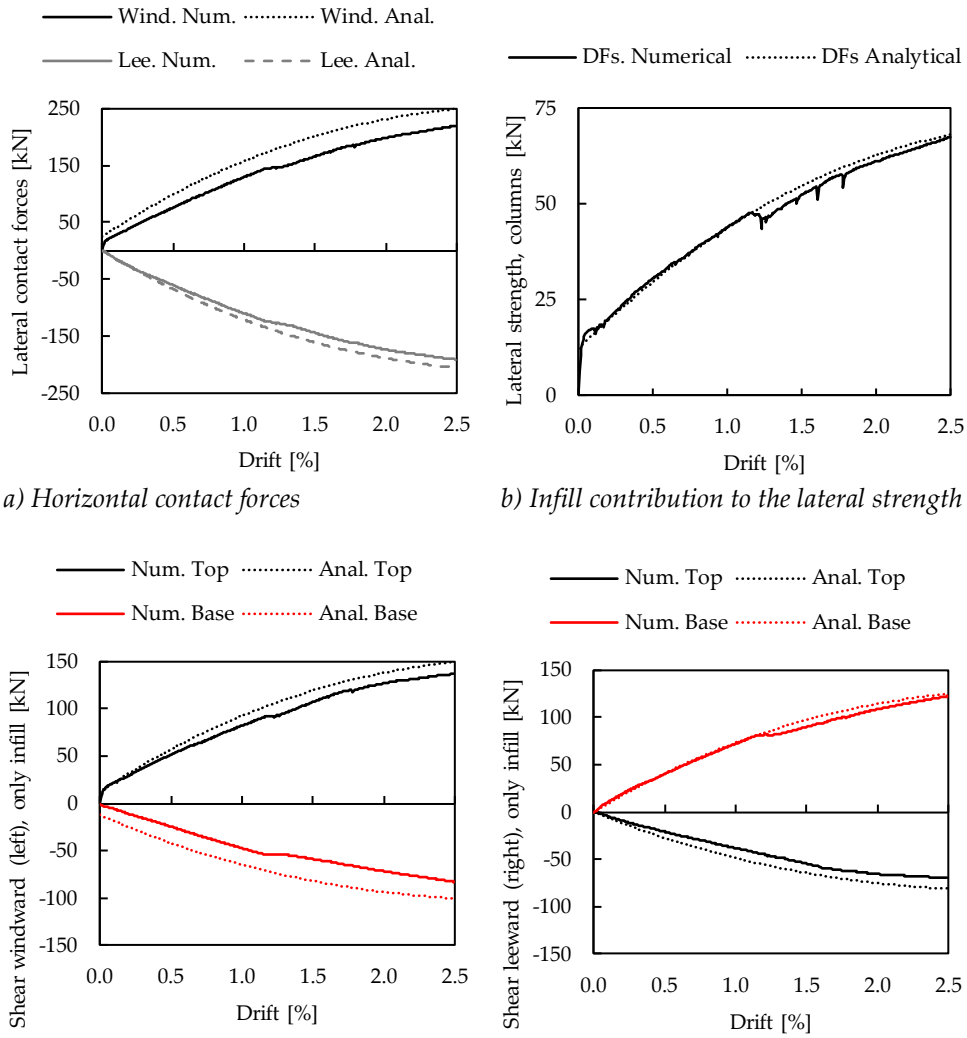

a) Horizontal contact forces

b) Infill contribution to the lateral strength

c) Shear actions on the windward column

d) Shear action on the leeward column

Figure 5.7: Comparison of the numerical and analytical results of the model characterised by an infill length equal to 610cm.

APPENDIX B. REFERENCE SRUCTURE DETAILS

B.1. Details of the designed frames

B.1.1. Frame "DCM" designed according to a behaviour factor equal to 3.9

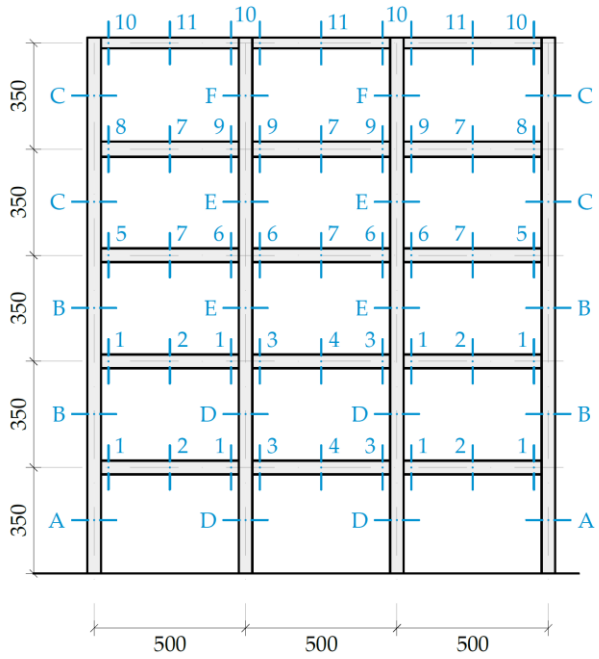

Figure 5.8: Indication of the main sections of beams and columns of frame "DCM".

Beams reinforcement					
Sect.	B [mm]	H [mm]	Reinf. Upper	Reinf. Low	Stirrups
1	350	450	4ϕ16+2ϕ20	5ϕ16	ϕ10/10
2	350	450	3ϕ16	4ϕ16	ϕ10/24
3	350	450	3ϕ16+2ϕ20	5ϕ16	ϕ10/10
4	350	450	3ϕ16	3ϕ16	ϕ10/24
5	350	450	3ϕ16+2ϕ20	4ϕ16	ϕ10/10
6	350	450	5ϕ16	4ϕ16	ϕ10/10
7	350	450	3ϕ16	3ϕ16	ϕ10/24
8	350	450	3ϕ16+1ϕ20	3ϕ16	ϕ10/10
9	350	450	4ϕ16	3ϕ16	ϕ10/10
10	350	350	3ϕ16	3ϕ16	ϕ10/10
11	350	350	3ϕ16	3ϕ16	ϕ10/24
Columns reinforcement					
Sect.	B [mm]	H [mm]	Reinf. Vertex	Reinf. Sides	Stirrups Conf. / Inner
A	450	450	4ϕ24	4ϕ20	3ϕ10/10 / 3ϕ10/15
B	450	450	4ϕ20	4ϕ20	3ϕ10/10 / 3ϕ10/15
C	450	450	4ϕ20	4ϕ16	3ϕ10/10 / 3ϕ10/15
D	450	450	4ϕ20	8ϕ20	4ϕ10/12 / 4ϕ10/19
E	450	450	4ϕ20	8ϕ16	4ϕ10/12 / 4ϕ10/19
F	450	450	4ϕ16	8ϕ16	4ϕ10/12 / 4ϕ10/19

Table 5.1: Reinforcement details of frame "DCM".

B.1.2. *Frame "DCM_2" designed according to a behaviour factor equal to 2.7*

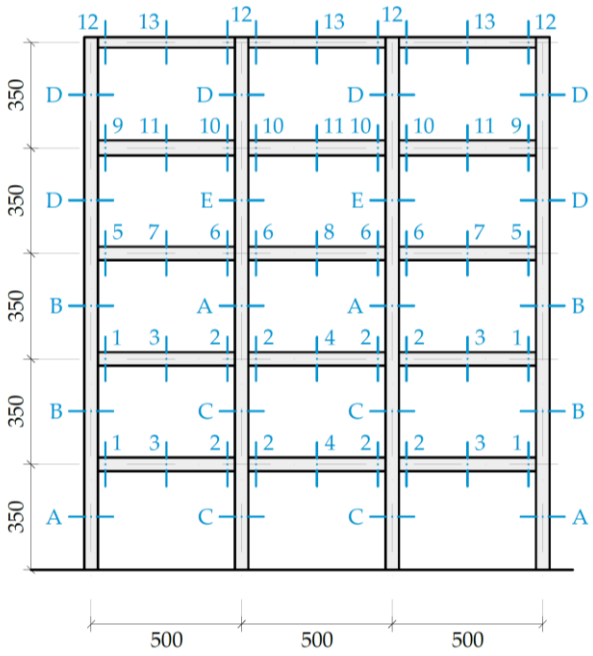

Figure 5.9: Indication of the main sections of beams and columns of frame "DCM_2".

Beams reinforcement					
Sect.	B [mm]	H [mm]	Reinf. Upper	Reinf. Low	Stirrups
1	400	550	7ϕ20	6ϕ20	ϕ10/10
2	400	550	6ϕ20	5ϕ20	ϕ10/10
3	400	550	3ϕ20	4ϕ20	ϕ10/15
4	400	550	3ϕ20	3ϕ20	ϕ10/20
5	400	500	6ϕ20	5ϕ20	ϕ10/10
6	400	500	5ϕ20	4ϕ20	ϕ10/10
7	400	500	3ϕ20	4ϕ20	ϕ10/15
8	400	500	3ϕ20	3ϕ20	ϕ10/15
9	400	500	3ϕ20 + 2ϕ16	5ϕ16	ϕ10/10
10	400	500	3ϕ20 + 1ϕ16	5ϕ16	ϕ10/10
11	400	500	3ϕ20	4ϕ16	ϕ10/20
12	350	450	3ϕ16	3ϕ16	ϕ10/10
13	350	450	3ϕ16	3ϕ16	ϕ10/20
Columns reinforcement					
Sect.	B [mm]	H [mm]	Reinf. Vertex	Reinf. Sides	Stirrups Conf. / Inner
A	500	500	4ϕ24	12ϕ20	4ϕ12/15 / 4ϕ12/20
B	500	500	4ϕ20	12ϕ20	4ϕ12/15 / 4ϕ12/20
C	500	500	4ϕ24	12ϕ24	4ϕ12/15 / 4ϕ12/17.5
D	500	500	4ϕ20	8ϕ20	4ϕ10/10 / 4ϕ10/20
E	500	500	4ϕ24	8ϕ20	4ϕ10/15 / 4ϕ10/17.5

Table 5.2: Reinforcement details of frame "DCM_2".

B.1.3. Ground motions

Code	Recorder ID	ID ITACA	Scale factor
OP1	IT.CSA.00.HN.IT-1997-0006	IT-1997-0006	N: 1.000
OP2	IT.MSCT.00.HG.EMSC-20161030_0000029	EMSC-20161030_0000029	N: 1.000
OP3	IV.RM33..HN.EMSC-20160824_0000006	EMSC-20160824_0000006	N: 1.000
OP4	IT.CRP.00.HN.IT-2012-0010	IT-2012-0010	N: 1.000
OP5	IV.T1256..HN.EMSC-20161030_0000029	EMSC-20161030_0000029	N: 1.000
OP6	IT.SPD.00.HG.EMSC-20161030_0000029	EMSC-20161030_0000029	N: 1.000
OP7	IT.CRP.00.HN.IT-2012-0011	IT-2012-0011	E: 1.000

Table 5.3: Ground motions selected for the OP limit state.

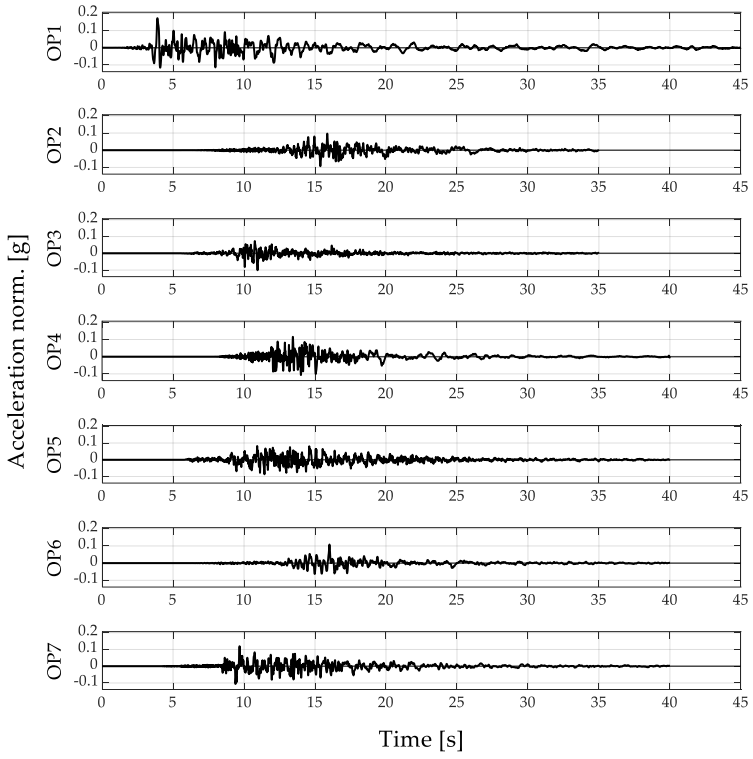

Table 5.4: Time history of the ground motions considered at the OP limit state.

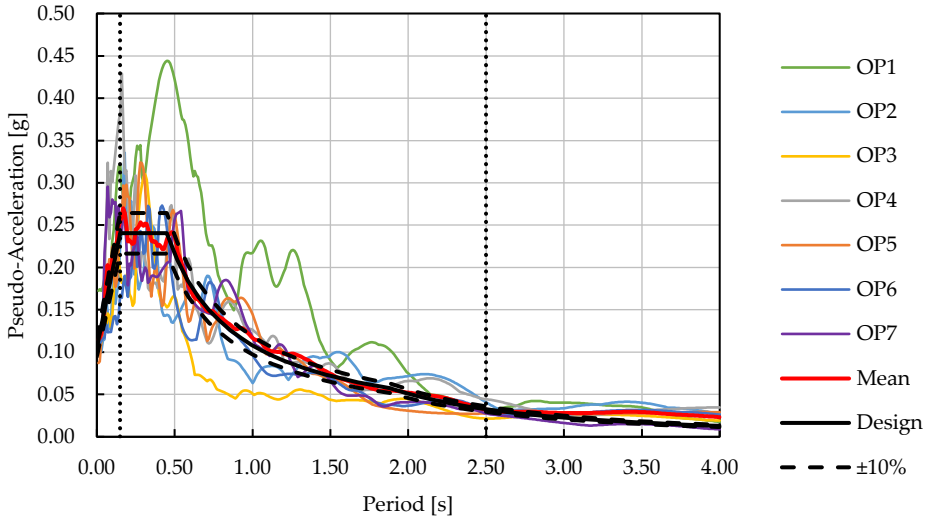

Table 5.5: Pseudo acceleration spectra of the ground motions at the OP limit state, average spectrum, design spectrum, and period and ordinates limit for the spectrum-compatibility evaluation.

Code	Recorder ID	ID ITACA	Scale factor
DL1	IT.CSA.00.HN.IT-1997-0006	IT-1997-0006	N: 1.000
DL2	IT.NOR.00.HG.EMSC-20161026_0000095	EMSC-20161026_0000095	N: 1.000
DL3	IT.MMO.00.HG.EMSC-20161026_0000095	EMSC-20161026_0000095	N: 1.000
DL4	BA.MIRH.00.HL.IT-2012-0011	IT-2012-0011	E: 1.000
DL5	IV.T1256..HN.EMSC-20161030_0000029	EMSC-20161030_0000029	E: 1.000
DL6	IV.T0824..HN.IT-2012-0011	IT-2012-0011	N: 1.000
DL7	E.SRC0.00.HN.IT-1976-0030	IT-1976-0030	N: 1.000

Table 5.6: Ground motions selected for the DLLS.

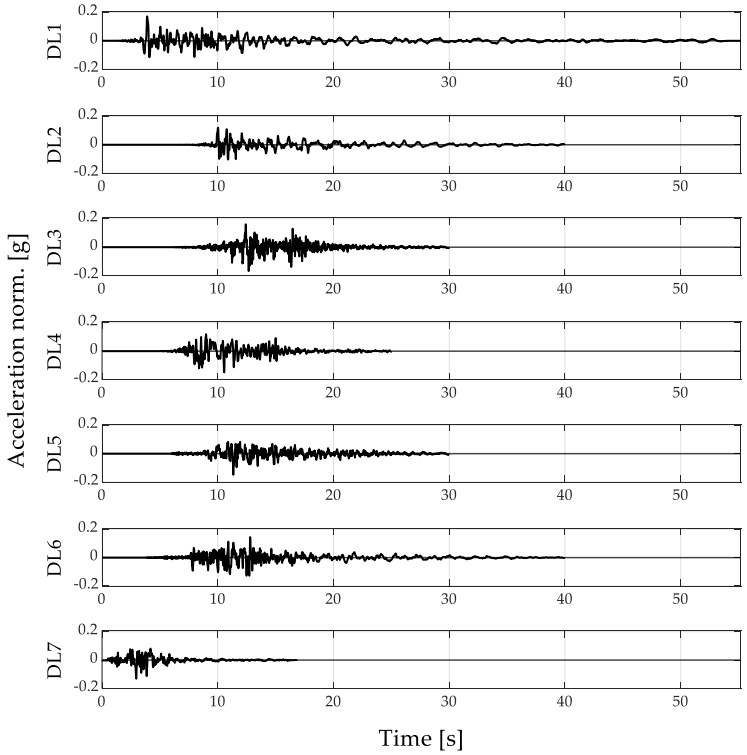

Table 5.7: Time history of the ground motions considered at the DL limit state.

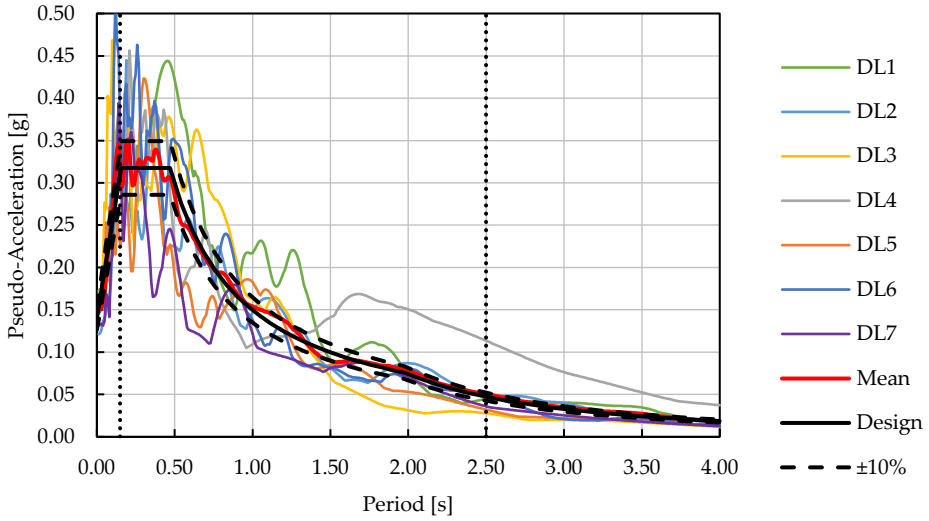

Table 5.8: Pseudo acceleration spectra of the ground motions at the DL limit state, average spectrum, design spectrum, and period and ordinates limit for the spectrum-compatibility evaluation.

Code	Recorder ID	ID ITACA	Scale factor
NC1	IT.MRN.00.HN.IT-2012-0008	IT-2012-0008	N: 1.603
NC2	IT.MTR.00.HG.EMSC-20160824_0000006	EMSC-20160824_0000006	E: 5.242
NC3	BA.MIRE.00.HL.IT-2012-0011	IT-2012-0011	N: 1.562
NC4	IT.MRN.00.HN.IT-2012-0008	IT-2012-0008	E: 1.613
NC5	IT.CSA.00.HN.IT-1997-0006	IT-1997-0006	E: 4.002
NC6	IT.SAN0.00.HN.IT-2012-0011	IT-2012-0011	E: 2.427
NC7	IT.NOR.00.HG.EMSC-20161026_0000095	EMSC-20161026_0000095	N: 3.505

Table 5.9: Identification of the ground motions selected for the NC limit state.

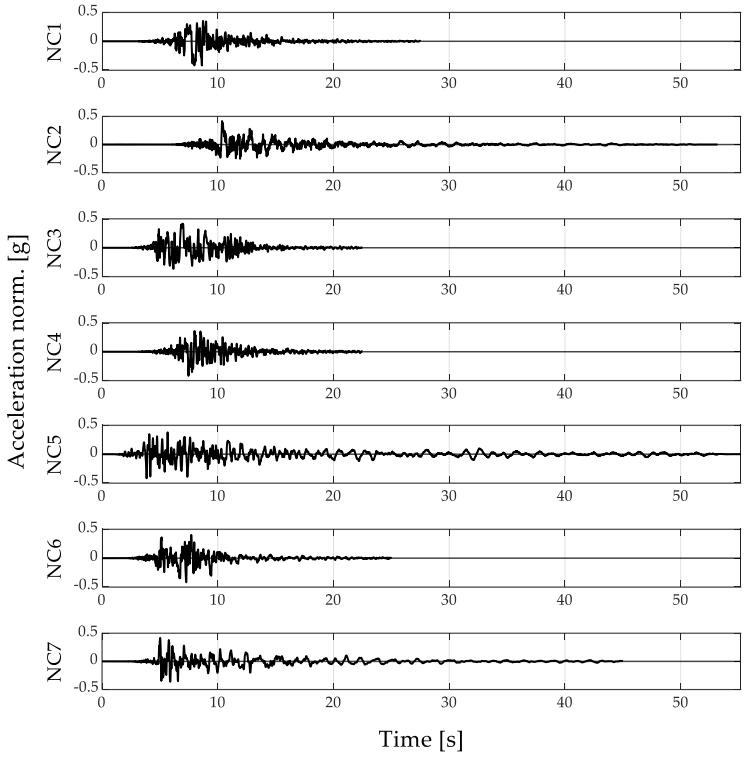

Table 5.10: Time history of the ground motions considered at the NC limit state.

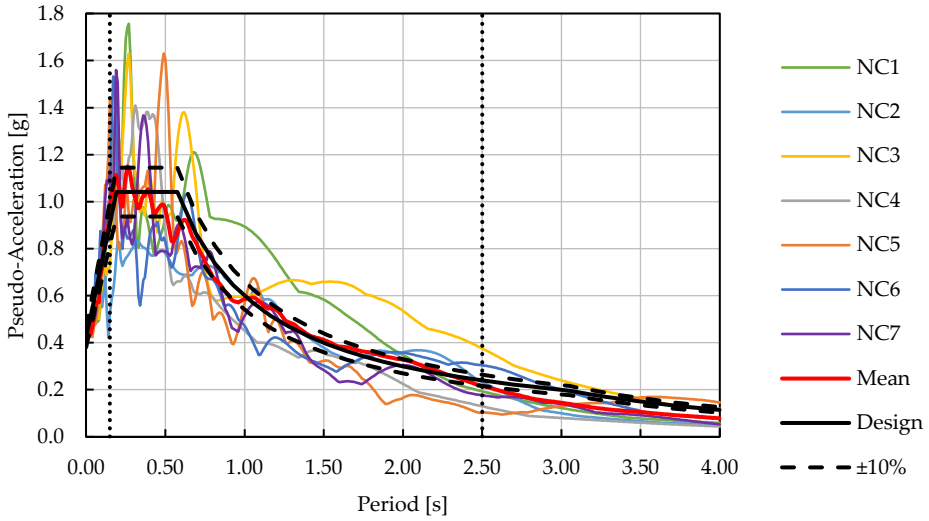

Table 5.11: Pseudo acceleration spectra of the ground motions at NC limit state, average spectrum, design spectrum, and period and ordinates limit for the spectrum-compatibility evaluation.

APPENDIX C. NUMERICAL RESULTS

C.1. Influence of ductility level and infill characteristics

C.1.1. Ductility level

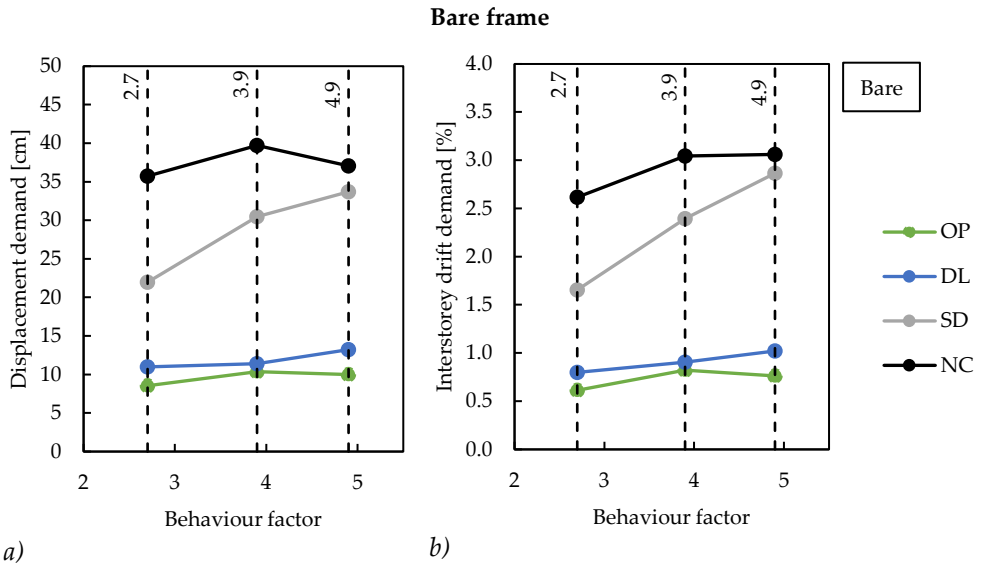

Figure 5.10: Comparison of the displacement a) and interstorey drift b) profiles at different limit states for different design behaviour factor in the bare frame.

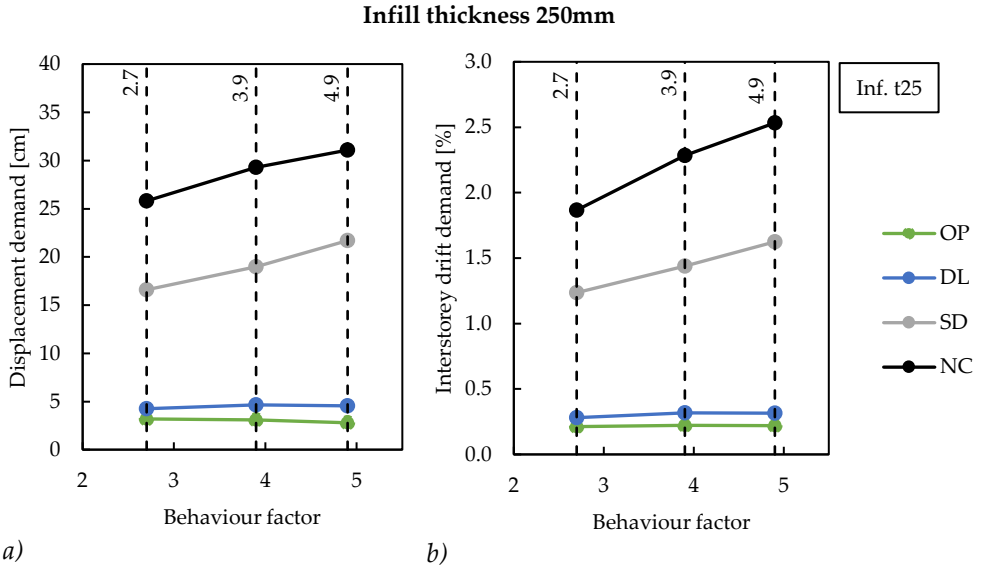

Figure 5.11: Comparison of the displacement a) and interstorey drift b) profiles at different limit states for different design behaviour factor in the infilled configuration with infill thickness equal to 250mm.

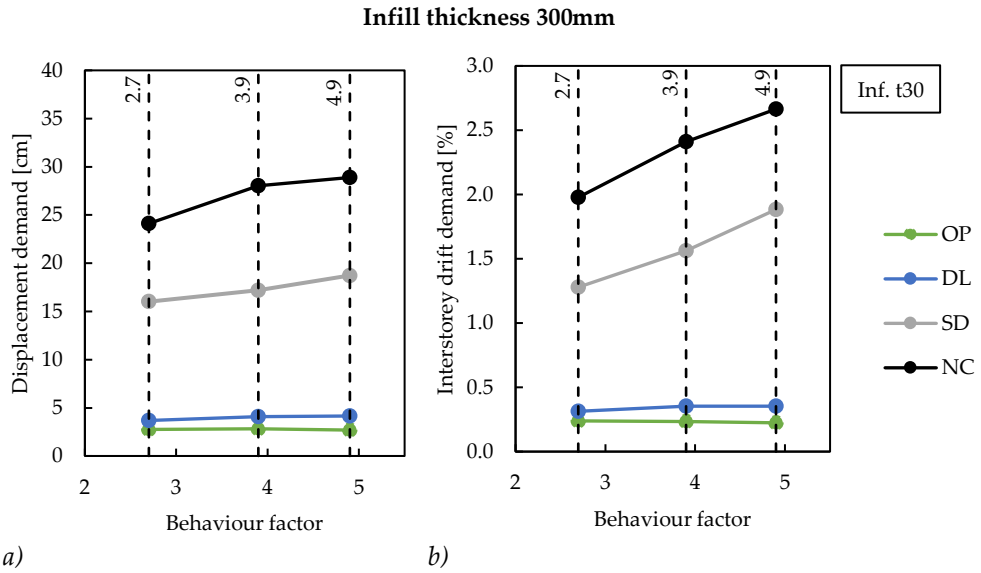

Figure 5.12: Comparison of the displacement a) and interstorey drift b) profiles at different limit states for different design behaviour factor in the infilled configuration with infill thickness equal to 300mm.

C.1.2. *Infill characteristics*

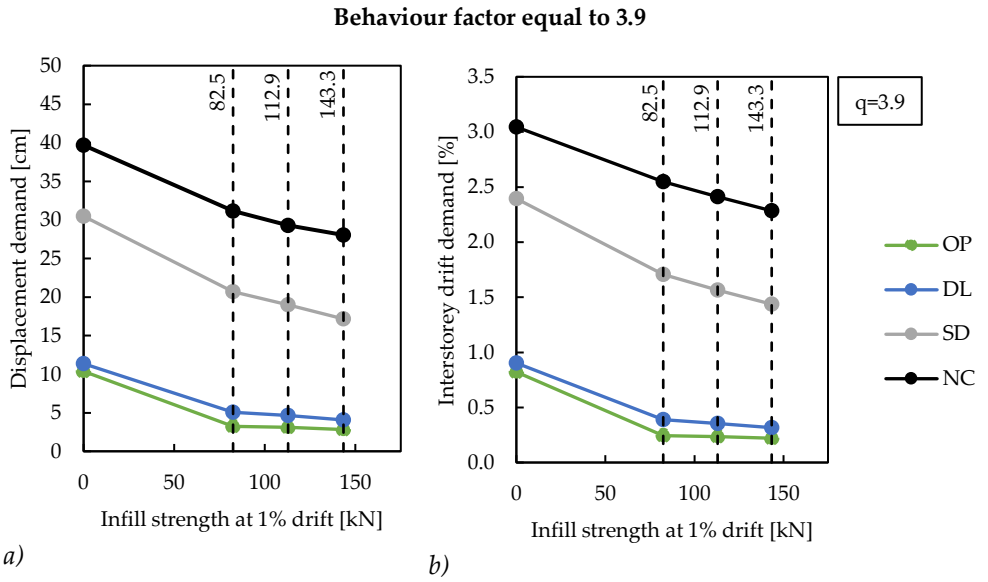

Figure 5.13: Comparison of the displacement a) and interstorey drift b) profiles for different infill characteristics on frame "DCM" (behaviour factor equal to 3.9).

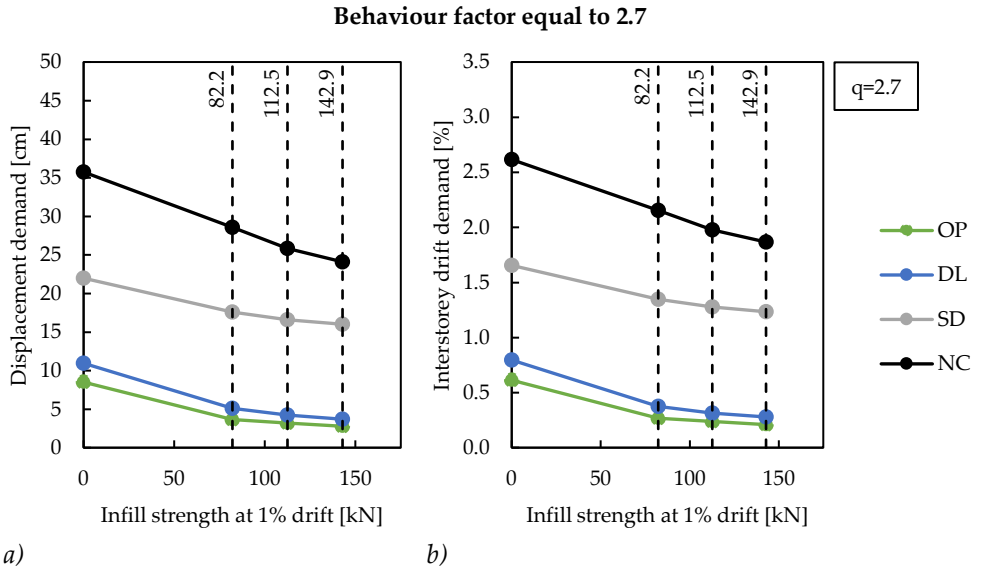

Figure 5.14: Comparison of the displacement a) and interstorey drift b) profiles for different infill characteristics on frame "DCM_2" (behaviour factor equal to 2.7).